NANOPARTICLE DISPERSED DEEP EUTECTIC SOLVENTS AS LOW-COST HEAT TRANSFER FLUID FOR CONCENTRATED SOLAR POWER

Submitted in Partial Fulfilment of the Requirements

for the Degree of

DOCTOR OF PHILOSOPHY

By

PYARIMOHAN DEHURY

DEPARTMENT OF CHEMICAL ENGINEERING

INDIAN INSTITUTE OF TECHNOLOGY GUWAHATI

January, 2021

भारतीय प्रौद्योगिकी संस्थान गुवाहाटी
रासायनिक अभियांत्रिकी विभाग
गुवाहाटी ७८१ ०३९, असम, भारत

INDIAN INSTITUTE OF TECHNOLOGY GUWAHATI
Department of Chemical Engineering
Guwahati 781039, Assam, India

CERTIFICATE

This is to certify that the work contained in the thesis entitled "***Nanoparticle Dispersed Deep Eutectic Solvents as Low-Cost Heat Transfer fluid for Concentrated Solar Thermal Power Plant***" is the result of investigations carried out by **Pyarimohan Dehury**, under my supervision and is submitted to the Indian Institute of Technology Guwahati Guwahati-781039, Assam, India for the award of degree of Doctor of Philosophy. This work has not been submitted elsewhere for a degree.

_____

Date:

Prof. Tamal Banerjee

Professor,

Department of Chemical Engineering

भारतीय प्रौद्योगिकी संस्थान गुवाहाटी
रासायनिक अभियांत्रिकी विभाग
गुवाहाटी ७८१ ०३९, असम, भारत

INDIAN INSTITUTE OF TECHNOLOGY GUWAHATI
Department of Chemical Engineering
Guwahati 781039, Assam, India

DECLARATION

I hereby declare that the matter embodied in this thesis is the result of investigations carried out by me in the Department of Chemical Engineering, Indian Institute of Technology Guwahati, Assam, India under the supervision of **Prof. Tamal Banerjee**, Department of Chemical Engineering and is submitted to the Indian Institute of Technology Guwahati, Guwahati-781039, Assam, India for the award of degree of Doctor of Philosophy. This work has not been submitted elsewhere for any degree or diploma of any institute or university to the best of my knowledge and belief.

In keeping with the general practice of reporting scientific observations, due acknowledgements have been made wherever the work of other investigators are referred, and copyright licenses have been taken from respective publishers.

Guwahati — **PYARIMOHAN DEHURY**

September 2020 — Roll No: 156107021

Dedicated
To
My Parents

ACKNOWLEDGEMENT

I would like to thank all who contributed to this thesis work and supported me to complete my PhD.

Firstly, I express my sincere thanks and deepest gratitude to my supervisor, **Prof. Tamal Banerjee**, for his continuous support, encouragement, motivation and guidance throughout the tenure of Ph.D. It has been a great privilege and honour for me to work under him.

I am grateful to Doctoral committee members, **Dr. Pankaj Tiwari, Dr. Partho Sarathi Gooh Pattader** and **Prof. S. Kanagaraj** for their comments, suggestions and time for reviewing this work.

I would like to thank **IMPRINT India, Ministry of Human Resources and Development, Government of India** for funding this project (4077).

I would like to express my sincere thanks to **Prof. Dipankar Bandyopadhyay, Prof. Kaustav Mohanty** and **Dr. V. Vaibhav Goud** for their comments and suggestions during my annual progress review. I take this opportunity to thank all the faculty members for their valuable suggestions and cooperation during my Ph.D. work. I am grateful to **Prof. Anugrah Singh**, Head, Department of Chemical Engineering for his administrative support. Furthermore, I extend my gratitude to other faculty and staff members of Department of Chemical Engineering for their assistance.

I am indebted to **Prof. Amaresh Dalal** and his student **Mr. Rahul Kumar Chaudhary** for helping me with *AnuPravaha* Simulation. I convey my sincere thanks to **Mr. Jarandan Singh** (M.Tech, IITG) for assisting me with COMSOL simulations.

Special thanks to my seniors and friends: **Dr. D. V. Rabari**, **Dr. Anand Bharti**, **Dr. Basudhrity Banerjee**, **Dr. Sanjukta Bhoi**, **Dr. Mood Mohan**, **Dr. Papu Kumar Naik** for their invaluable suggestions, comments and friendship. I acknowledge my research group members: Dhirendra, Nikhil, Nabendu and Sambita for providing a co-operative research environment in the laboratory.

I would like to acknowledge **Central Instruments Facility (CIF), Analytical Laboratory, Department of Chemical Engineering** and **Department of Chemistry** of IIT Guwahati for providing me necessary characterization facilities.

Finally, I would like to express my sincere gratitude to my family, father **Mr. Harsha Chandra Dehury**, mother **Mrs. Kuni Pradhan**, and sister **Mrs. Priyadarshini Dehury**. Their blessings and never-ending support are the real stimulus that constantly inspires me to do my best. Last but not the least, my deepest gratitude goes to my wife, **Mrs. Upasana Mahanta,** for her constant encouragement, unlimited sacrifices and patience, sincere prayers, continuous support and motivation for the completion of this thesis work. Furthermore, I am thankful to my father-in-law **Mr. Chakrapani Mahanta,** mother-in-law **Mrs. Mina Mahanta,** brother-in-law **Mr. Devabrat Mahanta.**

Above all, I would like to thank the "**LORD JAGANNATH**" for his blessings and providing the unseen moral support that directed me through my good as well as hard times.

Guwahati **PYARIMOHAN DEHURY**

September 2020

Synopsis

Concentrated Solar Power (CSP) is one of the emerging renewable energy technologies, where sunlight is concentrated from a large area and stored in a collector filled with heat transfer fluid (HTF). In a CSP, increased heat transfer effect is a key deliverable which is usually obtained by enhancing the thermophysical properties of HTF. The HTF usually works as a heat storage and transfer media simultaneously. Some of the commercially used HTFs are Therminol VP1, synthetic oil and molten salt mixtures. However, these HTFs have some drawbacks like high vapor pressure, high melting point and their corrosive nature. In this context Deep Eutectic Solvents (DESs) are the emerging group of new generation green solvents which are low cost and easy to prepare. DESs are the mixture of two components namely hydrogen bond acceptor (HBA) and hydrogen bond donor (HBD) having their melting point lower than the individual components.

The current thesis explores DESs as HTFs primarily for CSP. The eutectic point of the DES is initially computed through the quantum chemical-based COSMO-SAC (COnductor-like Screening MOdel-Segment Activity Coefficient) model. Six set of DESs are prepared to explore the potential HTFs. Initially DL-menthol + Oleyl alcohol (DES1) and DL-menthol + Oleic acid (DES2) with a molar ratio of 1:1 and 1:1.4 were prepared respectively. Thereafter Diphenyl ether + DL-menthol (DES3), Diphenyl ether + Benzophenone (DES4), Benzophenone + Biphenyl (DES5) and Methyl triphenyl phosphonium Bromide (MTPB) + Ethylene glycol (DES6) with a molar ratio of 1:1.1, 1.7:1 ,1.66:1 and 1:4 respectively, were also prepared and explored. In order to confirm the formation of DES, Nuclear Magnetic Resonance (NMR) Spectroscopy including ^{1}H, ^{13}C and NOESY (2D) NMR spectra were scanned and recorded. The moisture content of DESs

were around ~1% by weight, the only exception being DES6. Further the vapour pressure and thermal stability of the DESs were also measured by a Stirred-Flask Ebulliometer and through TGA analysis respectively.

In order to enhance the thermal properties of DES or base fluids, the Nanoparticles Dispersed Deep Eutectic Solvents (NDDES) were prepared by adding nanoparticles in specific weight percent. Three different shapes of nanoparticles (namely Al_2O_3 spherical, Al_2O_3 cylindrical and *h*-BN hexagonal) at three different weight percentage (0.02, 0.05, 1.0 wt.%) are selected for the synthesis of NDDES. The stability of the nanoparticles was confirmed by sedimentation image capturing, centrifugal method, zeta potential, microscopic imaging method and transmission electron microscopy method.

The thermophysical properties namely density, viscosity, thermal conductivity and specific heat capacity are measured within the temperature range 298.15 - 353.15 K. The density of DESs and NDDES were found to decrease with increase in temperature while the rheological measurements suggest a Newtonian fluid with its shear viscosity decreasing exponentially with increasing temperature. Further the nanoparticles are found to have negligible effect on physical properties (density and viscosity) on the base fluid thereby limiting the pressure drop and also the coefficient of friction. For its potential application as thermal fluids for CSP, the thermal properties for DESs and NDDESs are also measured. The thermal conductivity of DESs and NDDESs is found to be decreasing with increase in temperature. The thermal conductivity of NDDES is found to be higher as compared to the DES. The specific heat capacity of the DES and NDDES is measured and found to be increasing with temperature. Further an overall enhancement of the specific heat capacity is observed with addition of nanoparticles. Further, based on these four thermophysical properties, the Mouromtseff number (M_o) was calculated to rank the NDDESs. The

nanofluid consisting of DES3 + *h*-BN hexagonal nanoparticles (0.02 wt. %) gave the highest M_o value and hence it was further considered for the experimental forced convection study and process simulation using Aspen Plus simulator.

The performance of these solvents was evaluated in a forced convective heat transfer configuration under both laminar and turbulent flow conditions with varying Reynolds number and heat flux. The convective heat transfer experiments of DES1 under laminar flow condition demonstrated the fact that the thermal entrance length of the DES1 is very large due to its high viscosity and low thermal conductivity. The convective heat transfer data, namely heat transfer coefficient and Nusselt number were compared with the in-house *AnuPravaha* CFD simulator under laminar conditions. The forced convection experiments are also conducted for both DES2 and NDDES10 (DES2 + 0.02 wt. % Al_2O_3 spherical nanoparticles) under laminar condition (Re=124, 186 and 250). The enhancement in local heat transfer coefficient were found to be higher when compared to their thermophysical properties. This was due to the nanoparticle migration resulting in a non-uniform distribution of both thermal conductivity and viscosity fields. This inherently were found to reduce the thermal boundary layer thickness. In the final section, the heat transfer coefficient and the Nusselt number were also validated with COMSOL Multiphysics simulation. Further the forced convection experiments for the DES3 and NDDES25 (DES3 + 0.02 wt. % *h*-BN hexagonal nanoparticles) are carried out under both laminar and turbulent region. The temperature profiles, heat transfer coefficient and Nusselt number (*Nu*) are evaluated and compared for nanofluid NDDES25 (DES3 + 0.02 wt. % *h*-BN hexagonal nanoparticles) with the corresponding base fluid (DES3). The flow behaviour of the thermal fluid along the characteristic length of the test section was investigated for both the laminar and turbulent regimes.

Eventually ASPEN plus flowsheet is conceptualized to ascertain the steam generation rate and overall heat transfer coefficient of these novel solvents. In this respect, overall performance of a two-stage steam generator consisting of a U-tube (U-T) heat exchanger and a shell and tube (S-T) heat exchanger are explored. Initially benchmarking simulations are performed on known storage media based on nitrate salts. A reported combination of nitrate-based molten salt was used as a thermal fluid. The simulation was performed with three different flow rates of molten salt, i.e., 1, 1.5 and 2 m^3/hr with a constant water flow rate of 25 kg/hr. The inlet temperature of molten salt was varied between 583.15 - 673.15 K. The results from the simulation agreed well with respect to the overall heat transfer coefficient, heat flux, steam generation rate and efficiency. Thereafter the simulation has been performed using the new thermal solvent system namely DES2. As DES is not available in the commercial simulator such as ASPEN Plus, a pseudo-component approach was adopted using the COSMO-SAC base method using its thermophysical properties as input. The inlet flow rate of DES was varied from 2-3 m^3/hr between the inlet temperature range of 503.15-603.15 K. Overall within the same exchanger network and operating conditions, the thermal properties such as heat transfer coefficient, heat flux, steam generation rate and thermal efficiency were an order of magnitude higher than the molten salts thereby holding promising application. Further the ASPEN Plus simulation was also performed using NDDES25 (DES3 + 0.02 wt. % *h*-BN hexagonal nanoparticles) and the effectiveness of the HTF in terms of steam generation capacity was predicted and it was observed that the nanofluid with 0.02 wt.% was able to successfully convert 100 % of the input water (15 kg/hr) into superheated steam at 494.15 K.

An overall summary of the thesis is presented in Figure 1 as below.

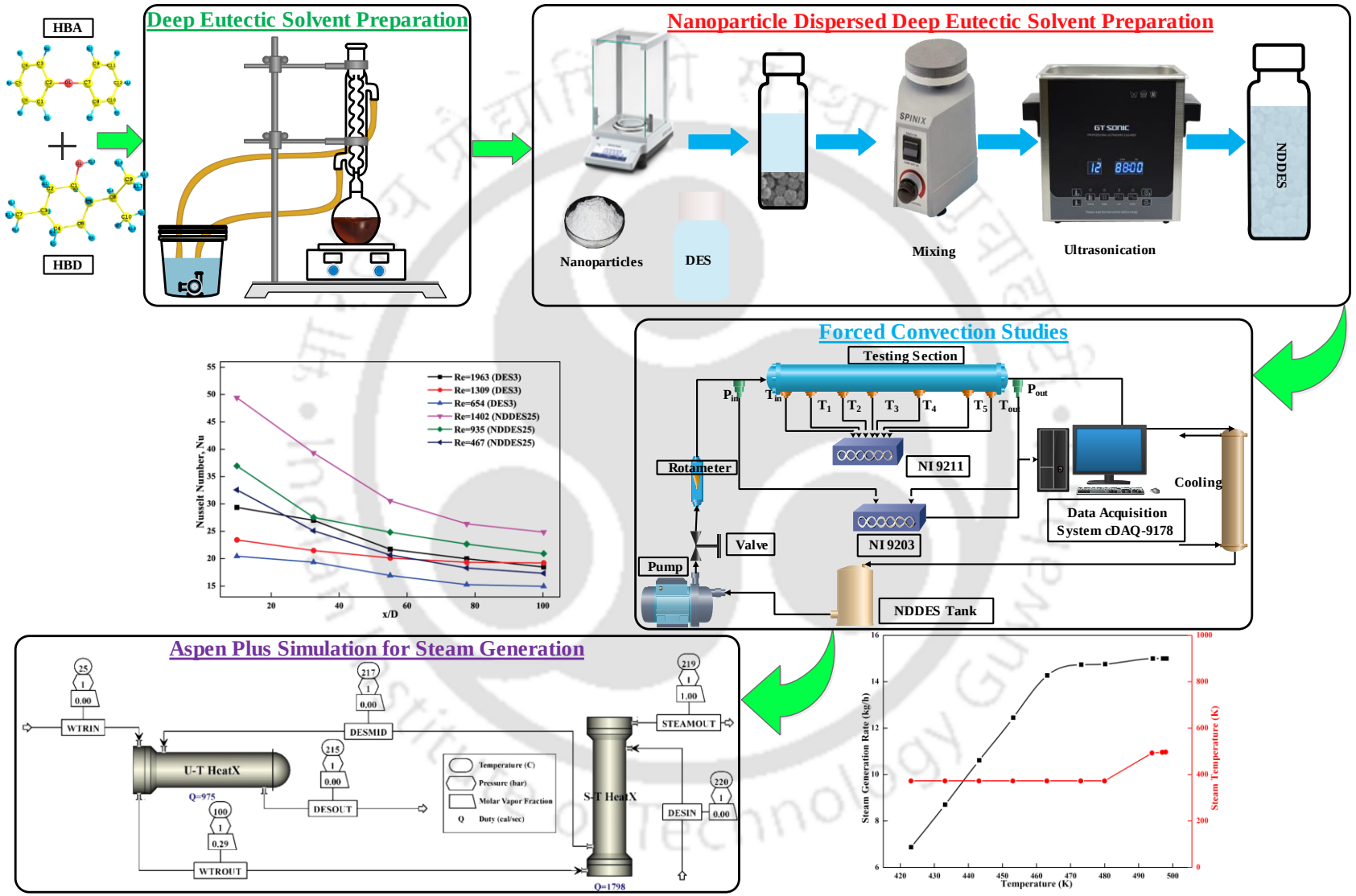

Figure A: Graphical Summary of the Thesis Work

TABLE OF CONTENTS

LIST OF FIGURES

LIST OF TABLES

Abbreviations

AMW	Average Molecular Weight
ASTM	American Society for Testing and Materials
BN	Boron Nitride
$CDCl_3$	Chloroform-d
CFD	Computational Fluid Dynamics
COSMO-SAC	COnductor-like Screening MOdel-Segment Activity Coefficient
CSP	Concentrated Solar Power
DES	Deep Eutectic Solvent
DFT	Density Functional Theory
DMSO-d_6	Dimethyl Sulfoxide-d6
DSC	Differential Scanning Calorimetry
EDL	Electrical Double Layer
EDR	Exchanger Design and Rating
HeatX	Heat Exchanger
HBA	Hydrogen Bond Acceptor
HBD	Hydrogen Bond Donor
HTF	Heat Transfer Fluid
IL	Ionic Liquid
KFT	Karl Fischer Titration
LTTM	Low Transition Temperature Mixture
MTPB	Methyl Triphenyl Phosphonium Bromide
NADES	Natural Deep Eutectic Solvent
NDDES	Nanoparticles Dispersed Deep Eutectic Solvents

NI	National Instrument
NMR	Nuclear Magnetic Resonance
NOESY	Nuclear Overhauser Effect Spectroscopy
PV	Photovoltaics
SALTIN	Molten Salt Inlet
SALTMID	Molten Salt Intermediate
SALTOUT	Molten Salt Outlet
SLE	Solid-Liquid Equilibria
STEAMOUT	Steam Outlet
S-T	Shell and Tube
TC	Thermal Conductivity
TEM	Transmission Electron Microscopy
TGA	Thermogravimetric analysis
U-S	U-tube
WTRIN	Water Inlet
WTROUT	Water Outlet

Symbols

α'	misfit energy interaction constant (kcal Å^4/ (mol e^2))
σ_{HB}	hydrogen-bonding interaction (e/Å^2)
c_{HB}	hydrogen-bonding interaction constant (kcal Å^4/ (mol e^2))
γ_{solute}	activity coefficient
x_{solute}	mole fraction
ΔH_f	enthalpy of fusion (J/mol.K)
ΔT_{bM}	contribution to the normal boiling temperature (K)
ΔT_m	LMTD (K)
τ_{ij}	stress tensor
ρ	Density (kg/m^3)
^{1}H	Proton NMR
^{13}C	Carbon NMR
A	heating surface area (m^2)
a_{eff}	surface area of the segment (Å^2)
C_p	specific heat capacity of DES (J/kg.K)
D	Inner diameter of the pipe (m)
d_0	outer diameter (m)
h_{in}	inlet enthalpies of water/steam (J/kg)
h_{out}	outlet enthalpies of water/steam (J/kg)
$h(x)$	local heat transfer coefficient (W/m^2.K)
I	input current (A)

k_f	thermal conductivity of the liquid
k_s	thermal conductivity of stainless steel
L	heating length of testing section
l	testing section length
L_h	length of hydrodynamic entry region
L_t	length of thermal entry region
$\overline{M}_w$	average molecular weight
M_i	molecular weight of component *i*
M_o	Mouromtseff number
N_i	number of molecules of component *i*
N_u	Nusselt Number
n_i	frequency of appearance of the i^{th} group of atoms in the molecule
T_m	melting point (K)
P_r	Prandtl number
Q	power (watt)
Q_{ab}	heat absorbed by cold fluid (water/steam) (Watt)
q	heat flux (kW/m^2)
$q_{v,DES}$	volumetric flow rate of DES in K. (m^3/hr)
$q_{m,w}$	mass flow rate of water/steam (kg/hr)
R_e	Reynold's number
r_i	inner radius (m)
r_o	outer radius (m)

S_{tot}	heat transfer area of the steam generator (m^2)
T_b	boiling point (K)
T_{fi}	liquid inlet temperature (K)
$T_f'(x)$	local temperatures of the liquid (K)
T_{in}	inlet temperature of DES (K)
T_{out}	outlet temperature of DES (K)
$T_w(x)$	outer surface local temperature (K)
$T_w'(x)$	local temperatures of the inner surface (K)
U	overall heat transfer coefficient ($W/m^2.K$)
V	input voltage (V)
V'	volumetric flow rate (m^3/s)

CHAPTER 1

1 INTRODUCTION

1.1 Motivation

India's most critical issue in the recent global world are its energy demand. According to the BP Energy Outlook 2019[1] report, India has a primary energy demand of roughly double (i.e., ~11%) by 2040 as compared to total global primary energy demand. Among the new energy demand, 42% is acquired by coal, which leads to doubled CO_2 emission by 2040. This results in the increase of average surface temperature by 0.6°C[2] over the last century which is further expected to increase by 1.4-5.8°C by 2100[3]. The rapidly increasing global warming due to the CO_2 emission from the burning of fossil fuel like coal in energy production has now became a matter of concern for the environmental activists and researchers. Environmental concerns, swift depletion and increasing prices of conventional fossil fuel has forced the researchers in exploring consistent and economically sustainable alternate source of energy[4]. Renewable source of energy is one of possible solution in terms of environmental, sustainable and economic perspective. The different sources of renewable energy are usually classified as wind, hydro, solar, biomass, biofuel, and geothermal. From the above sources of renewable energy, solar energy is one of the most abundant sources of energy in the world.

In general, there are two different types of solar energy utilization, namely solar photovoltaics[5] (PV) (direct conversion) and solar thermal system (indirect thermal storage system)[6]. In solar PV technology[5] direct sunlight is used to generate electricity by the help of semiconductor cells. Even though due to their low efficiency and high cost effective ratio of the solar PV cells[7], solar thermal system are still the acceptable technology for the next generation renewable energy technologies[8]. In solar thermal technology, the heat from the solar radiation is captured and utilized directly by different residential and commercial

applications[9,10]. The key benefit of the solar thermal technology is that the heat can be stored in HTF (Heat Transfer Fluid) which can be used in night. The heat is generally transferred to the HTF by using solar thermal collectors. Based on the design collectors, they are divided into three types namely, low temperature collectors, medium temperature collector and high temperature collector. The low temperature collectors operate at temperatures below 100°C. The medium temperature collectors are used for solar cooking. The high temperature collectors are used for electricity generation. Further the stored energy is converted into mechanical energy and in turn electricity, which is also known as concentrated solar power (CSP)[11]. In CSP technology the heat is stored in a heat transfer fluid (HTF) where high temperature is reached. The HTF heats the liquid media namely water, resulting in the production of steam which rotates a turbine (mechanical energy), thereby producing electricity. An additional capacity of 381.6 MW in 2019 to the global solar thermal capacity ensured a total installed capacity of 6,451 MW. As compared to 2018, there is an increment of 6.29 % in terms of solar thermal projects in 2019. China has successfully completed four new CSP projects with a capacity of 200 MW, which is 52.1 % of the global total CSP.

The CSP system uses different types of HTFs like molten salt mixtures[12], ionic liquids[13–18] and phase changing materials[19–21]. Predominantly, the efficiency of a CSP system depends on the maximum working temperature and the thermal stability of the working fluid i.e., HTF. The widely used HTFs are Dowtherm A (by Dow Chem) or Therminol VP1[22] (by Eastman), molten salt mixtures and synthetic oils. Therminol VP1[22] is a eutectic mixture of diphenyl ether and biphenyl. However due to the high vapour pressure at higher temperatures, Therminol VP1 creates storage problem[23]. On the other hand the higher melting molten salts freeze up at room temperature[24]. Ionic liquids are

superior to the above HTFs in terms of thermal performance, but the cost and availability are the main concern[25]. Finally, due to the above reported issues of HTFs, Deep Eutectic Solvents (DES) can be proposed as alternative to the currently used HTFs.

Deep Eutectic Solvents are the combination of two solvents/components which are formed by hydrogen bonding where their melting points are lower than that of both components. Typically, DES consists of two groups namely hydrogen bond acceptor (HBA) and hydrogen bond donor (HBD). These are also known as deep eutectic ionic liquids, low melting mixtures,[26,27] or low transition temperature mixtures (LTTMs). DESs are the group of green solvents which are having equivalent characteristics analogous to that of ionic liquids (ILs). Mostly, the DESs are low volatile, wide liquid range, water-compatible, non-flammable, nontoxic, biocompatible, and biodegradable in nature. Most of the DES has high thermal conductivity, thermal stability and nonflammability thereby coining them as green solvents. In addition to the above properties, the DESs due to their ease of preparation, favourable physical and chemical behaviour and low vapor pressure are currently being explored as potential HTF.

Nanofluids are the class of liquids which consists of small amount of nanoparticle dispersed in the solvent i.e., base fluid. In past decades, nanofluids are well-known for the enhancement of the thermal property of the base fluids. Earlier results have pointed out the fact that thermal conductivity of the IL-based heat transfer fluid increases as the diameter of the nanoparticle is reduced[13]. On the contrary, the main disadvantage of nanofluids is that the coefficient of friction and pressure drop rises with increase in volume fraction. Hence, an optimal volume or mass fraction of nanoparticles must be selected based on the thermophysical properties.

1.2 Research Goal and Objectives

The present research focusses on the preparation of DESs and NDDESs (Nanoparticle Dispersed Deep Eutectic Solvents). Further the thermophysical properties namely density, viscosity, thermal conductivity and specific heat capacity are measured to evaluate these thermal media. Thereafter the optimization of the NDDESs is done to recommend the best NDDES. Thereafter the heat transfer characteristics of the optimized NDDES and the corresponding DES under forced convection is performed. The objective of the research is divided into following sections:

(1) Preparation of DESs and NDDESs

(2) Experimental measurement of thermophysical properties of DESs and NDDESs and subsequent screening of NDDES based on the measured thermophysical properties.

(3) Forced convection experiments of optimized NDDES and corresponding DES as per objective 2

(4) ASPEN plus simulation and estimation of steam generation rate using the optimized NDDES and corresponding DES

1.3 Dissertation Layout

Chapter 2 presents a thorough review about DES and its properties as well as its applications. Further literature related to nanofluids and NDDESs (Nanoparticles Dispersed Deep Eutectic Solvents), along with their properties are also described.

Chapter 3 includes the experimental methods required for the present research objectives such as preparation of DESs and NDDESs, optimization, forced convection experimental setup and steam generation setup. Working principles of the measuring instruments such as density meter for density, interfacial rheometer for viscosity, and

thermal property analyzer for thermal conductivity and specific heat capacity measurements are also presented.

Chapter 4 discusses the Nuclear Magnetic Resonance (NMR) spectra including 1D (^{1}H and ^{13}C) and 2D (NOESY) of the prepared DESs. Further, the morphology study and zeta potential of NDDESs are discussed. Thereafter, the thermophysical properties such as density, viscosity, thermal conductivity, and specific heat capacity of all DESs and NDDESs are reported. In addition, the optimization of the NDDESs are carried out in order to select the best NDDES.

Chapter 5 describes the results obtained from forced convection experimental setup by using the optimized NDDES and corresponding DES.

Chapter 6, briefs the simulation result obtained from the Aspen Plus simulation steam generator using the optimized NDDES and corresponding DES.

Finally, chapter 7 concludes the results. This chapter also presents the future research direction.

CHAPTER 2

2 LITERATURE REVIEW

2.1 Introduction

Heat transfer fluids (HTFs) are one of the prominent technologies for the future thermal energy storage thereby providing a wide range of industrial applications. The maximum used HTFs at liquid stage is Therminol VP-1 or Dowtherm A which is a eutectic mixture of diphenyl ether and biphenyl. One of the important properties of the HTFs is the heat storage capacity which drives the efficiency of the system while reducing the operating cost. The aim of the research work is to study the heat transfer performance of DESs and NDDESs as an alternative for HTFs for solar thermal power plants.

There are numerous studies on ILs as a thermal fluid but few studies of DESs as an HTF. Here DESs shows similar behaviour with respect to physiochemical properties like ILs. This has motivated us to investigate DESs as a new generation thermal fluid. For IL, the toxicity part is a burning issue, as their starting materials makes their synthesis non-green. Further the purification and production costs have added to their disadvantages. Looking at this trend, hydrophobic DESs can replace some ILs so as to make them environmentally viable. The earlier studies on DESs are concerned about the basic physical properties. The current chapter discusses the brief literature review on DES, thermophysical properties of DESs, different applications of DESs, nanofluids, and NDDESs.

2.2 Deep Eutectic Solvents

DESs are the mixture of two groups namely hydrogen bond acceptors (HBA) and hydrogen bond donors (HBD) which includes both solid(s) or liquid(s). Figure 2.1 representing the SLE (solid-liquid equilibria) plot gives an idea about the eutectic point, where the dotted curve signifies the melting temperature of DES family at different molar

ratios. Region I denote the mixture in liquid phase which is in a shape of a del operator and the point at which the two curves meet each other in the valley is called as the eutectic point. II and III represents the mixture of HBA and HBD either in solid-liquid or liquid-solid phases. IV is a mixture of HBA and HBD which is in solid phase. At the eutectic point two or more compounds combine in specific ratio to form a clear liquid or the lowest point where the mixture exists as a liquid. This point is lower that the melting point from either HBA or HBA.

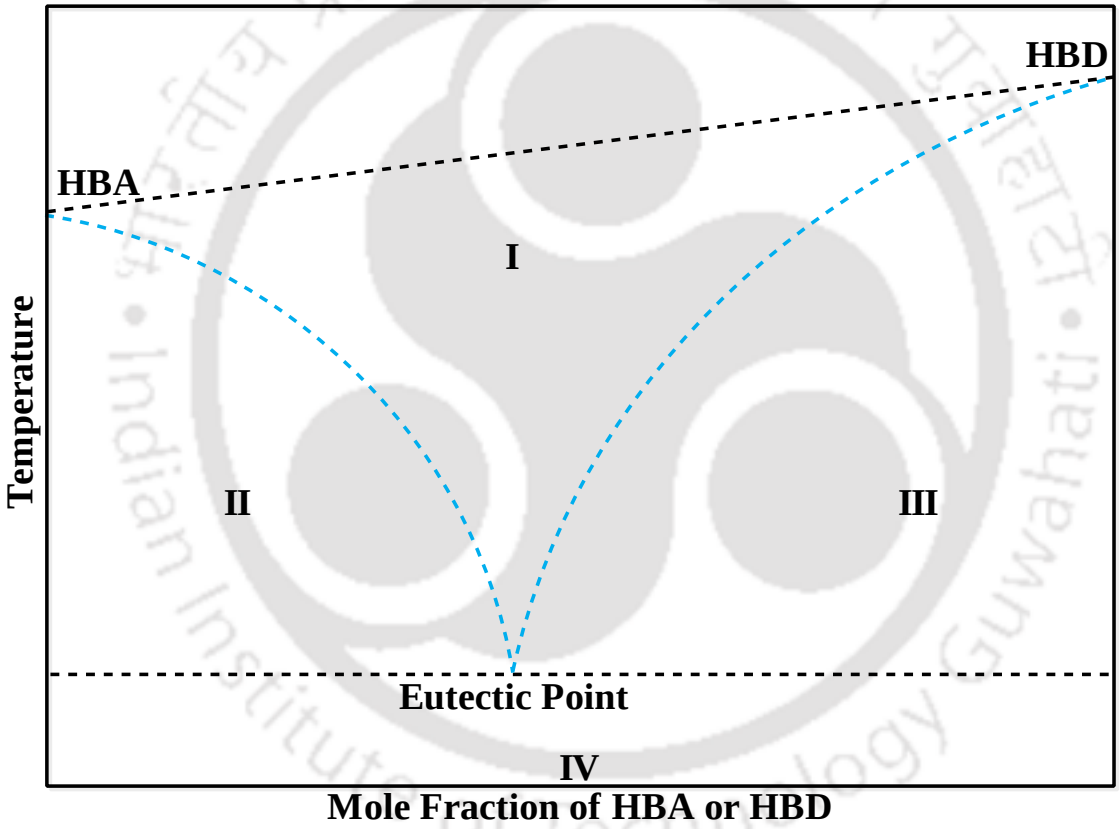

Figure 2.1: Formation of Deep Eutectic Solvent

DESs in liquid state have melting point lower than the individual solvents. Till date, four types of DES have been synthesized namely: (a) quaternary salt and metal halide, (b) quaternary salt and hydrated metal halide, (c) quaternary salt and hydrogen bond donor, and (d) metal halide and hydrogen bond donor. In this work a fifth type of DES is attempted

comprising of aromatic hydrocarbons, fatty acid or fatty alcohols. The structures of different types of HBAs and HBDs are shown in figure 2.2. Based on the water solubility, the DES are classified through two types namely hydrophobic DES and hydrophilic DES. Initially the term "Deep Eutectic Solvents" was first introduced by Andrew P. Abbott in the year 2004 [28]. Prior to that the an eutectic mixture of choline chloride and urea was developed in 2003 [29].

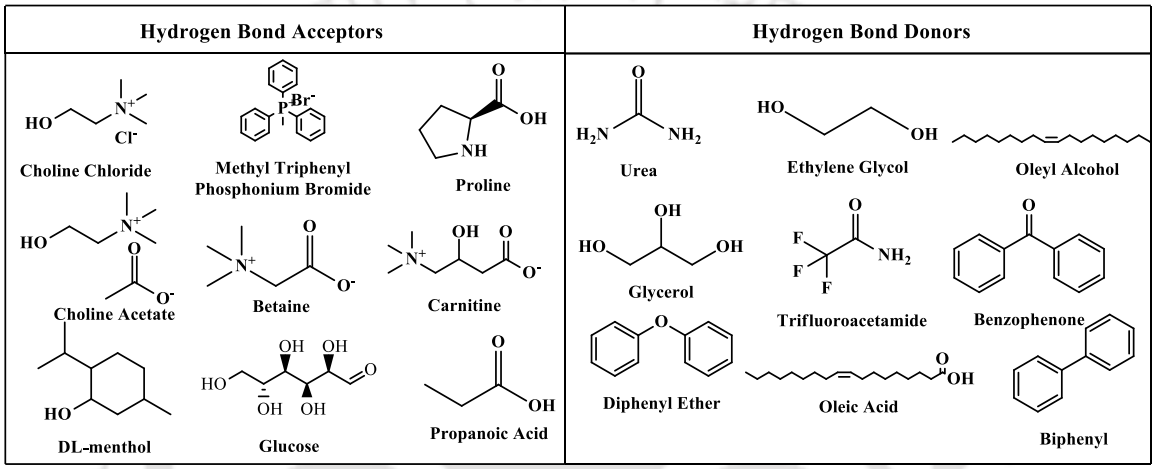

Figure 2.2: Chemical structure of common HBAs and HBDs

The same authors[28] again studied the solubility of metal oxides in Choline Chloride based DES[30] and also implemented the Hole theory for the enhancement of DES properties[31]. In 2007 subsequently electrochemical studies of DES were carried out[32,33]. In 2008 some new application of DES namely gold nanoparticles synthesis[34,35], ultrasonic electrodeposition[36], DFT topology study[37] and biotransformation[38] were explored. Thereafter few studies were carried out on different application such as electrolyte[39,40], gas storage media[41,42] , thermal media and active pharmaceutical ingredient[43]. Other applications include freeze drying approaches for DES synthesis[43] and metal extraction or leaching[43]. The year wise publications of DES are reported in figure 2.3. In the next sub-section, we shall be exploring the different applications of DES.

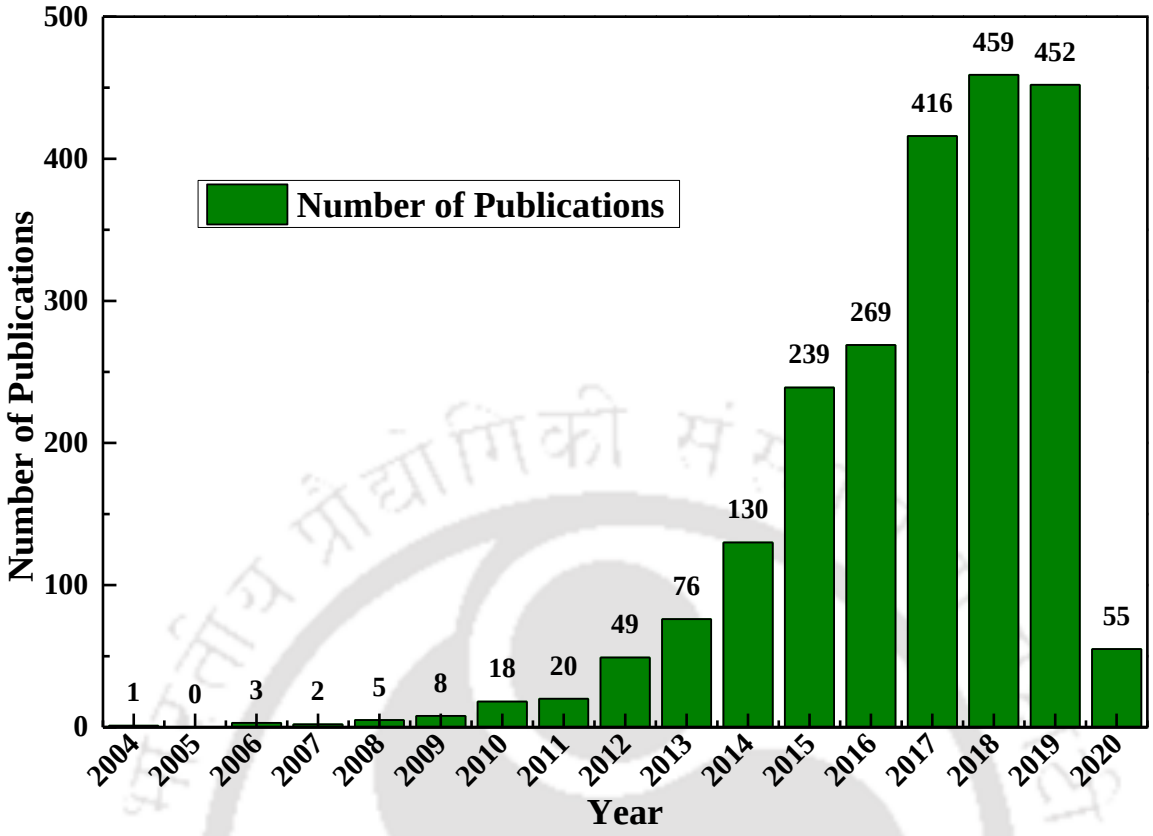

Figure 2.3: Number of articles published yearly from 2004 till date

2.3 Applications of Deep Eutectic Solvents

The research interest and publications of DESs are increasing due to the wide range of properties and low cost as compared to ILs. Also, DESs have comparable chemical, physical and thermal properties with respect to ILs. In a recent trend the researchers are now making combinations of different HBAs and HBDs to prepare DESs based on targeted applications. The wide range of applications of DESs includes biological applications[44–47], energy applications[48,49], as catalyst for different applications[50–54], nanotechnology[34,55,56], mass and heat transfer application[57–59] and electrochemistry[33,60,61]. As reported in figure 2.4 Wang *et al.*[44] has used choline chloride- glycerol based DES as solvent for the preparation of carbon dots. Wekene *et al.*[45] studied the Natural DES (NADES) consisting of citric acid : sucrose and a ternary DES (malic acid : fructose : glucose) as a solvent for photosensitisers

intended for antimicrobial photodynamic therapy. Zdanowicz *et al.*[46] studied the potential of DES as a starch plasticizer and crosslinking agent. Khataei *et al.*[47] has used choline based DES as an extractive solvent for the extraction of steroidal hormones from biological fluids or urine. Procentese *et al.*[48] have used DES for the pre-treatment of biomass for the fermentation process where the bio-butanol production was carried out. Boldrini *et al.*[49] have explored aqueous choline chloride based deep eutectic solvent as an electrolyte solution for dye-sensitized solar cells. Wang *et al.*[50] investigated the urea-based DES as a catalyst for the glycolysis of PET, where a shorter reaction time was observed under mild conditions. Alhassan *et al.*[51] have carried out the supercritical esterification of the waste tyre pyrolysis oil using choline chloride-based DES as a catalyst. Maka *et al.*[52] have used DES as a cationic catalyst for the curing of epoxy resin and concluded that the DES composed of ChCl and $SnCl_2$ is an efficient polymerization catalyst of epoxy resin and antiflaming agent. Shuwa *et al.*[53] investigated the mixture of DES and MoO_3 as a catalyst for the catalytic upgrading of the Omani heavy crude oil where no change in structure of DES was found. Dindarloo *et al.*[54] used [ChCl]/[$ZnCl_2$]$_2$ for the production of carbamates using amines, alkyl halides and carbon dioxide under mild conditions. Chen *et al.*[55] fabricated PbS thin film using ChCl/urea DES by ionothermal method. Wei *et al.*[56] used DES as a carrier for the development of overpotential dependent shape of Au NCs using electrochemically shape-controlled synthesis process and found a shape changing from concave cubes, octopods, cuboctahedral boxes, to hollow octahedra shape. Liao *et al.*[34] synthesized gold nanoparticles using DES for electrocatalysis application. Zulkurnai *et al.*[57] have used DES as an adsorbent where activated carbon was functionalized with DES in order to increase the efficiency of carbon dioxide capture. Fatma *et al.*[58] used three different DESs for the wet beneficiation of Indian bituminous coal to increase the carbon content.

Naik *et al.*[59] used DES as solvent for the extraction of aromatic and poly aromatic hydrocarbon from fuel oil. Saravanan *et al.*[60] synthesized DES consisting of choline chloride, $CrCl_3 \cdot 6H_2O$, $CoCl_2 \cdot 6H_2O$, KCl, and ethylene glycol and studied the electrodeposition of Co-Cr alloy in brass and mild steel substrates. Mahanta *et al.*[61] have tested IL based DESs as electrolytes for supercapacitors and the reported DESs resulted lower viscosity than ILs with satisfactory electrochemical stability.

Figure 2.4: Diverse applications of Deep Eutectic Solvents

2.4 Thermophysical Properties of Heat Transfer Fluids

The outstanding thermophysical properties namely density, viscosity, thermal conductivity and specific heat capacity makes DESs as potential alternative to organic

thermal solvents or heat transfer fluids (HTFs). Some of the properties of DESs are reported below (table 2.1). Further these properties vary depending on the selection of HBAs and HBDs.

Table 2.1: Properties of Conventional Heat Transfer Fluids[22]

Composition	Biphenyl/diphenyl ether
Maximum bulk temperature	400°C
Maximum film temperature	430°C
Normal boiling point	257°C
Crystallizing point	12°C
Flash point	124°C
Flash point	110°C
Autoignition temperature	601°C
Coefficient of thermal expansion at 200°C	0.000979/°C
Heat of vaporization	206 kJ/kg
Total acidity	<0.2 mg KOH/g
Average molecular weight	166
Pseudocritical temperature	499°C
Pseudocritical pressure	33.1 bar
Pseudocritical density	327 kg/m^3
Sulphur content	<10 ppm
Moisture content, maximum	300 ppm
Volume contraction on freezing	6.27%
Volume expansion on melting	6.69%
Surface tension in air at 25ºC	36.6 dynes/cm
Dielectric constant @ 23°C	3.35

2.5 Melting Point

In the previous discussion about DES the melting point plays an important role in the formation of DES while considering the DES for extractions, reactions, heat transfer fluids, and as electrolyte. DES have a low melting point, which is lower than the individual melting points of HBA and HBD. Abbott *et al.*[29] have reported the melting point of ChCl/urea based DES (12°C), which is lower than that of the HBA (ChCl at 302°C) and HBD (Urea at 133°C). They have reported that the melting point of DESs decreases with decreasing the size of cations. On the other hand, the melting point was observed in the order of $F^- > NO_3^- > Cl^- > BF_4^-$. Further, Kareem *et al.*[62] found that the melting point of DES is also influenced by the choice of HBD.

2.6 Density

The density of DESs is one of the elementary physical property to be measured prior to any application. Shahbaz *et al.*[63] have synthesized 24 different DESs from ammonium and phosphonium salts and measured the densities at room temperature. Further they have predicted the density by atomic contributions method using Lorentz–Lorenz equation and compared them with experimental data. The combined expanded uncertainties were found to be 1×10^{-5}g/cm^3. Zhang *et al.*[64] revealed the temperature dependent density of ethylamine hydrochloride (EaCl) and acetamide (AA) DES at different molar ratios. The density decreases with the increase of AA content in mixtures. They observed a linear decrease with the increase in temperature. Ijardar *et al.*[65] prepared six DESs consists of tetrabutylammonium bromide and Polyethylene Glycol (200, 400, 600) with two different molar ratios and measured the density with respect to temperature.

2.7 Viscosity

While choosing any liquid based on the flow properties, viscosity is one of the important properties. Viscosity of DESs is an essential physical property for designing any equipment which involves processes such as mass transfer, heat transfer and process piping. As the heat transfer fluid is associated with pumping and piping operation, the low viscosity liquid must be chosen while on the contrary higher viscosity fluids might be applied for lubrication applications. While comparing the DESs with the ILs, most of the ILs are highly viscous with a liquid viscosity ranging from 10 to 726 cP[66]. Siongco *et al.*[67] have synthesized two different DESs consisting of N, N-diethylethanol ammonium chloride-glycerol (DEACG) and -ethylene glycol (DEACEG) and measured the viscosity with temperature varying from 298.15 to 343.15 K. Decreasing trends in the viscosity was observed in both the DESs. Zhang *et al.*[64] have measured the viscosity of ethylamine hydrochloride (EaCl) and acetamide (AA) DES at different molar ratios and temperatures. A declining viscosity was observed with increase in temperature. They also used Vogel-Fulcher-Tammann (VFT) equation to correlate the viscosity data. Ijardar *et al.*[65] have measured the viscosity of six DESs consists of tetrabutylammonium bromide and Polyethylene Glycol (200, 400, 600) with two different molar ratios of each with respect to temperature. They have observed that the viscosity of DES suddenly decreases at higher temperatures. All of the above discussed results confirm that the viscosity of DESs as expected, decreases sharply with temperature.

2.8 Thermal Conductivity (TC)

Thermal conductivity is one of the vital thermal properties while selecting any fluid for heat transfer applications. Several analytical techniques are described in literature for measuring the thermal conductivity of liquids. Johnson *et al.*[68] and Jeong *et al.*[69] have

adopted Transient Grating Technique for the TC measurement while Mostert *et al.*[70] have used guarded parallel plate instrument method. Merckx *et al.*[71] have used Transient Hot-Wire Method for the measurement. Among all the above-mentioned methods, Transient Hot-Wire Method is widely used method for TC measurement. Gautam *et al.*[72] have measured the TC of three DESs namely Reline, n- Reline, Thio-reline over a temperature range from 298.15 to 343.15 K. The TC of all DES were found to decrease with increase in temperature. Yan *et al.*[73] measured the thermal conductivity of 11 different combinations of DESs where Methyltriphenylphosphoniumbromide (MTBP) and Choline Chloride as HBA and Ethylene Glycol and Triethylene Glycol as HBD were adopted. They found that the thermal conductivity of some DESs decreases with temperature, while some interestingly increases with temperature.

2.9 Specific Heat Capacity

Specific heat capacity or thermal capacity is the thermophysical property of a material which is defined as the quantity of heat energy required to raise the temperature of the material by unit of mass. Specific heat capacity is the most important thermal property of any heat transfer fluid. In literature, there are different methods of measuring specific heat capacity of DES such as differential scanning calorimetry (DSC)[74–76], microcalorimetry process[77] and Thermal Property analyzer (dual needle)[78]. Naser *et al.*[74] have measured the molar heat capacity of fifteen choline chloride, tetrabutylammonium chloride and MTPB based DESs by DSC. The results are reported as a function of temperature which increases linearly with temperature. Leron *et al.*[75] have also measured the molar heat capacity of three DESs (Reline, Ethaline and Ethaline) by DSC with a temperature ranging from 303.15 to 353.15 K. The results show that the molar heat capacity of the DESs increase with temperature. Overall within the same temperature range, the molar heat capacity values are

in the order of, reline < ethaline < glyceline, which signifies that the molar heat capacity rises with increase in DES molar mass. Siongco *et al.*[76] have measured the molar heat capacity of N, N - diethylethanolammonium chloride as HBA and (glycerol and ethylene glycol) as HBD using DSC with a temperature ranging from 303.15 to 353.15 K. A linear increase with temperature was observed which is due to the higher degrees of freedom at elevated temperatures. Zhang *et al.*[77] have measured the specific heat capacity of two functional DESs within a temperature range of 318.15 -363.15 K by using microcalorimetry process. The specific heat capacity of two DESs are lower than that of water. Fang *et al.*[78] have used a KD2Pro thermal properties analyser (using dual needle sensor) for the measurement of volumetric heat capacity of three different DESs.

2.10 Nanofluids

Choi *et al.*[79] first introduced the concept of nanofluid. Nanofluids are defined as the suspensions of metallic nanoscale particles in a liquid which is termed as base fluid. As the thermal conductivity of metals are higher than fluids it is estimated that a solid-fluid mixture will have higher thermal conductivity than that of base fluid. Further the presence of nanoparticles in the base fluid results in the enhancement of transport properties of the base fluid thereby enhancing the thermal conductivity and specific heat capacity, which eventually increases the heat transfer rate of nanofluids[80]. Due to the size of the nanoparticles (10^{-9} m), there is a very negligible pressure drop in nanofluids even when used in low concentrations. There are range of nanoparticles such as Al_2O_3, CuO, TiO_2, Cu, Ag, and Au used for stable nanofluids[81–83]. The core attention of the nanofluids is to enhance the thermophysical properties and heat transfer behaviour. Researchers have investigated various aspects of nanoparticle behaviour which aids in enhancing the thermophysical properties. There are many traditional theories which explains the TC

enhancement of nanofluids[84–88]. Hamilton *et al.*[85] have investigated the effect of shape of nanoparticles in the enhancement of TC. Murshed *et al.*[82] have studied the effect of shape, size and concentration of the nanoparticles and have found that the concentration plays a significant role in the enhancement of TC. Wei *et al.*[81] have studied the thermal conductivity of copper nanofluids and concluded that the presence of nanoparticles can either upgrade or downgrade the TC of nanofluids. Gaganpreet *et al.*[89] have theoretically predicted the effective thermal conductivity and relative viscosity as a function of particle volume concentrations and size. They found that the viscosity is independent of nanoparticle volume fraction. Leong *et al.*[90] have proposed a new model in which interfacial layer plays an important role in the enhancement of the effective thermal conductivity in nanofluids. Chen *et al.*[91] also studied the rheological behaviour of TiO_2-ethylene glycol nanofluids and also investigated the Newtonian behaviour. Further they have predicted the experimental viscosity by aggregation model. Putra *et al.*[92] have performed the natural convection experiment of Al_2O_3 and CuO-water based nanofluids in a horizontal cylindrical duct. Wen *et al.*[93] has performed the natural convection experiment on TiO_2-water based nanofluid under natural convective heat transfer conditions with different concentrations of nanofluid. They have found that the deterioration in heat transfer coefficient happens due to the nanoparticle concentration. Heris *et al.*[94] have performed the forced convection experiments of Al_2O_3-water nanofluids under laminar flow condition with constant wall temperatures in a circular tube. The heat transfer coefficient was found to increase with the Peclet number and nanoparticle concentration.

2.11 Nanoparticle with Deep Eutectic Solvents (NDDES)

The idea of DES as a base fluid is a novel concept, since DES behaves similar to IL in terms of physical and thermal characteristics. Here Nanoparticle Dispersed DES

(NDDES) has been explored to increase the specific heat capacity of the pure DES without any change in its thermal stability. An increased specific heat capacity indicates an efficient HTF in terms of energy storage. Many researchers used Al_2O_3 nanoparticles as an addition to a base fluid so as to enhance its thermal properties (thermal conductivity and specific heat capacity). It has also have proven to have negligible effect on physical properties (density and viscosity) on the base fluid[95]. Keeping these advantages in mind, the current work has adopted spherical Al_2O_3 nanoparticle to prepare the desired NDDES.

CHAPTER 3

3 Experimental and Computational Details

The initial part of the chapter shall discuss the preparation of the DES, then followed by NDDES. In the later sections the measurement and the comparison of the thermophysical properties for both class of fluids shall be presented.

3.1 Materials

DL-menthol of purity ≥ 95%, Diphenyl ether of purity ≥ 99%, Biphenyl of purity ≥ 98% and Benzophenone of purity ≥ 99% were purchased from Sigma-Aldrich. Oleyl alcohol of purity 80-85% was purchased from Alfa Aesar. Oleic acid having a purity of ≥ 90% was supplied by Otto Chemie Pvt. Ltd. Aluminium oxide (Al_2O_3) nanoparticles having a particle size of 50 nm as measured by TEM were bought from Sigma Aldrich. Aluminum oxide (Al_2O_3) nanowires having a length of 2-6 nm and diameter of 200-400 nm were bought from Sigma Aldrich. Hexagonal boron nitride (*h*-BN) nanoparticles (~70nm) were purchased from Lowerfriction Lubricants, Canada. Acetone (purity ≥ 99%) was supplied by Sigma-Aldrich which was used a rinsing agent throughout the experiments. Dimethyl sulfoxide-d_6 (DMSO-d_6, 99.8%) and Chloroform-d ($CDCl_3$, 99.8%) were used as the Nuclear Magnetic Resonance Spectroscopy (NMR) solvent and supplied by Merck (Germany). The chemicals were used as they were received. Purities of DL-menthol, diphenyl ether, biphenyl, benzophenone, oleyl alcohol and oleic acid were confirmed by ^{1}H NMR spectroscopy and analysis of peaks indicated negligible impurities. The chemical structure, CAS no, Source, purities and method of purification of the chemicals used in the work are listed in Table 3.1. The individual properties of all the solvents used are reported in Table 3.2.

Table 3.1: Chemical structure, CAS number, source and purities of all the chemicals used

Sl. No.	Solvent Name	Structure	CAS No.	Sources	Purity	Analysis Method
1	DL-Menthol	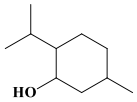	89-78-1	Sigma-Aldrich	≥ 95%	^{1}H NMR
2	Diphenyl Ether	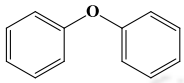	101-84-8	Sigma-Aldrich	≥ 99%	^{1}H NMR
3	Biphenyl	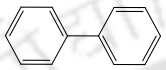	92-52-4	Sigma-Aldrich	≥ 98%	^{1}H NMR
4	Benzophenone	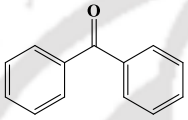	119-61-9	Sigma-Aldrich	≥ 99%	^{1}H NMR
5	Oleyl Alcohol	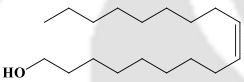	143-28-2	Alfa Aesar	80-85%	^{1}H NMR
6	Oleic Acid		112-80-1	Otto Chemie Pvt. Ltd	≥ 90%	^{1}H NMR
7	MTPB	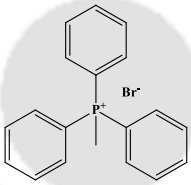	1779-49-3	Sigma-Aldrich	≥ 98%	^{1}H NMR
8	Ethylene Glycol	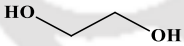	107-21-1	Sigma-Aldrich	≥ 99%	^{1}H NMR

Table 3.2: Basic properties of all the solvents used for DES

Sl. No.	Solvent Name	Density (kg/m^3)	Water Content (%)	T_m (K)	T_b (K)
1	DL-Menthol	891.34	0.001	307.15	489.15
2	Diphenyl Ether	1066.1	0.004	299.95	531.15
3	Biphenyl	1041.0	0.0002	342.15	529.25
4	Benzophenone	1110.0	0.0006	321.65	578.55
5	Oleyl Alcohol	845.87	0.05	292.15	633.15
6	Oleic Acid	895.68	0.09	287.15	633.15
7	MTPB	-	2.8	503.15	-
7	Ethylene Glycol	1110.0	2.5	260.75	471.8

3.2 Eutectic Point Prediction of DES by COSMO-SAC Calculations

In this study five different types of DESs were conceptualized for further study. As discussed earlier, DESs are formed due to the hydrogen bonding between a hydrogen bond acceptor (HBA) and a hydrogen bond donor (HBD). This gives birth to a new chemical entity having melting point lower than those of the initial compounds i.e., HBA and HBD. But not all ratios of HBA and HBD will give us a eutectic point or a liquid phase. It is those points or, in other words, the lowest temperature that needs to be computed in such a manner that a liquid phase of DES coexists. This can be initiated through quantum chemical calculations by adopting a statistical-based approach such as COSMO-SAC (COnductor-like Screening MOdel-Segment Activity Coefficient model). The detailed methodology of COSMO and COSMO-SAC are already available in our earlier work.[96] The applications of

COSMO-SAC are well known and documented in areas such as distillation, extraction, and absorption. Once the optimum ratio is known, we shall then proceed for preparation.

Table 3.3: Nomenclature of DESs along with molar ratios of respective HBA and HBD

Sl. No.	Hydrogen Bond Acceptor (HBA)	Hydrogen Bond Donor (HBD)	Molar Ratio	Nomenclature
1	DL-Menthol	Oleyl Alcohol	1:1	DES1
2	DL-Menthol	Oleic Acid	1:1.4	DES2
3	Diphenyl Ether	DL-Menthol	1:1.1	DES3
4	Diphenyl Ether	Benzophenone	1.7:1	DES4
5	Benzophenone	Biphenyl	1.66:1	DES5
6	MTPB	Ethylene Glycol	1:4	DES6

The geometry optimization on all the structures was carried out using the density functional theory (DFT) B3LYP along the optimized structure with SDD basis set. The COSMO file was generated by the BVP86/TZVP/DFT level of theory.[96] Gaussian 09[97] was used to generate the above procedure or also termed as COSMO file initiation. The global adjustable parameters for generating the activity coefficient via a statistical mechanical framework were the surface area of the segment (a_{eff} = 6.32 Å^2), the misfit energy interaction constant [α' = 8419 kcal Å^4/ (mol e^2)], the cut-off for hydrogen-bonding interaction (σ_{HB} = 0.0084 e/Å^2), and the hydrogen-bonding interaction constant [c_{HB} = 75,006 kcal Å^4/(mol e^2)]. Thereafter, the mole fraction was predicted for both HBD and HBA by the activity coefficient in either phase at different temperatures (T) (eq. 3.1) is given by:

$$\ln(\gamma_{solute} x_{solute}) = \frac{-\Delta H_f}{RT_m}\left(\frac{1}{T} - \frac{1}{T_m}\right) \tag{3.1}$$

where γ_{solute}, x_{solute}, ΔH_f and T_m are the activity coefficient, the mole fraction, the enthalpy of fusion, and the melting point, respectively.

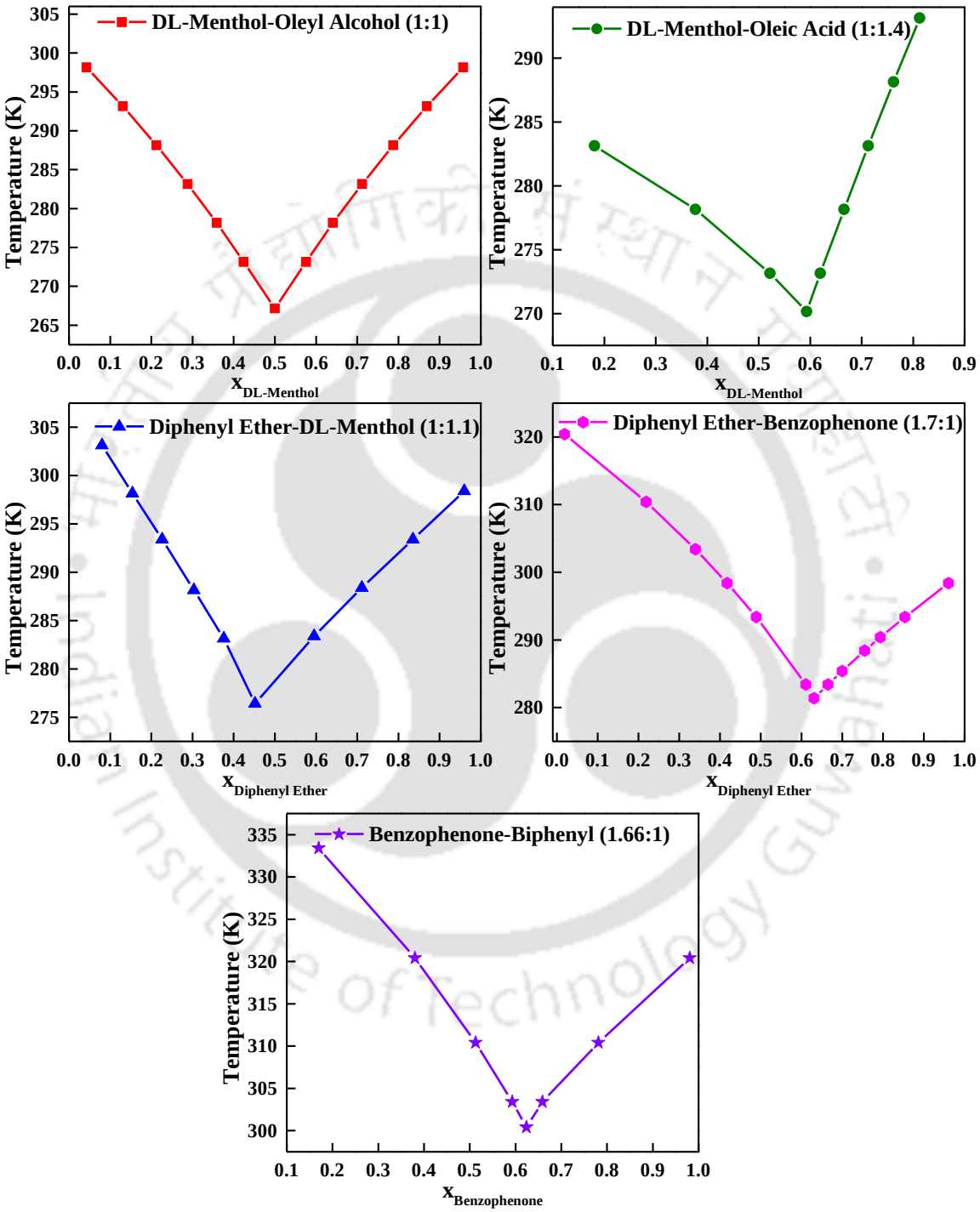

Figure 3.1: Solid -Liquid Equilibria plot of DESs

The solute here refers to HBA. The nomenclature of five different DESs along with molar ratios of corresponding HBA and HBD are reported in Table 3.3. The Solid-Liquid equilibria plots of all five set of DESs are reported in figure 3.1. We shall now discuss the preparation procedure in the ensuing sections.

3.3 Preparation of Deep Eutectic Solvents

As mentioned earlier, molar ratios of HBA and HBD was first inserted in a flat-bottom flask and heated till 343.15 K or above their individual melting point. A reflux condenser was fitted to the flask in order to prevent any solvent loss due to vaporization. This was then subjected to heating along with stirring for 12-24 hours so that a homogenous solution is obtained.

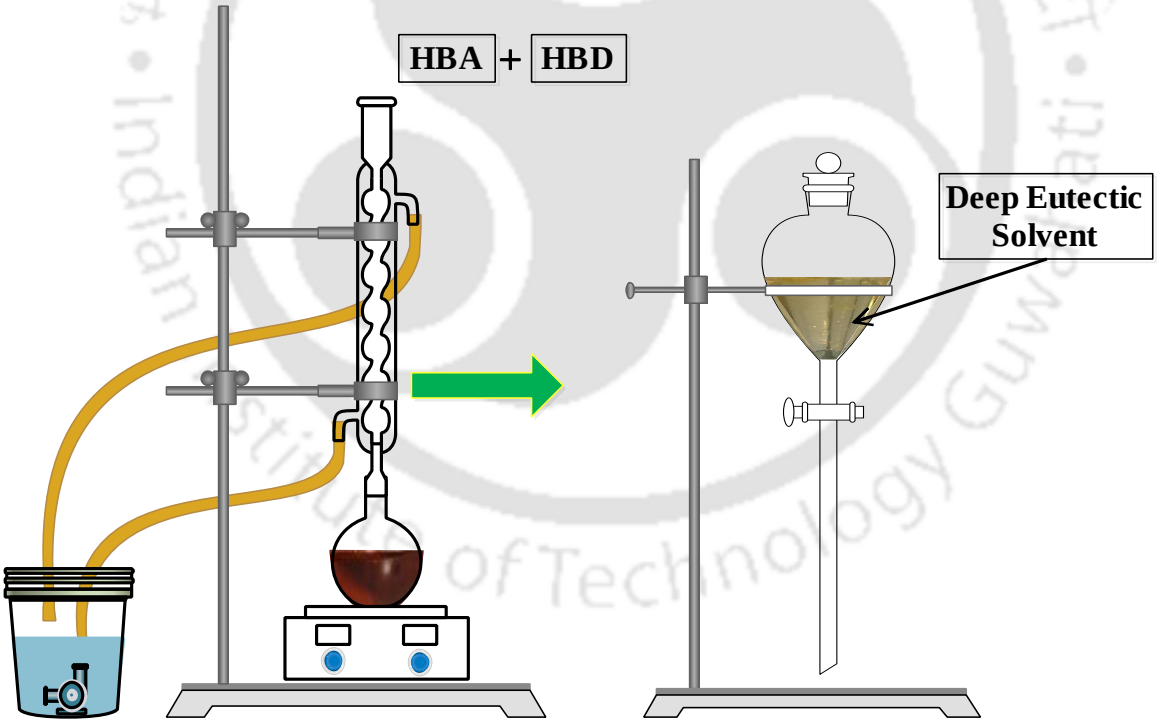

Figure 3.2: Preparation of DES

It was then cooled at a certain rate so as to provide time for the solid or crystal phase to appear. This was again heated so as to make the last solid disappear. This step helps us to exactly locate the phase transition point between solid and liquid phase. After getting a clear liquid, the mixture was kept at room temperature (298.15 K) overnight in order to observe any solidification event. For DES preparation the standard uncertainties were u(T) = 0.03 K, u(x) = 0.001 and u(p) = 3 kPa.

3.4 Measuring Principles of Basic Physicochemical Properties

3.4.1 Nuclear Magnetic Resonance (NMR) Spectroscopy Study of DESs

NMR spectroscopy is the primary technique to acquire the molecular fingerprint. Further, NMR spectroscopy provides the thorough and quantitative information on the functional groups, topology, dynamics and three-dimensional structure of molecules in solution and the solid state. The sample is initially placed within the high-power magnetic field and exposed to the radio wave, which further is processed to get the information about the composition of atomic groups within the molecule. The composition of the DES was established by NMR spectroscopy using both one dimensional (^{1}H and ^{13}C) and two-dimensional NMR (Nuclear Overhauser Effect Spectroscopy (NOESY))[98].

3.4.2 Thermal Stability of DESs

Thermogravimetric analysis (TGA)[99] is a characterization technique which is used for the thermal stability analysis of materials. In this method, the decrease in the weight of a sample is measured by gradually increasing the temperature. The highly sensitive measuring scale is used for the measurement of the change in weight due to heating. Further the apparatus is devised with a programmable furnace which controls the temperature of the sample. The TGA analysis of the DESs[100] were carried out by Netzsch thermogravimetric analyzer (TGA/STA 449 F3 Jupiter) at a 40 mL/min flow of Nitrogen

and at a heating rate of 10 °C/min. High temperature aluminium crucible was used for the analysis.

3.4.3 Moisture Content of DESs

Titration is a basic experimental technique used for the measurement of water/moisture content of a material. The technique of moisture content measurement was first developed by Karl Fischer with the method being known as Karl Fischer Titration (KFT)[101]. KFT is a reagent-based titration in which the KFT reagent reacts with water to convert water into a non-conductive chemical where dry methanol is used as the base solvent. In this thesis, a Volumetric Karl Fischer titration method was used[102]. The moisture content of all the DESs were measured by a Karl Fischer Titrator (870 KF Titrino plus).

3.4.4 Vapour Pressure of DESs

Vapour pressure is one of the important properties which is essential for the HTF. Vapour pressure plays an important role when the HTF is exposed to high temperature applications.

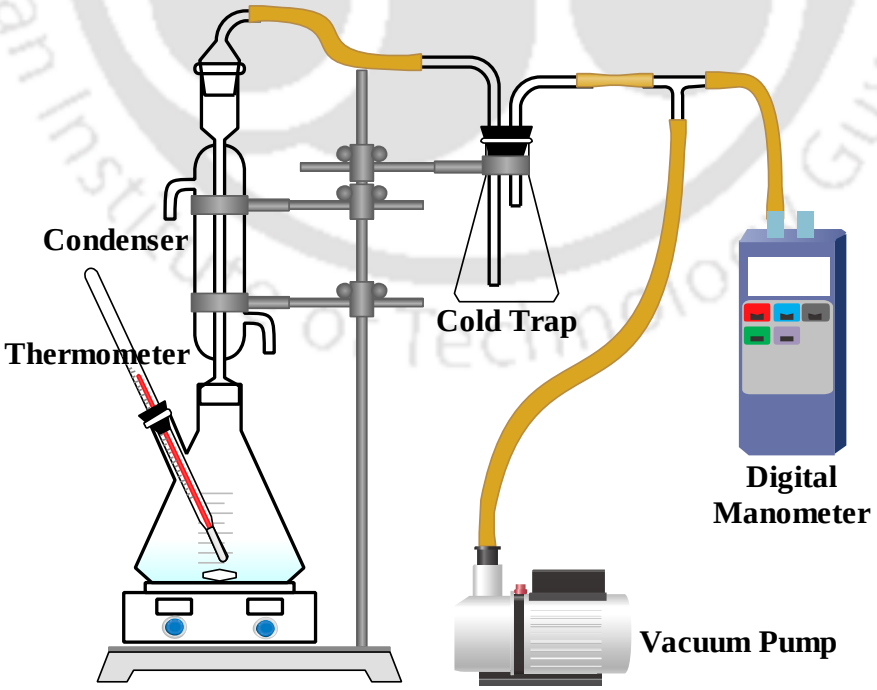

Figure 3.3: Stirred-Flask Ebulliometer for vapour pressure measurement

Vapour pressure was measured by single stage boiling using the Stirred-Flask Ebulliometer (figure 3.3) which follow the standard ASTM procedure (E1719-12)[103–105]. Ice and water were used as the coolant for the cold trap. A digital manometer (A to Z Instruments, GOLD.M-175) was engaged to measure the vapour pressure.

3.4.5 Physical Property Prediction

The weight average molecular weight ($\overline{M_w}$) of DESs was estimated by using the following equation[106]:

$$\overline{M_w} = \frac{\sum_i w_i M_i^2}{\sum_i w_i M_i} \tag{3.2}$$

The melting point (T_m) was also measured by allowing the DES to cool up to 270.15 K and then gradually increasing the temperature. The boiling point (T_b) was predicted using the modified Lydersen-Joback-Reid method.[107,108]

3.5 Preparation of NDDESs

For the preparation of NDDESs, three different types of nanoparticles (namely Al_2O_3 spherical, Al_2O_3 cylindrical and Boron Nitride (BN) hexagonal nanoparticles) with three different weight percentages were used. The nomenclature of the NDDESs is reported in table 3.5. An appropriate mass % of nanoparticles (0.02, 0.05 and 0.10 mass %) were added to the corresponding DESs (Table 3.5). Initially the mixture of DES and nanoparticle were kept on a vortex mixture (SPINIX MC-01, Tarsons) (figure 3.4) for thorough mixing.

Figure 3.4: Stepwise Preparation of NDDESs

One of the primary objectives of the nanofluids or NDDESs is to obtain a homogenous and uniform suspension of nanoparticles. This usually occurs by the minimization of agglomerated nanoparticles. To prevent any possible agglomeration, ultrasonication (GT-1990QTS, ANTECH) (figure 3.4) was applied for 2 hrs to get a homogenous distribution of nanoparticles. To confirm the particle suspension behaviour of the nanofluid, the zeta potential is considered to be an important parameter. The agglomeration of suspended particles primarily occurs due to the higher surface energy, which leads to precipitation. Further while dealing with the nanofluids the stability becomes an important factor. Hence four different methods were adopted to measure the stability of the nanofluids.

Table 3.4: Nomenclature of NDDESs to be used in the thesis

DES	Al_2O_3 spherical			Al_2O_3 cylindrical			*h*-BN hexagonal		
	Nanoparticles mass %								
	0.02%	0.05%	0.10%	0.02 %	0.05 %	0.10 %	0.02 %	0.05 %	0.10 %
DES1	NDDES1	NDDES2	NDDES3	NDDES4	NDDES5	NDDES6	NDDES7	NDDES8	NDDES9
DES2	NDDES10	NDDES11	NDDES12	NDDES13	NDDES14	NDDES15	NDDES16	NDDES17	NDDES18
DES3	NDDES19	NDDES20	NDDES21	NDDES22	NDDES23	NDDES24	NDDES25	NDDES26	NDDES27
DES4	NDDES28	NDDES29	NDDES30	NDDES31	NDDES32	NDDES33	NDDES34	NDDES35	NDDES36
DES5	NDDES37	NDDES38	NDDES39	NDDES40	NDDES41	NDDES42	NDDES43	NDDES44	NDDES45
DES6	NDDES46 (1wt.%Al_2O_3 Spherical Nanoparticles)								

3.6 Stability of NDDESs

3.6.1 Sedimentation Image Capturing Method

A primary technique for stability evaluation is sedimentation[81,109]. This practice is based on settlement of the nanoparticles at the bottom of the base fluid due to gravity. The higher sedimentation time indicates the higher stability of nanofluid. The prepared suspensions (NDDESs) were kept for eight weeks and the photographs were captured. Further the initial and final photographs were compared to check the rate of sedimentation of nanosuspensions. The photographs were captured using digital single-lens reflex camera (Canon 1300D, 18-55mm lens). Three types of sedimentation behaviour occur in any unstable nanofluid, namely dispersed sedimentation, flocculated sedimentation and mixed sedimentation[110].

3.6.2 Centrifuge Technique

Nanofluid centrifugation is an alternative sedimentation technique and a faster method for determining the stability of the nanofluids[111]. In this method, the centrifugal force is applied to the nanofluids to accelerate the sedimentation process. The NDDESs were centrifuged using a bench top centrifuge (REMI, RM-12C DX). A volume of 5 ml of each NDDES was added to centrifuge tubes and placed inside the centrifugal system. The samples were centrifuged at room temperature for 15 min at 1000 rpm.

3.6.3 Zeta Potential Measurements

The zeta potential technique evaluates the stability of nanofluids through the observation of electrophoretic behaviour of the fluid[112,113]. When nanoparticles are dispersed in the base fluid, the liquid layer surrounding the particle is divided into two parts, namely; stern layer, and diffuse layer. In stern layer, the charged ions are strongly attached

to the particle but in diffuse layer, the charged ions are loosely bounded and diffusive in nature.

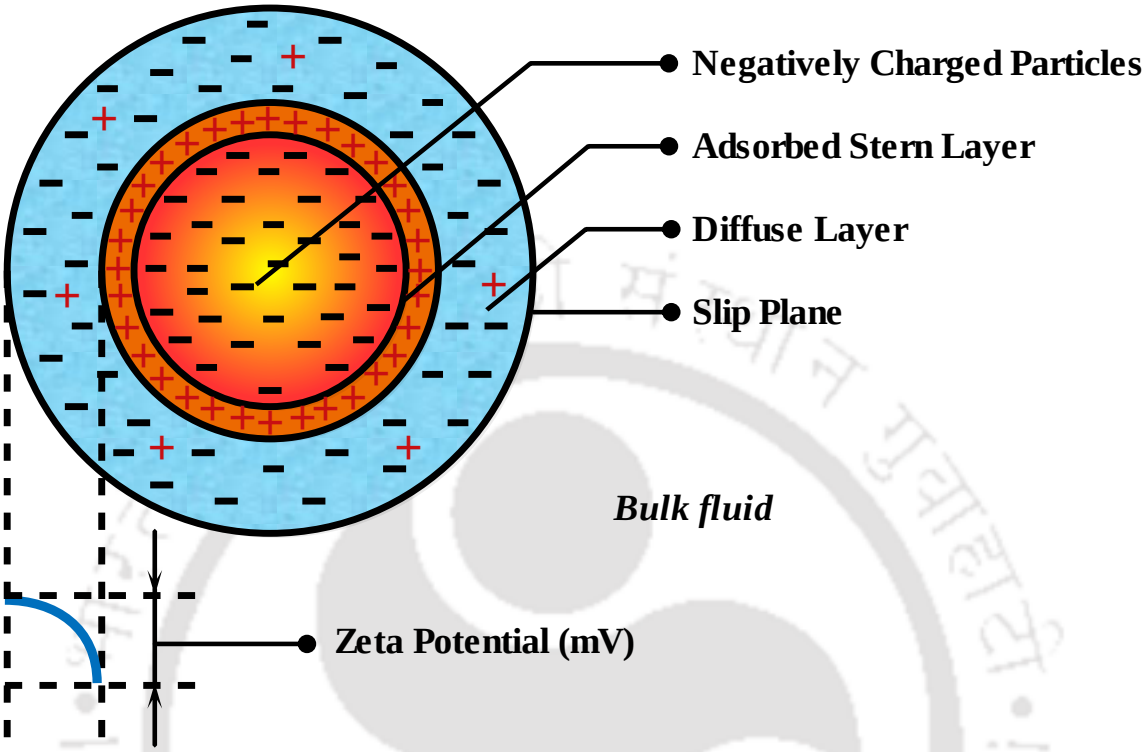

Figure 3.5: Zeta potential of nanoparticles

The combination of surface charge, stern layer, and diffuse layer is known as electrical double layer (EDL) (figure 3.5) which consists of both positively and negatively charged ions but being overall electrically neutral. The zeta potential is the potential difference between the base fluid and the stern layer attached to the particles and is measured in millivolts. According to Vandsburger[114], when the zeta potential is close to ±30 mV, the nanofluids are expected to be moderately stable. If the zeta potential is near ±45 mV, then the stability of nanofluids is guaranteed. The zeta potential value above ±60 mV illustrates an excellent stability of the nanofluid system. The zeta potential analysis of the NDDESs were performed by Delsa Nano (Delsa Nano C, BECKMAN COULTER).

3.6.4 Optical Microscopy

Optical microscopic images were captured using a high resolution microscope (Axiostar plus, Carl Zeiss, Germany) at a magnification of 50X[115,116]. The microscopic images were further used to evaluate the uniform dispersion of nanoparticles as well as the qualitatively analysis of the cluster size in each NDDES.

3.6.5 Transmission Electron Microscopy

Transmission Electron Microscopy (TEM) is a very useful tool for the analysis of shape, size and distribution of nanoparticles. However, it cannot provide the real state of nanoparticles in nanofluids as the analysis requires dried samples. The standard procedure was followed for sample preparation[117]. Here FETEM (JEOL, 2100F) was used for the experiment.

3.7 Measuring Principles of Thermophysical Properties

In the present sub-section, the measuring principles of the thermophysical properties of the Deep Eutectic Solvents (DESs) and the Nanoparticle Dispersed Deep Eutectic Solvents (NDDESs) are briefly described. The thermophysical property measurement equipment's are density meter, interfacial rheometer and thermal property analyzer.

3.7.1 Density

The densities of DESs and NDDESs were measured by the Anton Paar density meter (DMA 4500 M). The principle used for the measurement is the oscillating U-tube method (figure 3.6). The sample is injected into a U-shaped borosilicate glass tube which oscillates at corresponding characteristic frequency. The change in the characteristic frequency basically depends on the density of the sample. The characteristic frequency is then used to measure the density by a mathematical conversion. The measuring temperature here ranges

from 273.15 K to 363.15 K with a maximum pressure up to 10 bar. The accuracy of the measured densities is ±0.00002 g/cm³.

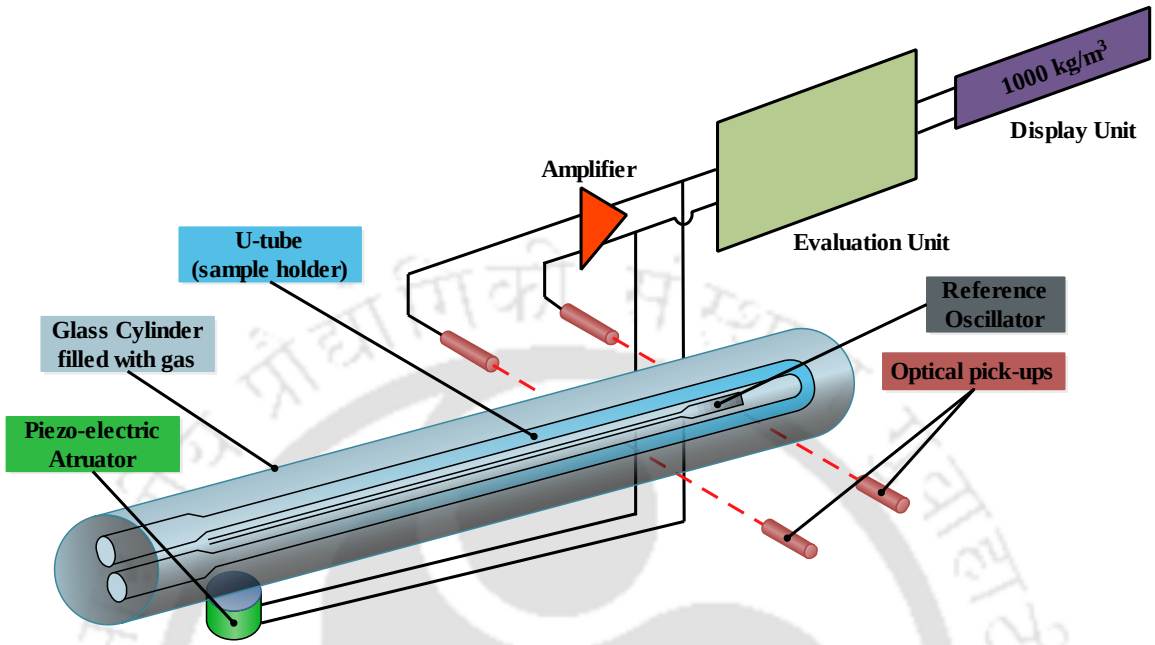

Figure 3.6: Measuring Principle of Density

3.7.2 Viscosity

The viscosity of the DES was determined using the Anton Paar interfacial rheometer, (Phsica MCR301) by the parallel plate method. Nearly, 1 mL of sample was used for viscosity measurement. The parallel plate type (PP-50) was used for the measurement along with inbuilt thermal jacket arrangement to maintain a constant sample temperature with an accuracy within ±273.17 K.

3.7.3 Thermal Conductivity

The thermal conductivities of both DESs and NDDESs were measured using a KD2 Pro thermal property analyzer (Decagon Device, USA) (figure 3.7). The device's measuring principle is based on the traditional hot-wire method. The device consists of two parts namely controller and sensor. The sensor namely "KS-1" (figure 3.7) having 1.3 mm in diameter and 6 cm length was used for the measurement. The sensor is inserted vertically

into the sample holder. The sample holder is a borosilicate glass vial of 1.5 cm diameter and 10 cm length. For controlling and conducting the measurements, the probe is connected to the controller.

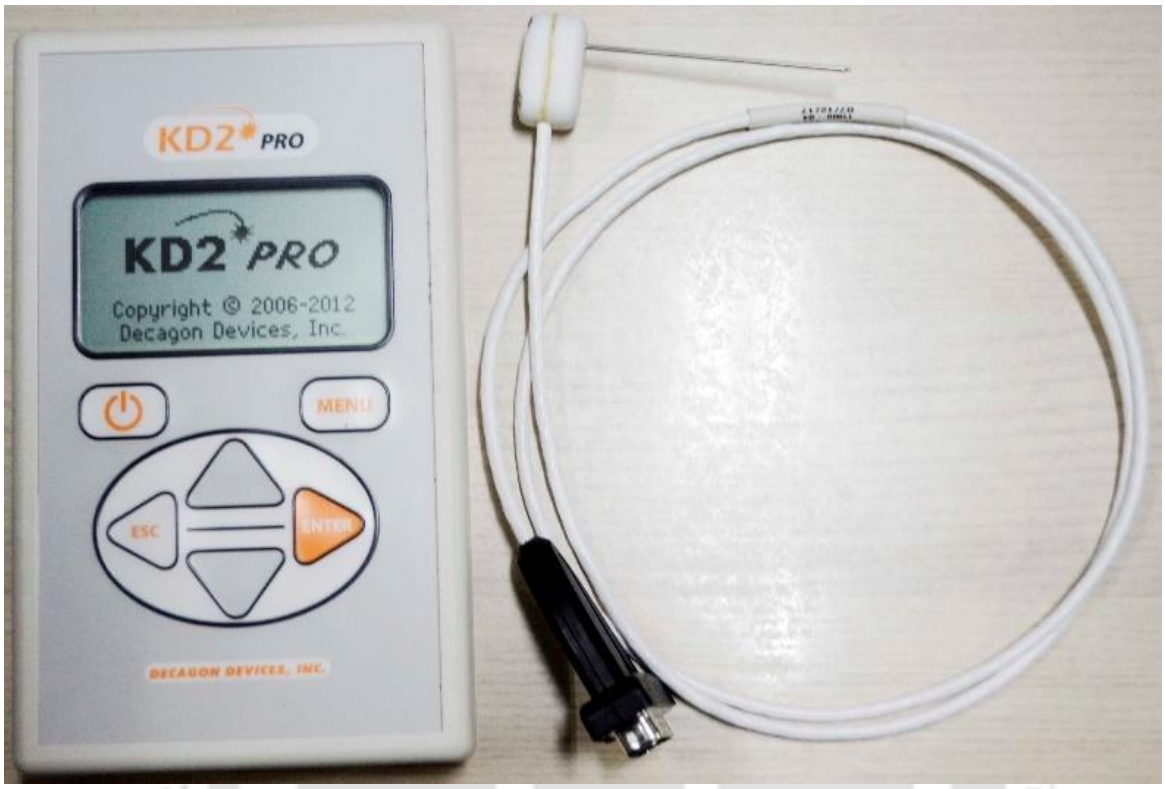

Figure 3.7: KD2 Pro Thermal Property Analyzer

Prior to the measurements, standard glycerine and Millipore water were used as the calibrating agents. To maintain a constant temperature and free convection of the measuring sample, a heating plate with silicone oil bath was used. The temperature accuracy of the bath was within ±273.52 K. The operating temperature of the sensor is 223.15 K to 423.15 K. The accuracy of the sensor is ±5%.

3.7.4 Specific Heat Capacity

Initially the volumetric heat capacity of the DESs and NDDESs were obtained from the same thermal property analyzer to measure the thermal conductivity. A dual needle sensor namely “SH-1” having 1.3 mm diameter, 3 cm long and 6 mm spacing was used to

measure the volumetric heat capacity of the DESs and NDDESs at different temperatures[78]. As the coefficient of expansion for liquids is very small the volumetric heat capacity is equal to the specific heat capacity[118].

3.8 Optimization of NDDESs

While dealing with different volume fraction of nanowires and two different base fluids i.e., DESs it is necessary to choose the best nanofluid i.e., NDDES. In order to select the best nanofluids, all the four thermophysical properties namely density, viscosity, thermal conductivity and specific heat capacity need to be considered. The multi objective optimization of the nanofluid is done on the basis of their thermal behaviours. Mouromtseff number [119] is used to achieve the highest heat transfer capability of the nanofluid. Mouromtseff (M_o) number is not dimensionless. The expression of Mouromtseff number is given below:

$$Mo = \frac{k^{0.6}\rho^{0.8}Cp^{0.4}}{\mu^{0.4}} \tag{3.3}$$

The higher M_o number signifies a better nanofluid in terms of heat transfer rate.

3.9 Forced Convection Studies

3.9.1 Experimental Studies

Figure 3.8 represents the schematic of the forced convection flow set up used for our experiments. The set up includes a chemical pump, flow control valve, rotameter, stainless steel testing section, cooling unit, HTF tank, thermocouples and pressure transducer. The pump was attached to a control valve followed by the rotameter. The test section tube with 9 mm inner diameter, 12 mm outer diameter, and 1000 mm length was made of stainless steel. To maintain uniform heating throughout the test section, flexible heating tape (Brisk

Heat SDCJCA-BIH101060L) was used. Power to the heater was provided by a DC power (GATTS MX1174A) supply.

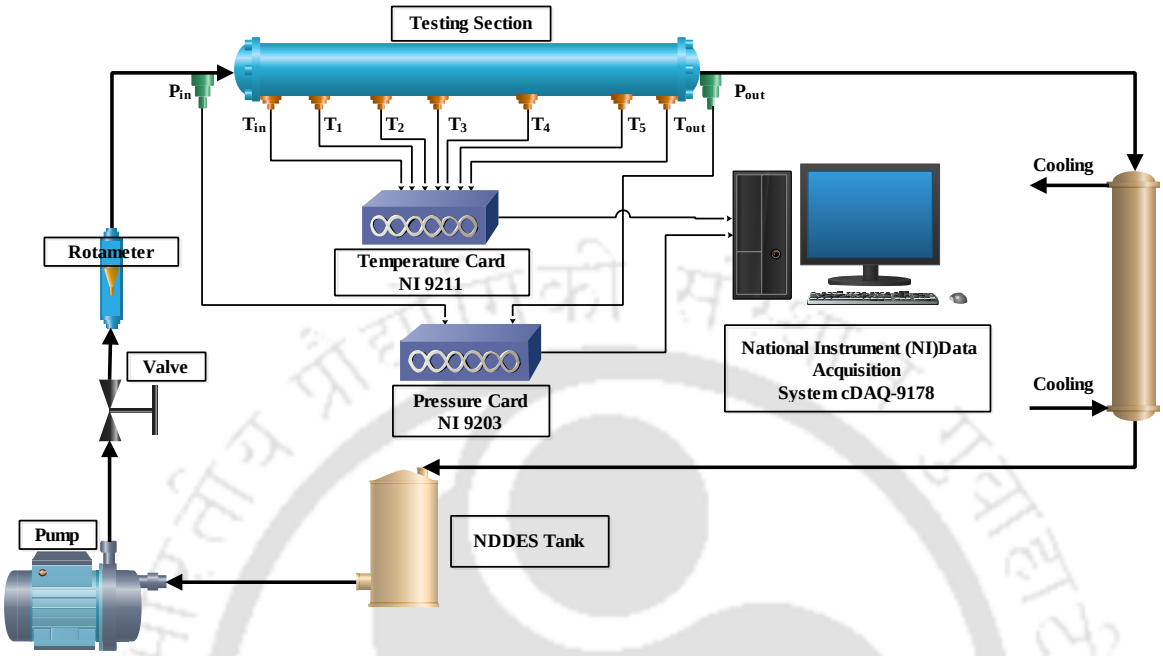

Figure 3.8: Schematic of the forced convection setup

The test section was insulated with fiberglass insulation to minimize the heat loss and maintain constant heat flux condition. Five J-type thermocouples were welded on the surface of the test section and two more were welded at the inlet and outlet of the test section so that inlet and exit liquid temperatures can be measured. Two pressure transducers were connected at the inlet and outlet of the test section to measure the pressure drop. All thermocouples (±2°C) and pressure transducers (±0.2mV) were connected to a National Instrument (NI) data acquisition system cDAQ-9178 via a temperature card NI 9211 and pressure card NI 9203 which were interfaced with a computer. The LabVIEW software was used for data processing.

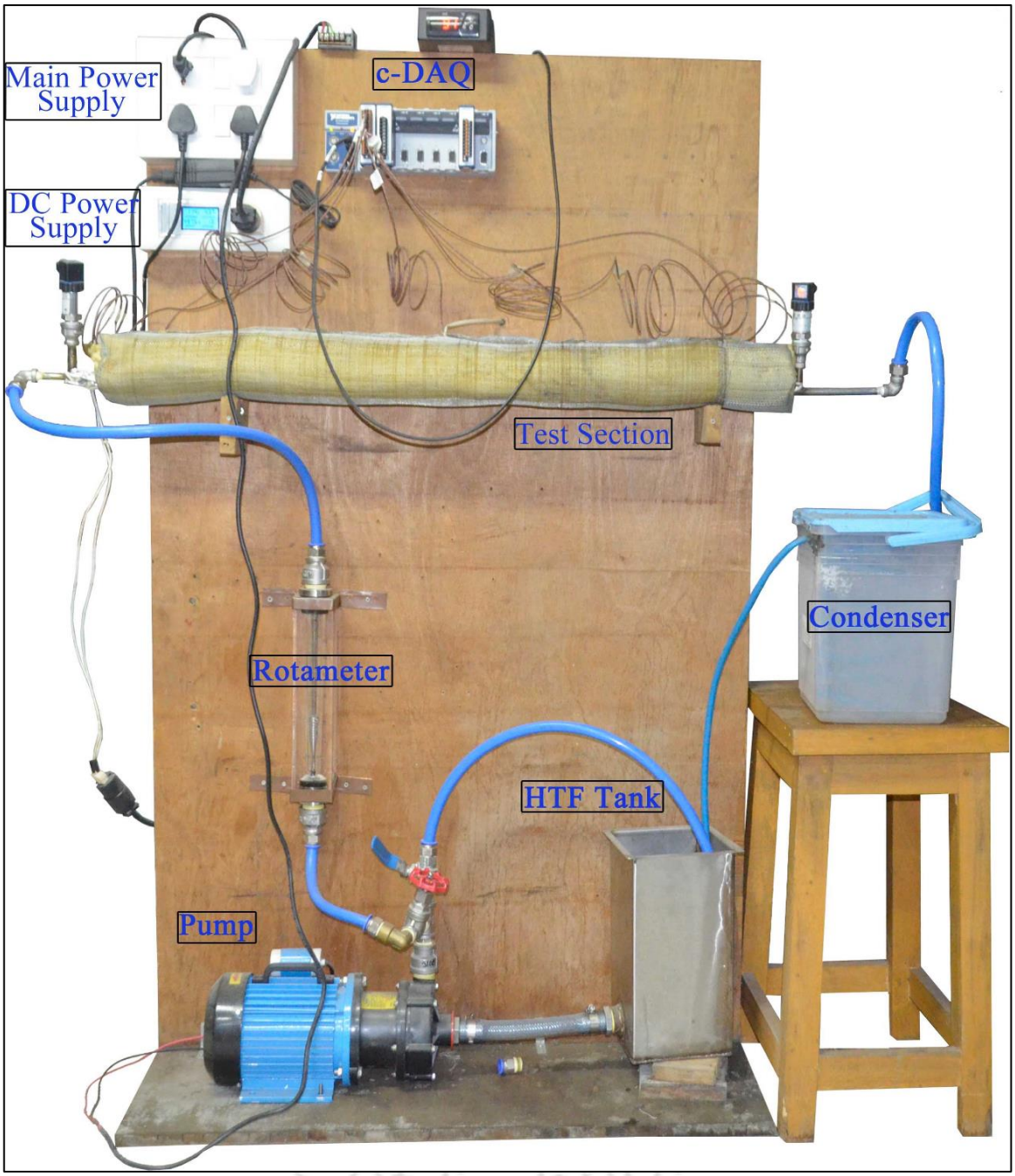

Figure 3.9: Forced Convection Setup

3.9.2 Experimental procedure

At the onset of experiment, the pump was run by deionized water to remove any grime and further with air to remove any water bubbles present inside the test section. Then the HTF was poured to the tank followed by pumping, where the desired flow rate is simultaneously maintained and measured by the control valve and rotameter respectively.

Once the steady state was obtained, temperatures at definite points of the test section were recorded with the help of LabVIEW software. Further next set of data was collected by increasing the desired flow rate of the pump (Taha PMD-15).

3.9.3 Data processing

The heat flux (q) was measured from the heater input power (Q) and heating surface area (A) using the following equation:

$$q = \frac{Q}{A} = \frac{VI}{\pi d_0 l} \tag{3.4}$$

Here d_0 represents the outer diameter of the tube and l depicts the testing section length, while V and I are the input voltage and current respectively.

The calculation of local heat transfer coefficient across the testing section, $h(x)$, was done by the following equation:

$$h(x) = \frac{q}{T_w^{'}(x) - T_f^{'}(x)} \tag{3.5}$$

Where $T_w^{'}(x)$ and $T_f^{'}(x)$ signifies the local temperatures of the inner surface and liquid respectively. By using a constant heat flux boundary condition i.e., the one-dimensional steady state heat conduction equation, the inner surface local temperature was calculated. The final expression of the inner surface temperature is given below:

$$T_w^{'}(x) = T_w(x) - \frac{Q \ln\left(r_o / r_i\right)}{2\pi L k_s} \tag{3.6}$$

Here $T_w(x)$ is the outer surface local temperature measured by the thermocouples. r_o and r_i are the outer and inner radius of the testing channel, respectively. k_s is the thermal conductivity of stainless steel. L is the heating length of testing section. Similarly, the liquid local temperature can be calculated from the energy equation:

$$T_f(x) = T_{fi} + \frac{Q}{\rho C_p V'} \frac{x}{L} \tag{3.7}$$

Where T_{fi} is the liquid inlet temperature of the test section, ρ and C_p are the density and heat capacity of the liquid respectively, and V' is the volumetric flow rate (in m^3/s). x is the axial distance. The accuracy of thermocouples, voltage, and current are in the range of ±0.57 C, ±2 V, and ±0.1 A respectively. The uncertainties of the Reynolds number and Nusselt number were estimated to be ±6.54 % and ±5.21 % respectively.

3.10 Numerical Studies

3.10.1 *Anupravah* Simulation

The flow inside the tube for present range are assumed to be incompressible, Newtonian, and within laminar regime. The governing equations for flow can be expressed as:

Continuity equation:

$$\frac{\partial u_j}{\partial x_j} = 0 \tag{3.8}$$

Momentum equations:

$$\frac{\partial(\rho u_i)}{\partial t} + \frac{\partial(\rho u_j u_i)}{\partial x_j} = -\frac{\partial p}{\partial x_i} + \frac{\partial \tau_{ij}}{\partial x_j} \tag{3.9}$$

Energy equation:

$$\frac{\partial\left(\rho C_p T\right)}{\partial t} + \frac{\partial\left(\rho C_p u_j T\right)}{\partial x_j} = \frac{\partial}{\partial x_j}\left(k_f \frac{\partial T}{\partial x_j}\right) \tag{3.10}$$

where k_f indicates the thermal conductivity of the liquid, τ_{ij} is the stress tensor and is given as

$$\tau_{ij} = \mu\left(\frac{\partial u_i}{\partial x_j} + \frac{\partial u_j}{\partial x_i}\right) \tag{3.11}$$

All equations were discretized using the finite volume method in a collocated grid arrangement[120,121]. Rhie and Chow[122] momentum interpolation scheme was used to avoid the pressure–velocity decoupling. The convective term was approximated by linear combination of upwind differencing scheme and central difference scheme, while diffusive term was approximated by central difference scheme. Constant heat flux and no-slip boundary conditions were used at the wall of the tube. At the inlet, average velocity and temperature boundary conditions were used, while at outlet, outflow boundary conditions were used.

3.10.2 COMSOL Simulation

The development of flow through a pipe in the laminar flow regime is depicted in figure 3.10. This was used for the numerical modelling studies using COMSOL (Version: 5.2a). For COMSOL, the continuity equation is written in vector form as:

$$\rho\nabla.(u) = 0 \tag{3.12}$$

The equation of motion for an incompressible fluid in vector form is then written as:

$$\rho\frac{\partial u}{\partial t} + \rho(u.\nabla)u = \nabla.\left[-p + \mu(\nabla.u) + (\nabla.u)^T\right] + F \tag{3.13}$$

The first two terms of the left-hand side signify the inertia term, while the first term in the right-hand side represents the pressure gradient. The second term in the right side represents the diffusion term, while the last term is the body force term. In a similar manner, the equation of energy takes the form as given below:

$$\rho C_P\frac{\partial T}{\partial t} + \rho C_P u.\nabla T + \nabla.q = Q^{'} + Q^{'}_{vd} \tag{3.14}$$

$$q = -k\nabla T \tag{3.15}$$

The first two-term in the energy equation represents the accumulation term and convection term respectively, while the last term is due to heat conduction. On a similar note the first term on the right side of equation 3.14 represents the heat source terms, while the second term denotes the viscous heat dissipation term.

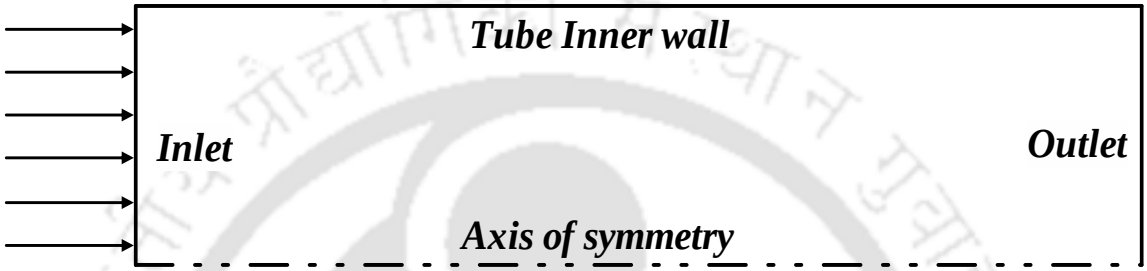

Figure 3.10: Schematic of pipe flow in laminar region

3.11 Steam Generation Procedure

Aspen Plus simulation tool (V11.0) was used to evaluate the effectiveness of the best performing HTF obtained from the forced convection set up. A two-stage heat exchanger (HeatX) scheme was adopted for the generation of steam using HTF. The U-tube (U-T) heat exchanger was introduced followed by shell and tube (S-T) heat exchanger. The detail specifications of the heat exchangers are reported in table 3.5[12]. Initially a benchmarking simulation of steam generation was carried out using molten salt mixture (figure 3.11)[12], while the stream details are given in table 3.6. The detailed flowsheet for the DES and NDDES can be found in Figure 3.12. Water inlet temperature is 298.15 K and the same for NDDES was in the range of 423.15-498.15 K. The HTF flow rate was maintained at 4 m^3/hr, while the water flow rate was fixed at 15 kg/hr. The HBA, HBD and nanoparticle used in our work are not available in standard compound list of Aspen Plus. Therefore, all

the components including water were added under the *pseudocomponent* mode for performing the simulation.

Table 3.5: Detailed Specifications of Heat Exchangers

Parameters	U-tube (U-T) heat exchanger	Shell and Tube (S-T) heat exchanger
Shell Inner Diameter (mm)	224	164
Shell Thickness (mm)	2.5	2.5
Tube Inner Diameter (mm)	32	25
Tube Thickness (mm)	2	2
Tube Length (mm)	1850	719
Number of Tubes	3 (U-Shaped)	9

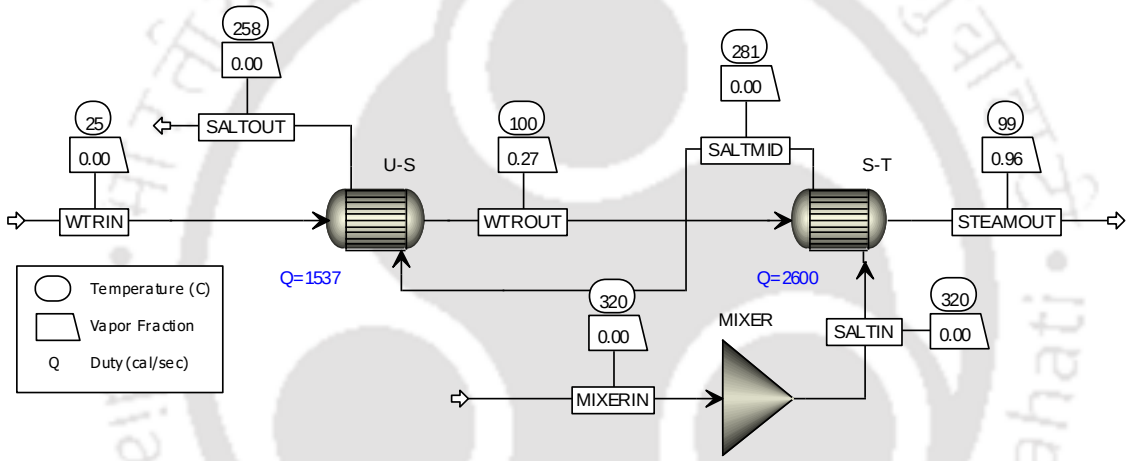

Figure 3.11: Aspen plus simulation system of a two-stage steam generator for Nitrate based Molten Salt as Thermal Media

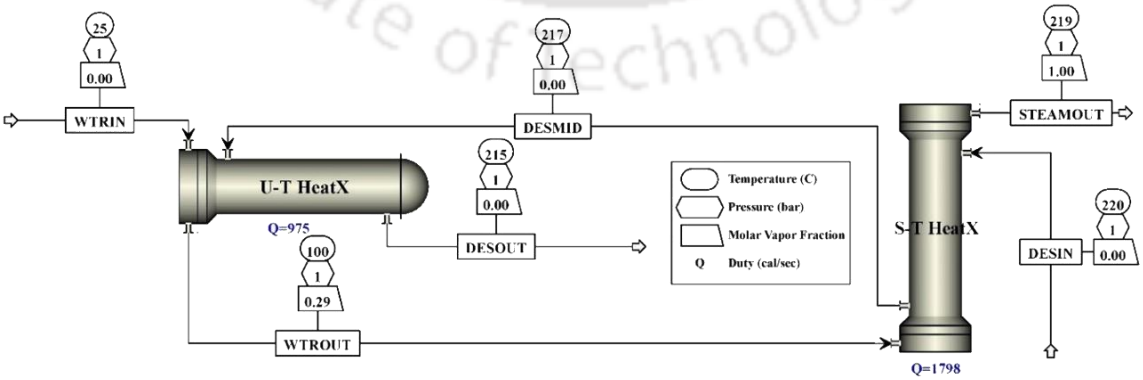

Figure 3.12: Process flow sheet for Aspen Plus simulation for DES and NDDES

Table 3.6: Stream summary of Nitrate based Molten Salt as Thermal Media

Material							
Stream Name	**Units**	**SALTIN**	**SALTMID**	**SALTOUT**	**WTRIN**	**WTROUT**	**STEAMOUT**
From		MIXER	S-T	U-T		U-T	S-T
To		S-T	U-T		U-S	S-T	
Phase		**Liquid Phase**					**Vapour Phase**
Temperature	K	673.15	653.03	636.46	298.15	372.74	390.65
Mass Enthalpy	kJ/kg	-4034.89	-4064.64	-4089.13	-15864.3	-14683.2	-13249.2
Mass Density	kg/m^3	602.63	606.06	608.88	994.69	1.51	0.55
Average MW		84.29	84.29	84.29	18.02	18.02	18.02
Volume Flow	m^3/sec	0.00	0.00	0.00	0.00	0.00	0.01
Heat capacity, mixture	J/mol.K	124.62	124.62	124.62	75.38	59.93	34.16
		Vapour Phase					
Mass Enthalpy	kJ/kg	**No Vapour Phase Detected**				-13283	-13249
Mass Density	kg/m^3					0.58	0.55
Average MW						18.02	18.02
Std. vap. Vol. flow	m^3/h					0.00	31.10
Heat capacity, mixture	J/mol.K					34.026	34.168

The concept of *pseudo component* in Aspen Plus simulation was previously introduced for CO_2 absorption and aromatic extraction using ILs[123,124]. Aspen requires screening charge density (σ) and COSMO volume along with boiling point, density, viscosity and average molecular weight to define it as a *pseudocomponent*. The sigma profiles of the molecules were generated and provided in figure 3.13 and figure 3.14. The average molecular weight ($\overline{M}_w$) concept was employed for the calculation of molecular weight of DES as per following equation.

$$\overline{M}_w = \frac{\sum_i N_i M_i^2}{\sum_i N_i M_i} \qquad (3.16)$$

where N_i is the number of molecules of component i; and M_i is the corresponding molecular weight. The boiling point (T_b) of the DES was calculated by the group contribution method, named as Joback Method using equation 8[107].

$$T_b = 198.2 + \sum n_i \Delta T_{bM_i} \tag{3.17}$$

Where n_i is the frequency of appearance of the i^{th} group of atoms in the molecule, ΔT_{bM} is their contribution to the normal boiling temperature (K). Other thermophysical properties were evaluated from the experimental measurement within this work.

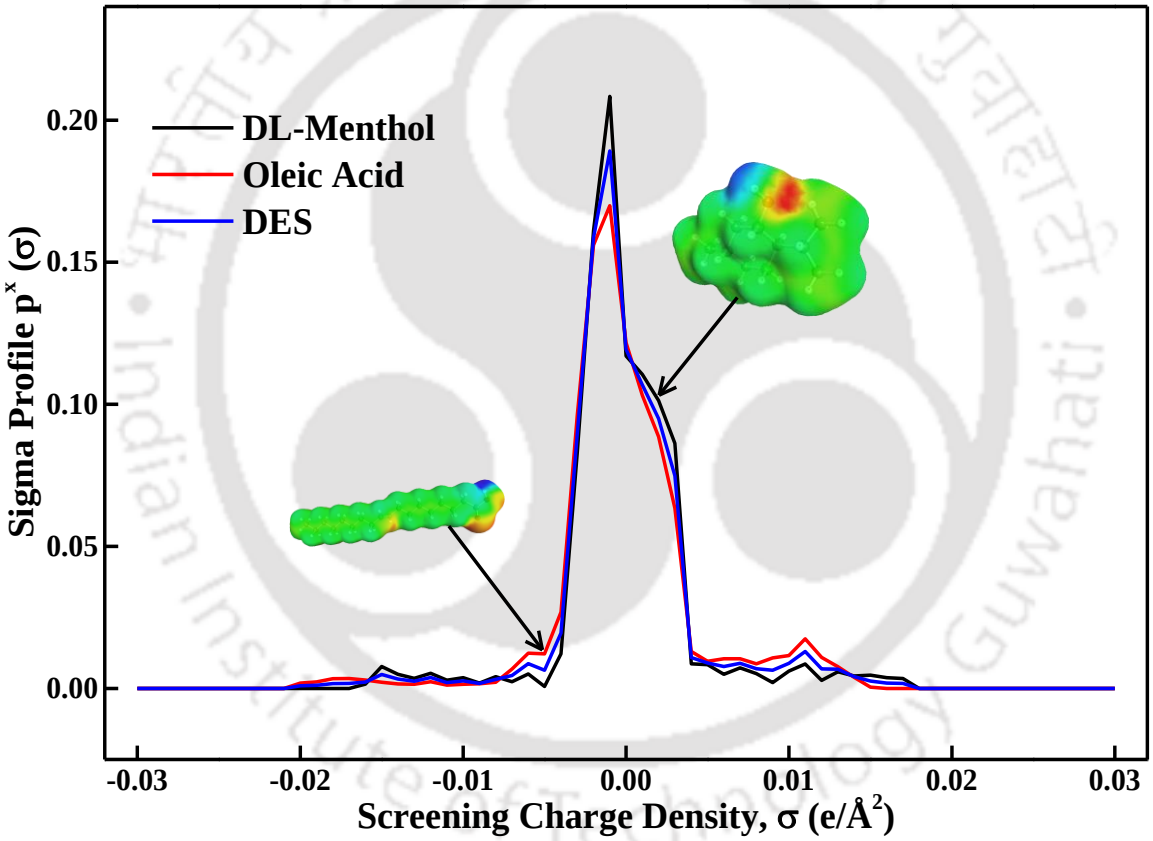

Figure 3.13: Sigma Profile of DL-Menthol, Oleic Acid and DES

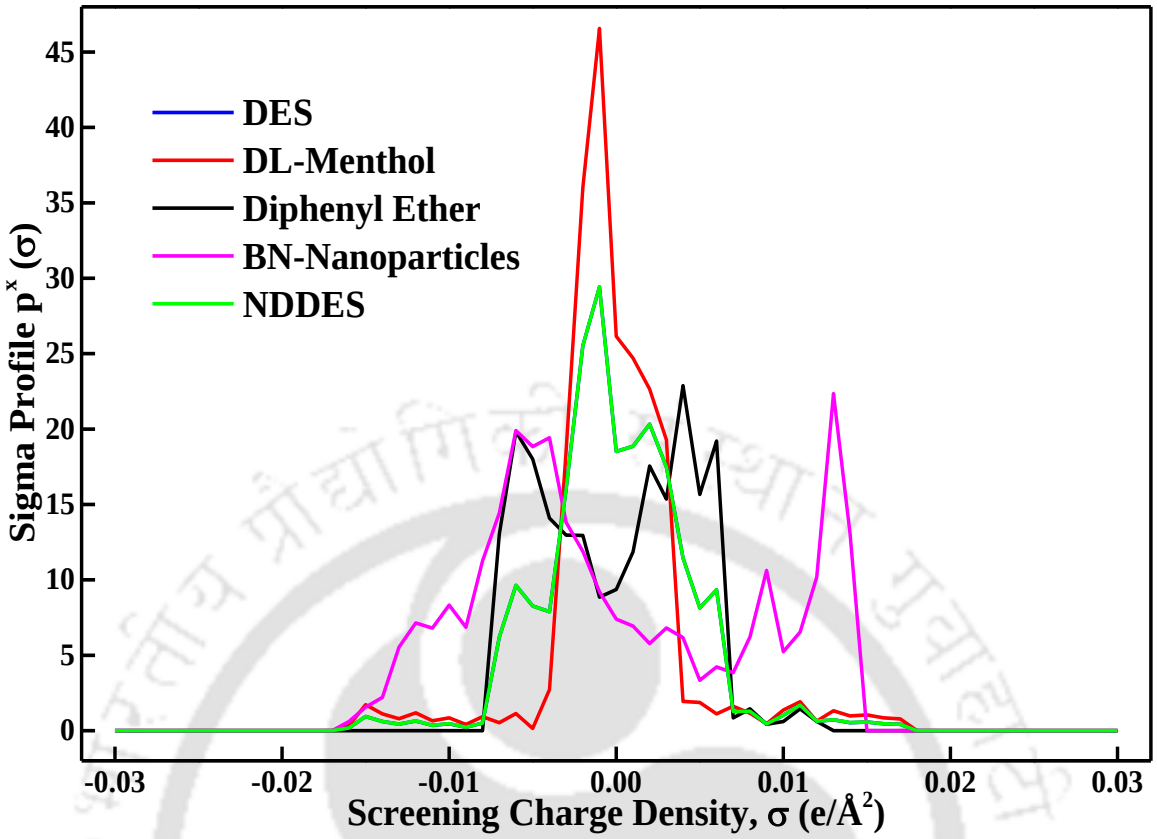

Figure 3.14: Sigma profiles for Diphenyl Ether, DL-menthol, DES3, *h*-BN nanoparticle and NDDES25

The module of Aspen Exchanger Design and Rating (EDR) was used to design the heat exchangers used in this study. EDR uses the structural information and the corresponding dimensions of the heat exchanger to get a complete optimized design based on the cost effectiveness while satisfying the restriction (namely the desired input or output variable) of the process. Further, the optimized design gives the performance characteristics and a complete geometry of the exchanger along with the specification details and layout drawings. Figures 3.15 and 3.16 represent the EDR browsers for S-T and U-T heat exchangers respectively.

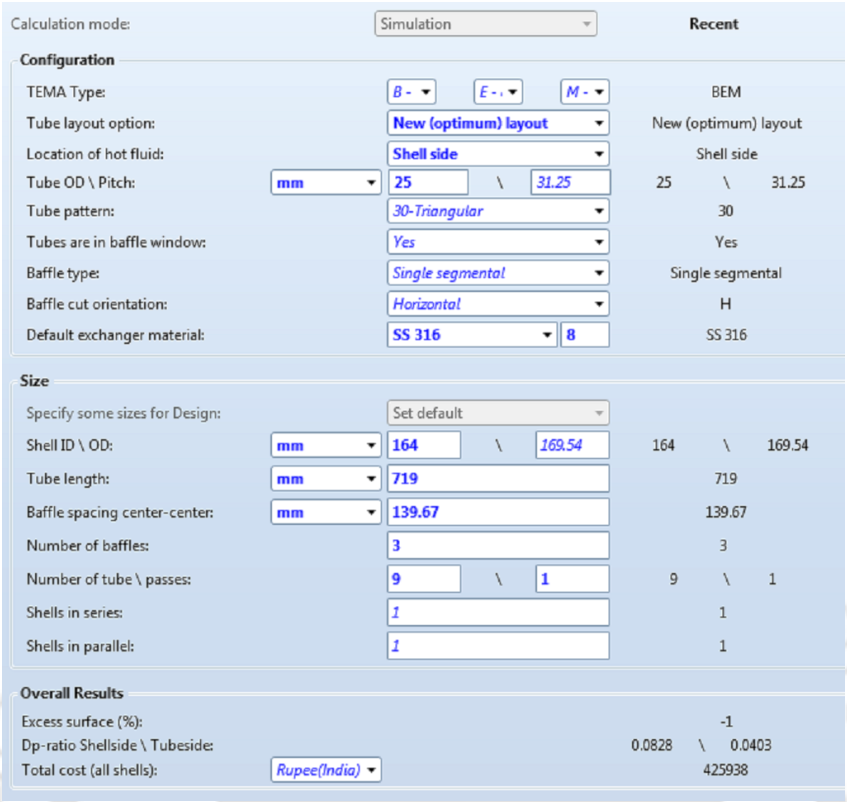

Calculation mode:	Simulation		Recent
Configuration			
TEMA Type:	B - E - M -		BEM
Tube layout option:	New (optimum) layout		New (optimum) layout
Location of hot fluid:	Shell side		Shell side
Tube OD \ Pitch:	mm	25 \ 31.25	25 \ 31.25
Tube pattern:	30-Triangular		30
Tubes are in baffle window:	Yes		Yes
Baffle type:	Single segmental		Single segmental
Baffle cut orientation:	Horizontal		H
Default exchanger material:	SS 316	8	SS 316
Size			
Specify some sizes for Design:	Set default		
Shell ID \ OD:	mm	164 \ 169.54	164 \ 169.54
Tube length:	mm	719	719
Baffle spacing center-center:	mm	139.67	139.67
Number of baffles:		3	3
Number of tube \ passes:		9 \ 1	9 \ 1
Shells in series:		1	1
Shells in parallel:		1	1
Overall Results			
Excess surface (%):			-1
Dp-ratio Shellside \ Tubeside:			0.0828 \ 0.0403
Total cost (all shells):	Rupee(India)		425938

Figure 3.15: EDR browser for S-T heat exchanger

Calculation mode:	Simulation		Recent
Configuration			
TEMA Type:	B - E - M -		BEM
Tube layout option:	New (optimum) layout		New (optimum) layout
Location of hot fluid:	Shell side		Shell side
Tube OD \ Pitch:	mm	32 \ 39	32 \ 39
Tube pattern:	30-Triangular		30
Tubes are in baffle window:	Yes		Yes
Baffle type:	Single segmental		Single segmental
Baffle cut orientation:	Horizontal		H
Default exchanger material:	SS 316	8	SS 316
Size			
Specify some sizes for Design:	Set default		
Shell ID \ OD:	mm	224 \ 230.81	224 \ 230.81
Tube length:	mm	925	925
Baffle spacing center-center:	mm	231.25	231.25
Number of baffles:		3	3
Number of tube \ passes:		3 \ 2	3 \ 2
Shells in series:		1	1
Shells in parallel:		1	1
Overall Results			
Excess surface (%):			0
Dp-ratio Shellside \ Tubeside:			0.0741 \ 0.0075
Total cost (all shells):	Rupee(India)		522835

Figure 3.16: EDR browser for U-T heat exchanger

The released heat by hot fluid (DES) is:

$$Q_{rel} = q_{v,DES}\rho c_p(\mathrm{T}_{in} - \mathrm{T}_{out}) \tag{3.18}$$

Where $q_{v,DES}$, ρ, c_p symbolizes the volumetric flow rate, density and specific heat capacity of DES respectively, while T_{in} and T_{out} are inlet and outlet temperature of DES in K.

The heat absorbed by cold fluid (water/steam) is:

$$Q_{ab} = q_{m,w}(\mathrm{h}_{out} - \mathrm{h}_{in}) \tag{3.19}$$

Where $q_{m,w}$ is mass flow rate of water/steam, h_{in} and h_{out} are inlet and outlet enthalpies (J/kg) of water/steam. From the above equation, the total heat flux of the steam generator is given by:

$$q = \frac{Q_{ab}}{S_{total}} \tag{3.20}$$

Here S_{tot} is the required heat transfer area of the steam generator obtained from the simulation. The LMTD of the whole system is:

$$\Delta T_m = \frac{\Delta T_{in} - \Delta T_{out}}{\ln \frac{\Delta T_{in}}{\Delta T_{out}}} \tag{3.21}$$

Where ΔT_{in} and ΔT_{out} is temperature difference at the ends of the steam generator. The overall heat transfer coefficient is estimated as:

$$U = \frac{q}{\Delta T_m} \tag{3.22}$$

Substituting Eq. (6) in Eq. (7) and again Eq. (7) in Eq. (9) we get:

$$U\Delta T_m = \frac{q_{m,w}(\mathrm{h}_{out} - \mathrm{h}_{in})}{S_{tot}} \tag{3.23}$$

After the preliminary discussion, we shall see the effect of different temperature and DES flow rate on vapor generation rate, overall heat transfer coefficient, and total heat flux.

CHAPTER 4

4 Physiochemical and Thermophysical Results

4.1 Physiochemical Properties

4.1.1 Results from NMR

The prepared Deep Eutectic Solvents (DESs) were initially characterized by NMR spectroscopy. As mentioned in the previous chapter, three different types of NMR characterizations (^{1}H, ^{13}C and NOESY) were chosen for the confirmation of the DES formation. ^{1}H or proton NMR spectra of all the DESs along with their respective HBA and HBD are reported in figures 4.1 to 4.6. From the figures the peak shifting occurred which can be clearly identified by comparing their precursors, namely HBA and HBD. For example, in DES1, a negative peak shifting occurs. The chemical shift are due to various possible factors[125], such as π-π interaction, effect of hydrogen bonding due to the H-bond of HBD with HBA, C-H-π interaction between HBA and HBD, HBD effect and electrostatic field effect.

Further ^{13}C or carbon NMR spectroscopy were carried out and reported in figure 4.7. From the ^{13}C NMR, the absence of any new peaks confirms that there is no reaction[126]. Furthermore, the final confirmation of DES formation was carried out by NOESY (2D) NMR spectroscopy study (figure 4.8). NOESY spectra give the spatial arrangements of protons in terms of H-H interactions between HBA and HBD indicated by contours. However, in DES3 contours appear within the same molecule. DES3 is a combination of aromatic and cycloalkane compounds unlike other DESs. Hence, it can be stated that only eight NOESY scans may not be sufficient enough to detect H-H interactions between HBA and HBD for solvents like DES3. Literature also suggests that a greater number of NOESY scans can locate higher H-H interactions for DESs[98].

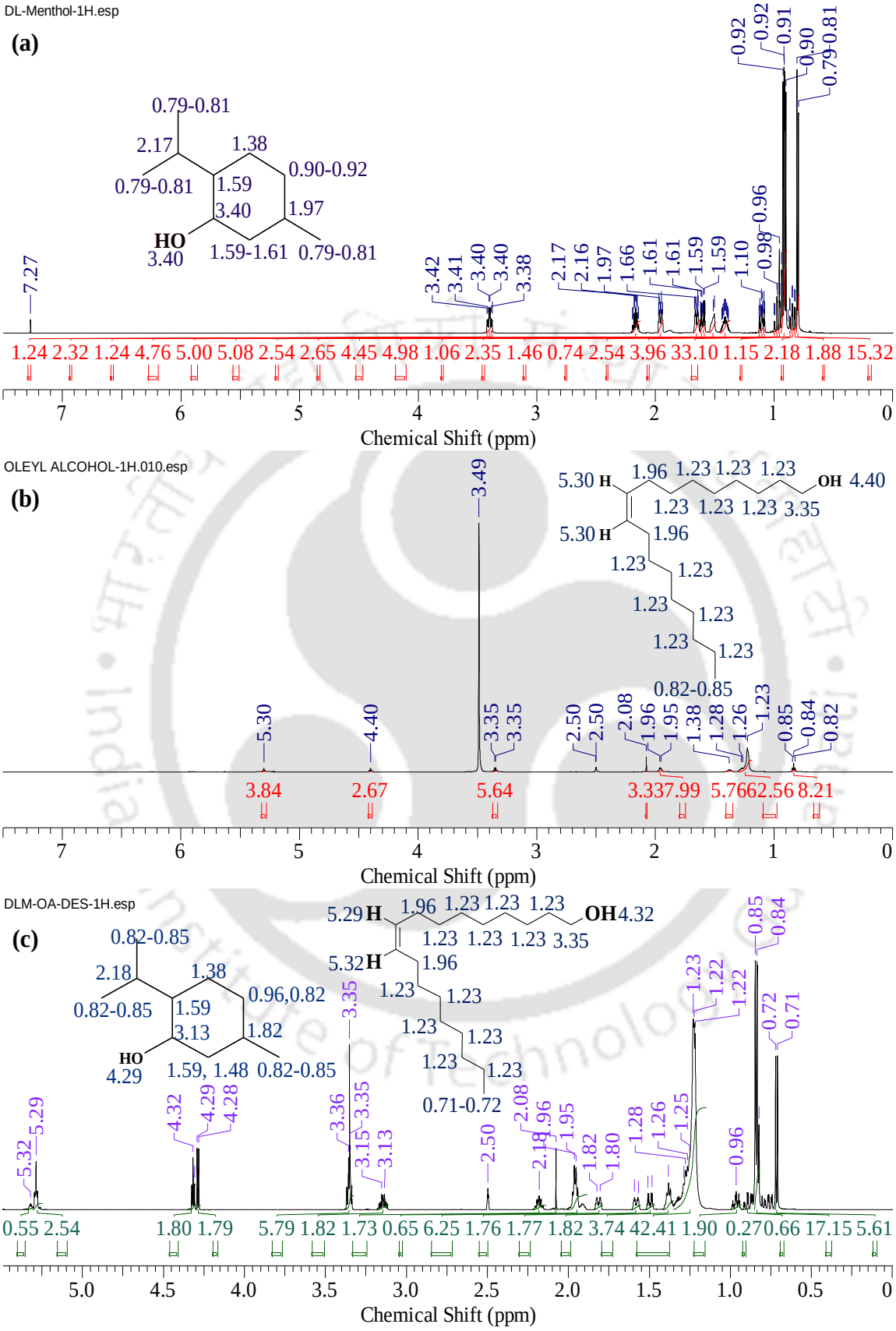

Figure 4.1: ^{1}H NMR spectra of (a) DL-Menthol, (b) Oleyl Alcohol and (c) DES1

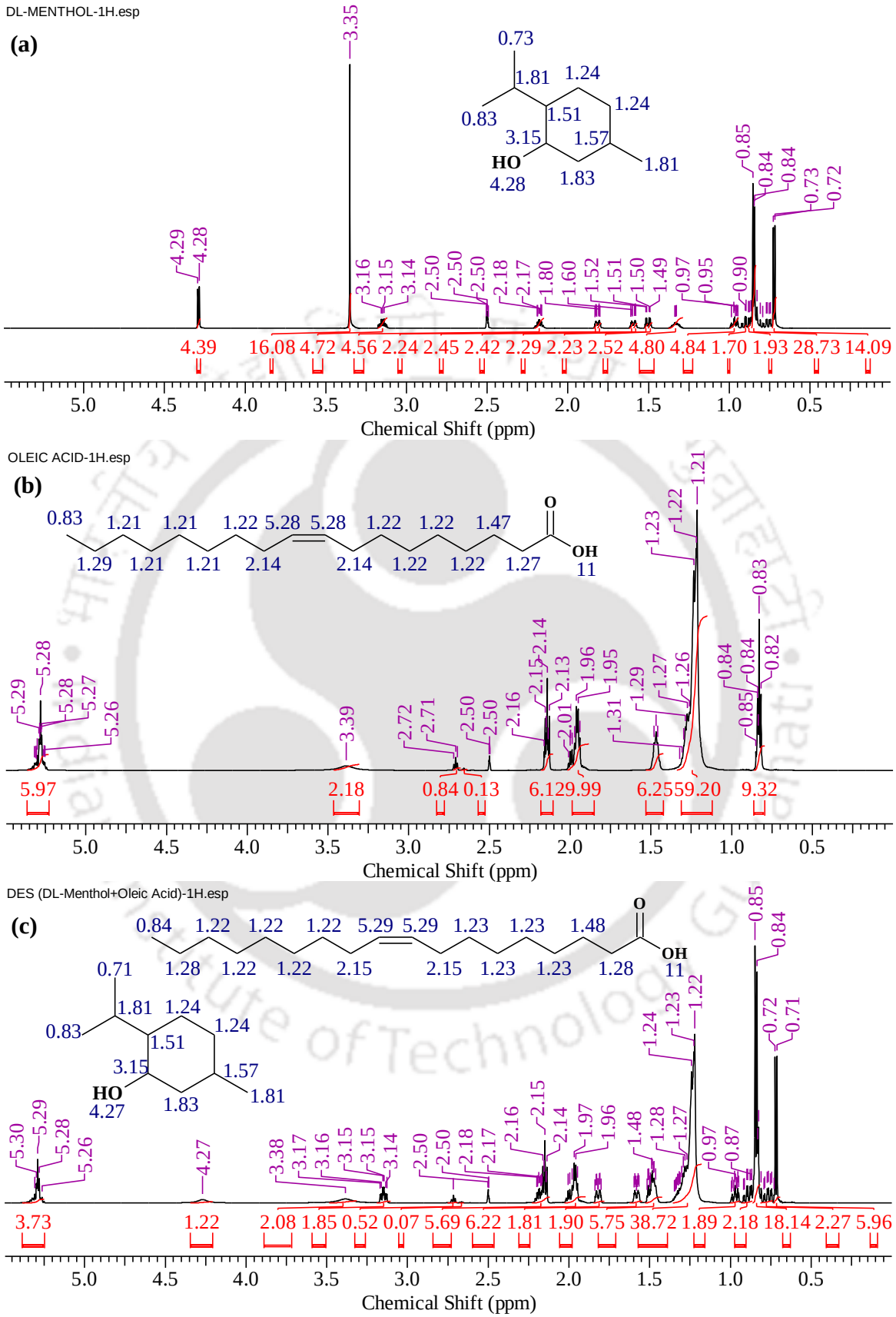

Figure 4.2: ^{1}H NMR spectra of (a) DL-Menthol, (b) Oleic Acid and (c) DES2

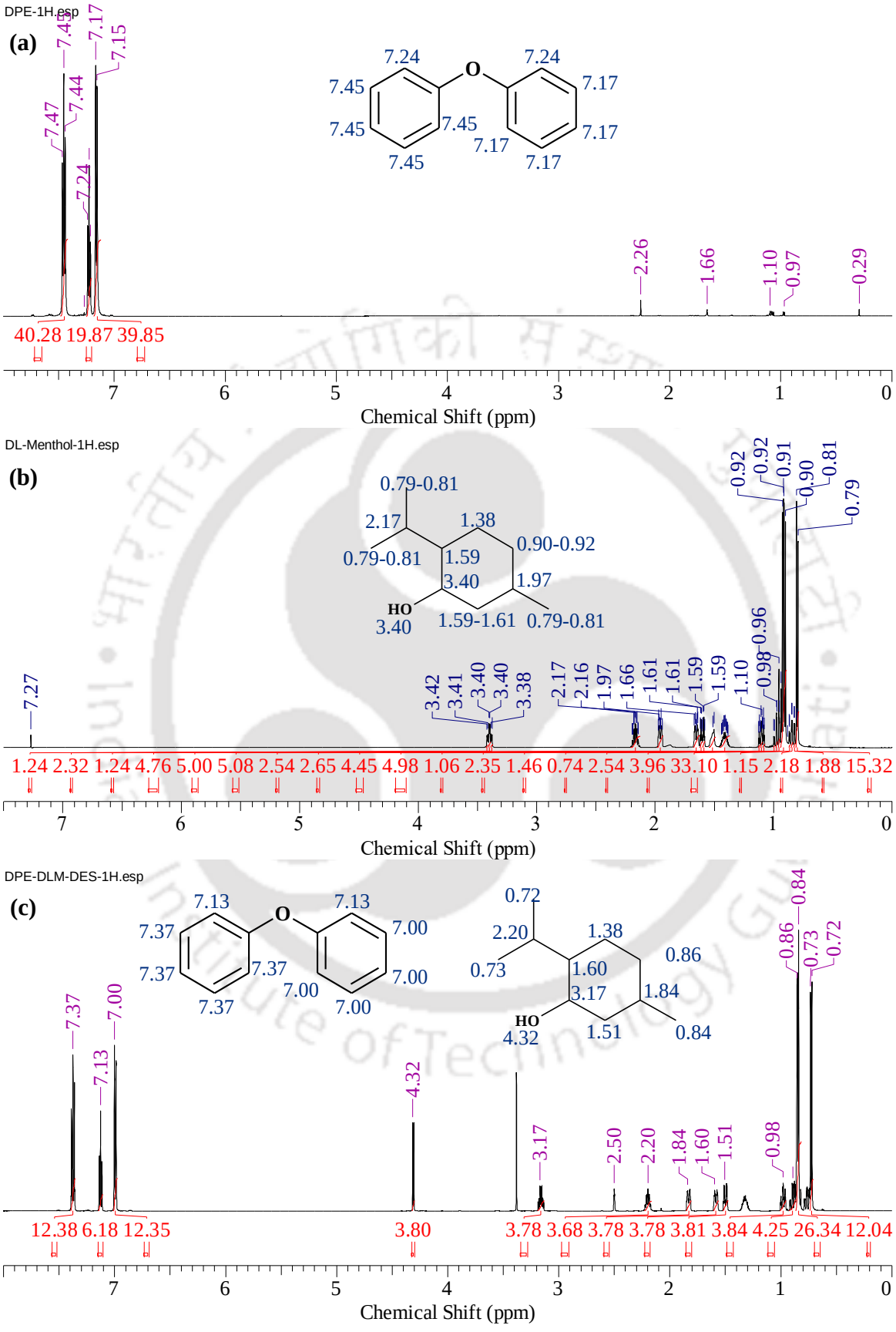

Figure 4.3: ^{1}H NMR spectra of (a) Diphenyl Ether, (b) DL-Menthol and (c) DES3

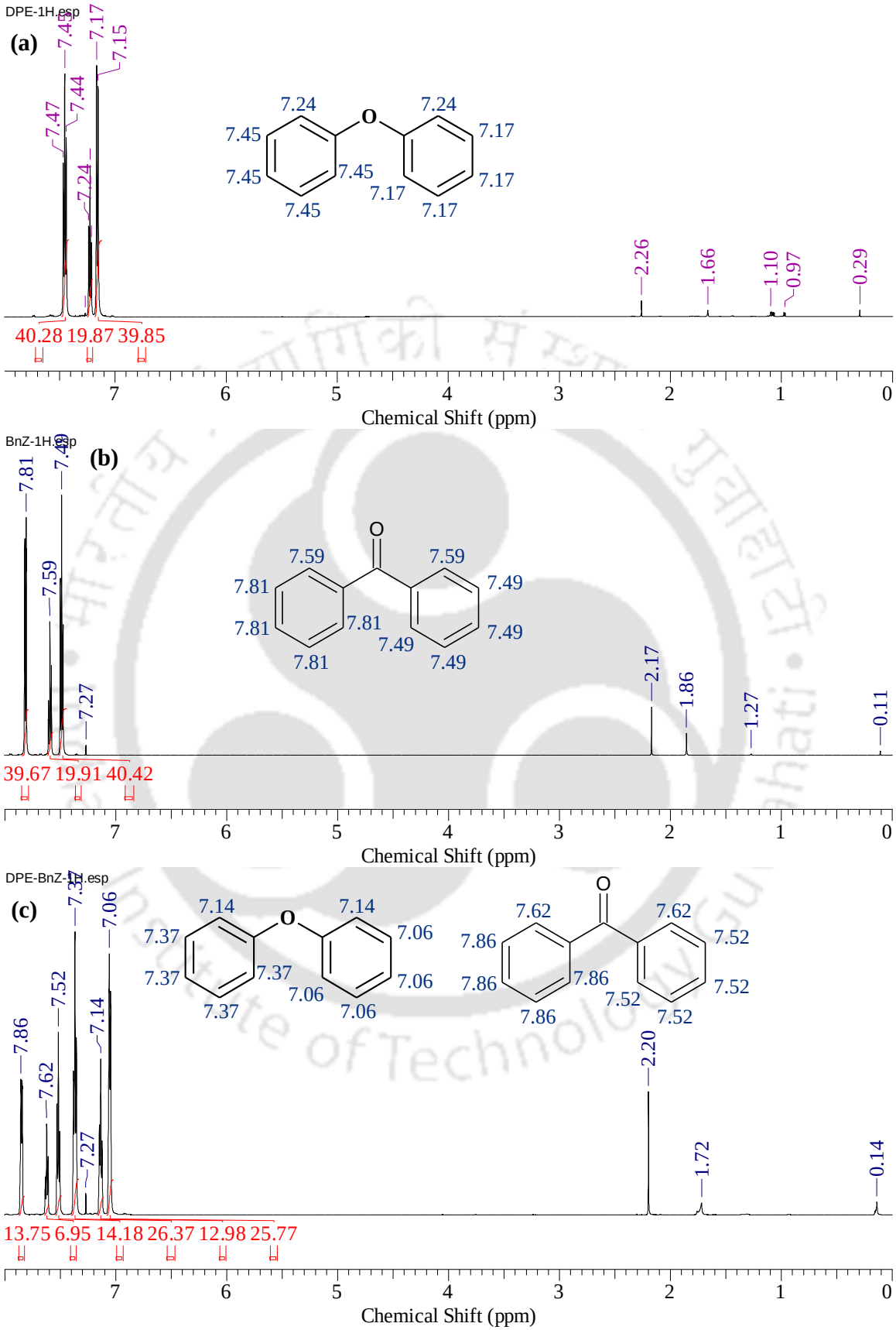

Figure 4.4: ^{1}H NMR spectra of (a) Diphenyl Ether, (b) Benzophenone and (c) DES4

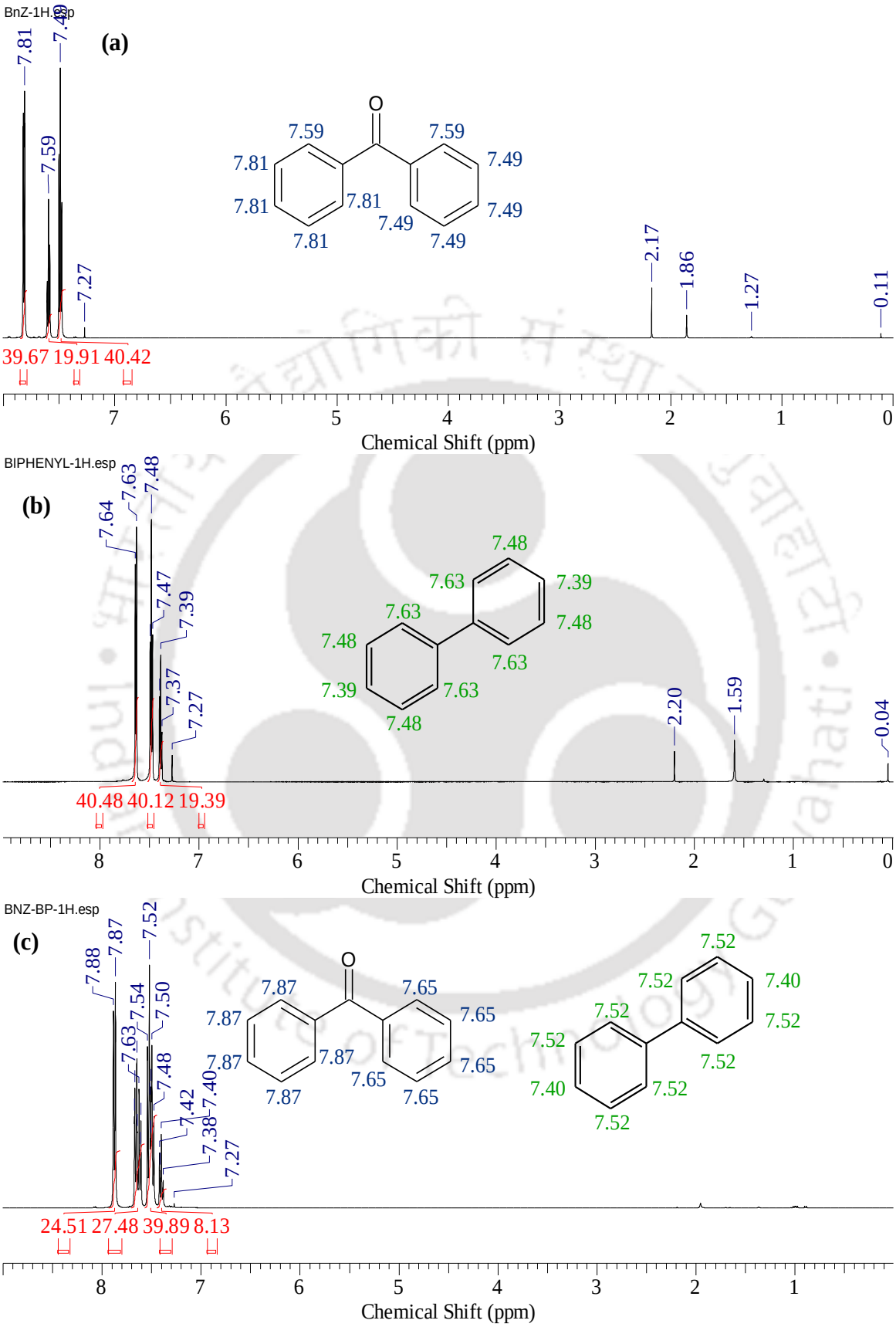

Figure 4.5: ^{1}H NMR spectra of (a) Benzophenone, (b) Biphenyl and (c) DES5

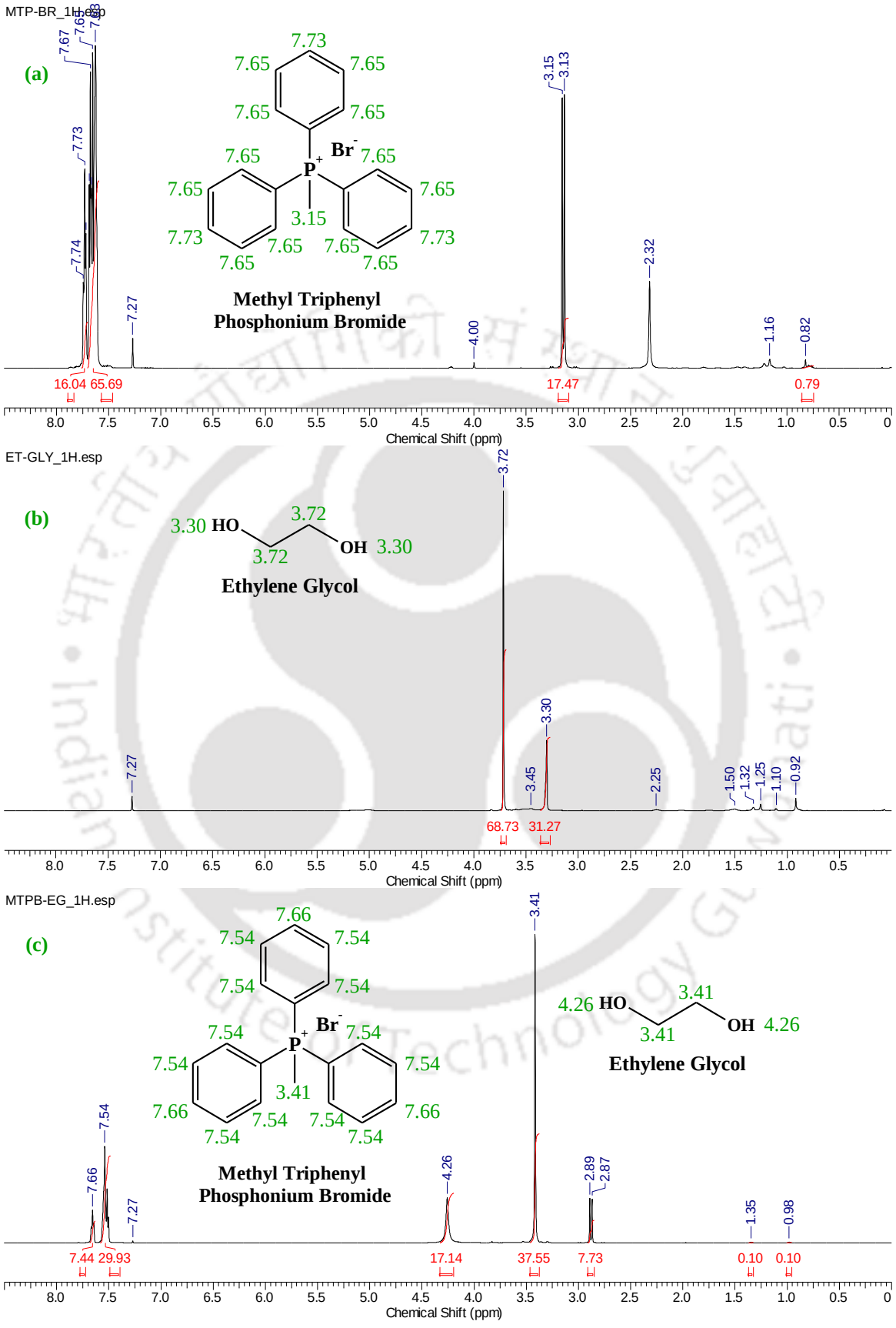

Figure 4.6: ^{1}H NMR spectra of (a) MTPB, (b) Ethylene Glycol and (c) DES6

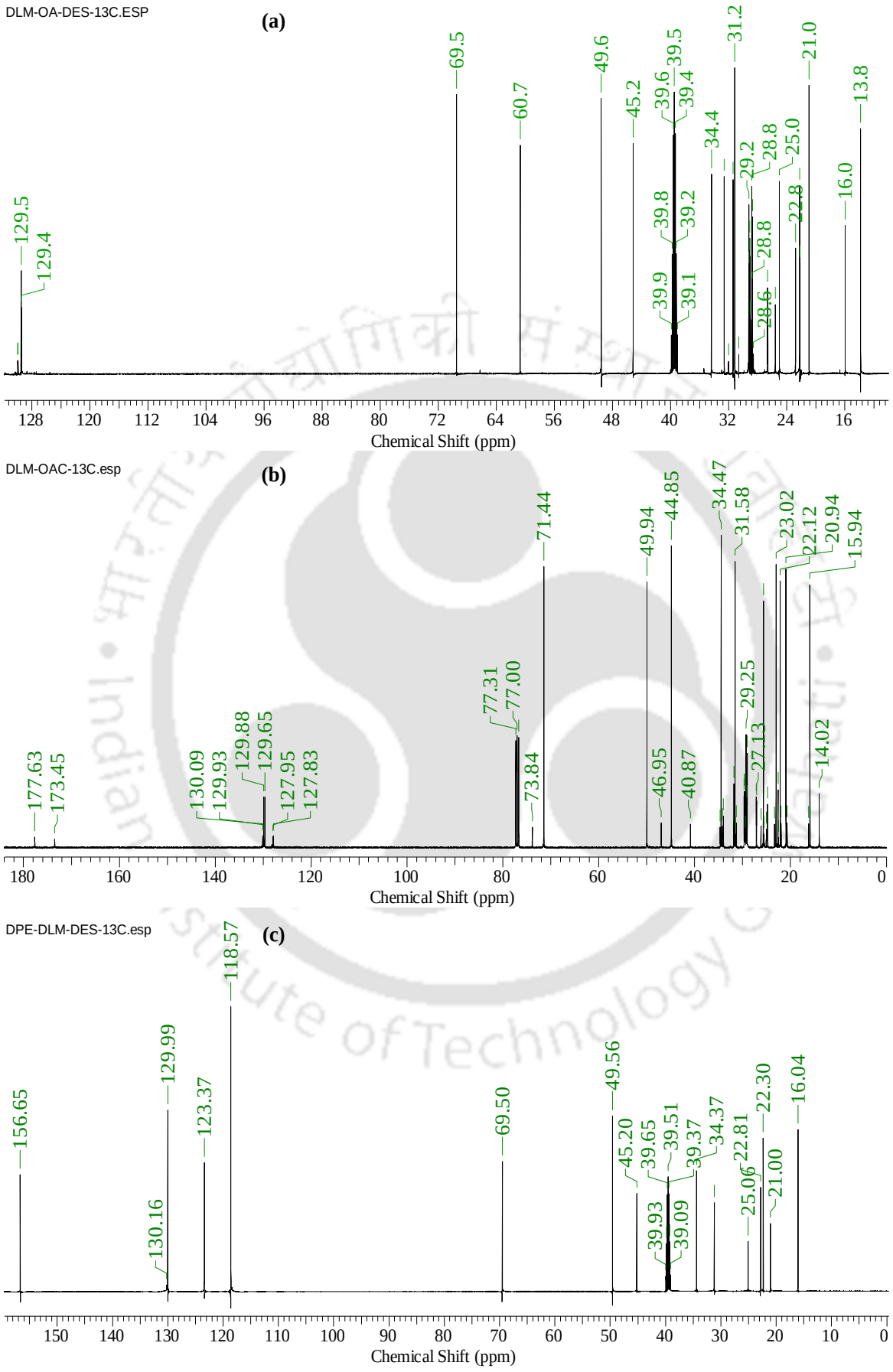

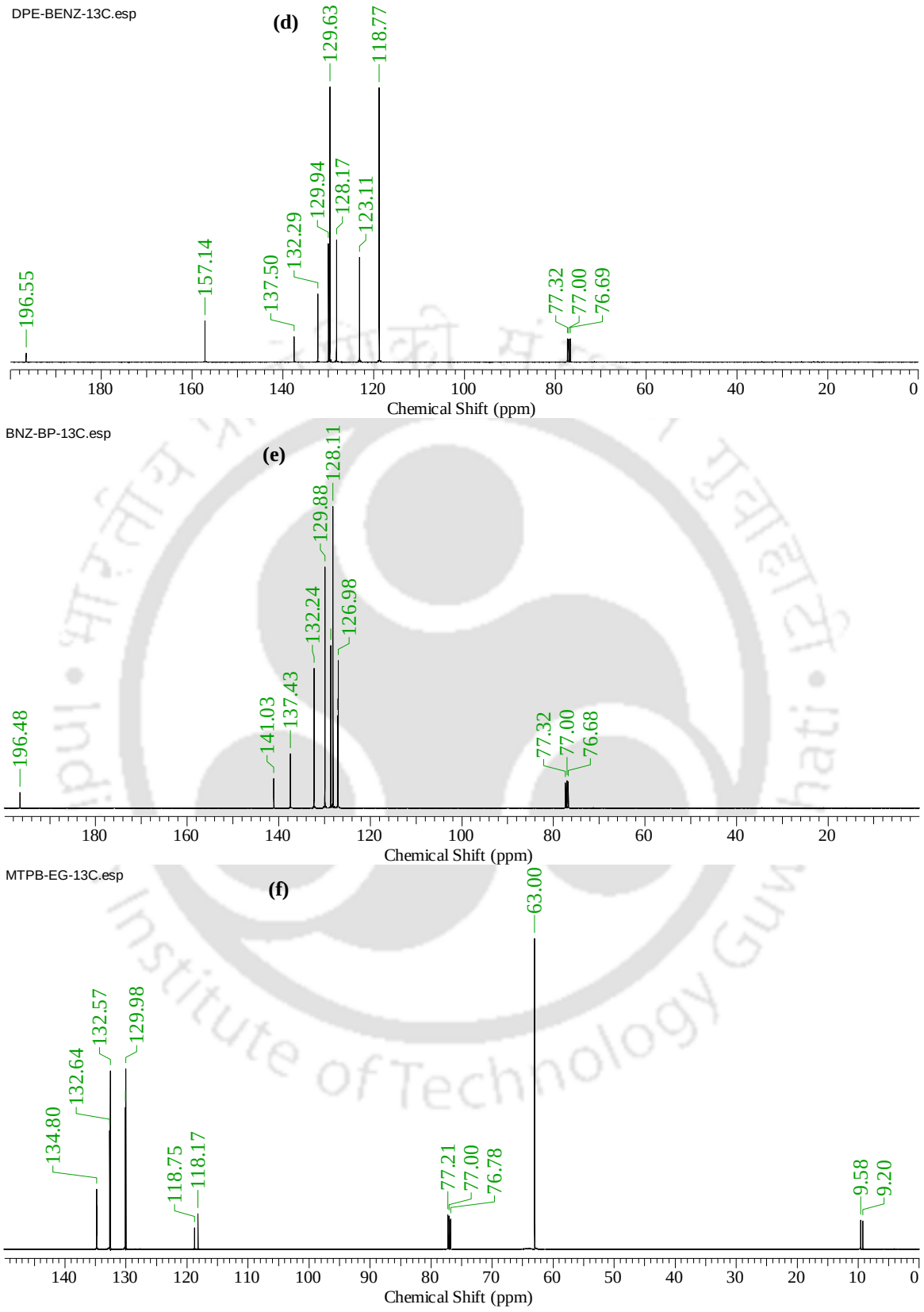

Figure 4.7: ^{13}C NMR spectra of (a) DES1, (b) DES2, (c) DES3, (d) DES4, (e) DES5 and (f) DES6

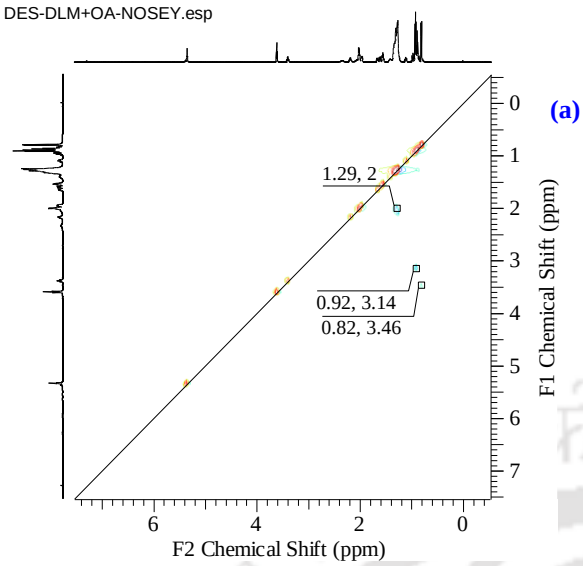

(a)

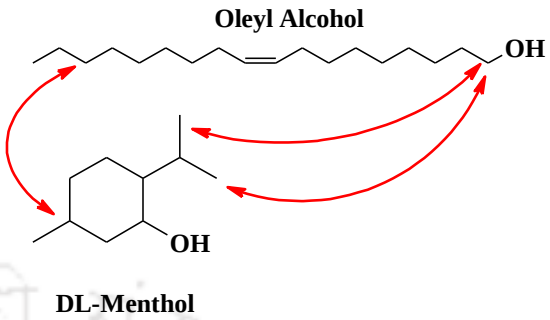

DL-Menthol

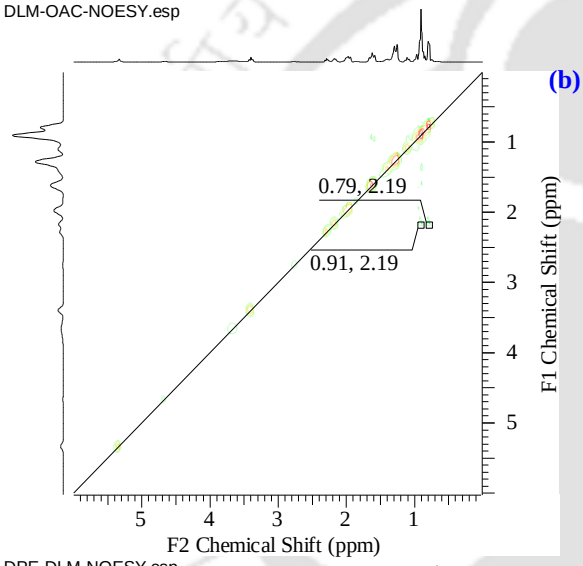

(b)

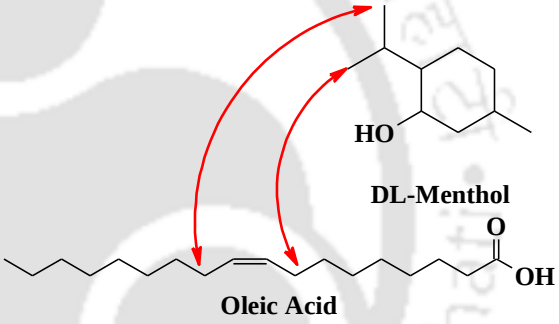

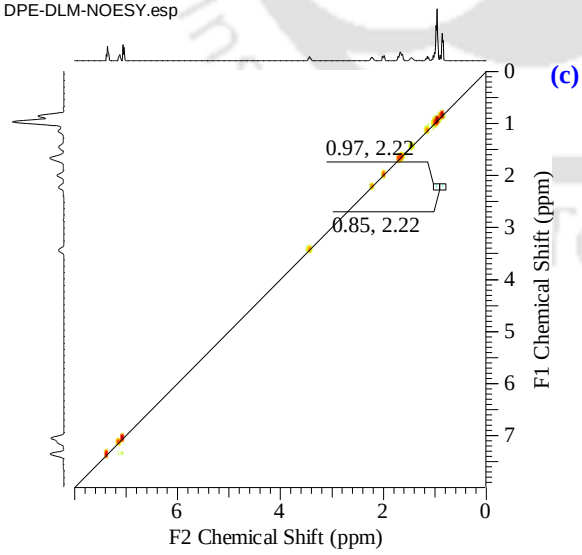

(c)

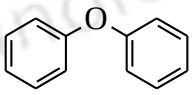

Diphenyl Ether

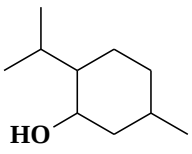

DL-Menthol

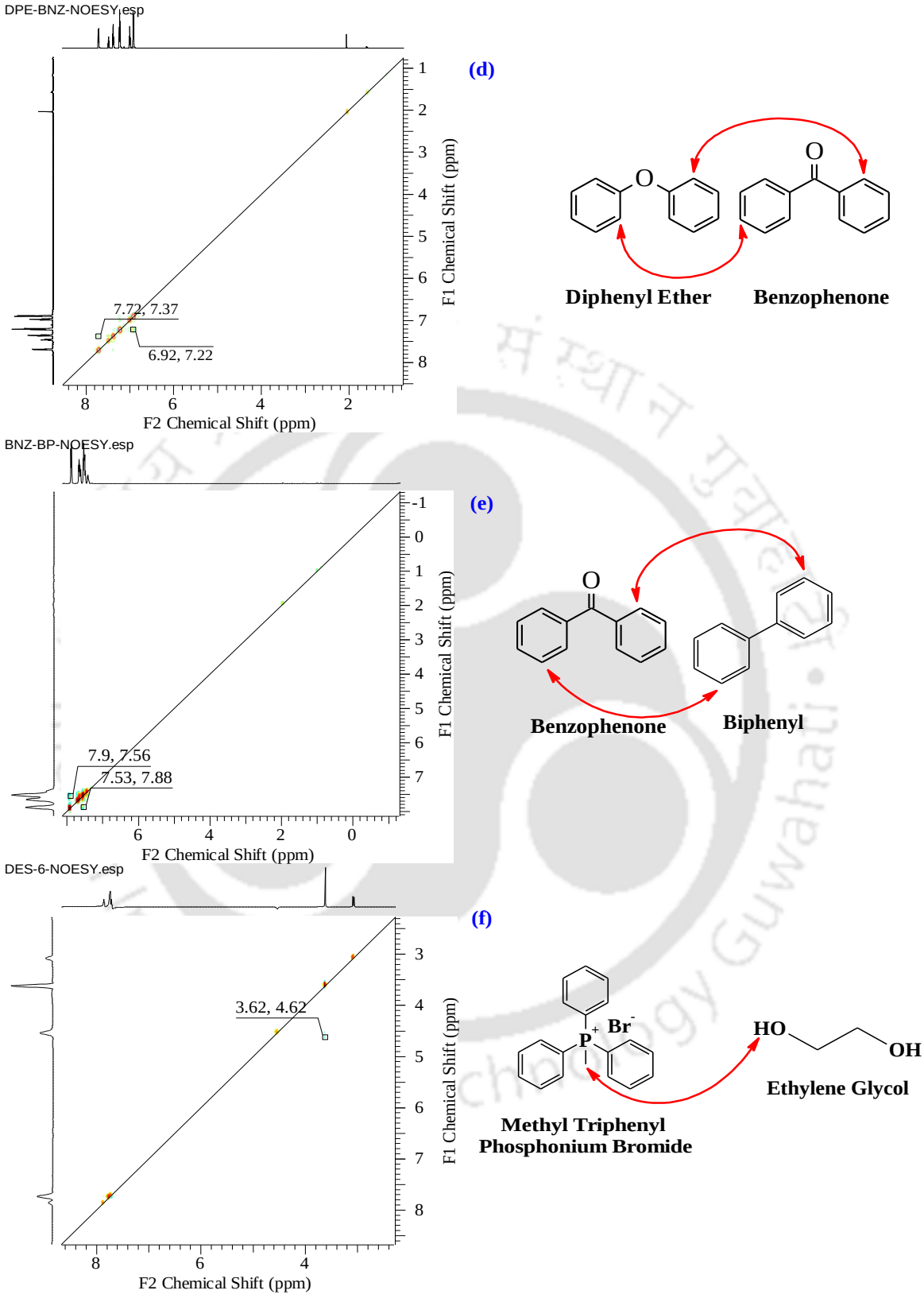

Figure 4.8: NOESY 2D NMR spectra of (a) DES1, (b) DES2, (c) DES3, (d) DES4, (e) DES5 and (f) DES6

4.1.2 Thermal Stability Analysis of DESs

Thermal stability of all the DESs were measured with a temperature range of 298.15 K to 673.15 K at a heating rate of 10°C/min. TGA plot representing the mass loss with respect to the temperature is reported in figure 4.9a. Further the dTG plot (figure 4.9b) is also reported. The mass loss trends for all the DESs are different from each other (figure 4.9a). In case of DES1 and DES2, two distinct mass loss slopes can be observed (figure 4.9a), which elucidate separate mass loss temperature regions for HBA and HBD. However, such a pattern is absent in DES3, DES4 and DES5. The first peak of mass loss occurs at nearly 450 K (figure 4.9b) for both DES1 and DES2. This corresponds to the degradation temperature of DL-menthol for DES1 and DES2. The second mass loss happens at 540 K (i.e., oleyl alcohol) and 560 K (i.e., oleic acid) for DES1 and DES2, respectively.

In DES3, while observing the dTG plot, the sharp peak at 450 K is the mass loss of DL-menthol and for diphenyl ether the mass loss happens at 460 K. The maximum mass loss of HBA (Diphenyl ether) and HBD (Benzophenone) of DES4 occur at 483 K and 493 K respectively. Similarly, the mass loss of HBA (Benzophenone) of DES5 happens at 501 K and for HBD (Biphenyl) maximum mass loss is found at 517 K. From TGA plot, a single slope of degradation is observed in DES3, DES4 and DES5. This is due to the stronger hydrogen bonding in the vicinity of degradation temperatures. Two slopes of degradation are observed in DES1 and DES2, which due to the weaker hydrogen bonding and higher degradation temperatures of HBDs.

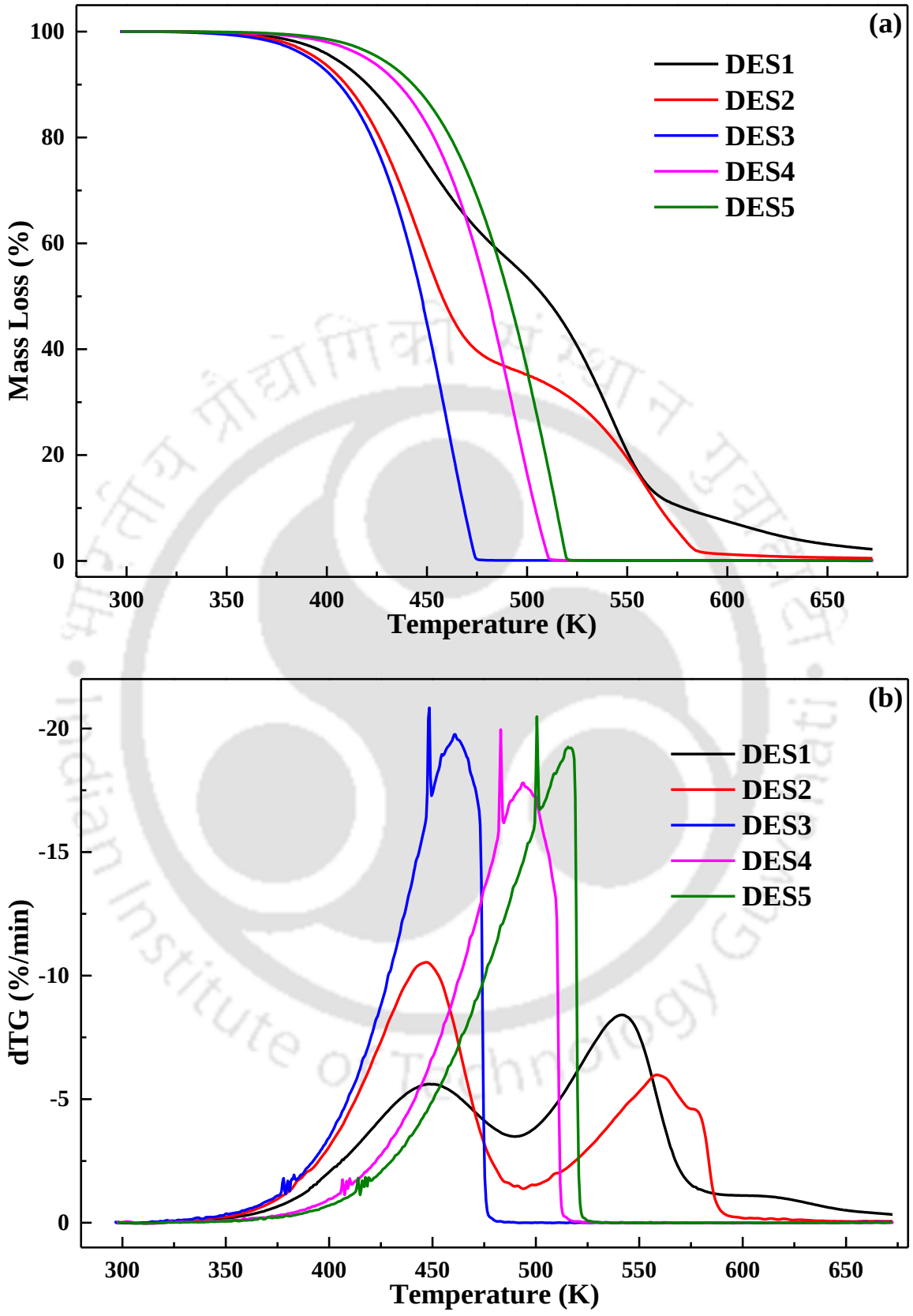

Figure 4.9: (a) TGA and (b) dTG plot of DESs

4.1.3 Moisture Content of DESs

Initially the DESs were vacuum dried overnight in order to remove any excess moisture. The moisture content of all the DESs are summarized in Table 4.1. All the measurements are repeated thrice and the average value is reported. DES4 has the lowest moisture content (0.10 wt.%) while DES1 has the highest moisture content (0.92 wt.%). Overall, the moisture content of the prepared DESs are in a range of 0.10-0.92 wt.% (Table 4.1).

Table 4.1: Moisture Content of DESs (wt.%)

Name	Moisture Content (wt.%)
DES1	0.92
DES2	0.50
DES3	0.30
DES4	0.10
DES5	0.51
DES6	3.00

4.1.4 Vapour Pressure of DESs

The vapour pressure of the DESs as a function of temperature are reported in figure 4.10. As expected, an increase in the vapor pressure can be observed with increase in temperature. The order of the vapour pressure of DESs are DES3<DES1<DES2<DES5<DES4. DES4 and DES5 have higher vapour pressure as compared to other DESs. This is due to the weaker intermolecular forces between the molecules.

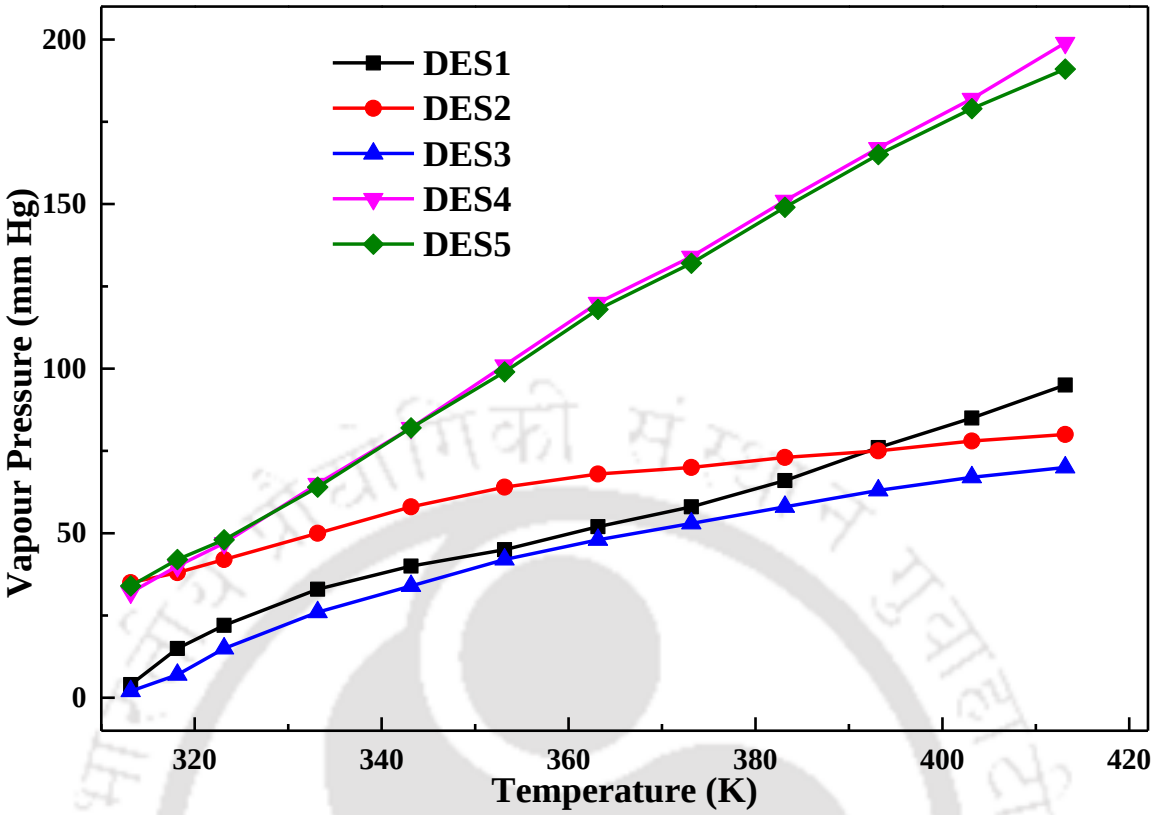

Figure 4.10: Vapour Pressure (mm Hg) of DESs

4.1.5 Physiochemical Properties

The measured properties namely density, viscosity and melting point are reported in Table 4.2. The predicted or calculated properties namely average molecular weight and boiling point are also reported in Table 4.2.

Table 4.2: Physiochemical Properties of DESs

Sl. No.	DES	A.M.W.	Density (kg/m^3)	Viscosity (Pa. s)	T_m (K)	T_b (K)
1	DES1	225.921	854.6	0.0127	297.765	619.07
2	DES2	237.53	885.76	0.0216	270.15	645.73
3	DES3	162.95	965.35	0.0026	276.4	539.25
4	DES4	174.84	1080.16	0.0030	281.4	576.81
5	DES5	172.76	1073.55	0.0044	300.4	575.42
6	DES6	-	1219.19	0.0413	-	-

4.2 Stability of NDDESs

4.2.1 Sedimentation Image Capturing Method

The sedimentation behaviours of NDDESs are reported in figure 4.11. From figure 4.11, it is observed that as the concentration increases, stability decreases in NDDES 17 and NDDES18. As the nanoparticle concentration is reduced, lower sedimentation is observed in NDDESs.

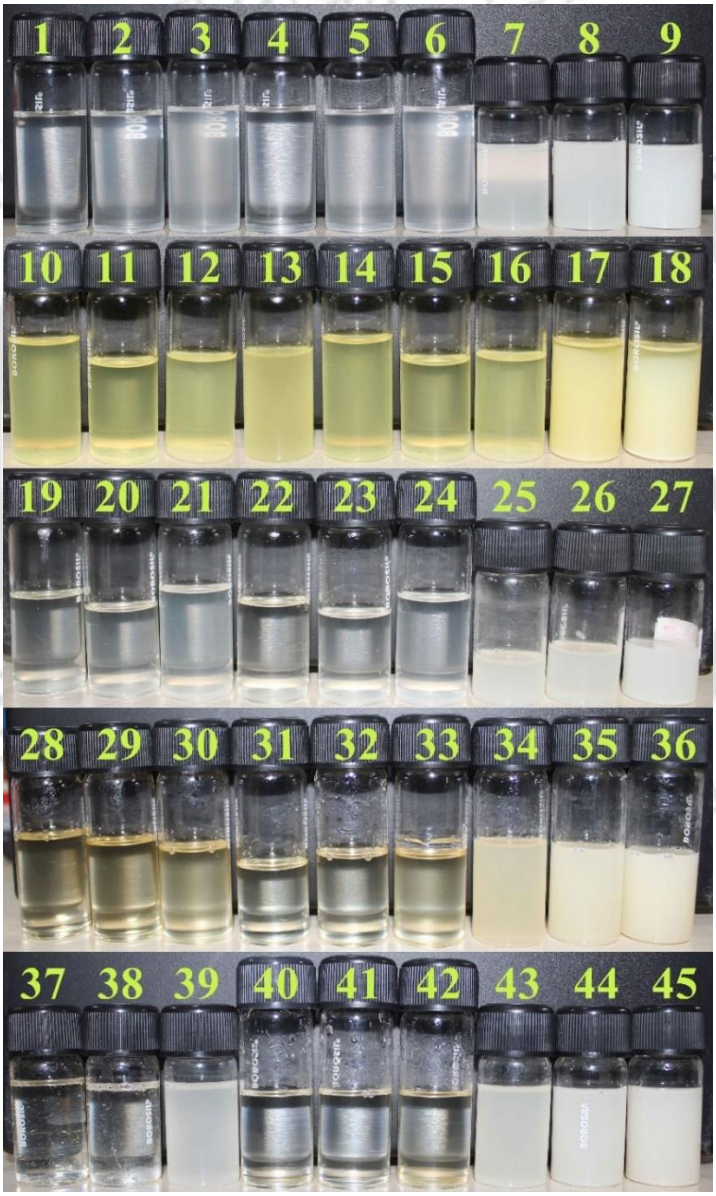

Figure 4.11: Visual observation of Prepared NDDES after 8 weeks (Numbers represent the NDDES from table 3.4)

4.2.2 Zeta Potential Measurements

Figure 4.12 demonstrates the scatter plot for the zeta potential of the NDDES samples. It can be observed from figure 4.12 that the zeta potential values of NDDES10 (+96.51 mV), NDDES22 (+101.51 mV), NDDES25 (-82.08 mV), NDDES26 (-60.77 mV), NDDES34 (-77.88 mV) and NDDES45 (-74.68 mV) show excellent stability. NDDES7, NDDES19, NDDES21, NDDES23, NDDES24, NDDES29, NDDES30, NDDES33, NDDES35 and NDDES36 result in good stability, while NDDES27, NDDES28, NDDES31, NDDES37, NDDES38, NDDES39, NDDES40, NDDES41and NDDES42 have low stability. The result indicates that the h-BN nanoparticles exhibit better stability compared to the Al_2O_3 spherical and cylindrical nanoparticles except for NDDES10 and NDDES22. All the readings are taken after six months of NDDES preparation.

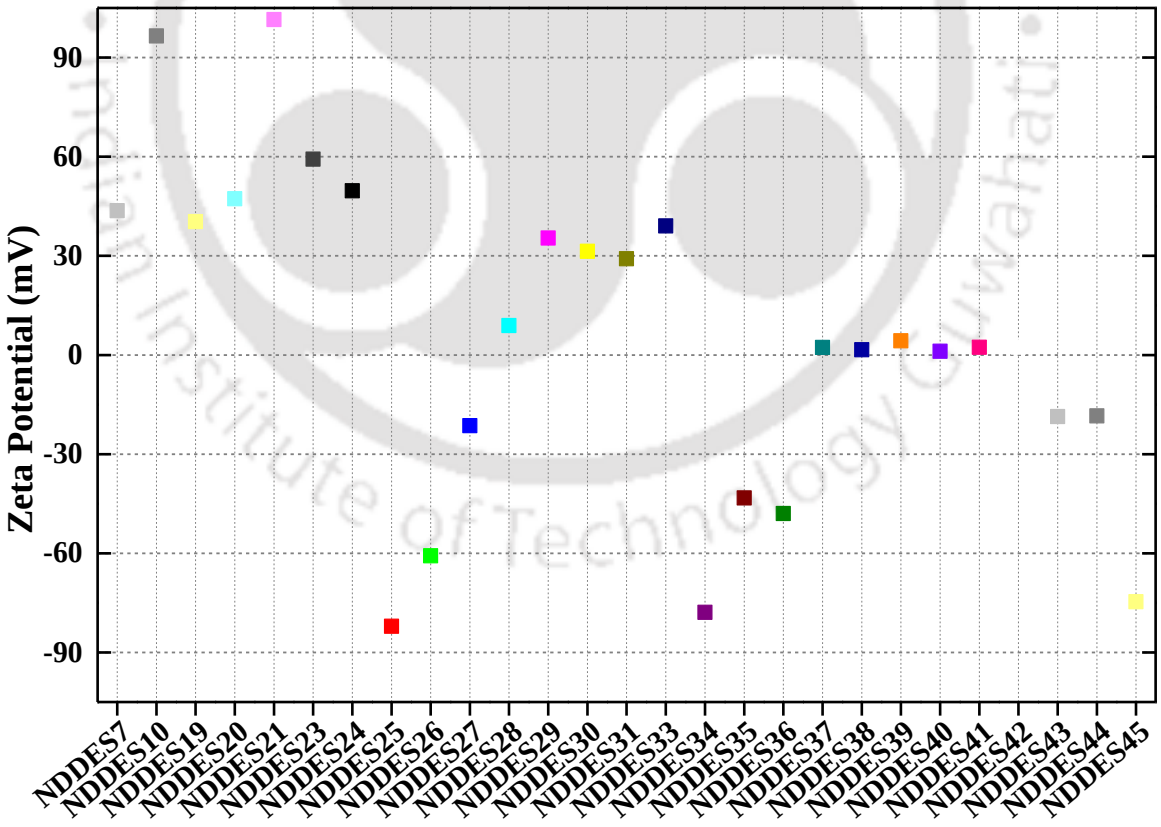

Figure 4.12: Zeta Potential of NDDESs (The number at the end of NDDES represent the convention as used in Table 3.4)

4.2.3 Optical Microscopy

Figure 4.13 represents the distribution for nanofluid samples NDDES1 to NDDES45 which is captured by high resolution microscope (Axiostar plus, Carl Zeiss, Germany) using a 50x magnification lens. A good dispersion of nanoparticles can be observed in the base fluids (i.e., DESs). With increasing nanoparticle concentration, an increase in the number and size of agglomerates are observed in the NDDESs. It should be noted that the clusters that are observed here are in the size of microns. The sizes of particles and clusters are less than 0.3 μm or below, hence cannot be seen under the optical microscope. In this regard, TEM/FETEM can provide statistics on clusters of large sizes, along with the particle size. However, it can give an impression or qualitative assessments of the cluster sizes in each nanofluid sample. The left, central and right column (figure 4.13) refers to the three weight percentages of nanoparticles (0.02, 0.05 and 0.10 wt. %).

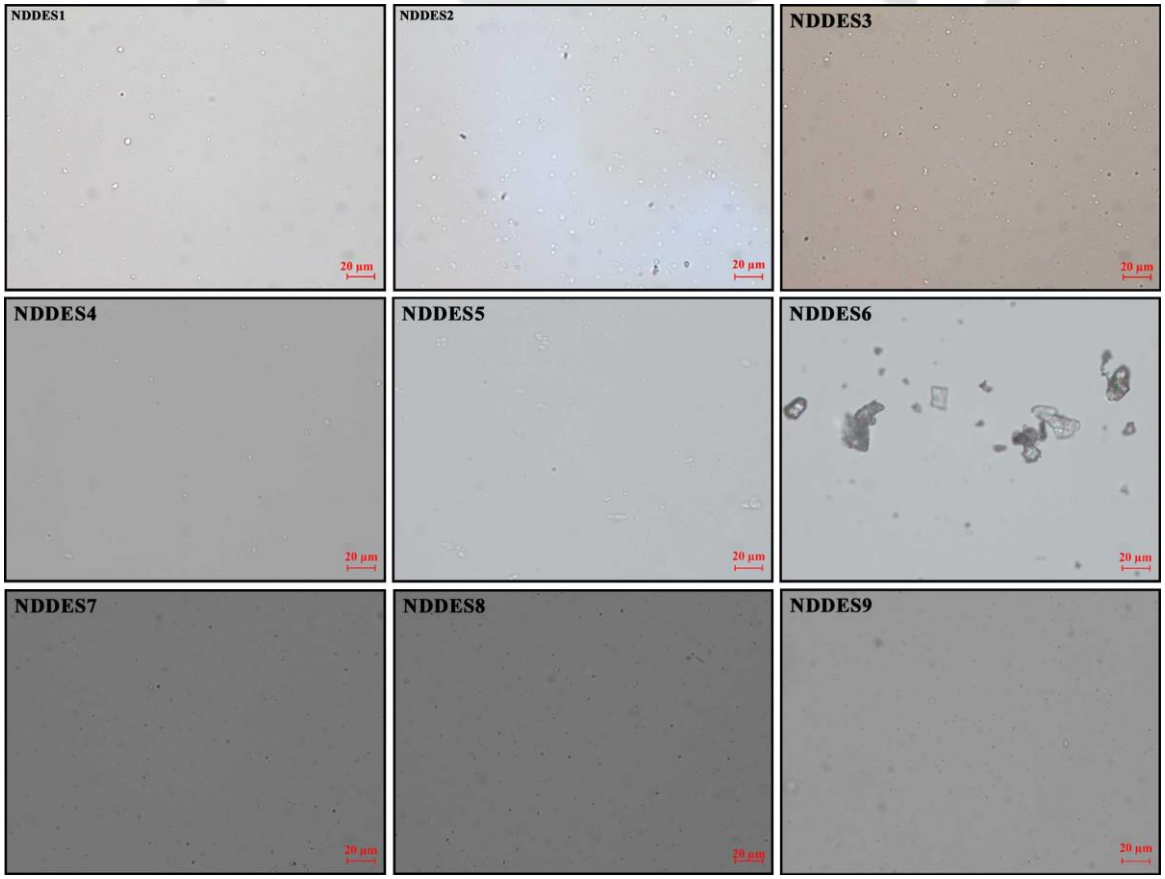

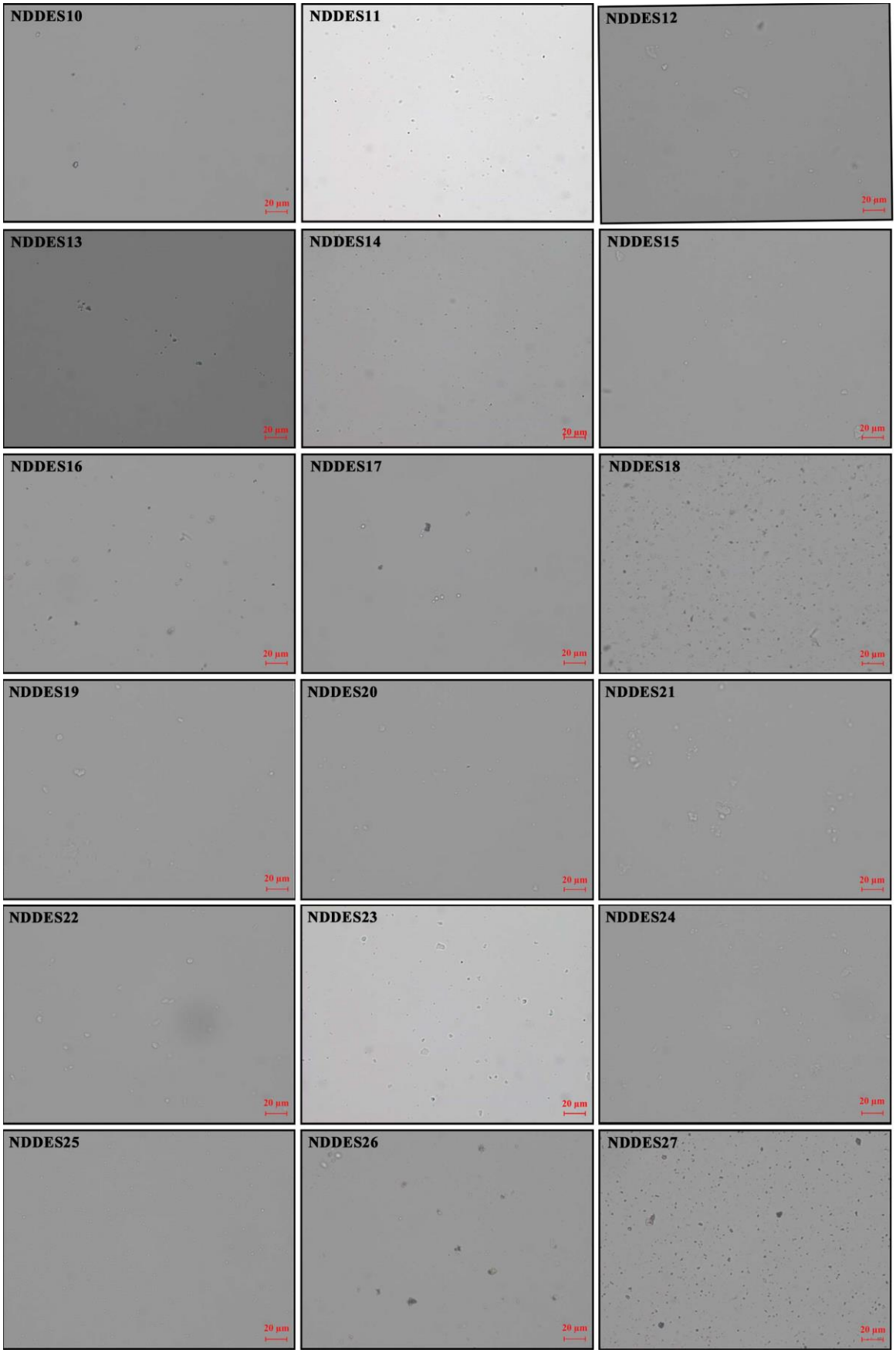

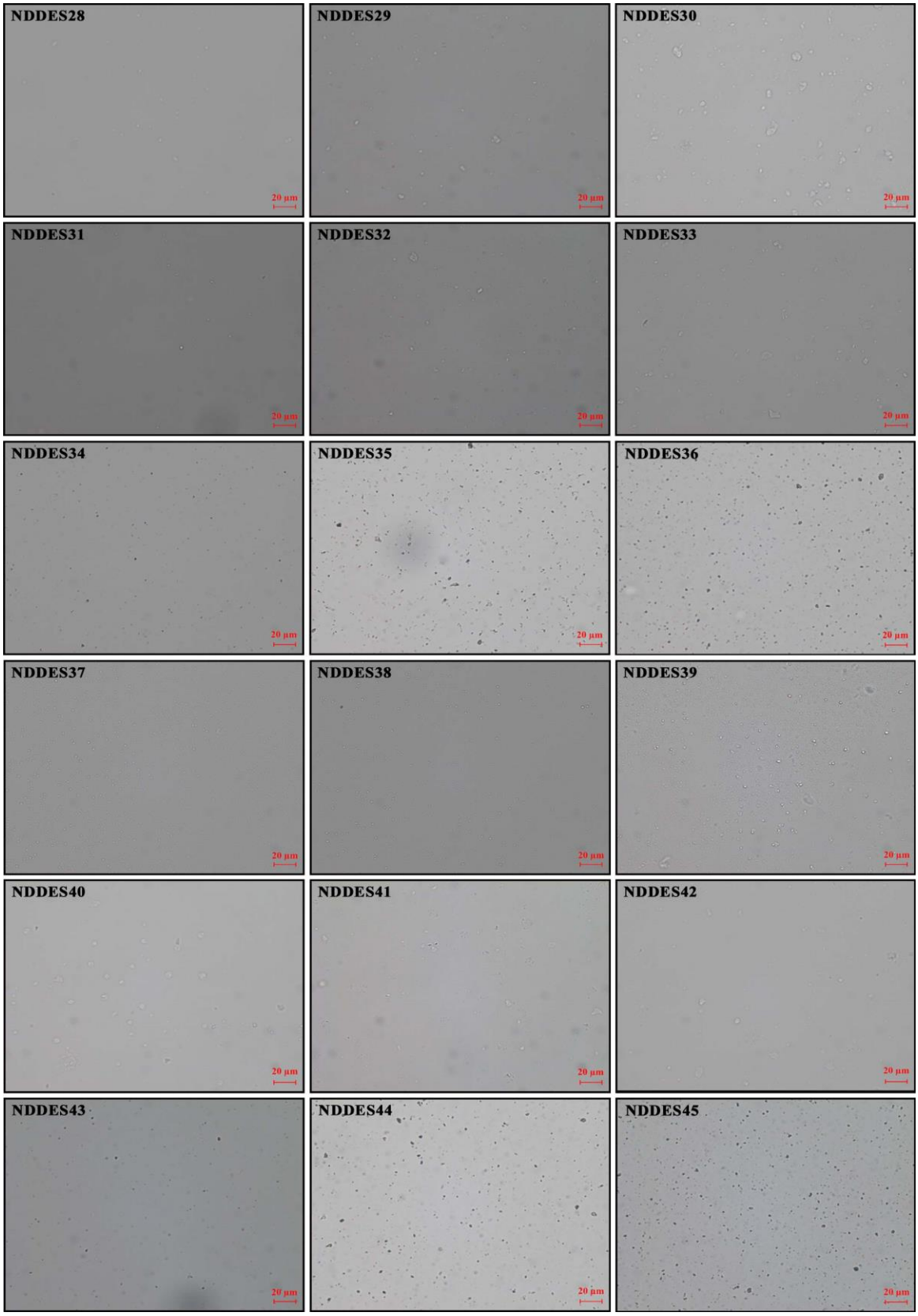

Figure 4.13: High Resolution Microscopic images of NDDESs with a scale of 20 μm

(The NDDES names are as reported from Table 3.4)

4.2.4 Transmission Electron Microscopy

TEM images of nanoparticles are reported in figure 4.14. Figure 4.14 (a) represents the TEM micrograph of Al_2O_3 spherical nanoparticles of size less than 50 nm. Figure 4.14 (b) represents the Al_2O_3 cylindrical nanoparticles with a length of 100-150 nm and diameter of 1-2 nm. While figure 4.14 (c) represents the TEM image of boron nitride nanoparticles which is in hexagonal shape and 90-100 nm size.

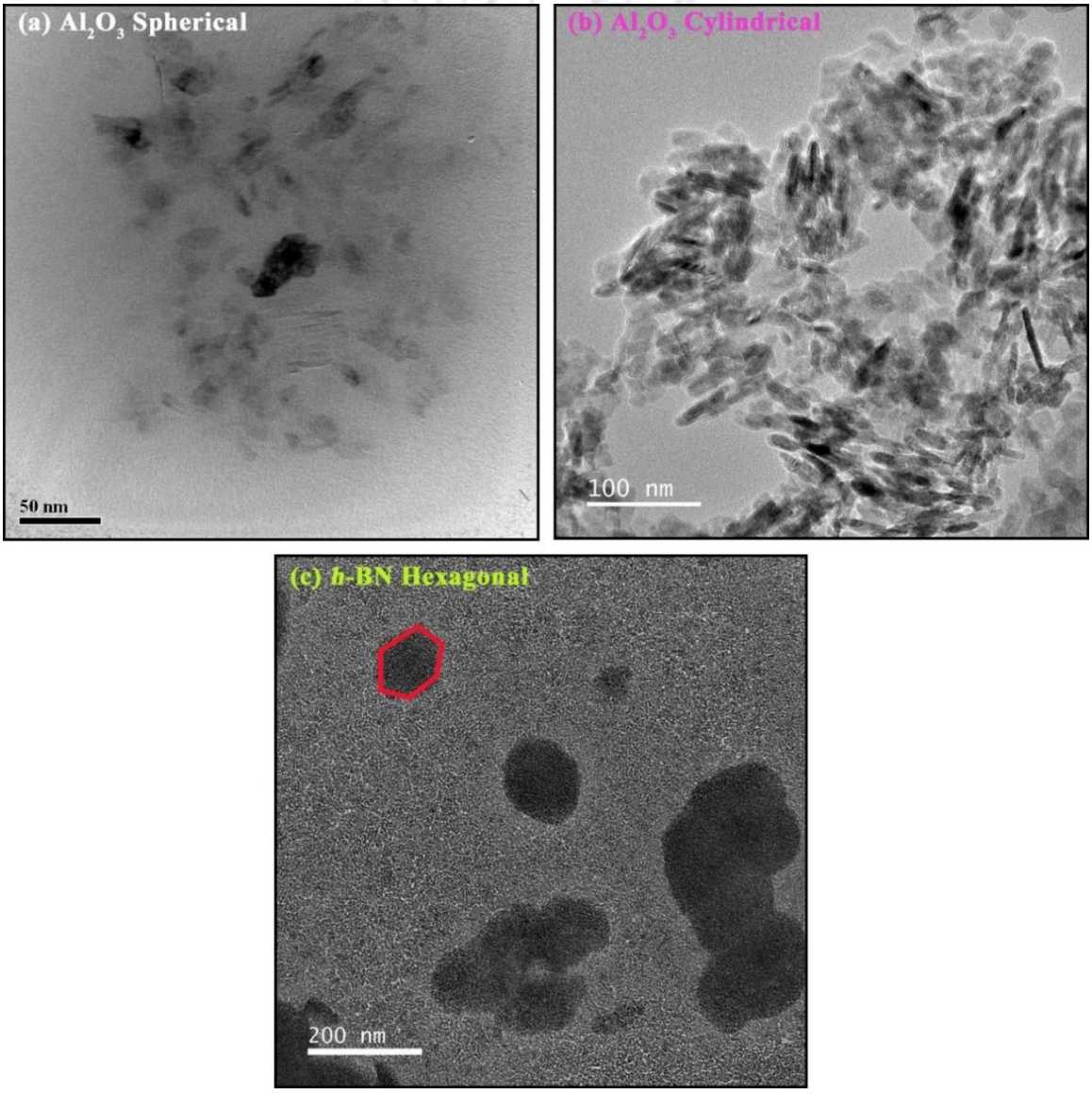

Figure 4.14: TEM images of (a) Al_2O_3 spherical, (b) Al_2O_3 cylindrical and (c) *h*-BN nanoparticles

4.3 Results of Thermophysical Properties

4.3.1 Density

A comprehensive study of density measurements was conducted for all DESs and their corresponding NDDESs with weight percentage of 0.02, 0.05 and 0.1 %. Figure 4.15 represents the density of all the DESs (base fluids) as a function of temperature ranging from 293.15 K to 363.15 K. The density of DES3 is higher than the DES1 and DES2 while the same is lower than DES4 and DES5. In addition, the density of DES1, DES2 and DES3 is lower than water while DES4 and DES5 have higher density compared to water.

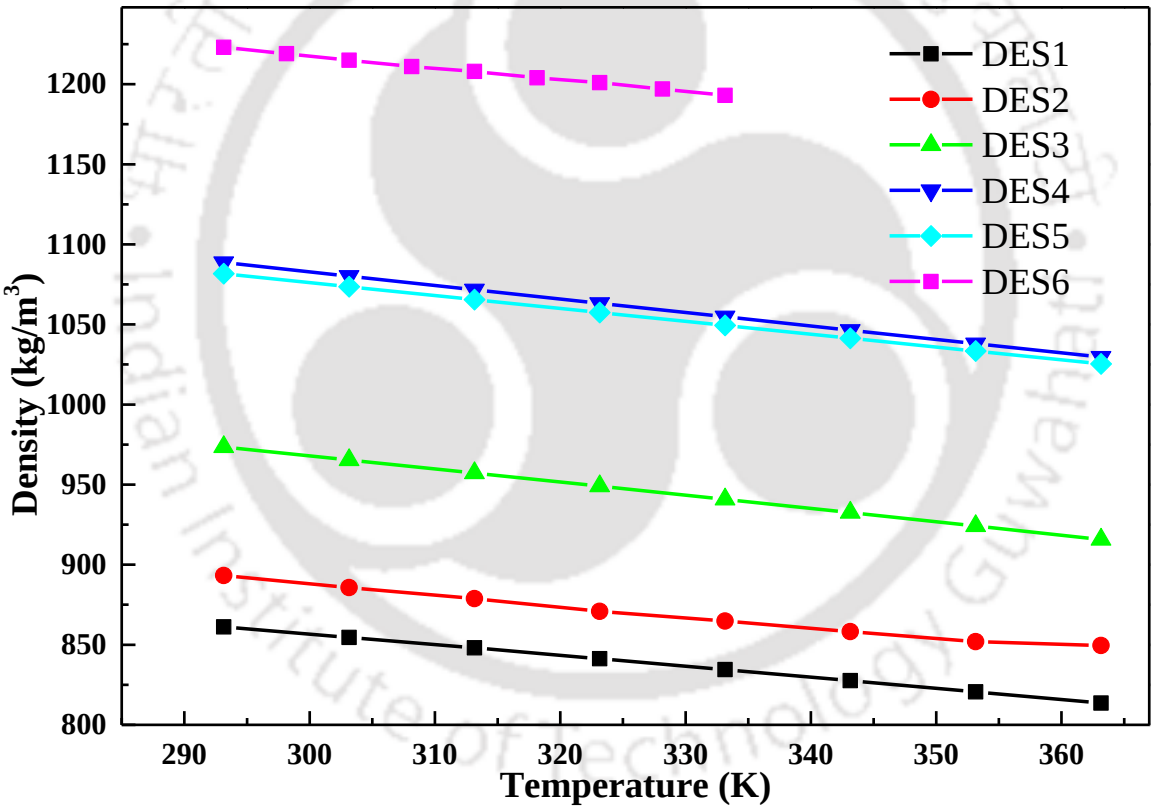

Figure 4.15: Density variation with temperature for DES1-DES6

The density of the all DESs are decreasing linearly with the increase in temperature. Further it can be observed that there is vary less variation in density with the temperature which is due to the negligible volumetric expansion at higher temperature. The order of density is in the form of DES1<DES2<DES3<DES5<DES4<DES6.

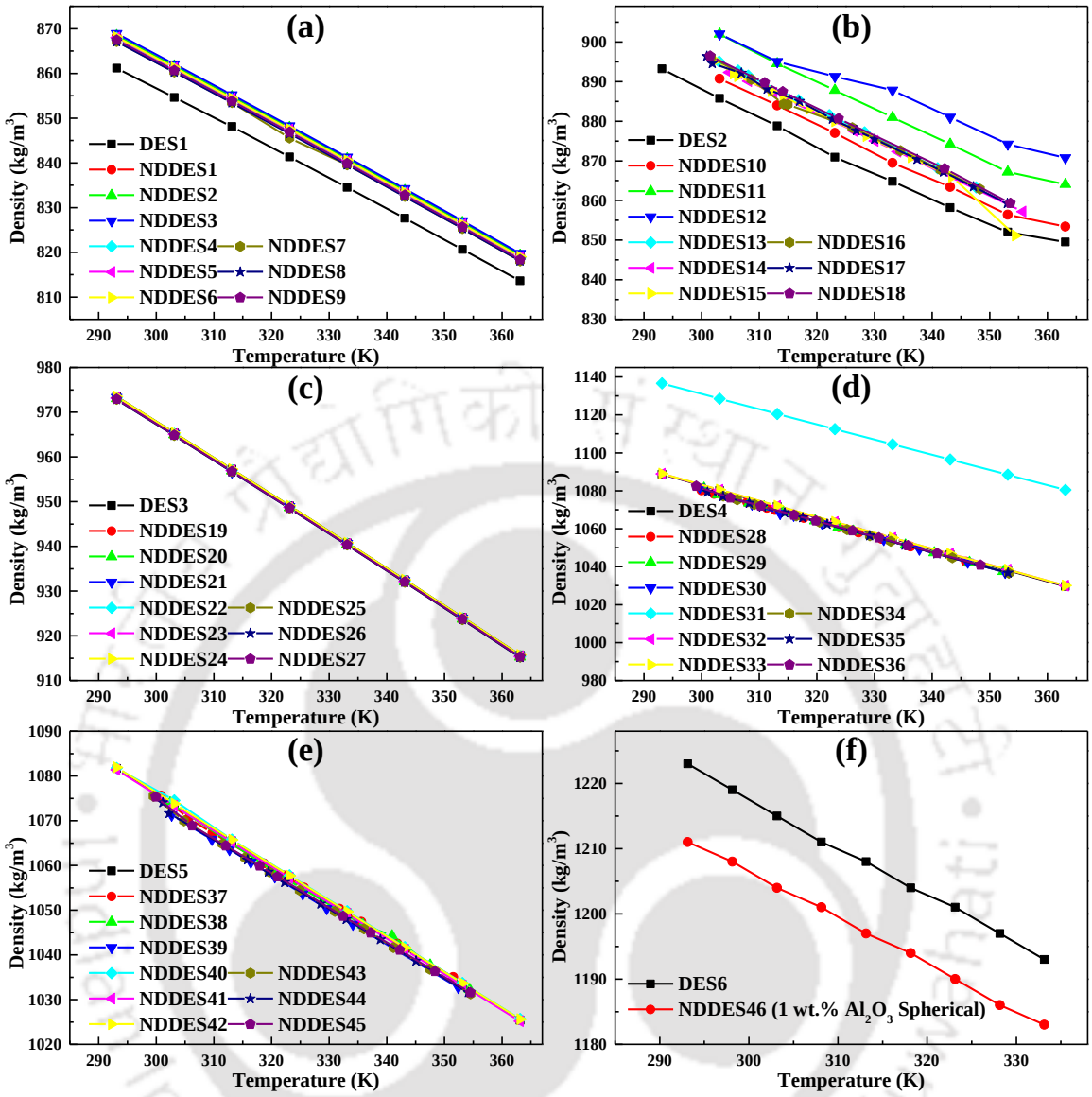

Figure 4.16: Density variation with temperature for NDDES1 to NDDES46

Figure 4.16 represents the density values of three different nanoparticles in three different weight percentages with corresponding DES. From figure 4.16(a), it can be observed that the density of NDDESs (i.e., NDDES1-NDDES9) are higher than the base fluid (DES1). In addition, the same behaviour has been observed in case of DES2 and the corresponding NDDESs (i.e., NDDES10-NDDES18) (figure 4.16(b)). In case of DES3, DES4, DES5 and their corresponding NDDESs (i.e., NDDES19-NDDES45), a negligible enhancement of density has observed (figure 4.16(c), (d) and (e)). The overall observation

from figure 4.16 is the density decreases with increase in temperature, which agrees well with the acceptable behaviour of the fluids. For NDDESs, the effect of the weight fraction of nanoparticles is very less on the density. Further, the density increases with nanoparticle concentration, as the nanoparticle being added are of higher density than the DESs. A linear decrement of density has been observed in all the DESs and NDDESs.

4.3.2 Viscosity

Figure 4.17 (a) displays the shear stress vs shear rate plot of DES1 at a temperature range of 298.15K to 378.15K. The linear shear stress and shear rate curve agrees well with the Newtonian behaviour of DES1. Figure 4.17 (b) indicates the shear viscosity of the DES1 as a function of shear rate for different temperatures. The shear stress vs shear strain for DES2 is depicted in figure 4.18 (a), where it was observed that the fluid obeyed a Newtonian behavior[127]. Further, the viscosity of DES2 is also measured as a function of shear rate, where the Newtonian behavior[127] was again confirmed (Figure 4.18 (b)). A strong temperature effect was observed on the viscosity of all the DESs.

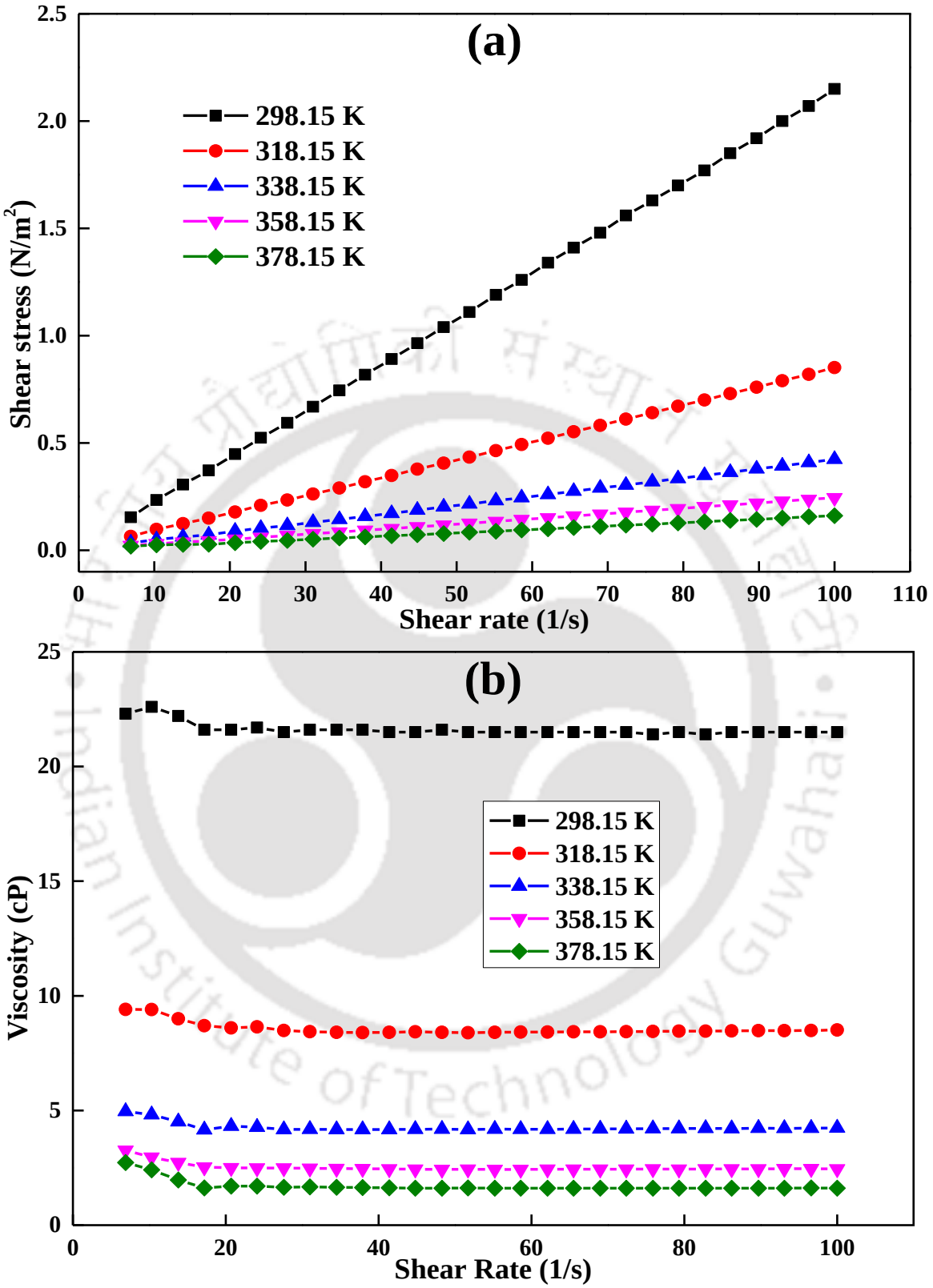

Figure 4.17: (a) Shear stress as a function of shear rate and (b) Viscosity as a function of shear rate at five different temperatures of DES1

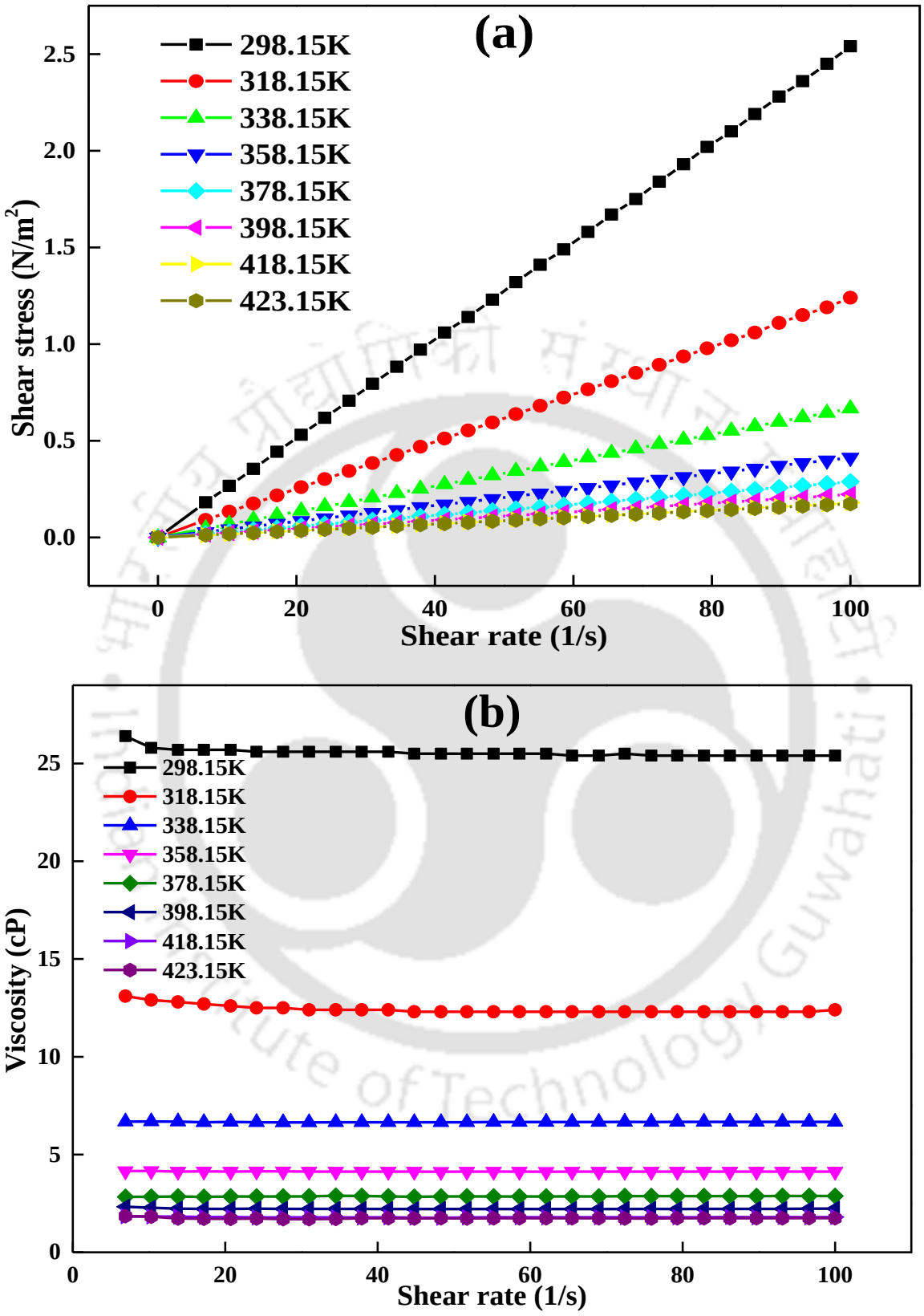

Figure 4.18: (a) Shear stress as a function of shear rate and (b) Viscosity as a function of shear rate at five different temperatures of DES2

The viscosity of the formulated DESs are reported in Figure 4.19 as a function of temperature from 293.15 to 363.15 K. As expected, the viscosity of the DES1 decreases at a higher rate from 0.0214 to 0.0016 Pa.s with an increase in temperature. The viscosity of the DES1 decreases at a higher rate from 0.0335 to 0.0028 Pa.s. However, the viscosities of DES3, DES4 and DES5 at room temperature are 0.004, 0.004 and 0.005 respectively which are very low as compared to that of DES1 and DES2. Overall, DES3 have the significantly lower viscosity among all the DESs. Further, the order of density is in the form of DES3<DES4<DES5<DES1<DES2<DES6. In addition the presented experimental data are again compared with commercially available thermal fluid Therminol VP1[22] and the previously published data of IL ([N4111][TF2N])[128,129]. The viscosity of DESs is found to be lesser than ILs, while at the higher temperature, DESs has equal viscosity as the Therminol VP1[22].

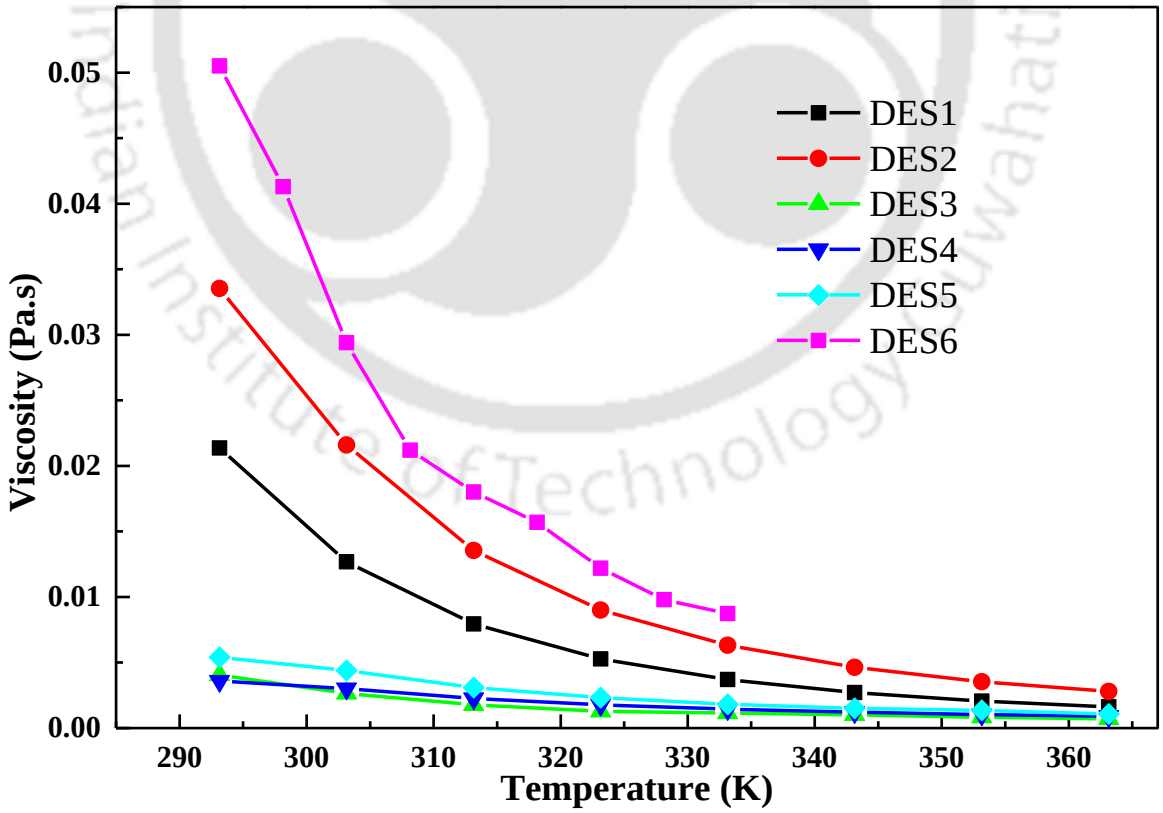

Figure 4.19: Measured viscosity as a function of temperature for base fluids

The decrease in viscosity of DES happens because of the increase in temperature as the cohesive force decreases, which results in higher kinetic energy. Hence, particles become free for easy movement. Along with density, we do also have a reduced viscosity when compared to other alternative solvents. Overall, the density of DES affects the viscosity. DES having low mass per unit volume is lighter, as a result, the molecules need less energy to move. Therefore, the rise in temperature decreases the viscosity and density of DES. To conclude, the lower viscosity reduces the pumping cost of the DES while using as a thermal fluid in CSP[130].

The viscosities of all the NDDESs with three different weight percentages and their corresponding DES are reported in Figure 4.20. Addition of nanoparticles shows both enhancement and curtailment in viscosity of NDDESs when compared to DES. In figure 4.20(a), the *h*-BN hexagonal nanoparticles based nanofluids (NDDES7, NDDES8 and NDDES9) exhibits an enhancement of viscosity as compared to the base DES, while a negligible effect is observed in case of Al_2O_3 spherical and cylindrical based nanofluids (NDDES1 to NDDES6). In figure 4.20(b) Al_2O_3 spherical based nanofluids (NDDES10, NDDES11 and NDDES12) exhibits an enhancement of viscosity compare to the base DES, while a curtailment in viscosity is observed in case of *h*-BN hexagonal and Al_2O_3 cylindrical based nanofluids (NDDES13 to NDDES18). Further, in figure 4.20(c) a similar trend is observed as in figure 4.20(a), which may be due to the effect of DL-menthol present in both DES1 and DES3. In figure 4.20(d), viscosity enhancement is observed with Al_2O_3 cylindrical based nanofluids (NDDES31, NDDES32 and NDDES33), while a negligible effect of viscosity is observed in case of Al_2O_3 spherical and *h*-BN hexagonal nanoparticles based nanofluids. However, DES5 based nanofluids do not confirm to any effect of enhancement or curtailment.

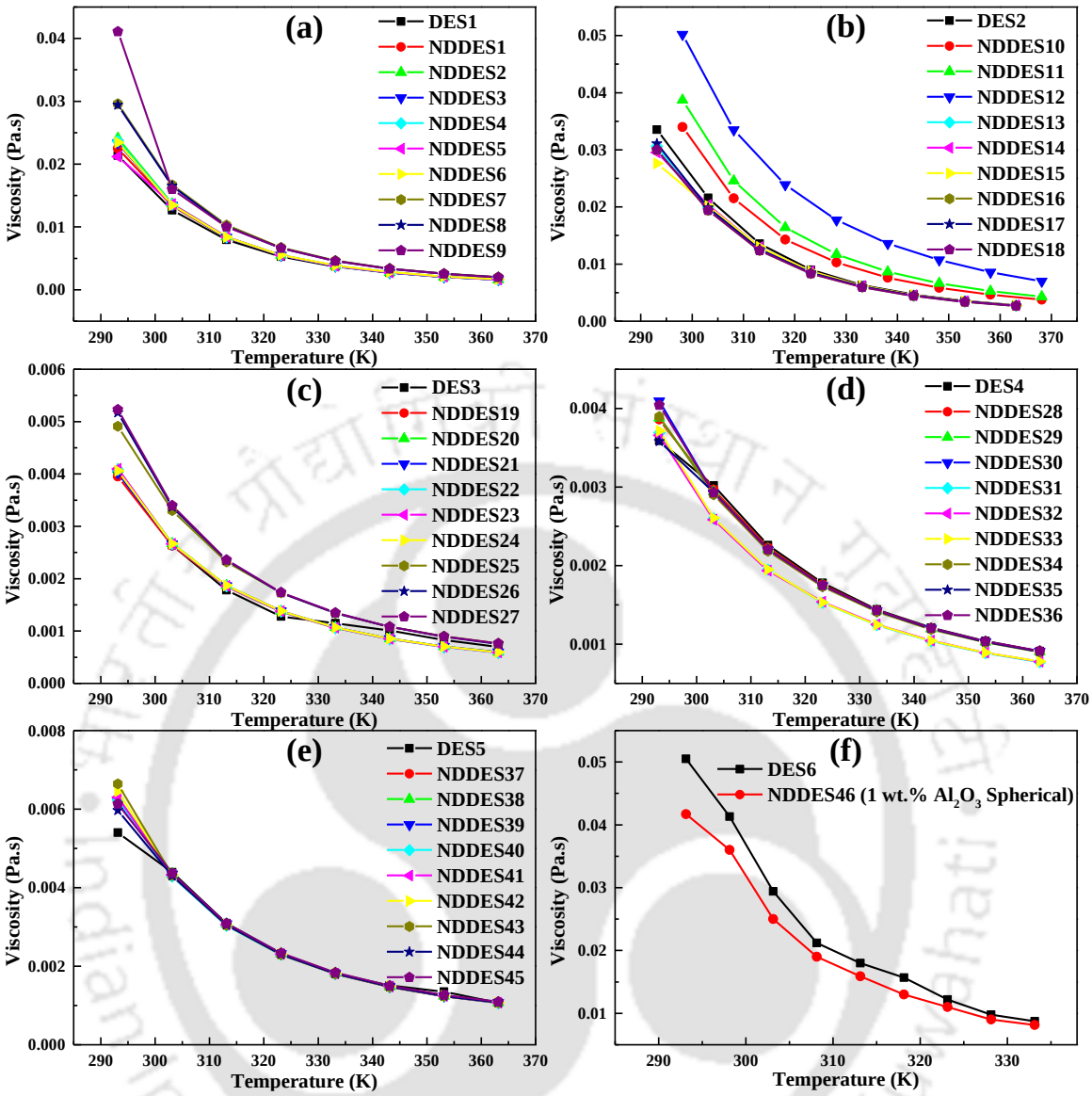

Figure 4.20: Measured viscosity as a function of temperature for NDDESs

In addition, DES6 and the corresponding nanofluid (NDDES46) has a very high viscosity and density (figure 4.16(f)), for which DES6 has not been considered for further experiments. Overall, negligible effect of nanoparticle weight % has been observed. In addition, the enhancement of viscosity by increasing nanoparticle concentration is not valid for all cases. Further the lower viscosity of all the DESs and NDDESs indicate a lower pumping cost since viscosity is a flow property of fluids.

4.3.3 Thermal Conductivity

Figure 4.21 represents the measured thermal conductivities of all the Prepared DESs with respect to the temperature. The lower thermal conductivity of DES1 and DES2 are observed due to the effect of weak hydrogen bonding between the respective HBAs and HBDs[131]. Further DES3, DES4 and DES5 exhibits higher thermal conductivity due to denser hydrogen bonding of HBA and HBD, which is earlier discussed in section 4.1.2. The thermal conductivity of DESs is in the order of DES1<DES2<DES3<DES6<DES5<DES4. Thermal conductivities of liquids generally decrease with increase in temperature except a few e.g. water and glycerine.[132]

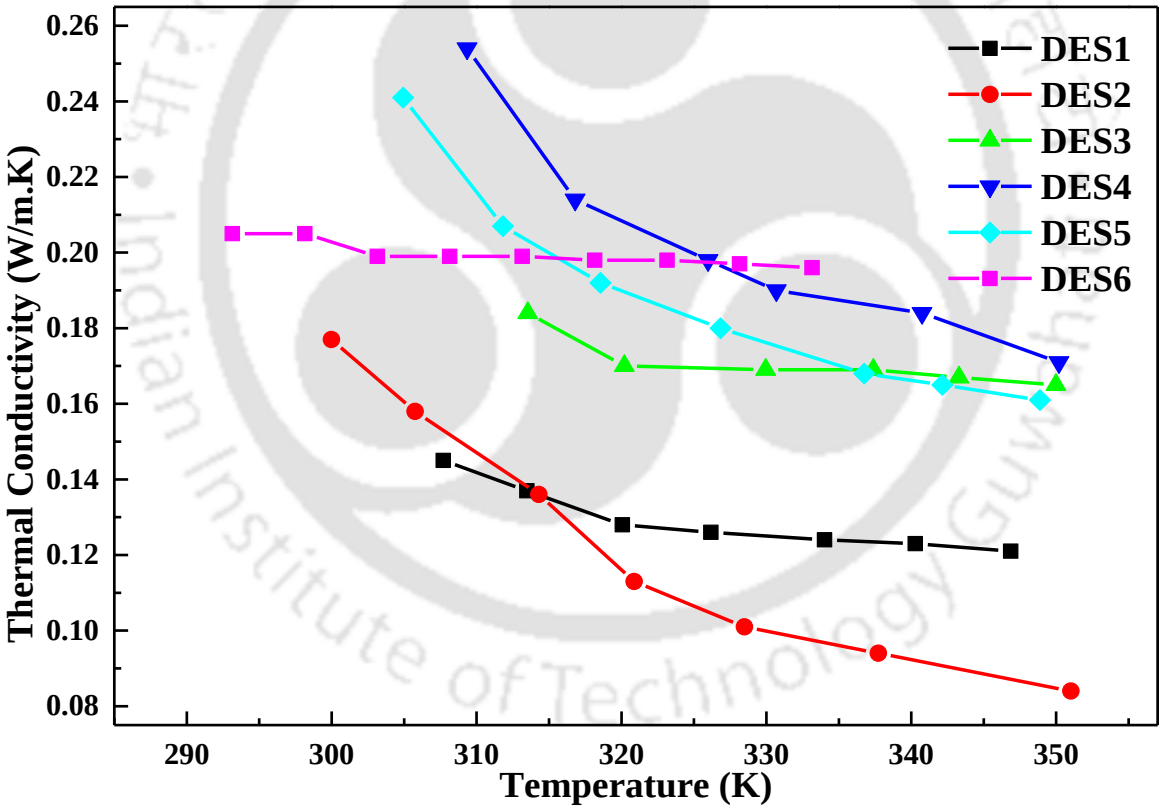

Figure 4.21: Thermal conductivity of DESs as a function of temperature

The thermal conductivities of all the NDDESs along with their respective DES are reported in figure 4.22. From figure 4.22(a), it may be observed that all *h*-BN hexagonal nanoparticles based nanofluids (NDDES7, NDDES8 and NDDES9), NDDES1 (0.02 wt.%

Al_2O_3 spherical), NDDES5 and NDDES6 (0.05 and 0.10 wt.% Al_2O_3 cylindrical) have higher values as compared to the base DES, while others have lower thermal conductivity. In figure 4.22(a), the thermal conductivity of all nanofluids are higher than the base DES.

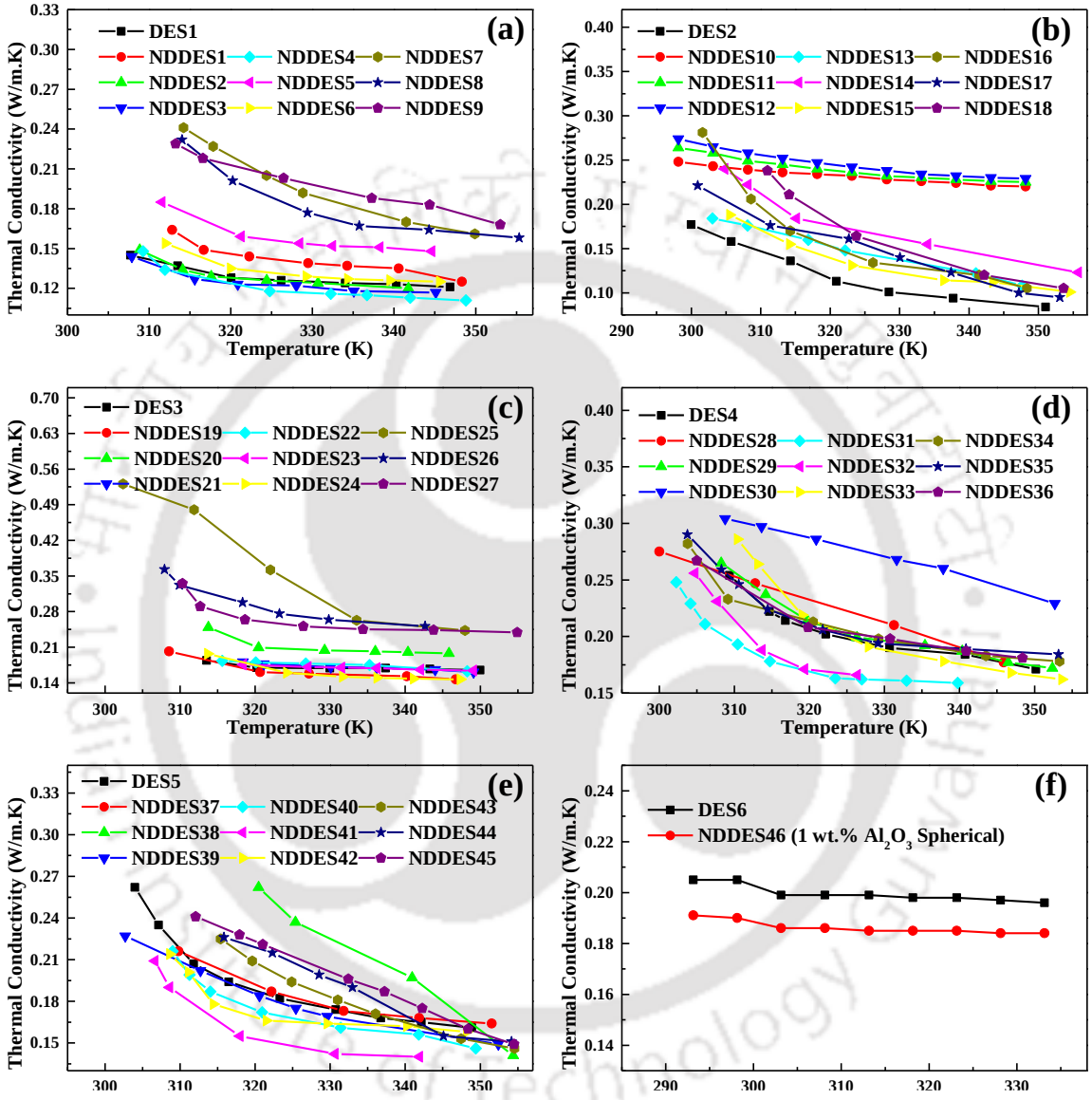

Figure 4.22: Thermal conductivity of NDDESs as a function of temperature

Again *h*-BN hexagonal nanoparticles based nanofluids (NDDES25-27, NDDES34-36 and NDDES43-45) exhibits an enhanced thermal conductivity as reported in figure 4.22(c), (d) and (e). However, NDDES19, NDDES24, NDDES31, NDDES32, NDDES39, NDDES41 and NDDES42 shows lower values from the base fluid's thermal conductivity.

This may occur due to agglomeration of nanoparticles. The enhancement of thermal conductivity is observed for DES modified NDDESs which is due to the presence of nanoparticle inside the base fluid. Nanoparticles transfer heat energy by the vibrations of atoms or molecules. The atomic or molecular vibrational energy of the solids or nanoparticles are called phonons and hence transfer of heat by the atomic vibrations is termed as phonon transport. Overall NDDES25 has the highest thermal conductivity at the beginning. In addition, NDDES25 also possesses better thermal conductivity than DES3 except at temperatures higher than 335 K, where both the HTFs have nearly equal thermal conductivities. Similar enhancement in thermal conductivity of nanofluids can also be found in literature.[133] Further after comparison the thermal conductivity of BN-based NDDESs have higher values than the Al_2O_3 spherical and cylindrical nanoparticle based NDDES.

4.3.4 Specific Heat Capacity

The measured specific heat capacity of all the DESs with respect to temperature are reported in figure 4.23. In contrast to thermal conductivity (figure 4.21), specific heat capacity of all the DESs tend to increase with increase in temperature. Further, DES2 have the highest specific heat capacity among all the DESs. The specific heat capacities of DESs is in the order of DES2<DES4<DES3<DES5<DES1.

In addition, temperature dependent specific heat capacity of different NDDESs are also investigated. The specific heat capacity of all the NDDESs with the respective DES are reported in figure 4.24. A universal trend has been observed: an increase in specific heat of NDDESs with the increase in temperature. In figure 4.24(a), the specific heat capacity of *h*-BN hexagonal nanoparticles based NDDESs (NDDES7 to NDDES9)

enhances while the Al_2O_3 spherical and cylindrical nanoparticles based NDDESs shows a curtailment trend except for NDDES5.

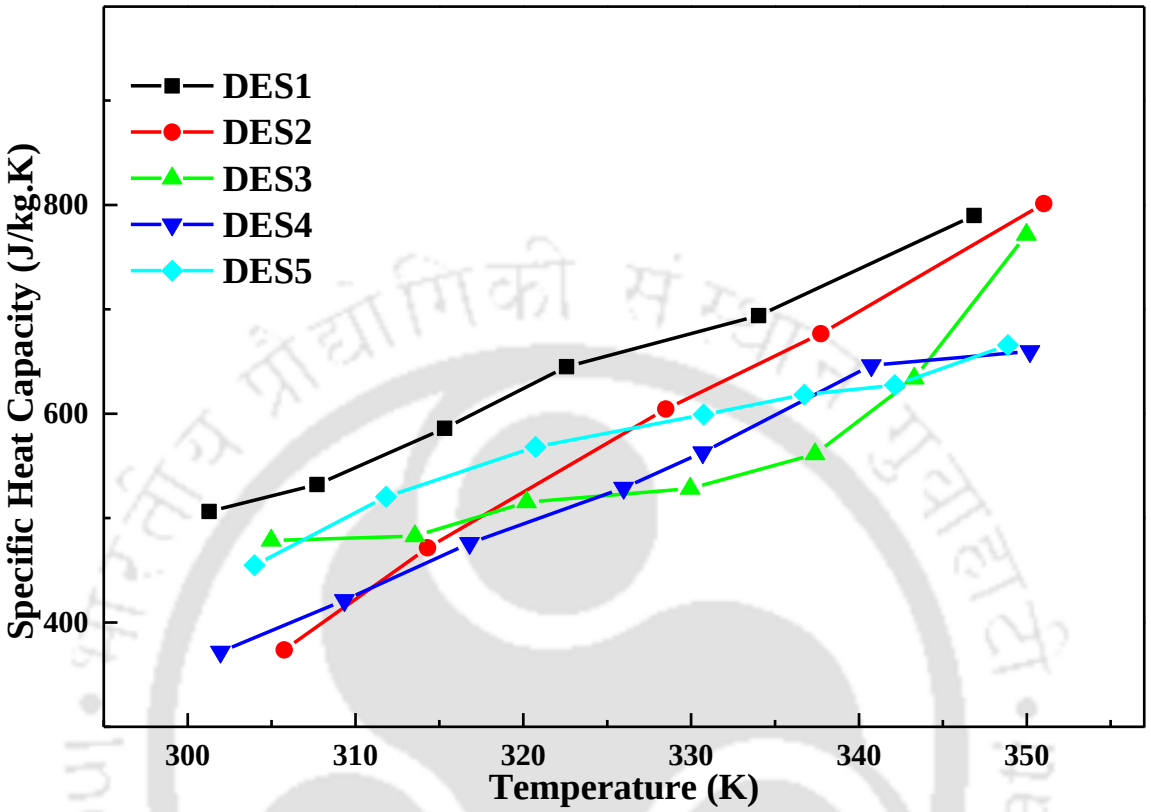

Figure 4.23: Specific Heat Capacity of DESs as a function of temperature

Further in figure 4.24(b) an enhanced specific heat capacity is observed in case of all the NDDESs. Similarly, in figure 4.24(c) specific heat capacity of all the NDDESs are higher than the base DES and interestingly the *h*-BN hexagonal nanoparticles based NDDES have the highest enhancement. From figure 4.24(d), both enhancement and curtailment are observed. The heat storage capacity of NDDES25 is highest among all the NDDESs. DES-1 derived *h*-BN hexagonal nanoparticles based nanofluids result in somewhat comparably better specific heat capacity than the base fluid. Reproducibility of thermal conductivity and specific heat capacity values are taken care of by repetition of experiments for three independent measurements. The deviation is found to be around ±4%.

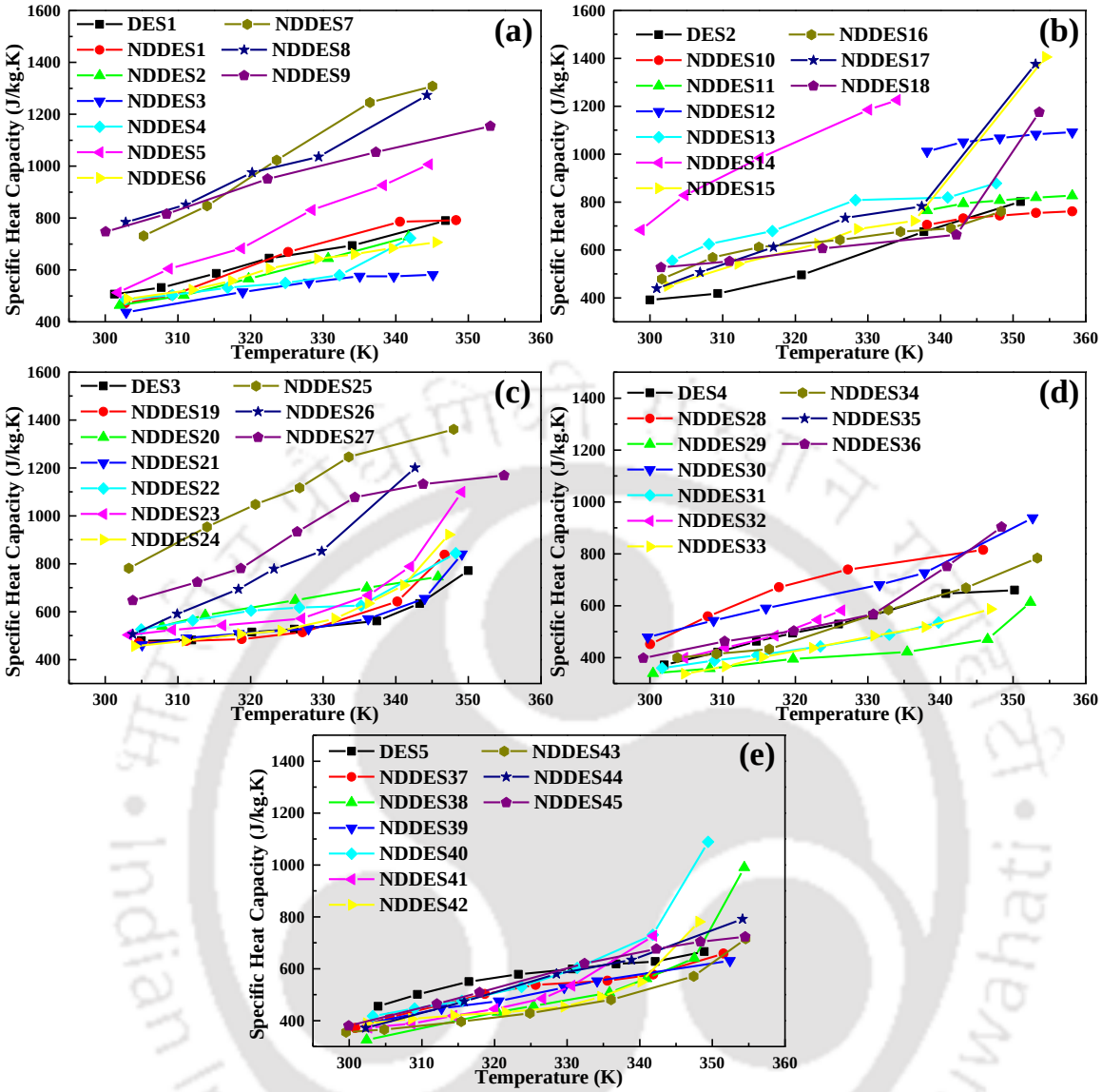

Figure 4.24: Specific Heat Capacity of NDDESs as a function of temperature

4.4 Optimization of NDDESs

The next step is to recommend and adopt a suitable nanofluid based on the thermophysical properties measured. The values of M_o number of all DESs are reported in figure 4.25. The M_o number of the DESs are in the order of DES2<DES1<DES5<DES4<DES3. DES3 shows a highest M_o number among all the DESs.

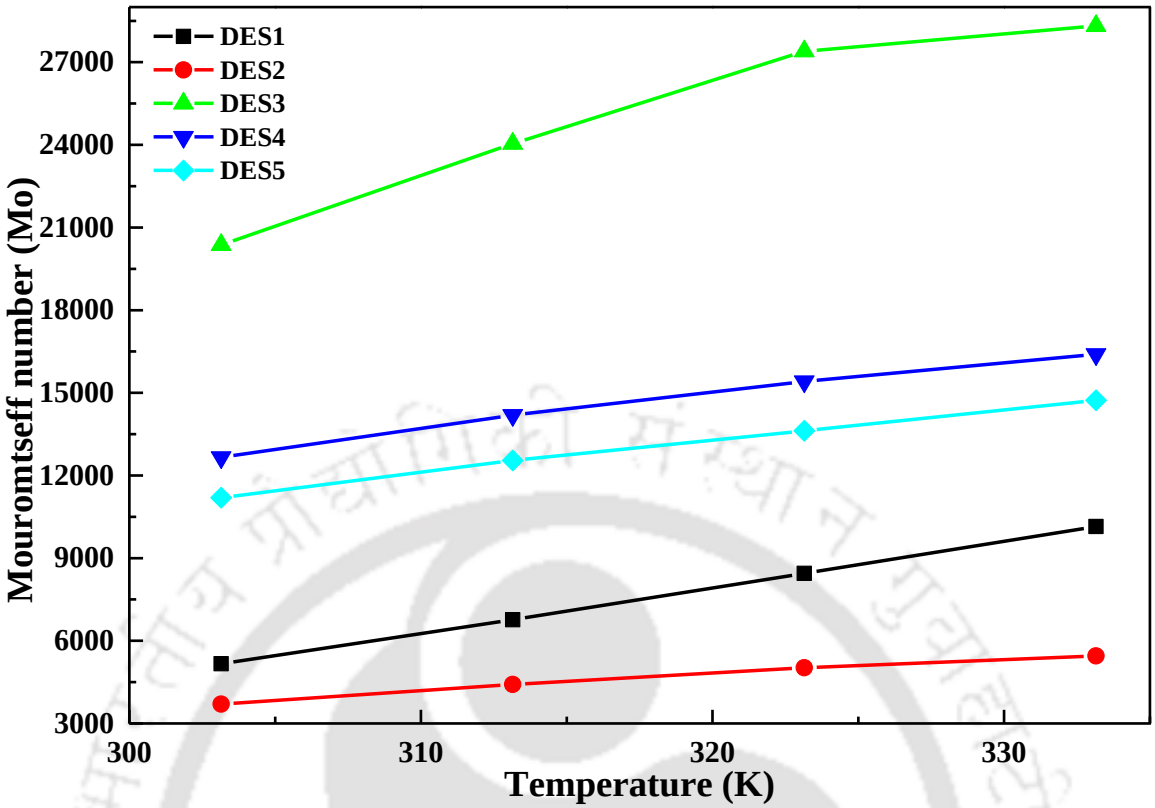

Figure 4.25: M_o number profiles of DESs (M_o=Mouromtseff number)

The calculated profiles of M_o number of all the NDDESs are reported in figure 4.26. For all the HTFs, M_o number increases almost linearly as a function of temperature. Significant enhancement in heat transfer performance can be observed. The profile indicates that NDDES25 is the most preferable HTF (Figure 4.26). Based on the M_o number values, NDDES25 is further selected for forced convection flow experiments and its associated Aspen simulation.

Table 4.3: Uncertainty in thermophysical properties measurements

Name	**Uncertainty**
Density	±0.05 kg/m^3
Viscosity	±0.0004 Pa.s
Thermal Conductivity	±0.0096 W/m^2.K
Specific Heat Capacity	±5.97 J/kg.K
The percentage error in M_o number calculation varies from 0.2% to 8.7%	

The measured uncertainty value for density, viscosity, thermal conductivity, specific heat capacity and percentage error associated with the calculation of M_o number is reported in Table 4.3.The propagation of percentage error for the independent variable (M_o) is calculated as per standard protocol given by Pallab Ghosh[134].

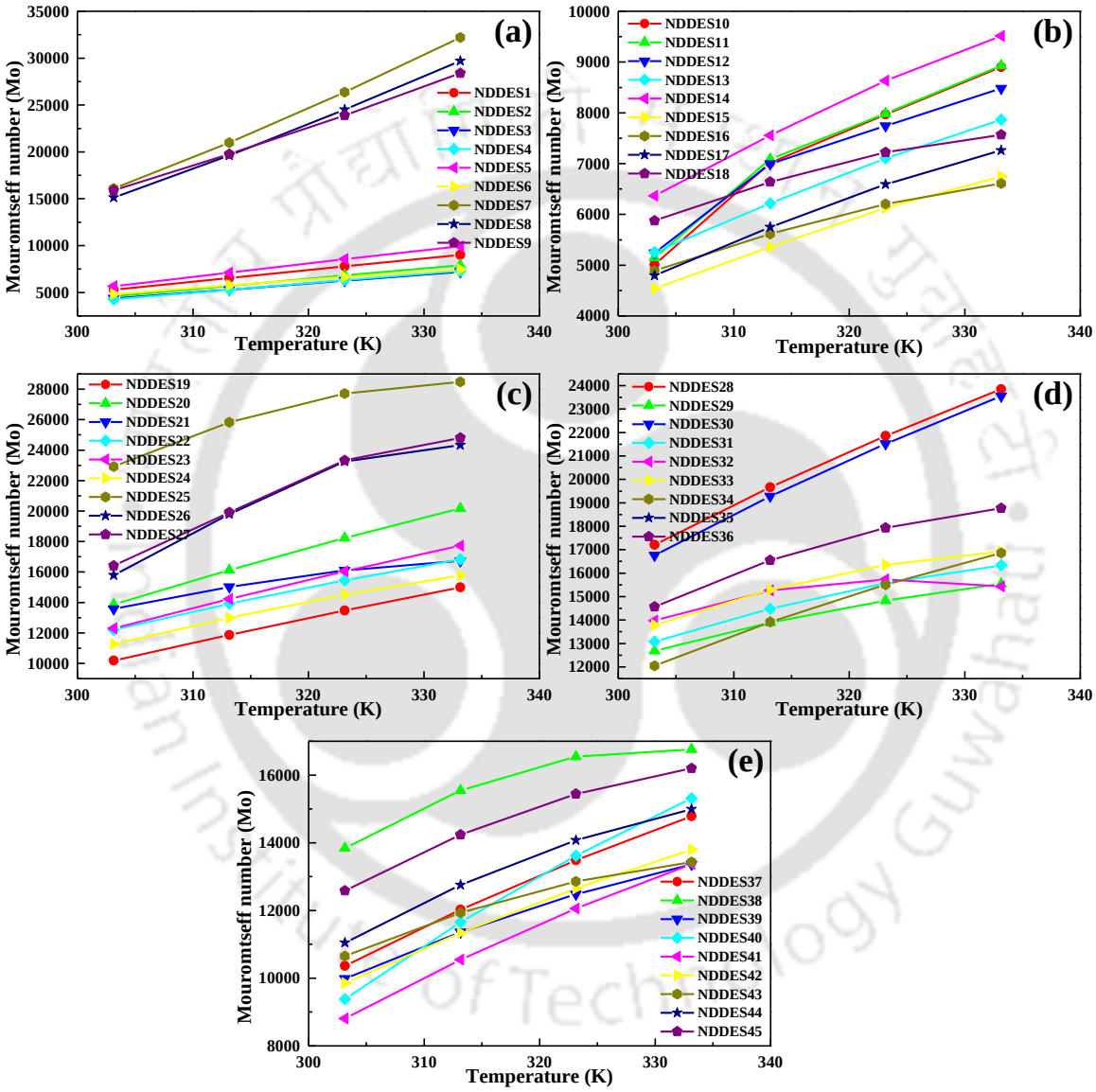

Figure 4.26: M_o number profiles of NDDESs (M_o=Mouromtseff number)

CHAPTER 5

5 Forced Convection Studies

5.1 Introduction

After the measurement of thermophysical properties, we shall now proceed with the forced convection studies. Forced convection studies are performed for the three different DESs (DES1, DES2, DES3) at different conditions. Initially the experiments are carried out with DES1 (DL-menthol + Oleyl Alcohol) under laminar flow regime with different Reynolds number and heat fluxes. The experimental findings are further validated by comparing with the numerical results. The numerical simulation is then performed using in-house *AnuPravaha CFD solver*[120]. In the next part, the forced convection experiment is carried out with DES2 (DL-menthol + Oleic Acid) and the corresponding Al_2O_3 spherical nanoparticle based nanofluid (NDDES10). The experiments are performed at constant heat flux and different Reynolds number under laminar flow regime. Further COMSOL simulation is carried out in order to validate the experimental findings. A detailed description is given in the subsequent sections. In the penultimate part, the forced convection studies are performed with the DES3 (Diphenyl Ether + DL-menthol) and NDDES25 (0.02 wt.% h-BN hexagonal nanoparticle). The experiments are carried out under both laminar and turbulent flow regime.

5.2 Forced Convection Study with DES1

The forced convection study with DES1 is carried out under laminar flow regime. The experimental system is first run by Millipore water to check the reliability of measurement technique. After validating the experimental setup, the experiments for DES1 are conducted for laminar flow environment. The experiments are carried out at four different Reynolds number with two different heat fluxes, i.e., 13514.86 W/m^2 and 13607.22 W/m^2 respectively.

5.2.1 Temperature Profile

Figure 5.1(a) and 5.1(b) represents the surface temperature profile throughout the axial distance. Figure 5.2(a) and 5.2(b) shows the typical fluid bulk mean temperature profile throughout the axial distance. The experimental findings are further compared with the *AnuPravaha CFD solver*[121] with the same experimental parameters. In the present work, the fluid bulk mean temperature is in the range of 298.15 to 320.15 K. From figure 5.2(a) and 5.2(b) due to constant heat flux boundary condition a linear increment of temperature can be observed along the axial distance and the same trend is observed in computational results. From figure 5.2(a) and 5.2(b) it is clear that the length of hydrodynamic entry region is, $L_h = 0.05\ R_e.D$ and the length of thermal entry region is, $L_t = 0.05 R_e.P_r.D$, where, R_e is Reynold's number, P_r is the Prandtl number and D is the diameter of the pipe.

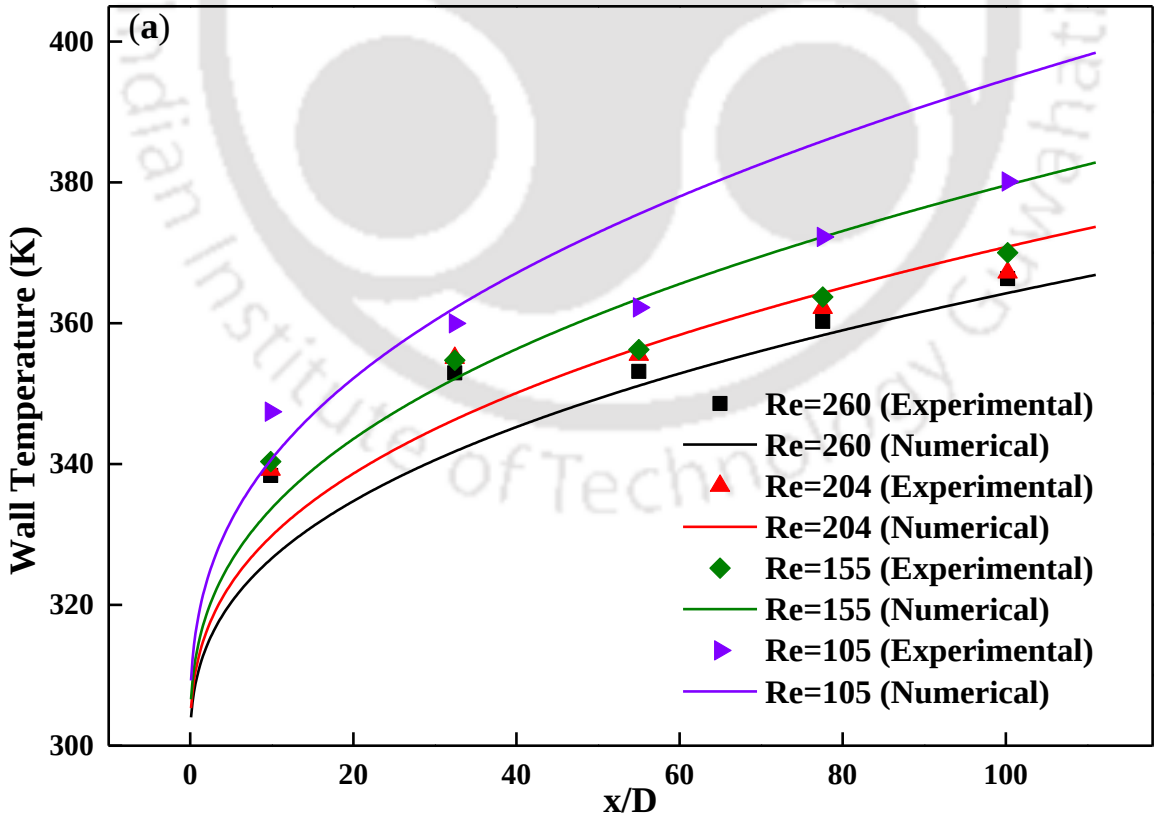

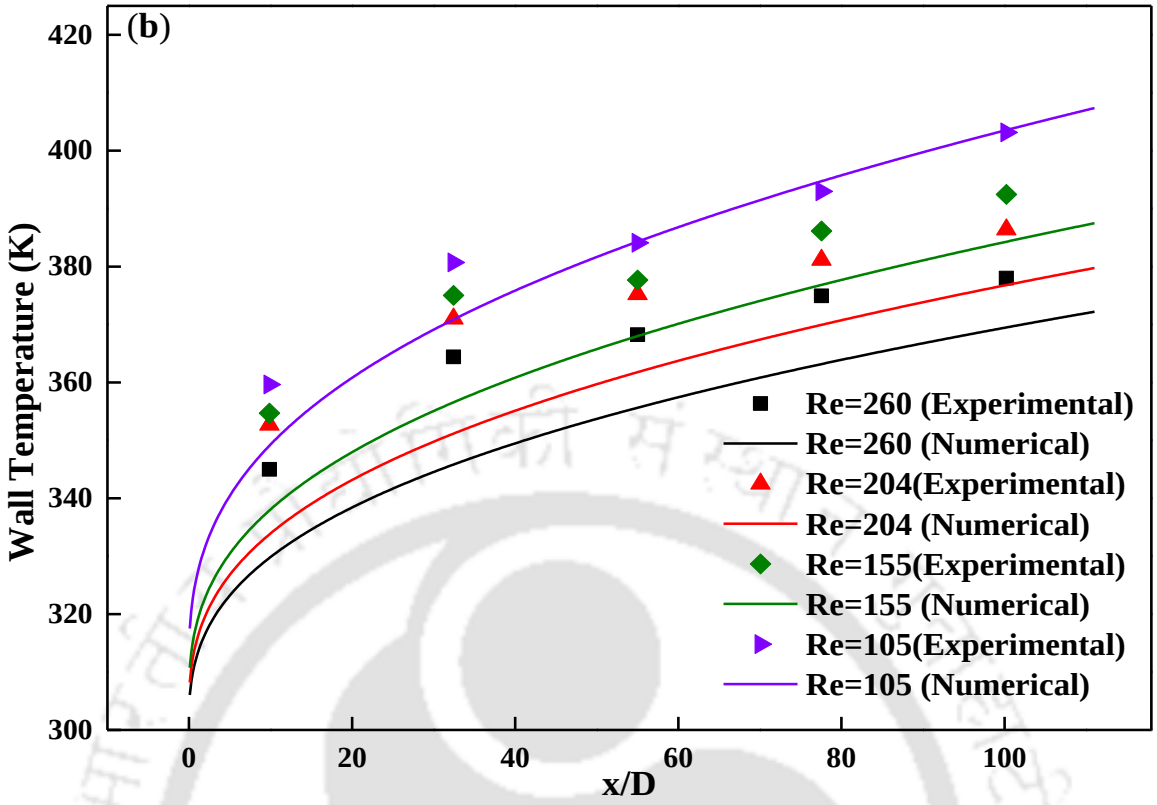

Figure 5.1: Surface temperature profile along the test section at different heat fluxes (a) 13514.86 W/m^2 and (b) 13607.22 W/m^2

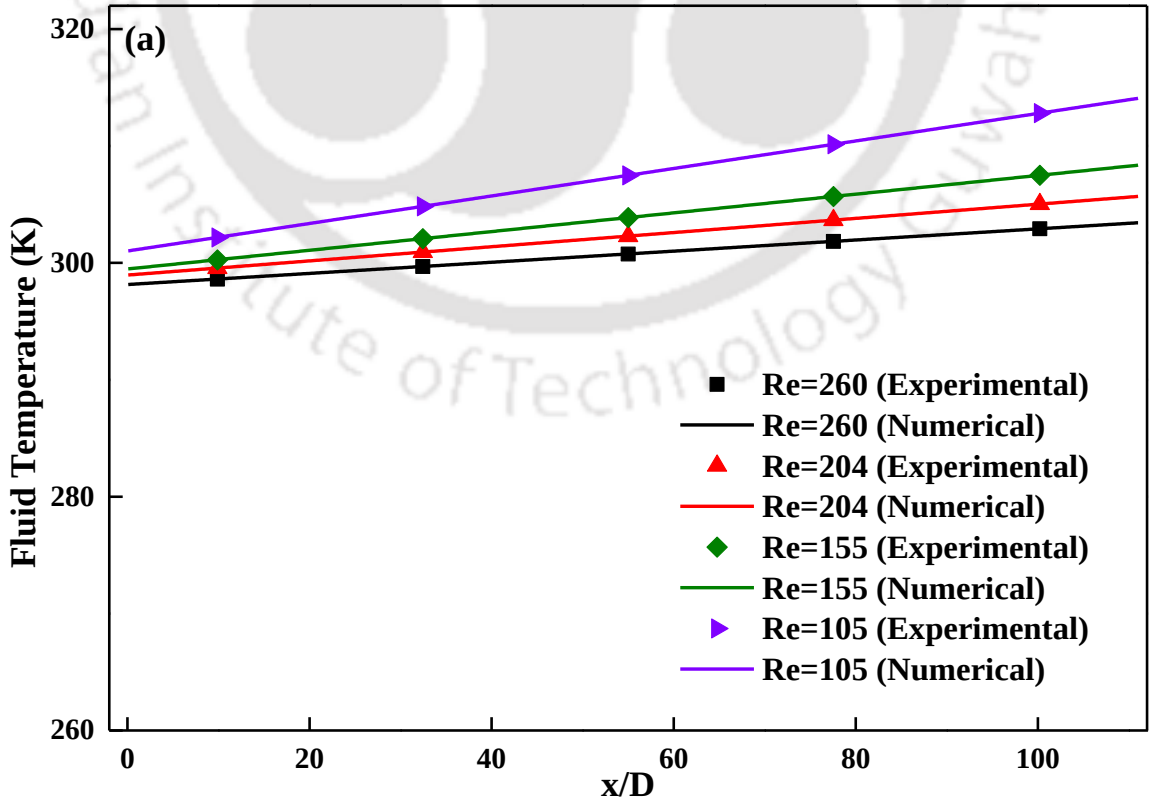

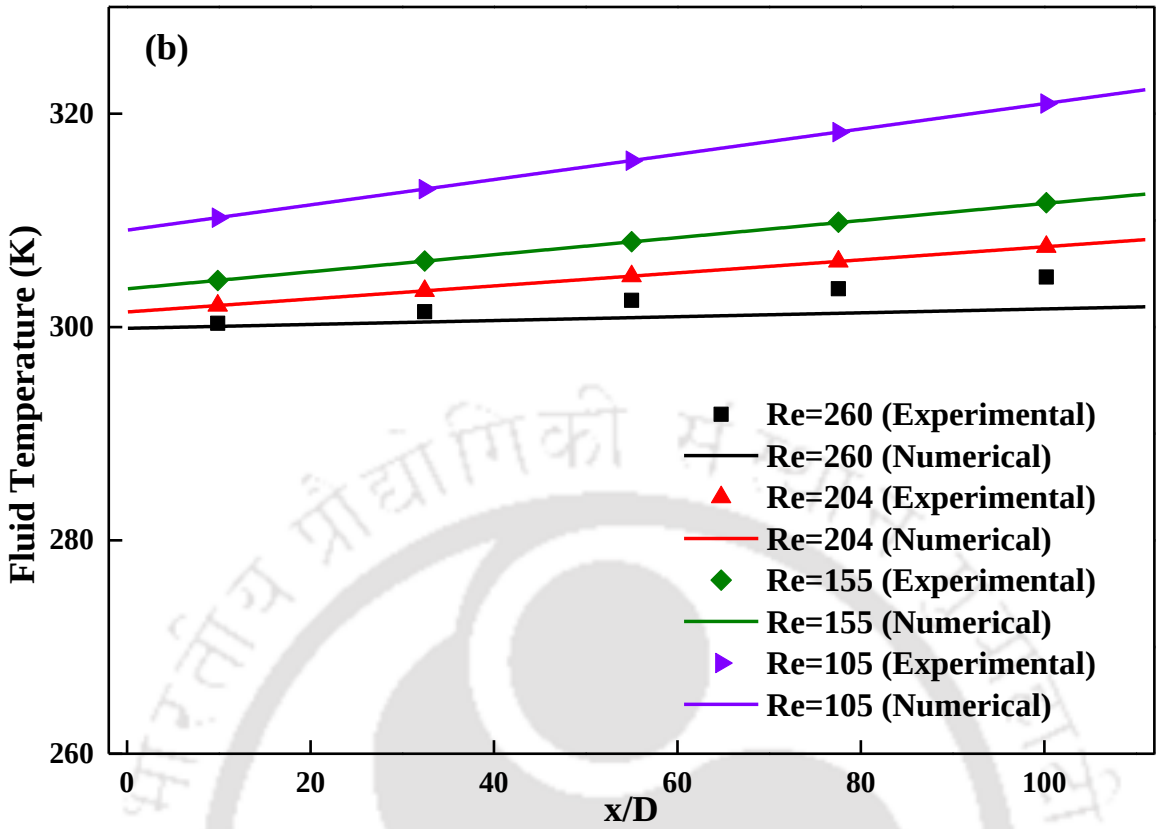

Figure 5.2: Typical temperature profile along the test section at different heat fluxes (a) 13514.86 W/m^2 and (b) 13607.22 W/m^2

5.2.2 Heat Transfer Coefficient

The comparison of heat transfer coefficients at different heat fluxes (a) 13514.86 W/m^2 and (b) 13607.22 W/m^2 can be seen in figure 5.3(a) and 5.3(b). It is obvious that the heat transfer coefficient of DES1 at heat fluxes 13607.22 W/m^2 is higher than 13514.86 W/m^2 heat flux. This is because at higher heat flux, the viscosity of DES1 decreases while the specific heat capacity increases.

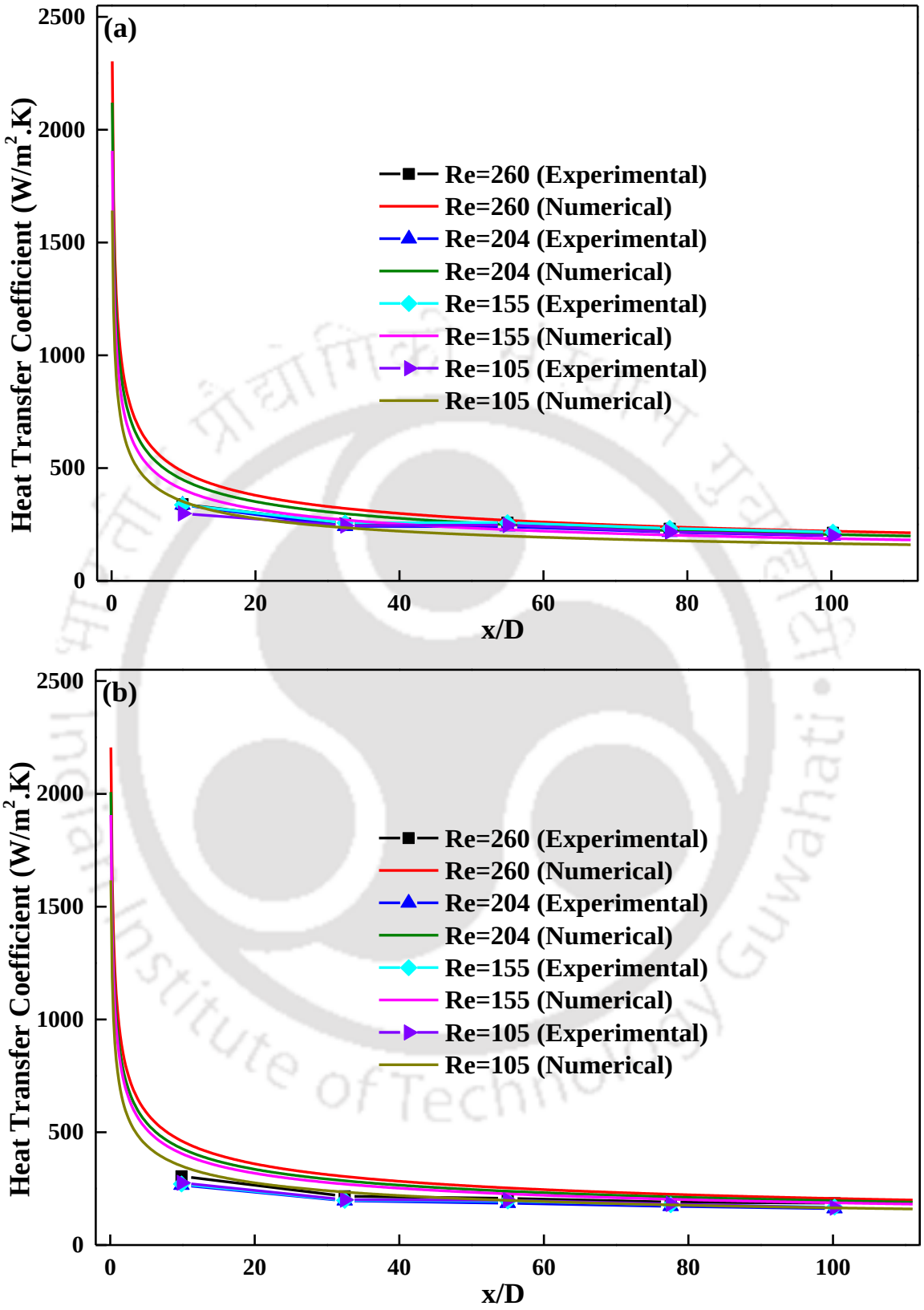

Figure 5.3: Heat transfer coefficient of DES1 as a function of axial distance at different heat fluxes (a) 13514.86 W/m^2 and (b) 13607.22 W/m^2

5.2.3 Nusselt Number

Figure 5.4(a) and 5.4(b) indicates the heat transfer performance of DES1 for four different Reynolds number and two different heat fluxes at the laminar flow region. The simulation results are compared in the plot, which shows a higher Nusselt number varying from 5-10% as compared to experimental results. The difference in experimental and simulation result is because of the heat loss from the heating tape of the experimental setup. The calculated laminar region as evident from Reynold's number also varies with the hydrodynamic entrance length. This length is defined in terms of a diameter which varies from x = 10D to 100D. On the contrary, the thermal entrance length varies as x = 1716D–4251D. This trend implies that the flow is only hydrodynamically developed, which is evident from figures 5.4(a) and 5.4(b).

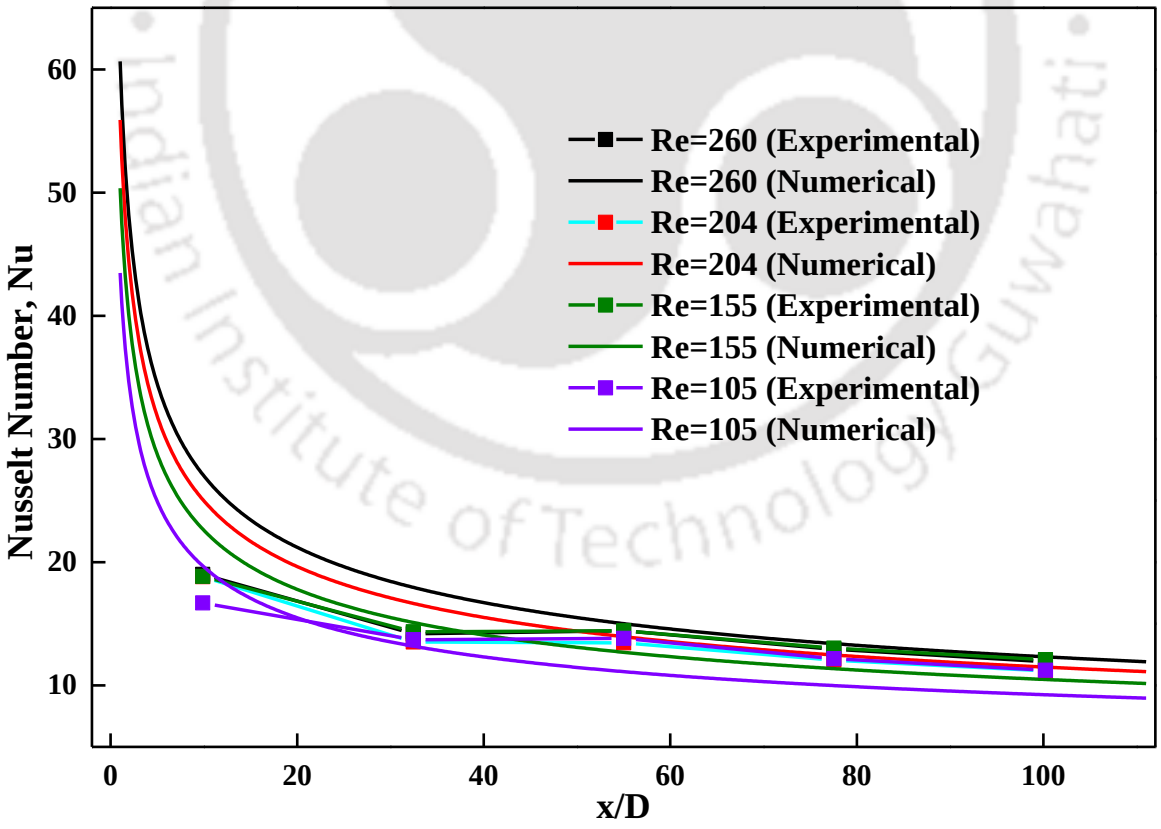

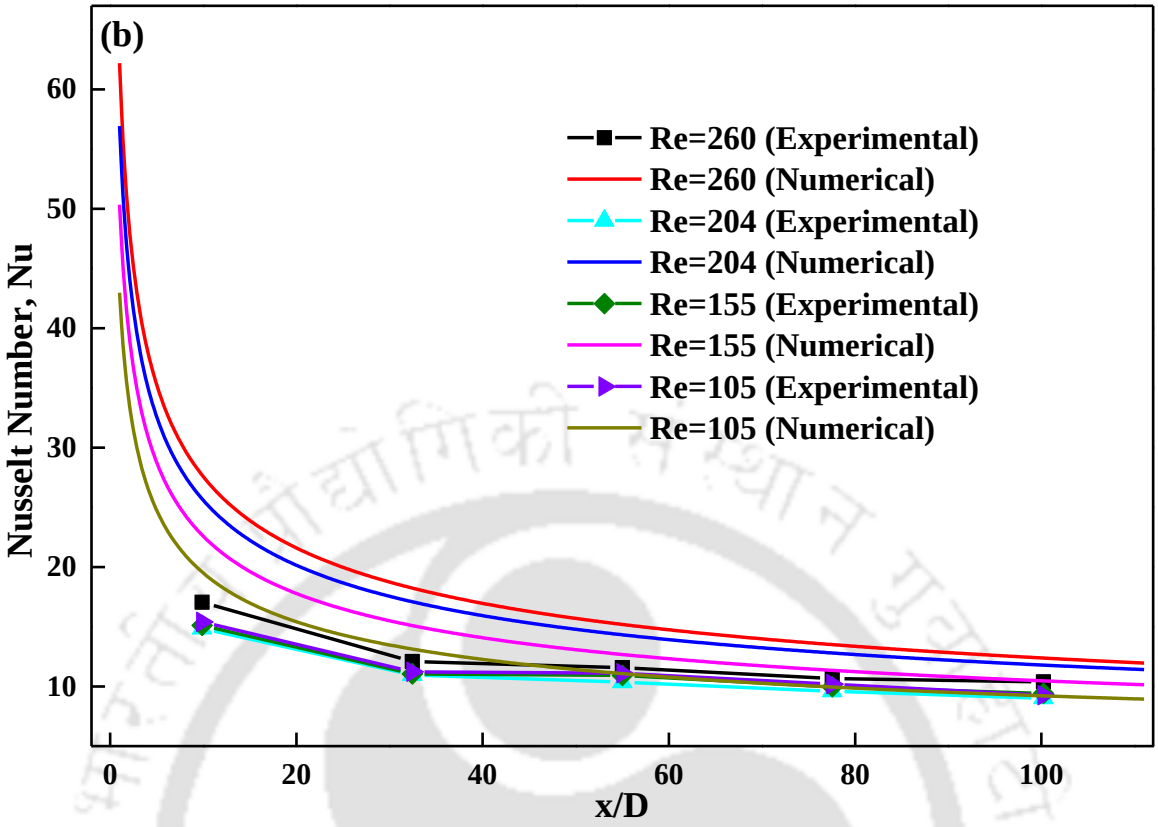

Figure 5.4: Heat transfer behaviour of DES1 at different heat fluxes (a) 13514.86 W/m^2 and (b) 13607.22 W/m^2

5.3 Forced Convection Study with DES2

The COMSOL simulations is performed in COMSOL Multiphysics (Version 5.2a). Initially the space dimension as *2D axisymmetric* is selected. A No slip boundary condition and uniform heat flux is applied to the wall. A time dependent study has been performed so as to ascertain steady state. The dimensions of the test section are assumed to be rectangle of length 1000 mm and width 9 mm. The two-dimensional tube geometry is generated by COMSOL inbuilt meshing tool where a total of 228680 mesh elements are created. Experimentally measured thermophysical properties (density, viscosity, conductivity and specific heat capacity) as given in Figures (4.13, 4.14(b), 4.17, 4.18(b), 4.19, 4.20(b), 4.21 and 4.22(b)) are used for the simulation. Thereafter the simulation is started with an initial guess which shall help us in solving the velocity and temperature

profile. A uniform heat flux of 13312 W/m^2 is applied to the wall. This is the same flux as used in figure 3.6 via heating tape. To solve the energy equation, velocity information is necessary. This is obtained by solving the continuity and momentum equation (equation 3.12-3.15). Here the flow coupling is added explicitly as provided under the *Multiphysics section*. While figures 5.5-5.7 discusses the heat transfer performance of DES2, figures 5.8-5.10 depicts the NDDES10 performance.

5.3.1 Temperature Profile

Figure 5.5 signifies the temperature profile of DES along the axial distance of the test section with three different Reynolds Number within the laminar regime. Further the experimental results are compared with the simulated results. The fluid temperature is in the range of 361.96 to 446.06 K.

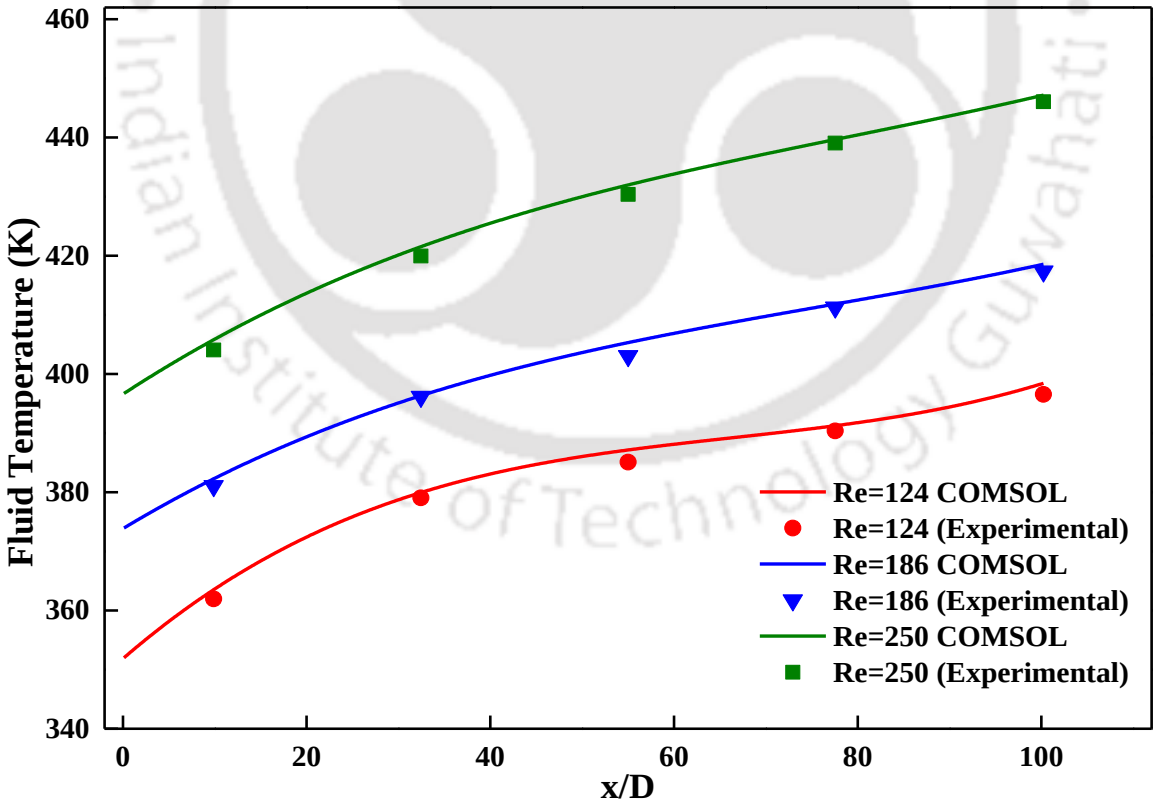

Figure 5.5: Temperature profile along the test section for DES2

A linear increment of temperature can be observed along the axial distance in both experimental and computational which is due to constant heat flux boundary condition.

5.3.2 Heat Transfer Coefficient

Figure 5.6 represents the heat transfer coefficient of DES2 along the axial distance at a heat flux of 13312 W/m^2 in three different Reynolds numbers.

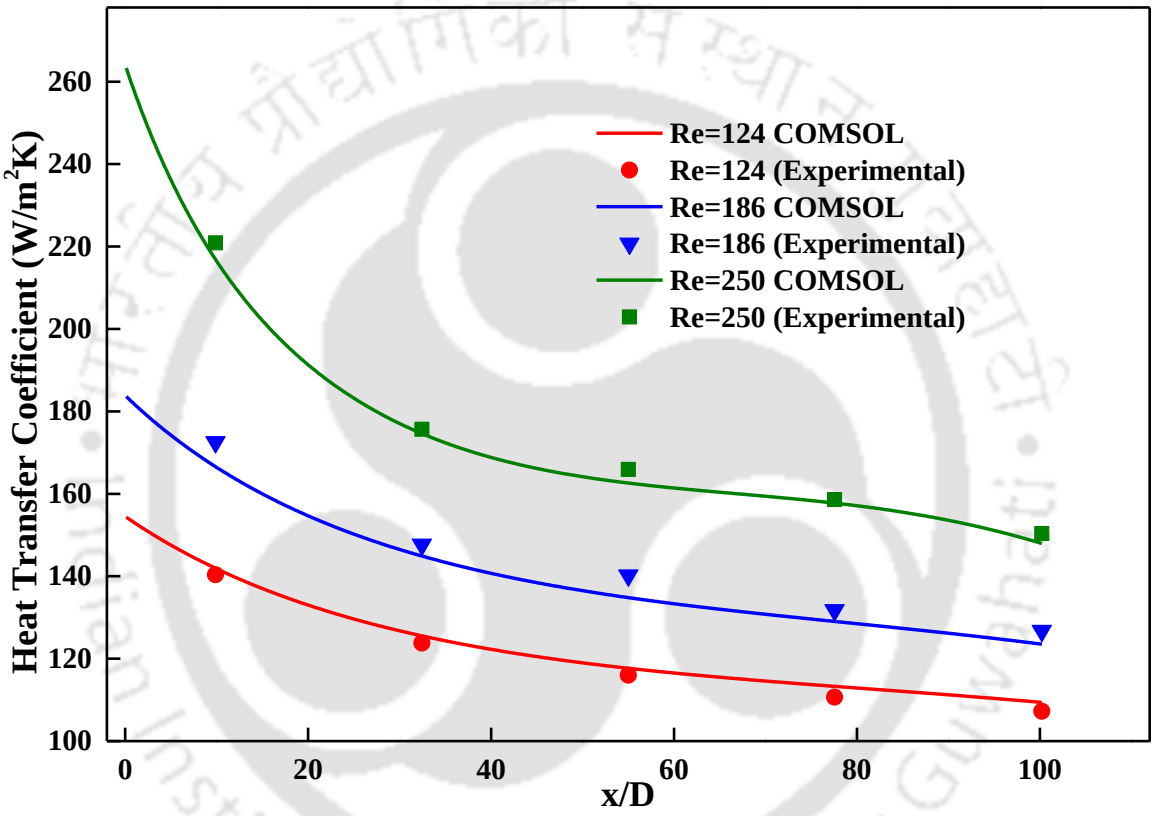

Figure 5.6: Heat transfer coefficient of DES2 as a function of x/D

The experimental heat transfer coefficient is compared with the numerical results where it gave negligible deviation. The DES2 gave enhanced heat transfer coefficient along the entire axial distance with the heat transfer coefficient decreasing with axial distance. As expected the heat transfer coefficient is also found to increase with increase in Reynolds number.

5.3.3 Nusselt Number

Figure 5.7 represents the Nusselt Number of DES2 along the axial distance at three different Reynolds number. Here the Nusselt Number increases with increase in Reynolds number. Al_2O_3 (spherical) nanoparticle of weight percentage of 0.02 wt.% has been chosen for the both experiment and simulation. A similar phenomenon is observed for NDDES10 with respect to temperature profile (Figure 5.8), heat transfer coefficient (figure 5.9) and Nusselt Number (figure 5.10).

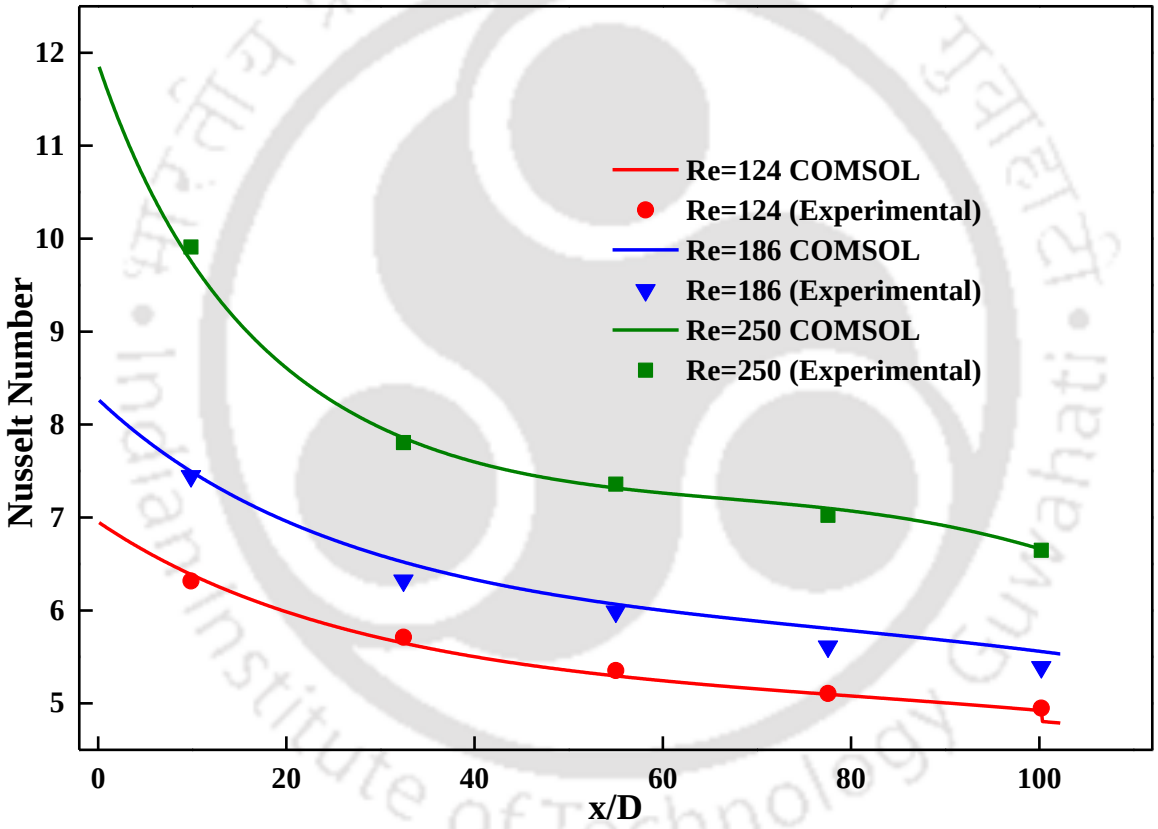

Figure 5.7: Nusselt Number of DES2 as a function of x/D

5.4 Forced Convection Study with NDDES10

In both the cases (DES2 and NDDES10) it has been found that the inside surface temperature of the tube is higher with decrease in Reynolds number. However, a decrease in Reynold number led to an ~10% enhancement in the surface temperature which is

evident near the entrance region. It should be noted that a one metre length pipe is sufficient for a flow to be considered hydrodynamically developed but the same cannot be said of its thermal layer. In both DES2 and NDDES10, at the entrance of the pipe, heat transfer coefficient is very large due to which boundary layer thickness is very small. It is found that the boundary layer thickness starts increasing while the heat transfer coefficient decreases along the pipe length. An appreciable increase in the coefficient of heat transfer is attributed to the increased thermo-physical properties of DES2 nanofluids and a delay in the development of the boundary layer in the entrance area.

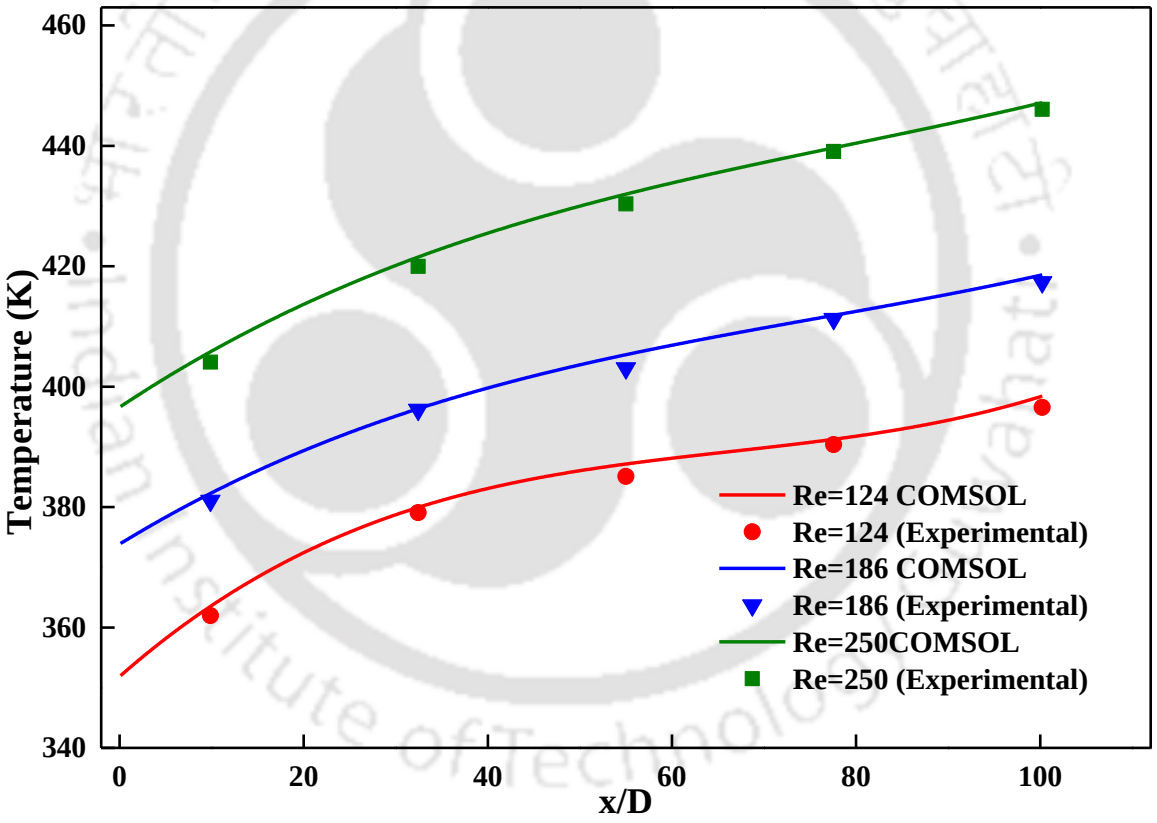

Figure 5.8: Temperature profile along the test section for NDDES10 at 0.02 wt.%

This behaviour indicates that measures could be taken such as creating "artificial entrance" regions along a pipeline to maximize the performance of these novel nanofluids.

The flow is not thermally developed as the value of Prandtl number is large for both DES2 and NDDES10 fluids.

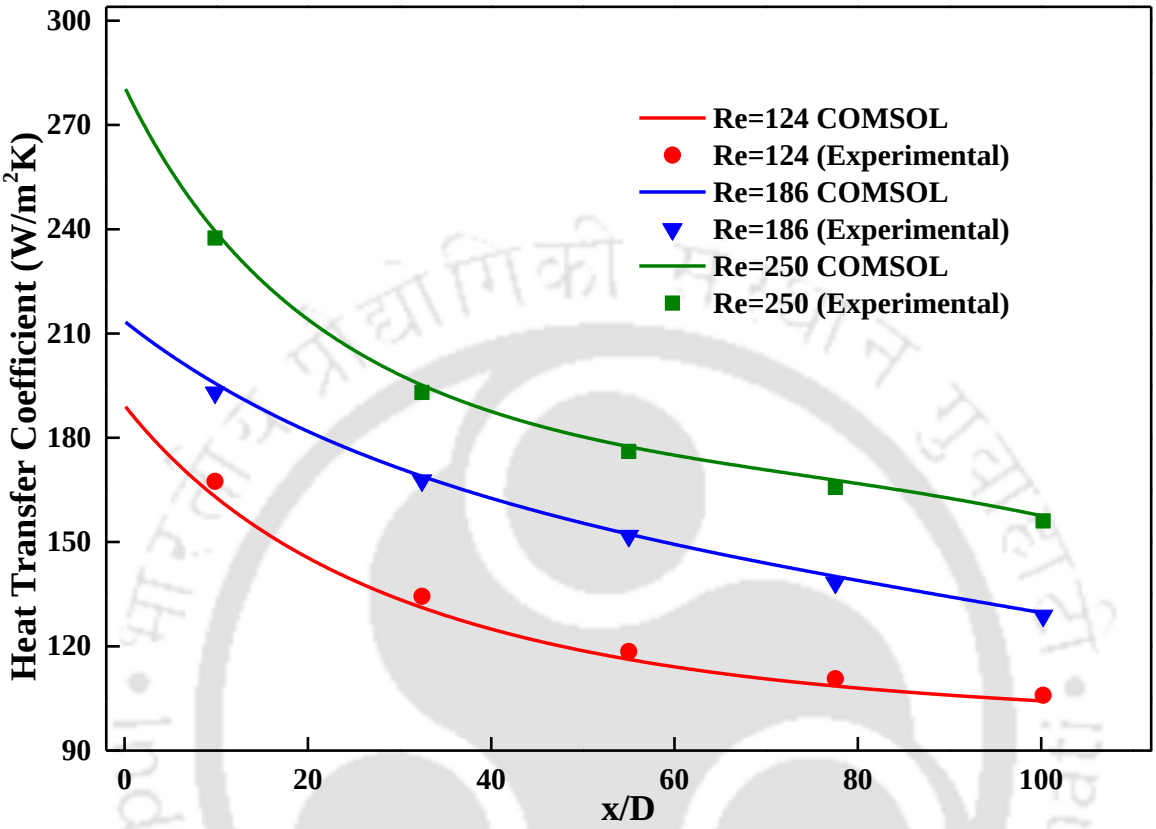

Figure 5.9: Heat transfer coefficient of NDDES10 (0.02 wt.%) as a function of x/D

Overall the thermal entrance length of the nanofluid flows has a longer length scale when compared to only DES2 flow. The enhancement of the local heat transfer coefficient is higher in magnitude when compared to the increase in the effective thermal conductivity within the test section. Thus, the use of NDDES10 nanofluids hence significantly improves the convective heat transfer, particularly at the entrance region. This may be due to the particle migration resulting in a non-uniform distribution of both thermal conductivity and viscosity. This eventually reduces the thermal boundary layer thickness. The benefit of NDDES10 as heat transfer fluid shall be determined based on the consideration between the increase of heat transfer performance with increase of pumping power. Further the

stability of nanoparticles is another concern. Its agglomeration ability is a critical problem faced in the practical application of nanofluid. This affects properties of nanofluid and impacts on the heat transfer performance of nanofluid. The agglomerates can have various sizes and configurations depending primarily on elapsed time. It invariably can affect the thermal conductivity of nanofluid. This agglomeration may also be due to the nanofluid preparation and the experimental study time along with different time duration of experimental study. However, use of surfactants can increase their stability. In some of the earlier reported work[135,136] these may be reached in low pH condition thereby making nanofluid difficult in many application systems.

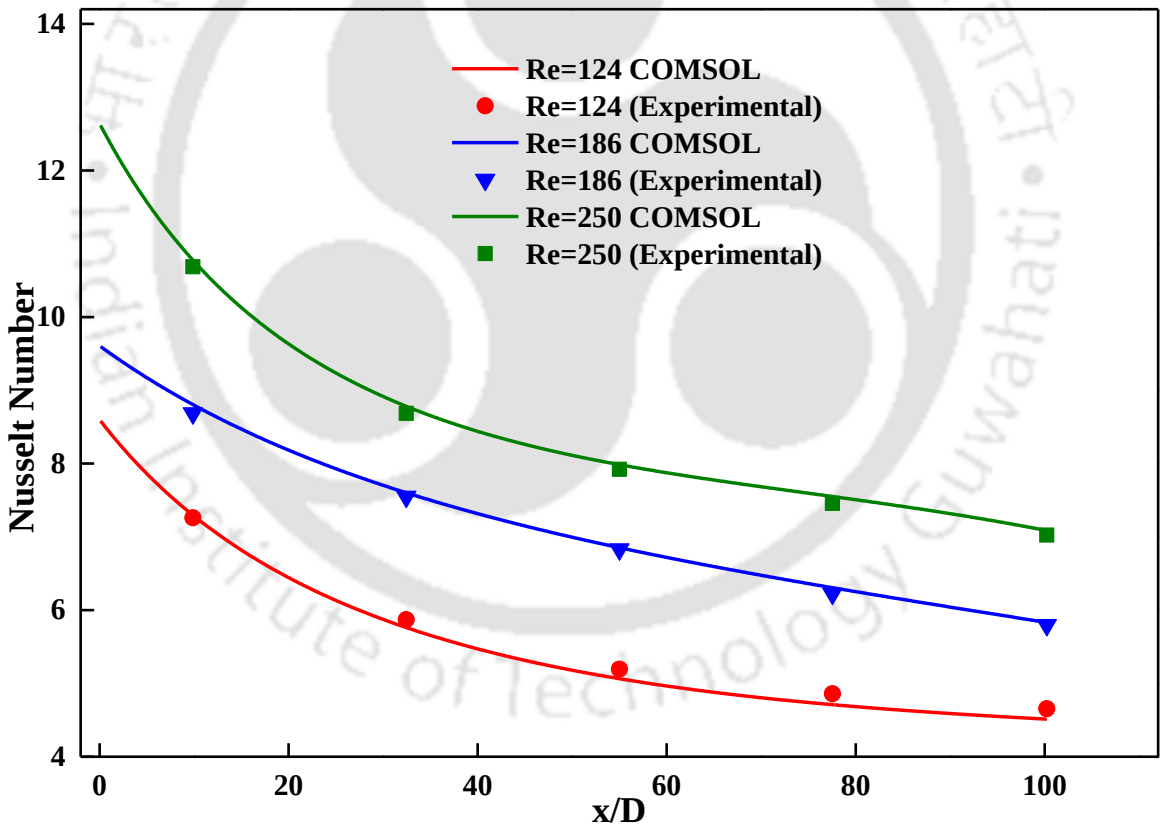

Figure 5.10: Nusselt number of NDDES10 (0.02 wt.%) as a function of x/D

5.5 Forced Convection Study with DES3 and NDDES25

The experimental set up was run at three different flow rates for both laminar and turbulent region with each HTF namely DES3 (Diphenyl Ether + DL-menthol) and NDDES25 (DES3 + 0.02 wt.% h-BN hexagonal nanoparticles).

5.5.1 Fluid Temperature

Figure 5.11 represents the testing section surface temperature of DES3 and NDDES25 for both laminar and turbulent regions along the axial direction. Figure 5.12 represents the wall temperature of DES3 and NDDES25 for both laminar and turbulent regions along the axial direction. From figure 5.12 (a) this can be observed that, under the laminar flow regime, temperature profiles show linear increment along the length of the test section due to longer residence time. However, for turbulent flow (figure 5.12 (b)), the temperature remains almost constant.

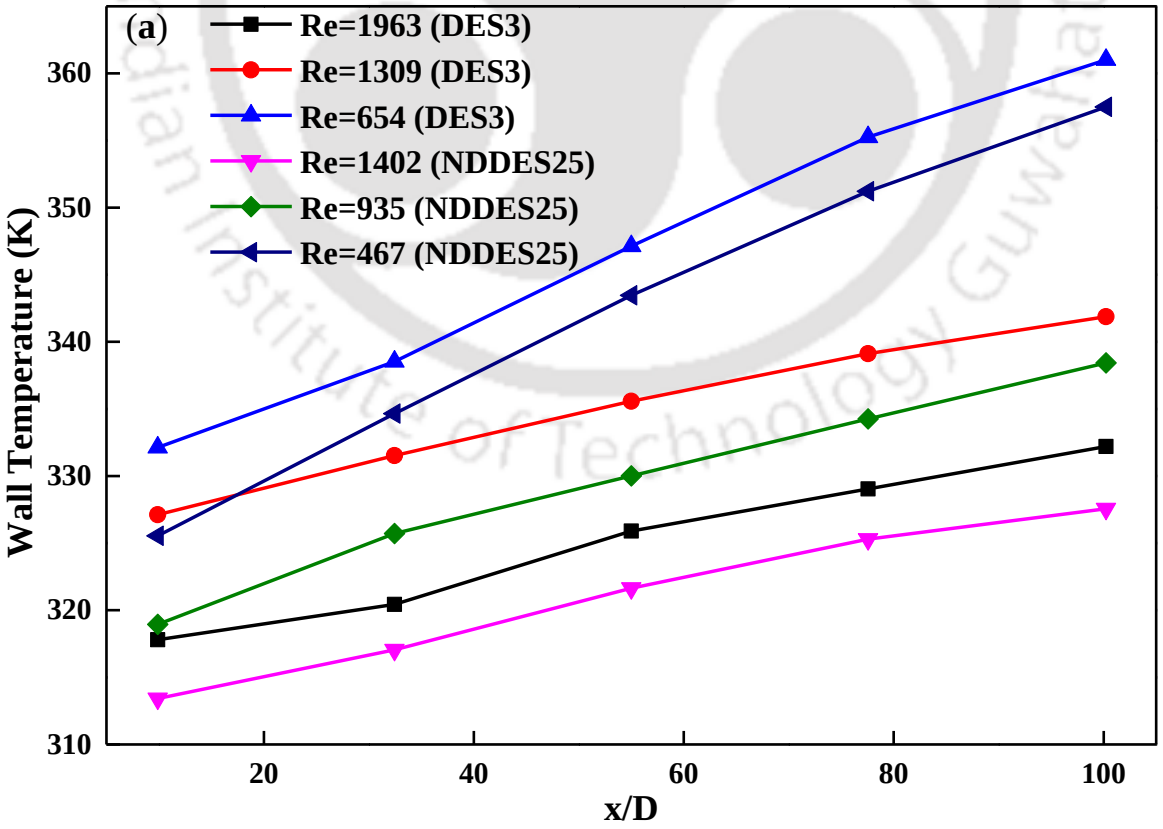

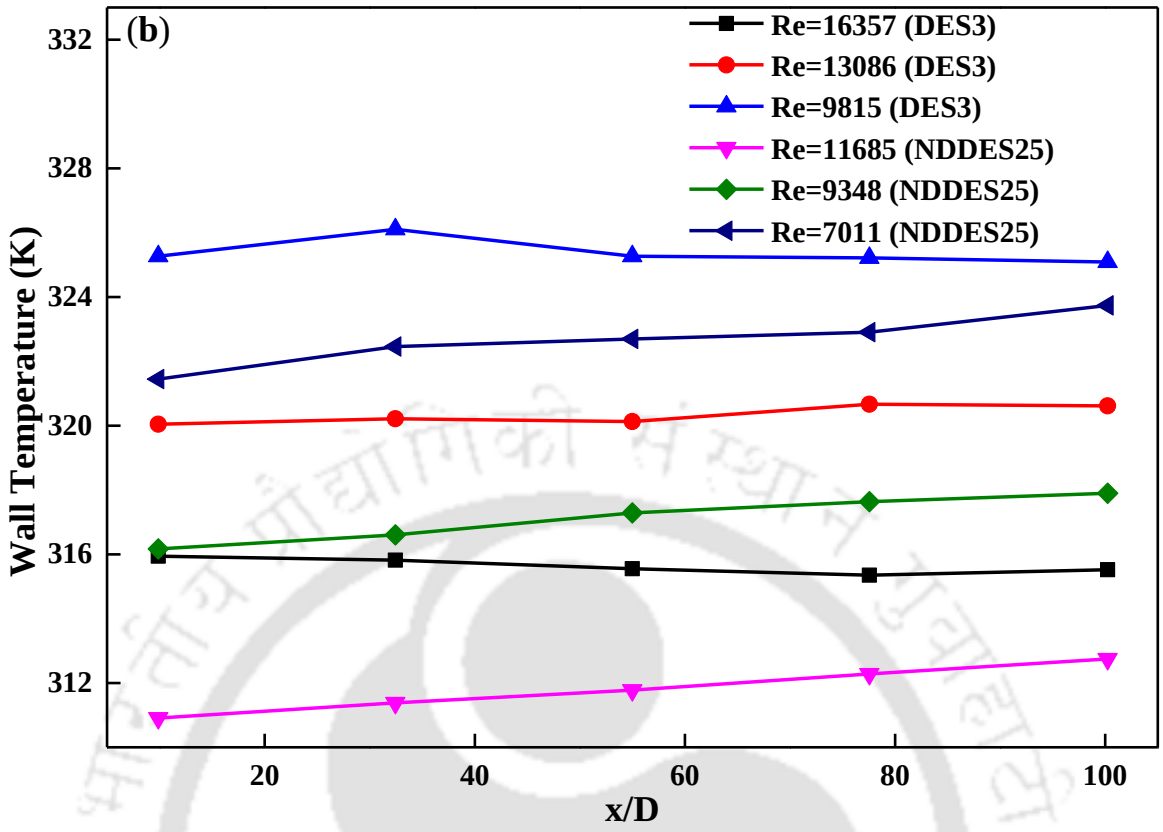

Figure 5.11: Wall temperature in (a) laminar and (b) turbulent flow regime

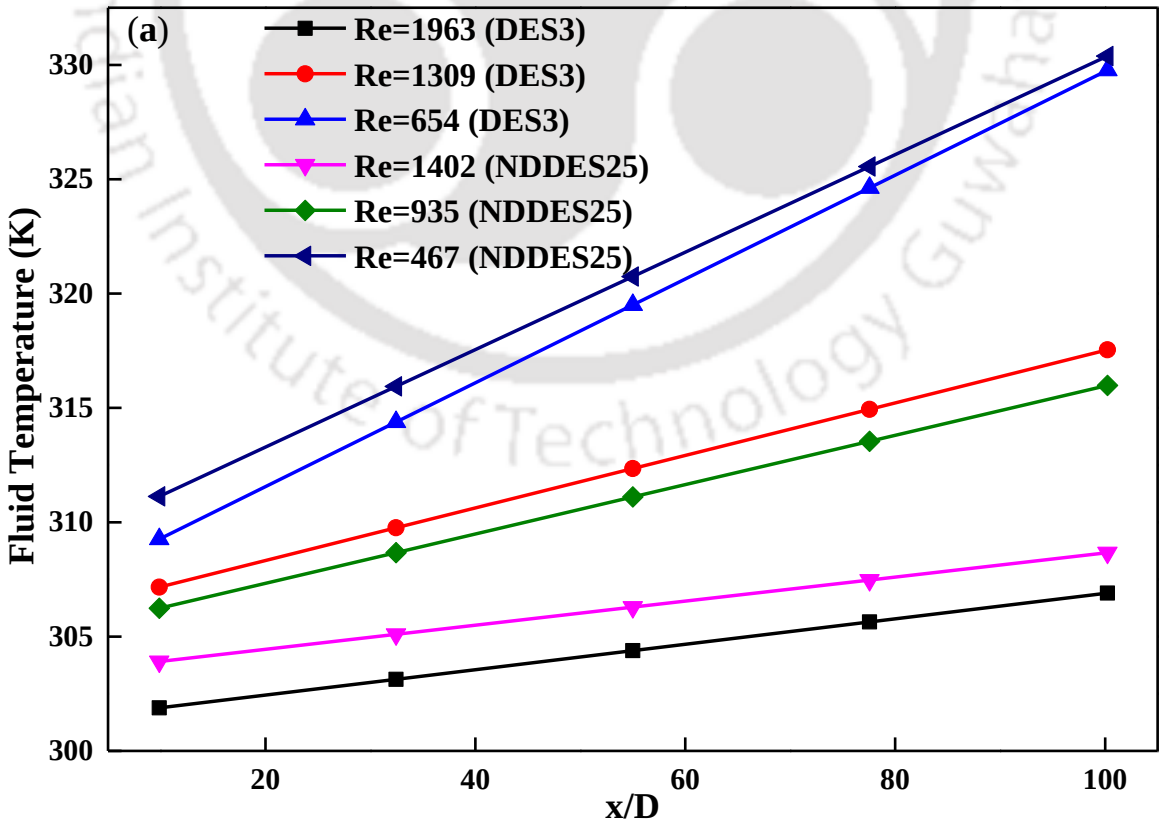

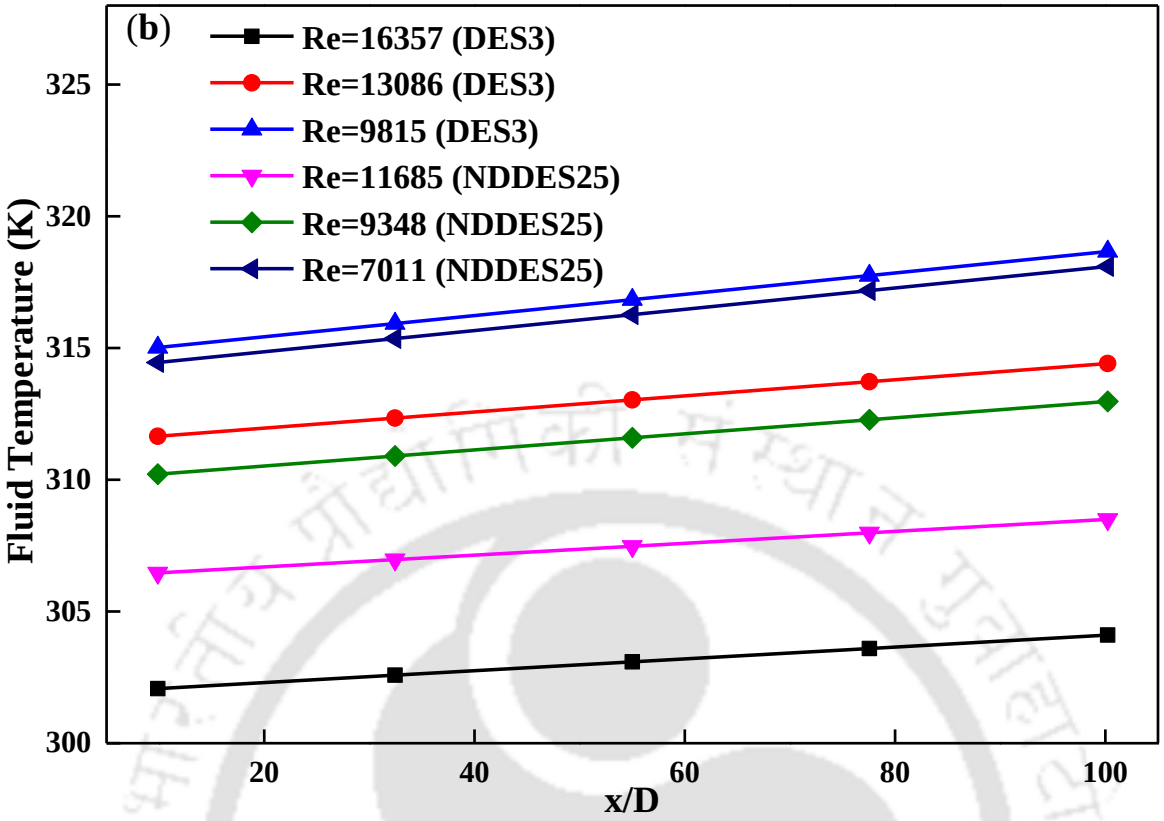

Figure 5.12: Fluid temperature in (a) laminar and (b) turbulent flow regime

5.5.2 Heat Transfer Behaviour under Laminar flow regime

Figure 5.13 predicts the thermal behaviour of both DES3 and NDDES25 as a function of characteristic length of the testing section when the flow is laminar. From figure 5.13 (a) this can be observed that NDDES25 at *Re*=1402 results are the highest heat transfer coefficient and hence the maximum *Nu* can be observed (figure 5.13 (b)). For laminar flow, a comparable observation of heat transfer coefficient and Nusselt number are made for DES1 and DES3.

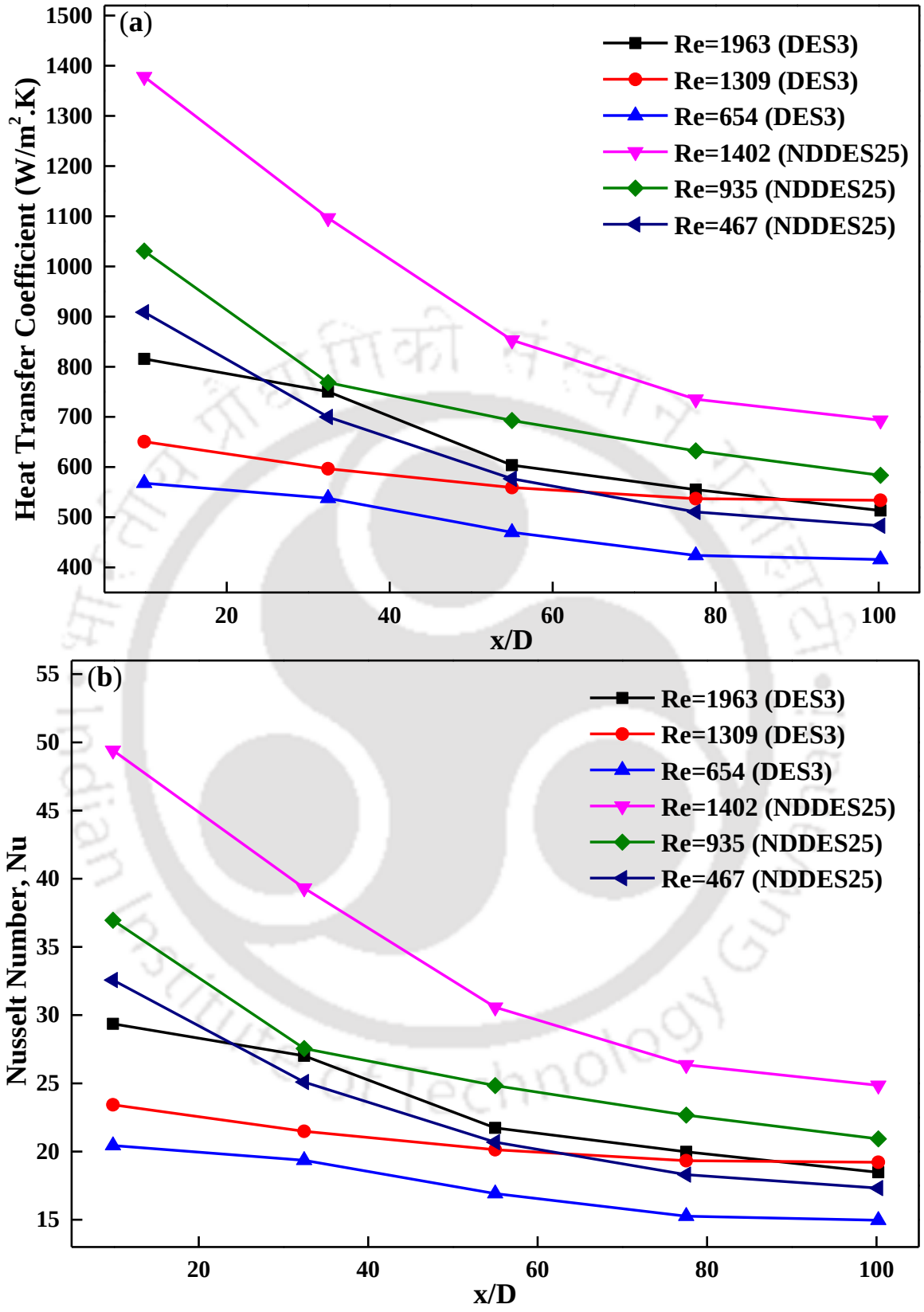

Figure 5.13: (a) Heat transfer coefficient and (b) Nusselt number within the laminar flow regime

5.5.3 Heat Transfer Behaviour under Turbulent flow regime

The observed values of the heat transfer coefficient and *Nu* are more for turbulent flow (figure 5.14 (a) and (b)) than the laminar regime (figure 5.13 (a) and (b)). For turbulent flow, the fluid particles encounter a higher number of intermolecular collisions with an increase in velocity and hence a higher heat transfer can be observed. Similar to laminar flow, NDDES25 also shows better thermal performance for turbulent flow. The heat transfer coefficient and *Nu* decrease with the progressing characteristic length for laminar flow behaviour. However, the heat transfer coefficient and *Nu* for turbulent flow are either constant or increase with an increase in characteristic length.

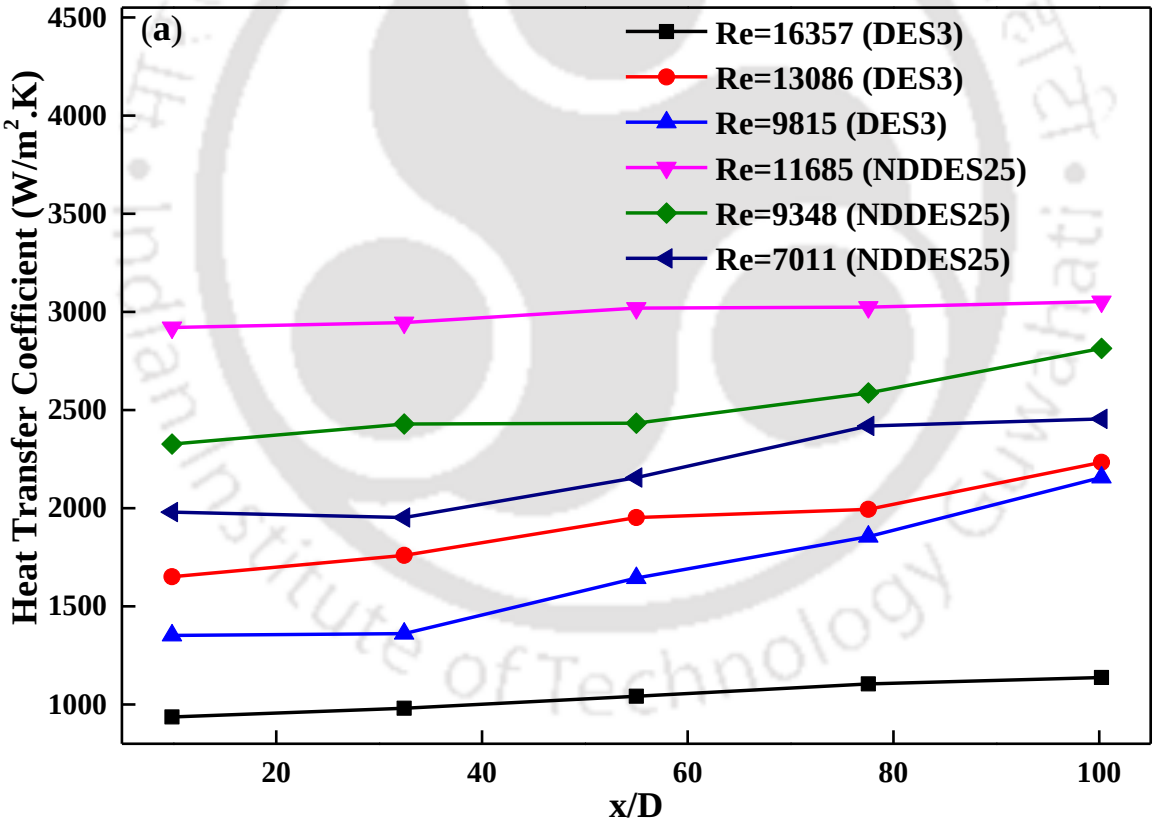

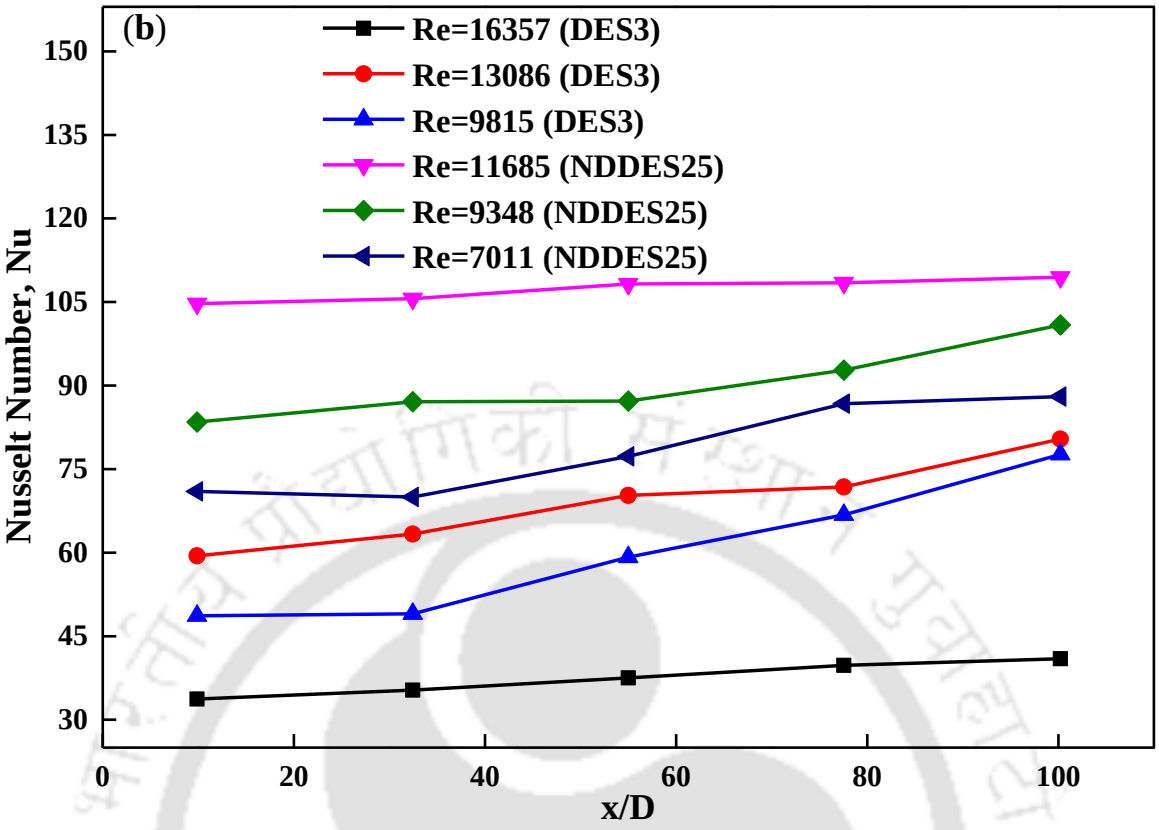

Figure 5.14: (a) Heat transfer coefficient and (b) Nusselt number for turbulent flow regime

CHAPTER 6

6 Aspen Plus Simulation for Steam Generation

Here we have initially benchmarked the procedure with known reported data on nitrate-based salts. Thereafter it has been reproduced for our own DES and NDDES systems.

6.1 Benchmarking of Aspen plus simulation using Molten Salts

The previously reported experimental procedure by He et al.[12] has been considered for the Aspen Plus simulation. The results obtained from the simulation are compared with the experimental results[12]. Table 3.6 shows the stream property, amount, energy, and phases for the entire steam generation system. From the stream table, all possible data can be extracted for a specific flow rate.

6.1.1 Heat Transfer Performance

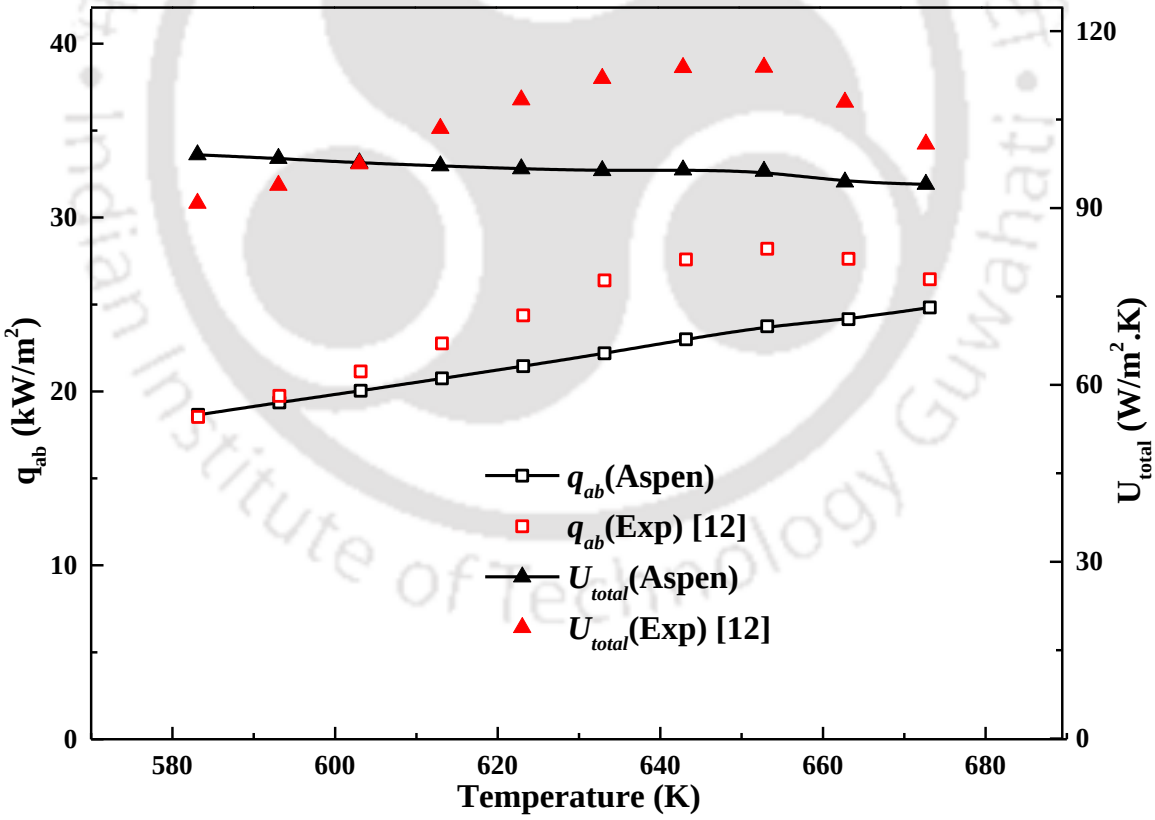

Figure 6.1: Overall heat transfer coefficient and Heat flux of molten salt at flow rate of 1 m^3/hr.

The overall heat transfer coefficient and heat flux absorbed by water/steam at a temperature range 583.15-673.15 K is illustrated in Figure 6.1. From the results, it has been found that when the inlet temperature of molten salt rises, the overall heat transfer coefficient increases and heat flux decreases. When the inlet temperature rises from 583.15 K to 673.15 K, a maximum overall heat transfer coefficient of 100.85 W/m^2 K can be observed at 673.15 K.

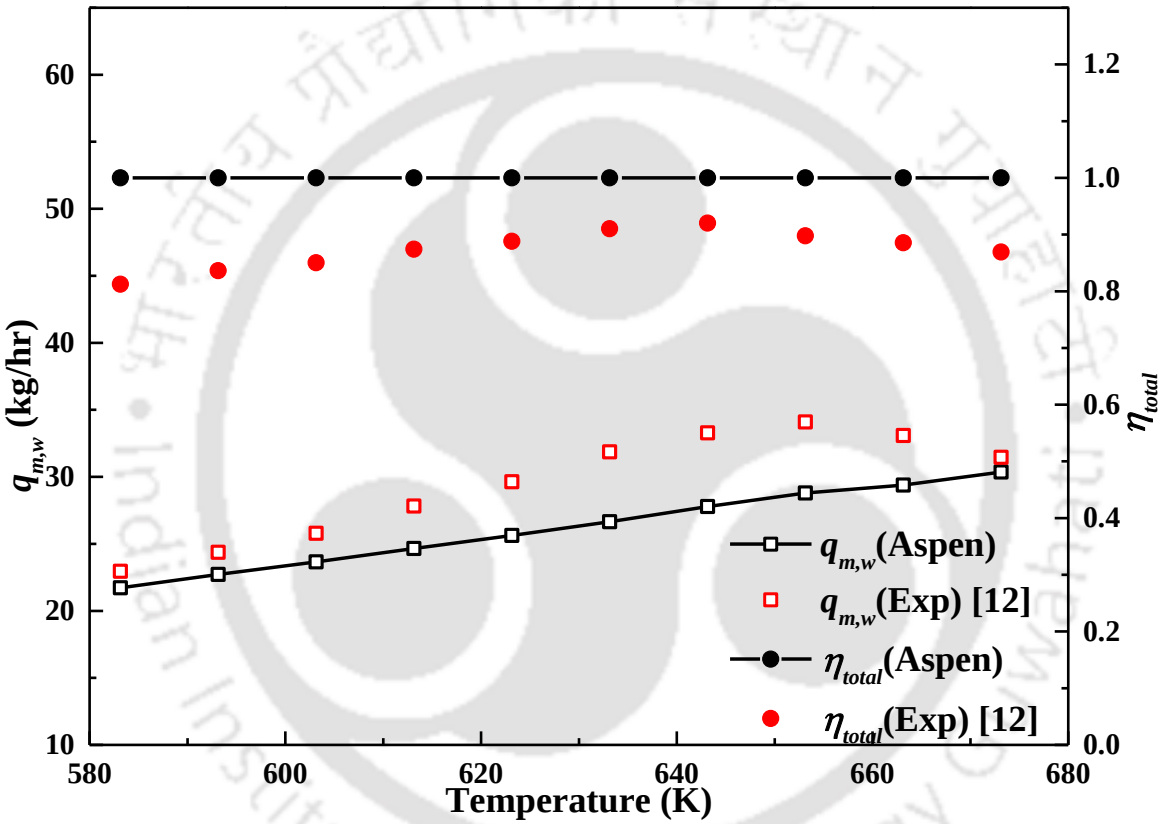

Figure 6.2: Steam generation rate and thermal efficiency of steam generation system at Molten Salt flow rate of 1 m^3/hr.

Figure 6.2 represents the rate of steam generation and efficiency of the whole system with respect to temperature at a molten salt flow rate of 1 m^3/h. As inlet molten salt temperature rises, the steam generation rate increases gradually while the thermal efficiency shows a constant trend. When the inlet temperature of molten salt increases from

583.15 K to 673.15 K, steam generation rate proportionately increases from 21.73 kg/h to 30.36 kg/h.

6.1.2 Thermal Performance at different flow rates of Molten Salt

Figure 6.3 shows the rate of vapor/steam generation with in a temperature range of 583.15-673.15 K for different flow rate of molten salt. The vapor generation rate primarily increases and then start to decrease with temperature for all the experimental values. On the other hand, the vapor generation rate in Aspen plus simulation for similar temperature range and flow rate of molten salt increases gradually with the temperature.

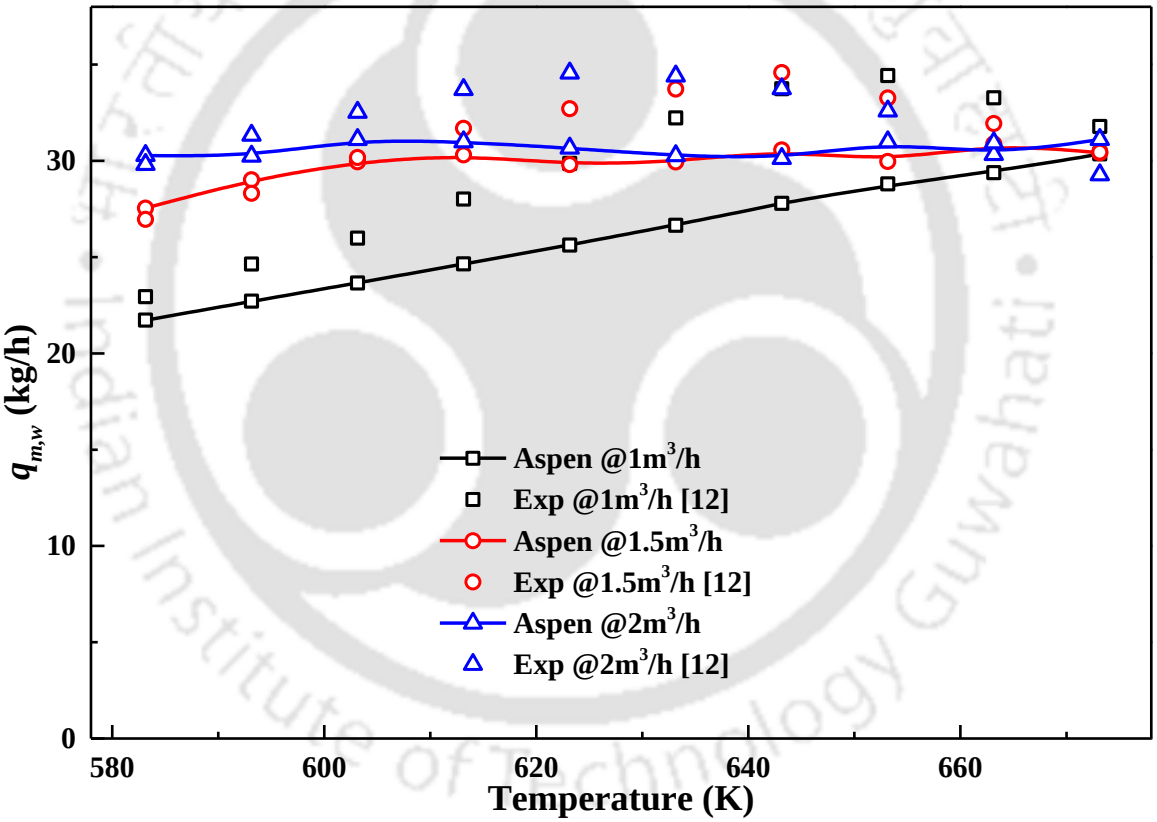

Figure 6.3: Steam generation rate with molten salt with different flowrates of Molten Salt

Figure 6.4 represents the overall heat transfer coefficient with the temperature varying from 583.15 K to 673.15 K for different flow rates of molten salt. Overall heat transfer coefficient again increases and then starts to decrease with temperature. The overall heat transfer coefficient for similar temperature range and flow rate also decreases

continuously for 1.5 and 2 m^3/h and is almost constant for 1 m^3/hr (figure 6.4). Within the experimental range, it is found that the boiling heat transfer coefficient starts to decrease at a higher temperature which is the reason for the decrease of overall heat transfer coefficient at a higher temperature. Such consideration in Aspen plus simulations is very difficult to incorporate.

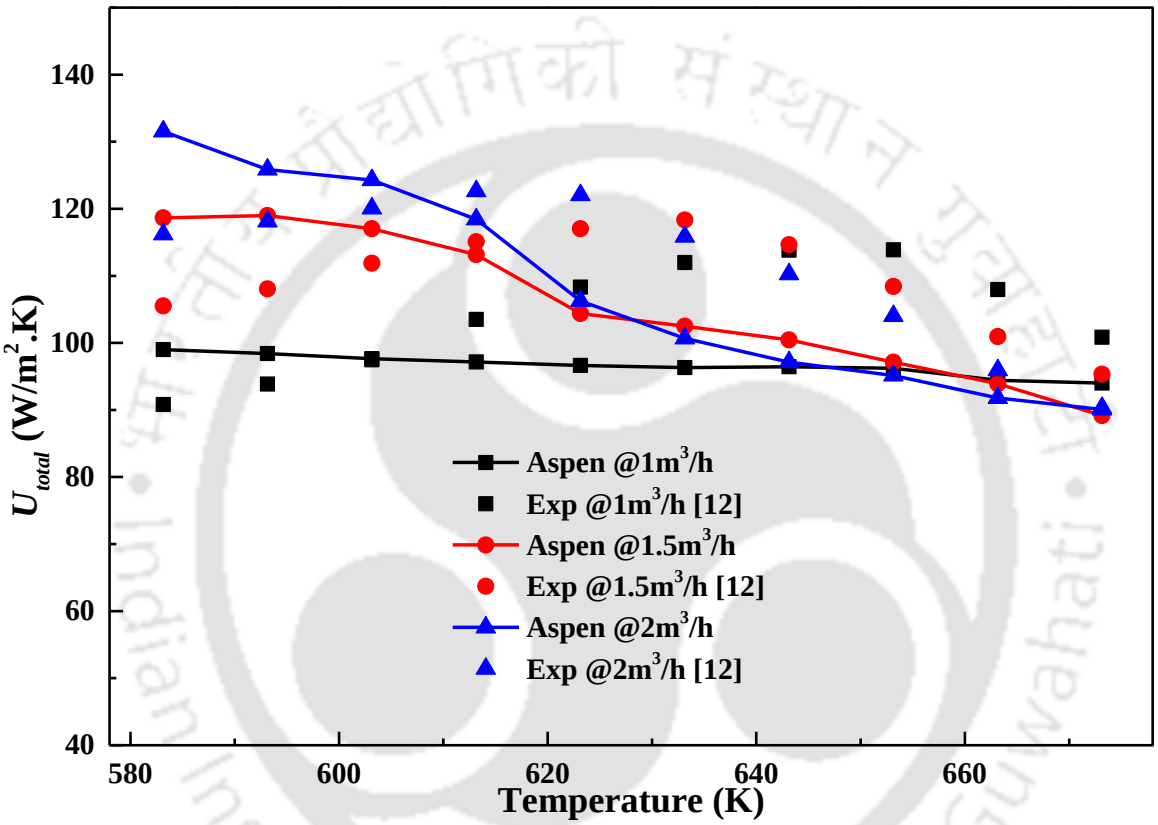

Figure 6.4: Overall heat transfer coefficient of steam generation system for molten salt with different flowrates of Molten Salt

In figure 6.5, total heat flux is shown in the temperature range of 583.15-673.15 K for the different flow rates of molten salt. Experimental values for total heat flux give a similar variation with respect to the overall heat transfer coefficient for molten salt. The simulated values are also observed to be increasing with the increase in temperature as well as flow rate of molten salt. In figure 6.4 it is found that for Aspen plus simulation values, the overall heat transfer coefficient decreases with increasing temperature, as the LMTD

increases rapidly with the temperature thereby making a marked effect in total heat transfer coefficient.

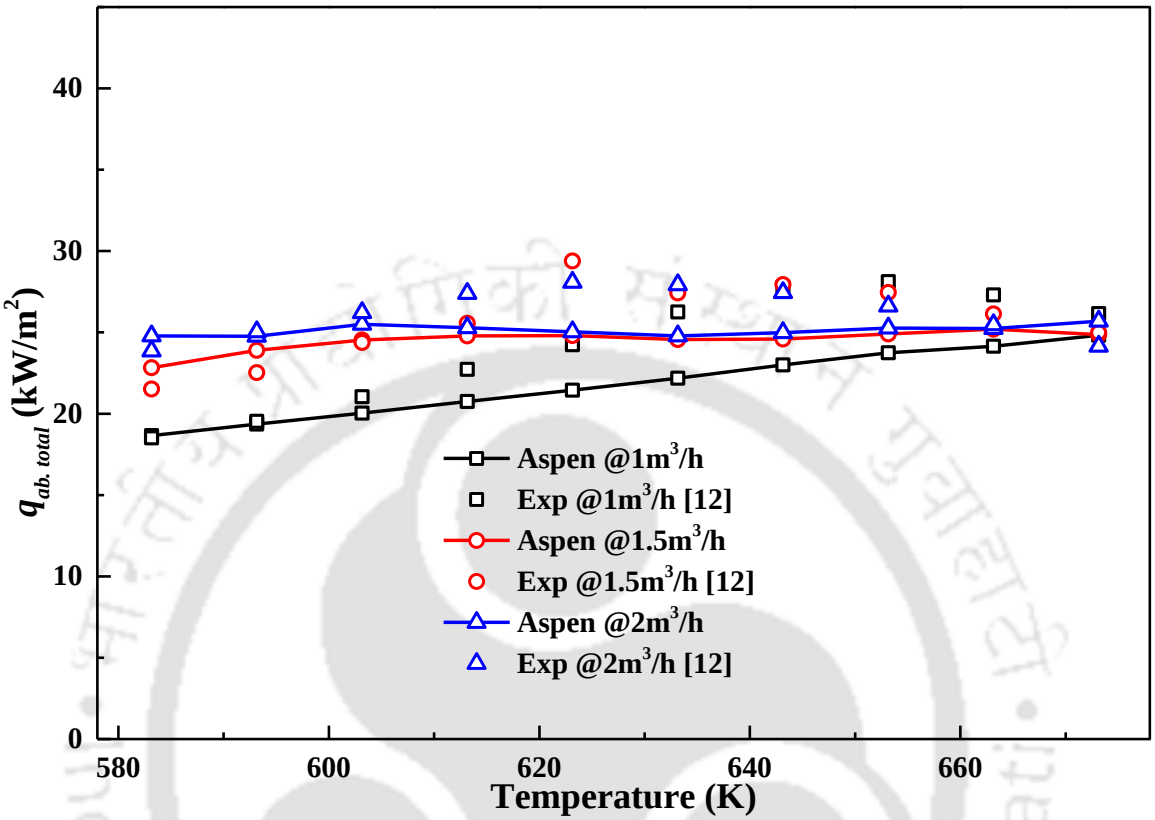

Figure 6.5: Heat flux of steam generation system for molten salt with different flowrates of Molten Salt

Now after desired benchmarking we shall move our discussion to the novel solvents that we propose namely the Deep Eutectic Solvents.

6.2 Aspen-based Simulation on DES2 System

In this simulation work, DES2 as a heat transfer fluid and has been used as *pseudocomponent* in Aspen plus simulation as discussed before. All design aspects are very similar to molten salt simulation, as discussed above.

6.2.1 Vapour and Thermal Fluid flow rate

Figure 6.6 shows an increasing pattern with temperature for vapor generation rate, using DES2 as a heat transfer medium for three different flow rates of 2, 2.5 and 3 m^3/hr

respectively. Here the water is in the tube side and DES2 is on the shell side. Thus, an increase in temperature of DES2 inlet will increase the temperature difference, which results in increased LMTD of the system. Further, an increase in the DES2 flow rate will also improve the heat transfer coefficient. This happens due to the phase change of the tube side fluid i.e., water. Eventually, the vapor generation rate also increases with the flow rate of DES2.

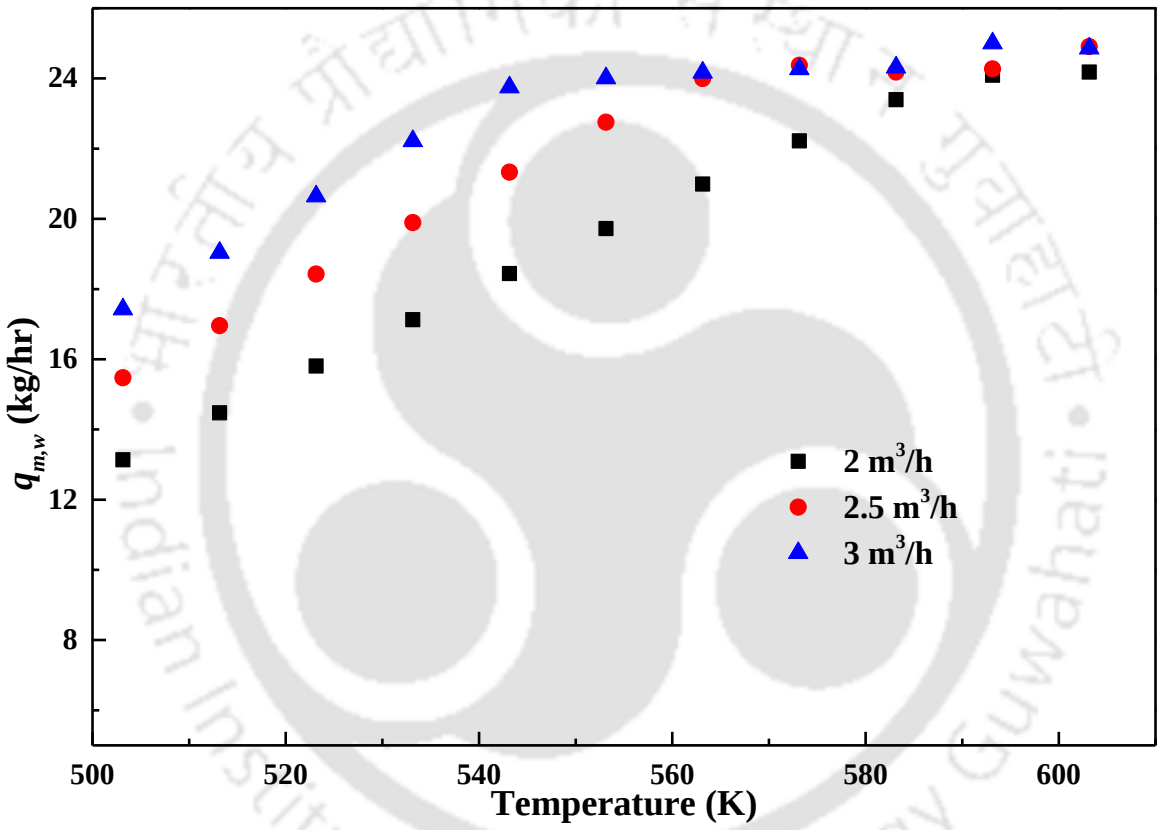

Figure 6.6: Steam generation (kg/hr) rate with DES2

6.2.2 Overall Heat Transfer Coefficient

Figure 6.7 depicts the change in the overall heat transfer rate with DES2 flow rate within the inlet temperature range 503.15-603.15 K. At lower Reynolds number, the overall heat transfer coefficient does not vary with change in flow rate. However, due to the high convective heat transfer between DES2 and water, the boiling heat transfer coefficient at

tube side is higher in magnitude and the overall heat transfer coefficient rises with both flow rate and inlet temperature of DES2.

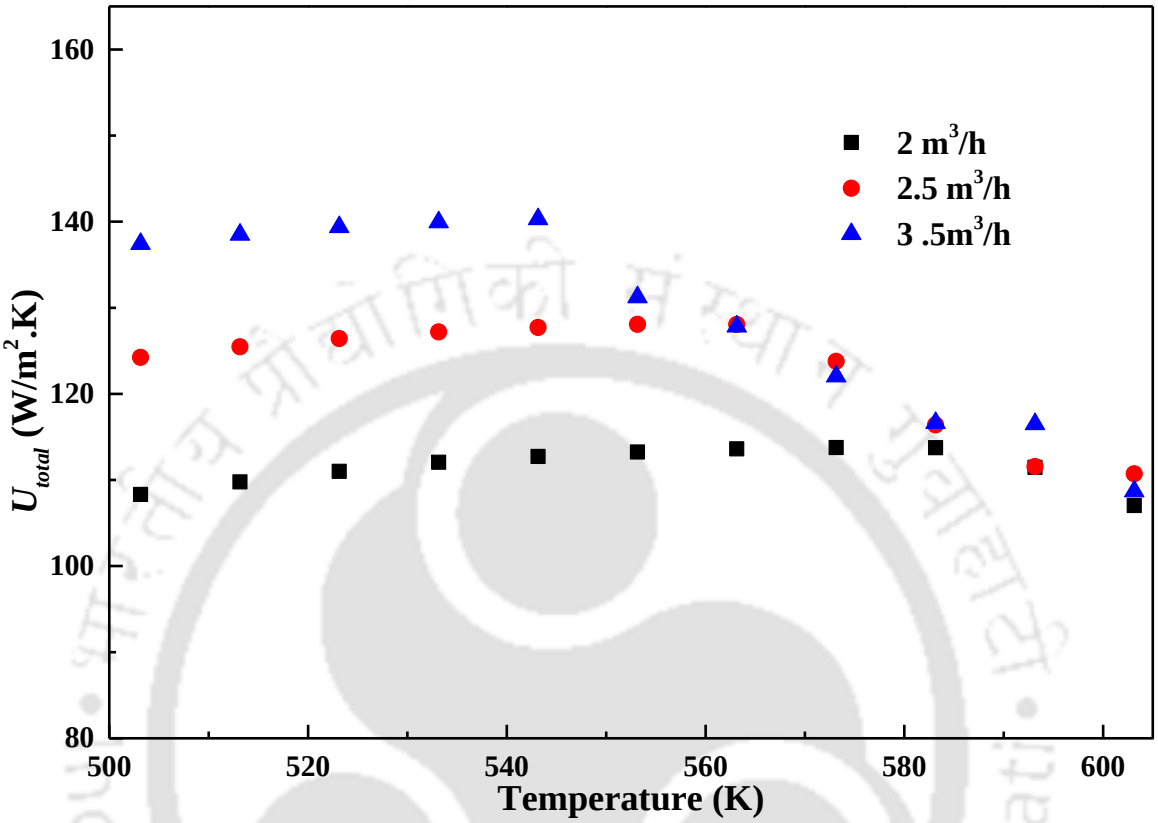

Figure 6.7: Overall heat transfer coefficient of steam generation system for DES

6.2.3 Total heat flux

Figure 6.8 shows the change in the total heat flux with DES2 flow rate and inlet temperature ranging from 503.15-603.15 K. By increasing the inlet temperature of DES2, the difference in wall temperature and the bulk temperature increases, which gives a higher LMTD. Similar enhanced behaviour of overall heat transfer coefficient is observed in both the properties including LMTD. Thus, the overall heat transfer coefficient follows an increasing total heat flux.

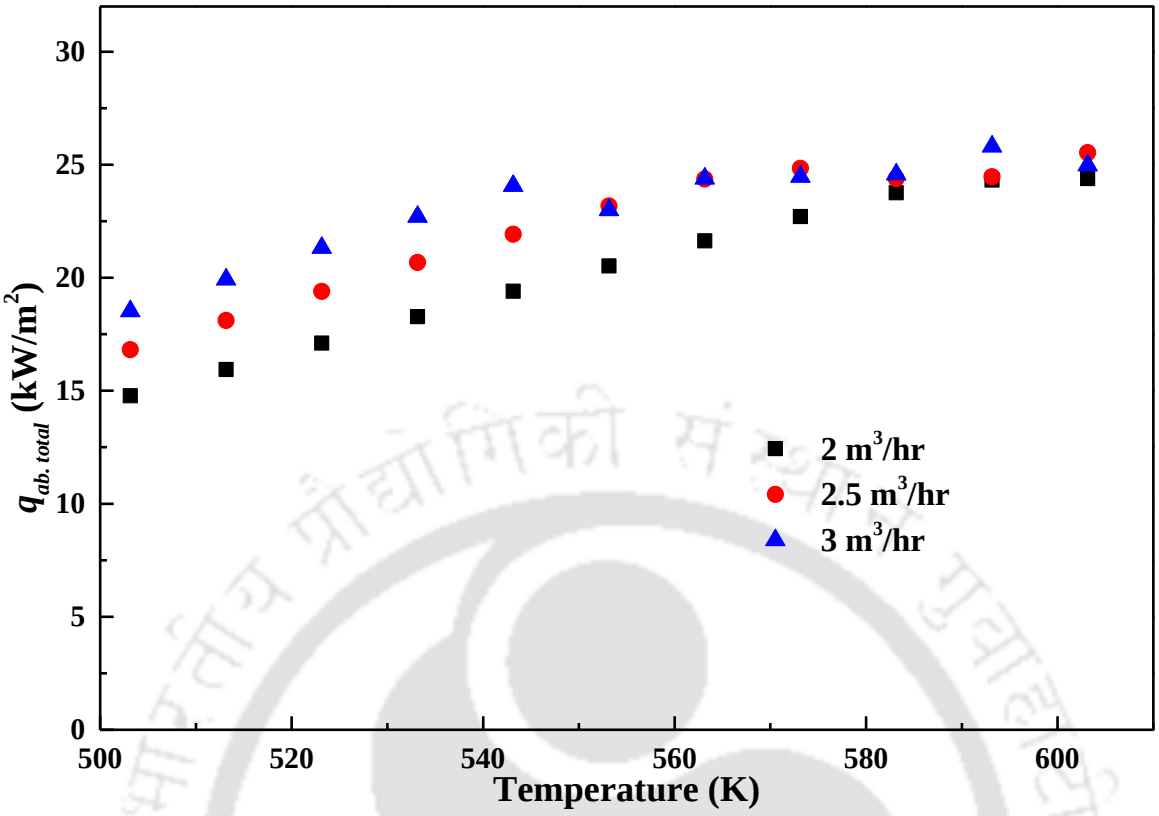

Figure 6.8: Heat flux of steam generation system for DES

6.2.4 Comparison of Total heat flux and Overall heat transfer coefficient

Figure 6.9 reports the change in the overall heat transfer coefficient and total heat flux with a DES flow rate of 2 m^3/hr within the inlet temperature range of 503.15-603.15 K. From figure 6.9, it is observed that the overall heat transfer coefficient is lower than that of total heat flux when compared with DES operating temperature. The maximum for the overall heat transfer coefficient and total heat flux were high at higher operating temperature.

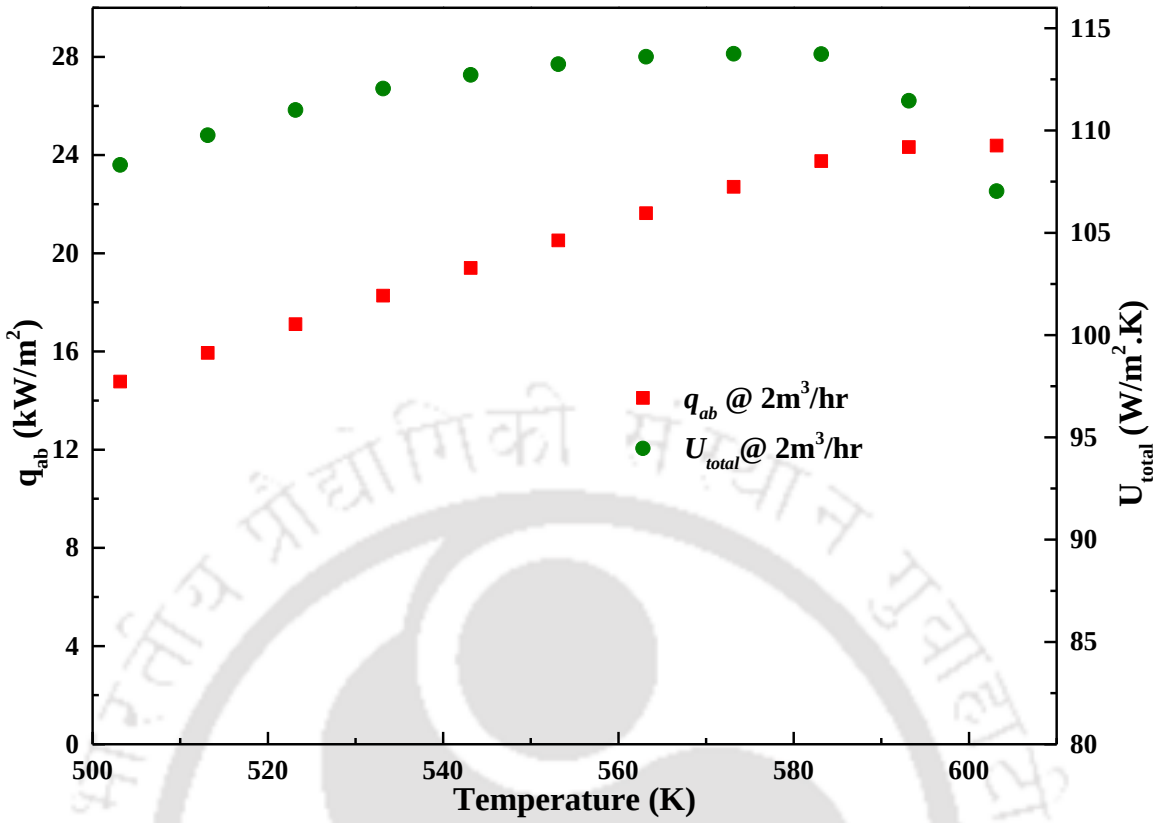

Figure 6.9: Overall heat transfer coefficient and heat flux with DES temperature

6.3 Aspen Plus Simulation with DES6

6.3.1 Effect of DES flow rate

In figure 6.10 the vapour generation rate is found to increase with both temperature and DES6 flow rate. Increasing flow rate of DES6 reduces the residence time of fluid but simultaneously increase the Reynolds number on the shell side pass. This increased Reynolds number shall increase the overall heat transfer coefficient which results in higher vapour generation rate as well as increasing temperature of DES6. It eventually increases the LMTD. With increasing DES6 flow rate as well as temperature, the gap between vapour generation rates are increasing implying that the overall heat transfer coefficient and LMTD increases with both flow rate of DES6 and temperature.

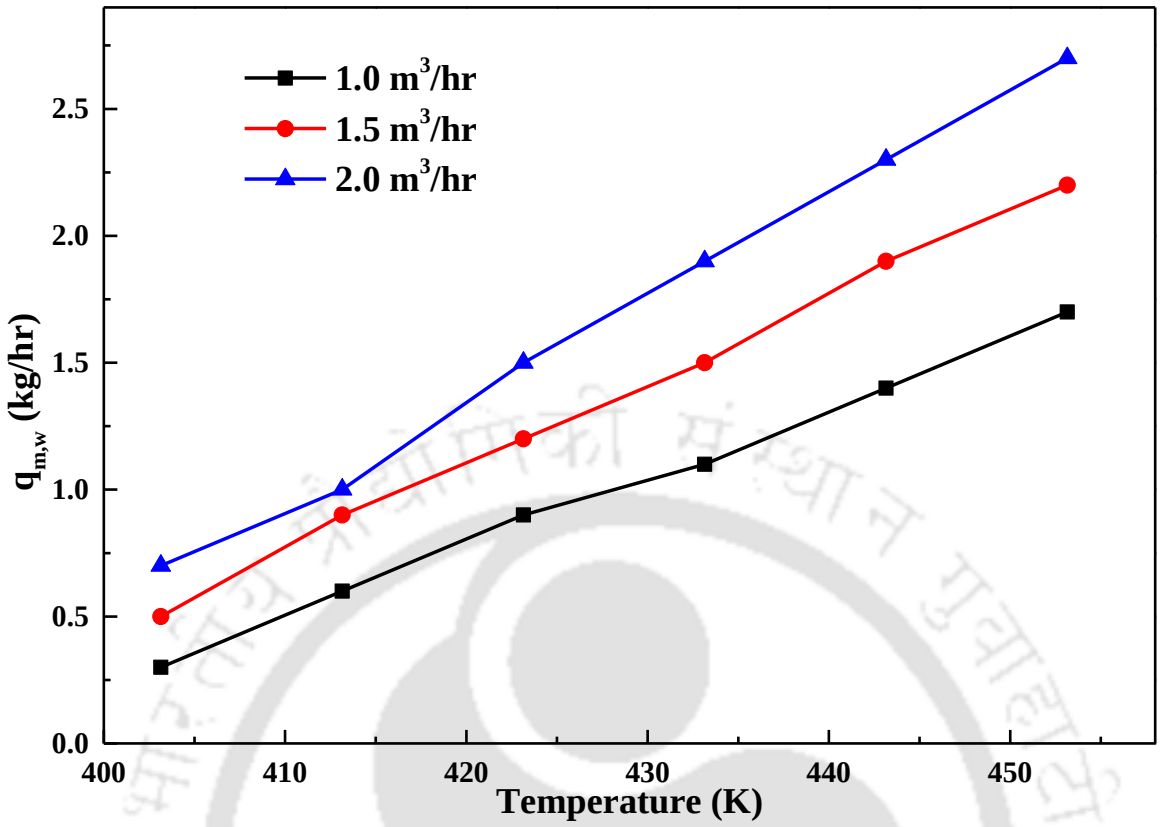

Figure 6.10: Steam generation rate with DES flow rate as a function of temperature

6.3.2 Average Heat Duty for Shell Tube and U-Shaped Heat exchanger

In this case the simulation result (figure 6.11) is plotted in the temperature range 403.15-453.15 K and 1 m^3/hr. flow rate of DES6. With rising DES6 inlet temperature, the average heat duty increases for both the Shell tube and U-shaped heat exchanger. Average heat duty slope is higher for the Shell tube heat exchanger because the primary DES6 input flowrate is given at shell tube heat exchanger with the highest temperature in the system. This causes higher LMTD, higher overall heat transfer coefficient resulting in higher heat transfer rate.

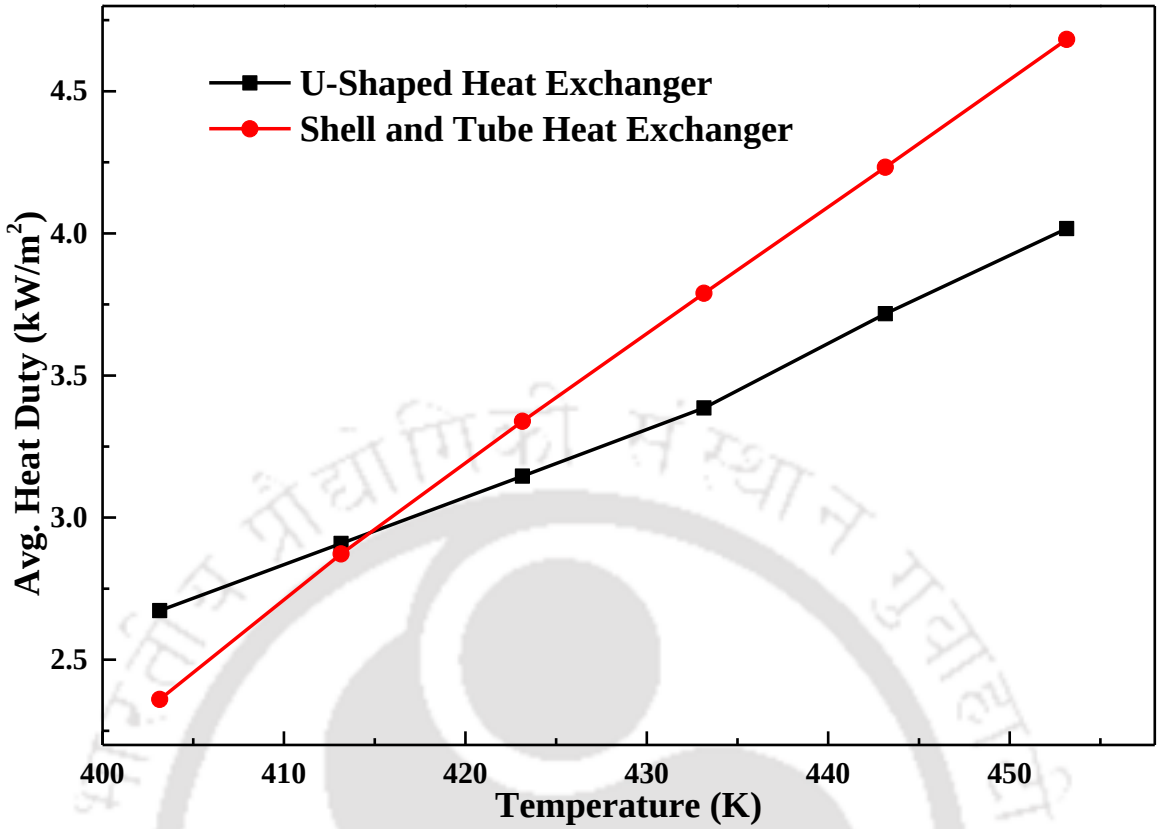

Figure 6.11: Average Heat Duty for Shell and Tube and U-Shaped Heat Exchanger as a function of temperature at flow rate of 1 m^3/hr.

6.3.3 Effect of Overall Heat Transfer Coefficient and Total Heat Duty

In Figure 6.12, the overall heat transfer coefficient is plotted in the temperature range 403.15-453.15 K for three different flow rates of DES. In general, overall heat transfer coefficient does not vary at low Reynolds number because of low interaction of particles causing lower heat transfer rate between the particles. However, the overall heat transfer coefficient tends to increase because of the high heat transfer rate between DES particles even at low Reynolds number.

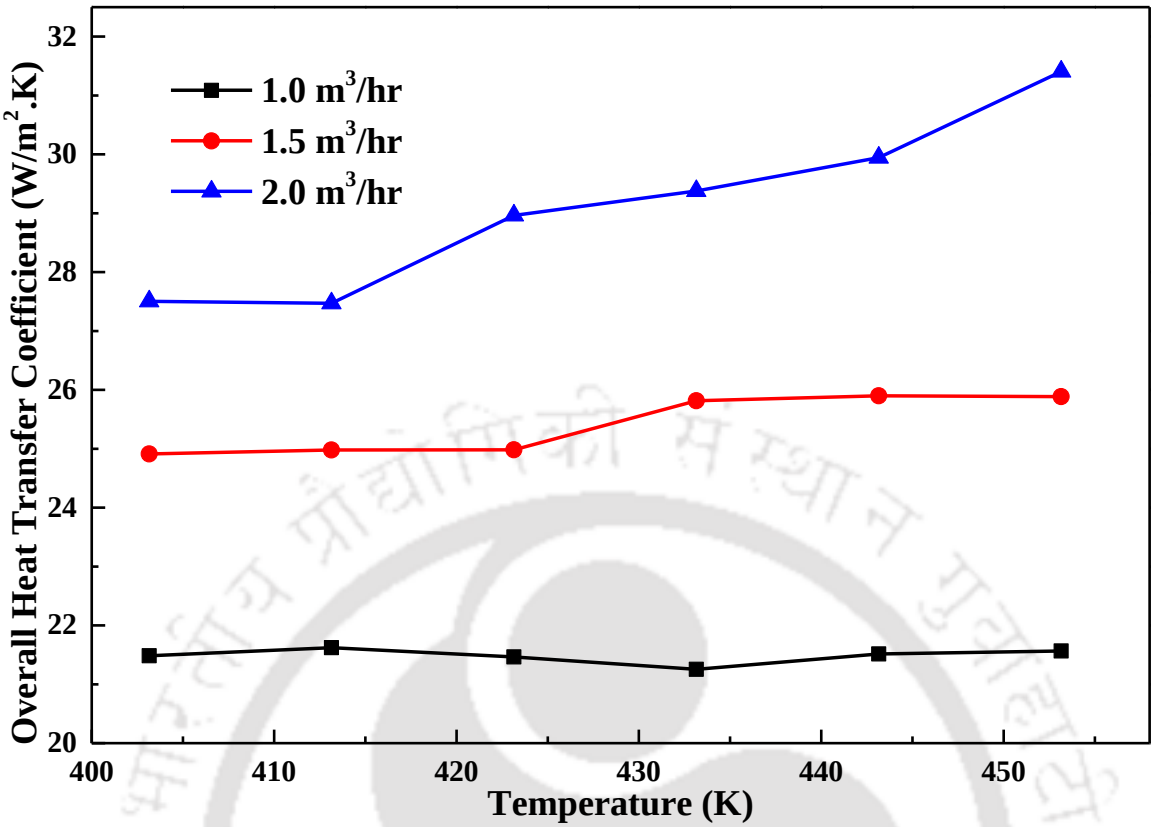

Figure 6.12: Overall Heat Transfer Coefficient of steam generation system as a function of temperature

In Figure 6.13, the total heat transfer rate is plotted in the temperature range 403.15-453.15 K for three different flow rates of DES. Total heat transfer rate is found to increase with inlet DES temperature and flow rate. Considering a single DES flow rate, the total heat transfer rate increases with an increase in the difference between wall temperature and bulk temperature. Similarly, for a particular temperature, the total heat transfer rate again increases which is due to the previous observation as in figure 6.11. The difference between total heat transfer rates is found to increase with temperature and LMTD.

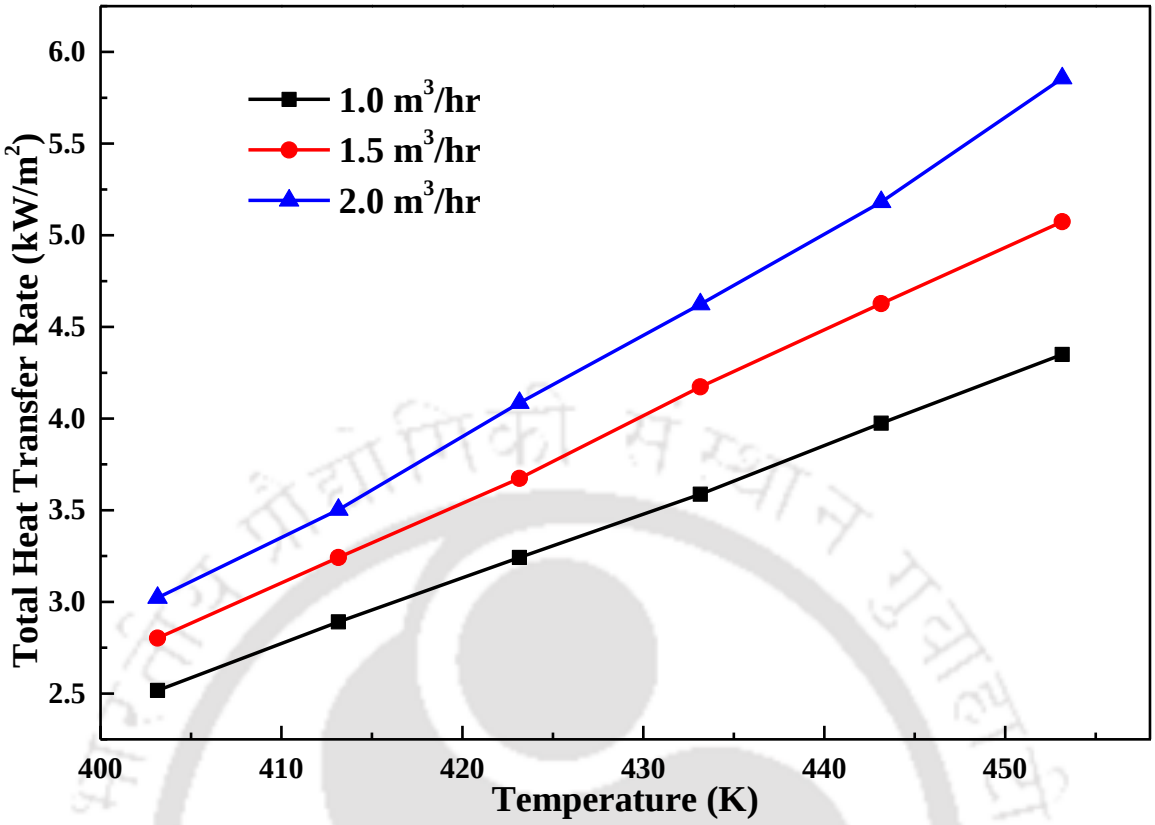

Figure 6.13: Total Heat Transfer rate of steam generation system as a function of temperature

In figure 6.14, the total heat transfer rate and overall heat transfer coefficient are plotted in the temperature range 403.15-453.15 K and 1 m^3/hr as the flow rate of DES. Overall heat transfer coefficient is almost constant for the range 403.15-453.15 K because temperature change does not make any significant effect on the heat transfer coefficient, since the total heat transfer rate is increasing with temperature. It can be concluded that total heat transfer rate increases with an inlet temperature of DES as well as flow rate of DES but overall heat transfer coefficient is constant with inlet DES temperature.

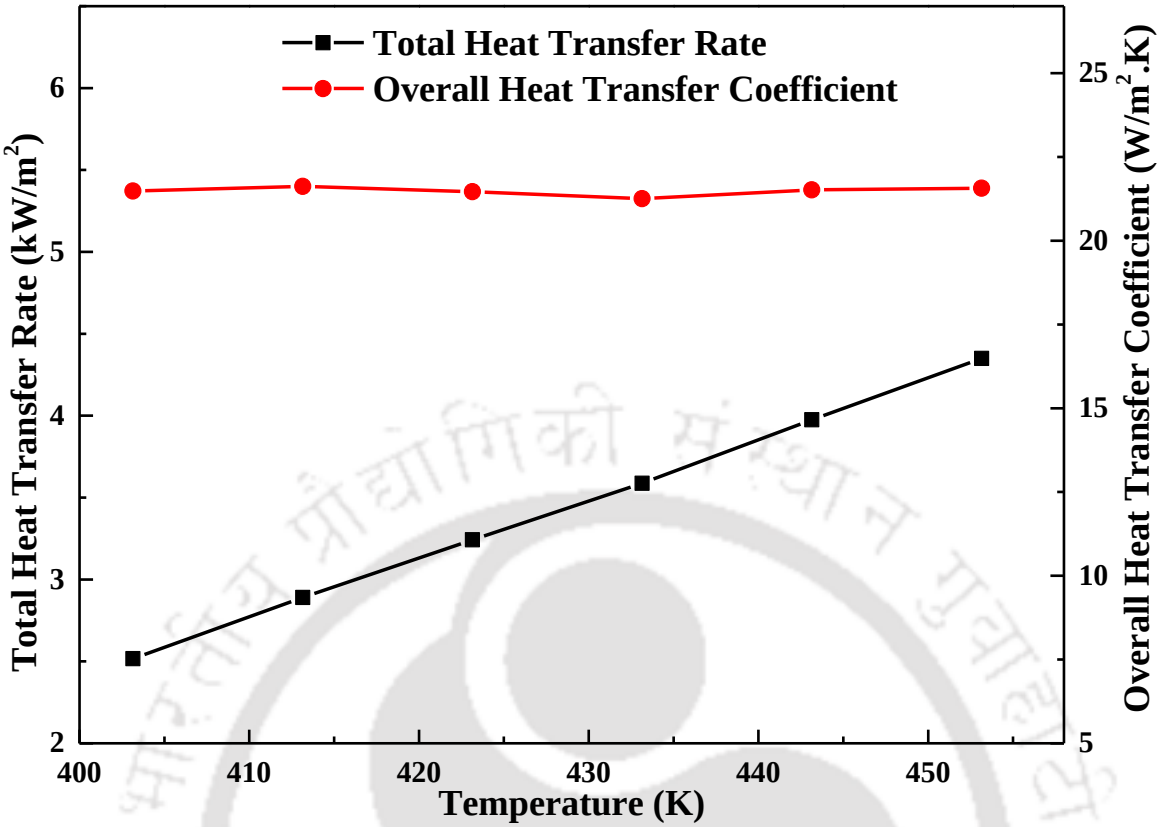

Figure 6.14: Total Heat Transfer rate and Overall Heat Transfer Coefficient within temperature range of 403.15-453.15 K

6.4 Aspen Plus Simulation with NDDES25

6.4.1 Thermodynamic Property of Steam

The amount of steam generated, and corresponding steam temperature are reported as a function of NDDES25's inlet temperature in Figure 6.15. With an increase in NDDES25's inlet temperature, the rate of steam generation gradually increases. Further, at temperature 494.15 K, steam generation is equal to the amount of water input i.e., 15 kg/h, which confirms the absence of any liquid fraction. After 494.15 K, superheated steam generation can be observed from a standard steam table.

The entropy and vapour fraction of the steam at the exit of the steam generation system are reported in Figure 6.16 as a function of HTF inlet temperature. As expected, the

vapour fraction and entropy at the exit increase gradually with the increase in the HTF inlet temperature; and after 494.15 K the vapour fraction reaches unity which indicates the complete conversion of water into steam. Further, the entropy of the superheated steam is also compared to the standard steam table and provided in Table 6.1.[137]

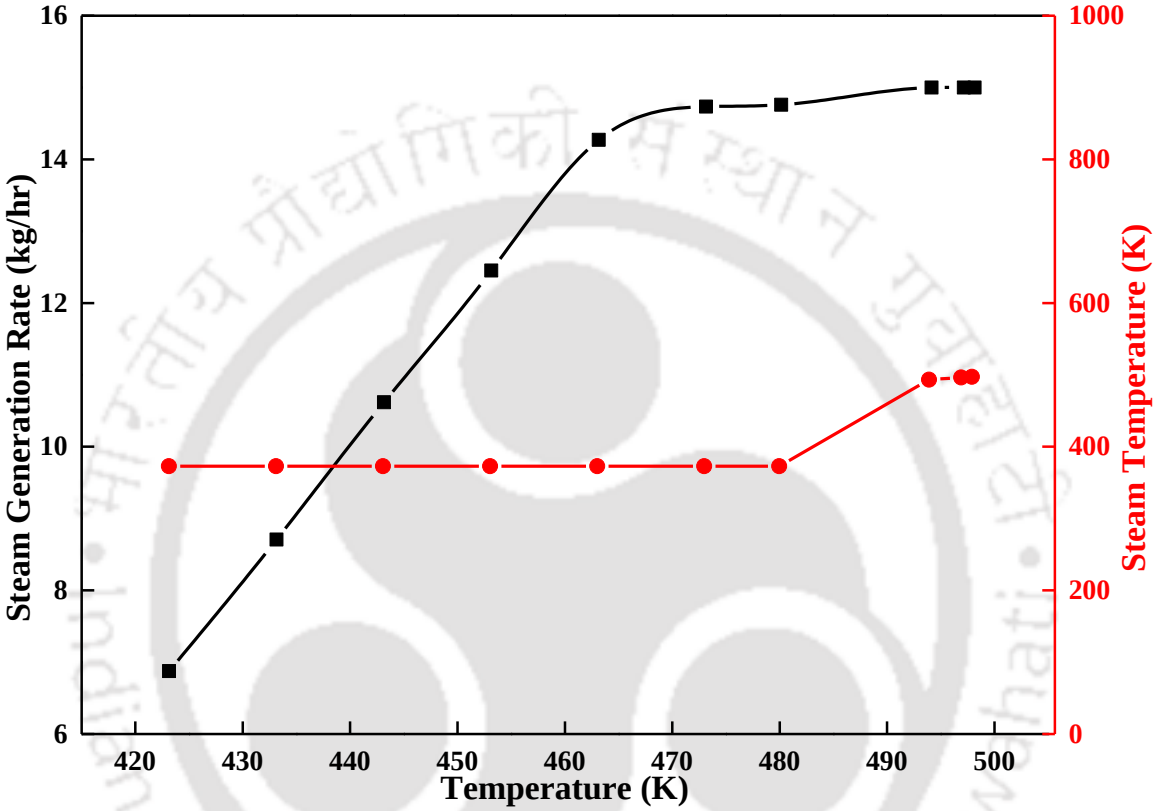

Figure 6.15: Steam generation rate and steam temperature with NDDES25

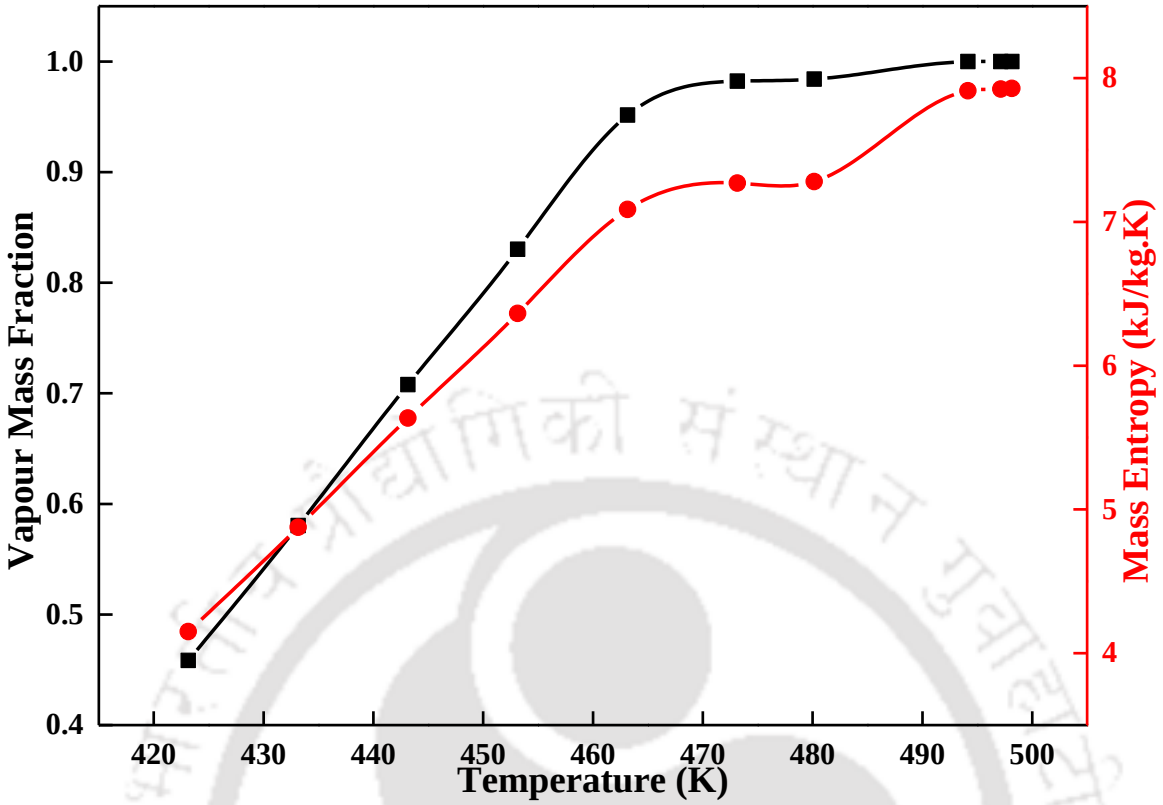

Figure 6.16: Vapour fraction and entropy of steam generation system for NDDES25

Table 6.1: Comparison of superheated steam properties with standard steam table

Simulation			Steam table		
Steam Temperature (K)	**Mass Entropy (kJ/kg.K)**	**Density (kg/m^3)**	**Steam Temperature (K)**	**Mass Entropy (kJ/kg.K)**	**Density (kg/m^3)**
494.15	7.9120	0.4376	493.15	7.9153	0.4413
497.15	7.9240	0.4349	-	-	-
498.15	7.9280	0.4340	498.15	7.9353	0.4368

6.4.2 Overall Heat Transfer Coefficient of the Heat Exchangers

Figure 6.17 presents the overall heat transfer coefficient of U-shaped and shell and tube heat exchanger at NDDES25 inlet temperature range of 423.15-498.15 K and a flow rate of 4.0 m^3/h. The overall heat transfer coefficients of both the heat exchangers increases, but in case of shell and tube heat exchanger it increases first and then decreases with the

increase in inlet temperature. This can be explained that at lower inlet temperature of NDDES25, the rise in overall heat transfer coefficient occurs due to the increase in the convective heat transfer coefficient. At higher inlet temperature of NDDES25 (after 463.15 K), the overall heat transfer coefficient of shell and tube heat exchanger decreases due to the increase in wall temperature and subsequent decrease in boiling heat transfer coefficient.

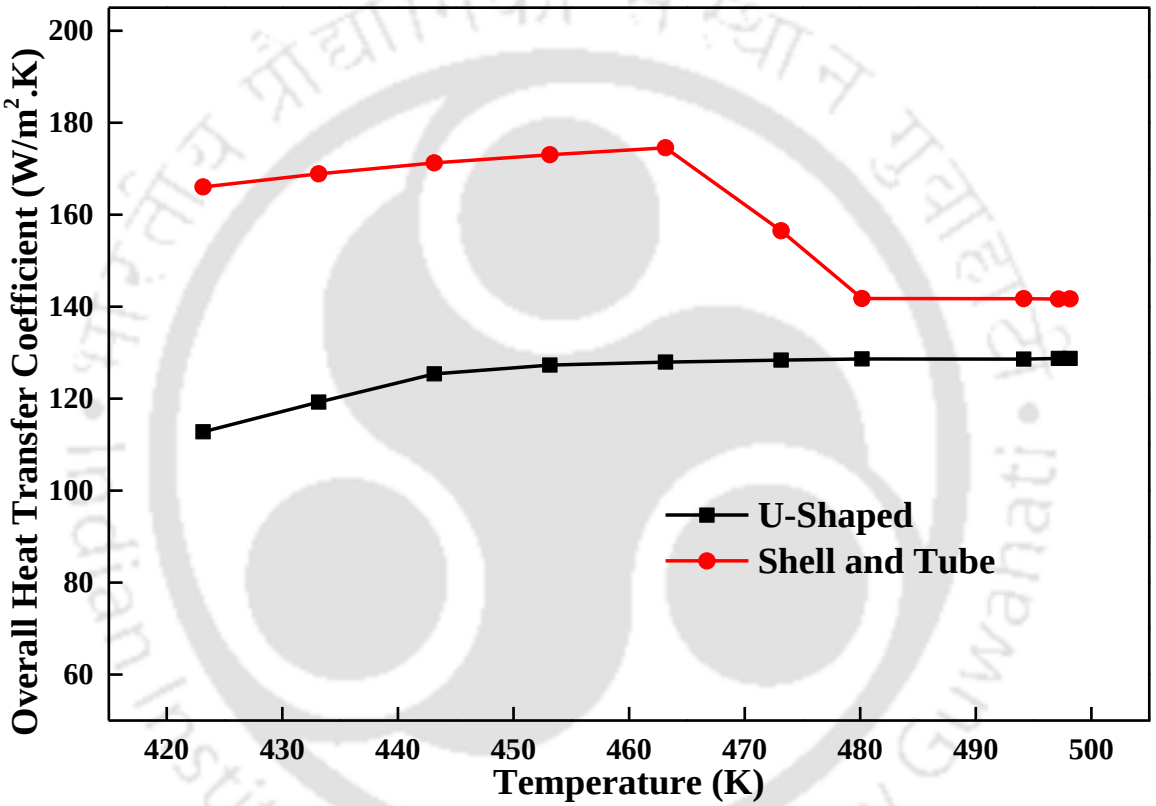

Figure 6.17: Overall heat transfer coefficient of both the heat exchangers for NDDES25

CHAPTER 7

Conclusion

A comprehensive study has been carried out to reveal the scope of DESs and NDDESs as HTF. COSMO-SAC model is used for the prediction of the eutectic composition of the novel DESs and the DESs is prepared successfully following standard preparation protocol. ^{1}H and ^{13}C NMR studies indicated the absence of chemical interactions between HBA and HBD. Further NOESY (2D) NMR studies are carried out to understand the hydrogen interaction between the HBA and HBD. TGA analysis revealed the thermal stability of the DESs. The hydrophobic nature of the DESs has been observed from the near absence of water content. Further the vapour pressure of the prepared DESs are investigated and DES3 (Diphenyl Ether : DL-menthol) has found to be lower vapour pressure compared other DESs.

The NDDESs are Prepared in order to enhance the thermophysical properties of the based fluids (DES). The stability study of the NDDESs are performed by different techniques. NDDES10 (DES2 + 0.02 wt. % Al_2O_3 spherical nanoparticles), NDDES22 (DES3 + 0.02 wt. % Al_2O_3 cylindrical nanoparticles), NDDES25 (DES3 + 0.02 wt. % *h*-BN hexagonal nanoparticles), NDDES26 (DES3 + 0.05 wt. % *h*-BN hexagonal nanoparticles), NDDES34 (DES4 + 0.02 wt. % h-BN hexagonal nanoparticles) and NDDES45 (DES5 + 0.10 wt. % *h*-BN hexagonal nanoparticles) exhibited excellent stability in terms of zeta potential values. The density of DESs and NDDESs is found to decrease with increase in temperature over the temperature range of 298.15 - 353.15K. The DES shows a Newtonian behaviour which is evident with its shear viscosity decreasing with increasing temperature. The temperature dependence takes an exponential form over the temperature range of 298.15K- 423.15K. The thermal conductivity of the DESs and

NDDESs was found to decrease with temperature and further the values are higher than other alternative solvents and commercial solvent *Therminol VP1*. The thermal conductivity of DESs are in the order of DES1<DES2<DES3<DES6<DES5<DES4. Overall the *h*-BN hexagonal nanoparticles are found to be more promising in the thermal conductivity enhancement. The specific heat capacity of the DESs and NDDESs are found to be increasing with the temperature. The specific heat capacity of DESs is in the order of DES2<DES4<DES3<DES5<DES1. In addition, similar to thermal conductivity the specific heat capacity of *h*-BN hexagonal nanoparticles based NDDESs are found to be more promising in the specific heat capacity enhancement. The observation the optimization i.e., *Mo* number concludes that NDDES25 (DES3 + 0.02 wt. % *h*-BN hexagonal nanoparticles) is the best HTF among all the nanofluids.

The thermal entrance length of the DES1 is very large due to high viscosity and low thermal conductivity. It is also observed that the convective heat transfer data correlates well with the *AnuPravaha CFD solver* in the laminar flow region. Thereafter forced convection experiments were carried out for DES2 and NDDES10 (DES2 + 0.02 wt. % Al_2O_3 spherical nanoparticles) in laminar regime. An appreciable increase in the coefficient of heat transfer was attributed to the increased thermophysical properties of DES2 based nanofluid (NDDES10) and a delay in the development of the boundary layer in the entrance areas. This behaviour indicates that measures could be taken such as creating "artificial entrance" regions along a pipeline to maximize the performance of these novel nanofluids. In the penultimate section, numerical modelling using COMSOL were also carried out to validate the heat transfer coefficient and Nusselt number. Forced convection results of DES3 and NDDES25 clearly represents a higher thermal performance for nanofluid. The

obtained heat transfer coefficient and Nu number are the highest for NDDES25 for both laminar and turbulent flow behaviours.

Simulations on nitrate-based molten salt are being performed and compared with the experimental data where a good agreement with respect to steam generation rate is observed. Further, a comparison within the same simulation has been invoked with novel solvents DES consisting of an equimolar ratio of DL-menthol and Oleic acid (DES2). The experiment is conducted at three different flow rates. The simulation process is then developed by designing a heat exchanger network using Exchanger Design and Rating (EDR). The DES is added as a new component to the Aspen Plus data bank within the *pseudocomponent* routine through continuum solvation calculations using the COSMO model. The simulations have been performed by setting the maximum operating temperature of the DES, i.e. 600.15 K, which is below their boiling point. Further, as compared to the molten salt, DES gave steam generation rate which suggests that the thermal media i.e., DES can be used as an alternative thermal fluid in Concentrated Solar Plants. The Aspen Plus simulation point out to the fact that the steam generation rate increases with both the temperature and the flow rate of DES6. The average heat transfer coefficient of the shell and tube heat exchanger is found to be higher than the U-shaped heat exchanger at a higher temperature. This eventually maximizes the steam generation rate, which implies that the DES can be used for enhancing the heat transfer coefficient in CSP plants. The usefulness of the HTF was adopted by allowing it to convert water into steam. Aspen simulation suggested 100% efficiency in steam generation using NDDES25 as the HTF.

Recommendation for Future Research

The present research was conducted on the thermal performance of the DESs and NDDESs. The experimental results illustrate that NDDESs has higher thermophysical properties compared to base DESs which makes them a potential heat transfer fluid for CSP. However, there is an extensive scope to NDDESs to evaluate the fluids in solar thermal applications. Suggestion for future research are as follows:

i. In the forced convection thermal behaviour, more specific mechanism (at the entrance length) of heat transfer enhancement of NDDES needs to be explored. The effect of nanoparticle size and shape also need to studied. Future research can be carried out to explore the effect of particle morphology on thermal performance of NDDESs and recommend specific nanoparticle size and shape for maximum enhancement.

ii. Molecular dynamic simulation can be performed in NDDESs to see the nanoparticle and ion interaction within HBA, giving insight into the mechanism of the thermophysical property enhancement.

iii. Free convection studies can also be performed.

iv. As steam generation is performed by Aspen Plus Simulation, an experimental setup can be fabricated for confirming the same. A pilot plant setup is already been started in our future work. A comprehensive cost analysis is being performed by considering it as a small capacity power plant.

Steam Generation System

References

(1) Outlook, B. P. E. *BP Energy Outlook – 2019 Insights from the Evolving Transition Scenario – India India ' s Share of Total Global Primary Energy Demand Is Set to BP Energy Outlook – 2019 Insights from the Evolving Transition Scenario – India*; 2019.

(2) Jones, S. Climate Change 2001 Synthesis Report. Edited by Robert T. Watson Cambridge University Press Cambridge, UK (2002). *Environ. Prog.* **2002**, *21* (3). https://doi.org/10.1002/ep.670210305.

(3) Arora, M.; Goel, N. K.; Singh, P. Evaluation de Tendances de Température En Inde. *Hydrol. Sci. J.* **2005**, *50* (1), 81–93. https://doi.org/10.1623/hysj.50.1.81.56330.

(4) Maradin, D.; Cerović, L.; Mjeda, T. Economic Effects of Renewable Energy Technologies. *Naše Gospod. Econ.* **2017**, *63* (2), 49–59. https://doi.org/10.1515/ngoe-2017-0012.

(5) Mickey, C. D. Chemical Principles Revisited: Solar Photovoltaic Cells. *J. Chem. Educ.* **1981**, *58* (5), 418–423. https://doi.org/10.1021/ed058p418.

(6) Goh, C. S. *Energy: Current Approach*; Elsevier Inc., 2019. https://doi.org/10.1016/B978-0-12-811749-1.00018-3.

(7) Kalogirou, S. A. *Solar Thermal Collectors and Applications*; 2004; Vol. 30. https://doi.org/10.1016/j.pecs.2004.02.001.

(8) Tian, Y.; Zhao, C. Y. A Review of Solar Collectors and Thermal Energy Storage in Solar Thermal Applications. *Appl. Energy* **2013**, *104*, 538–553. https://doi.org/10.1016/j.apenergy.2012.11.051.

(9) Norton, B. *Solar Energy Thermal Technology*; 1992. https://doi.org/10.1007/978-1-4471-1742-1.

(10) Gevorkian, P. *Alternative Energy Systems in Building Design*; McGraw-Hill Education, 2012; Vol. 23. https://doi.org/10.1007/978-0-85729-244-5_1.

(11) Santos, J. J. C. S.; Palacio, J. C. E.; Reyes, A. M. M.; Carvalho, M.; Freire, A. J. R.; Barone, M. A. Concentrating Solar Power. *Adv. Renew. Energies Power Technol.* **2018**, *1* (January 2004), 373–402. https://doi.org/10.1016/B978-0-12-812959-3.00012-5.

(12) He, C.; Lu, J.; Ding, J.; Wang, W.; Yuan, Y. Heat Transfer and Thermal Performance of Two-Stage Molten Salt Steam Generation System. *Appl. Energy* **2017**, *204*, 1231–

1239. https://doi.org/10.1016/j.apenergy.2017.04.010.

(13) França, J. M. P.; Reis, F.; Vieira, S. I. C.; Lourenço, M. J. V.; Santos, F. J. V.; Nieto De Castro, C. A.; Pádua, A. A. H. Thermophysical Properties of Ionic Liquid Dicyanamide (DCA) Nanosystems Dedicated to the Memory of the Late Professor Manuel Ribeiro Da Silva. *J. Chem. Thermodyn.* **2014**, *79*, 248–257. https://doi.org/10.1016/j.jct.2014.05.008.

(14) Ferreira, A. G. M.; Simões, P. N.; Ferreira, A. F.; Fonseca, M. A.; Oliveira, M. S. A.; Trino, A. S. M. Transport and Thermal Properties of Quaternary Phosphonium Ionic Liquids and IoNanofluids. *J. Chem. Thermodyn.* **2013**, *64*, 80–92. https://doi.org/10.1016/j.jct.2013.04.013.

(15) He, G. D.; Fang, X. M.; Xu, T.; Zhang, Z. G.; Gao, X. N. Forced Convective Heat Transfer and Flow Characteristics of Ionic Liquid as a New Heat Transfer Fluid inside Smooth and Microfin Tubes. *Int. J. Heat Mass Transf.* **2015**, *91*, 170–177. https://doi.org/10.1016/j.ijheatmasstransfer.2015.07.094.

(16) Wen, D.; Ding, Y. Experimental Investigation into Convective Heat Transfer of Nanofluids at the Entrance Region under Laminar Flow Conditions. *Int. J. Heat Mass Transf.* **2004**, *47* (24), 5181–5188. https://doi.org/10.1016/j.ijheatmasstransfer.2004.07.012.

(17) Reddy, R. G.; Zhang, Z.; Arenas, M. F.; Blake, D. M. Thermal Stability and Corrosivity Evaluations of Ionic Liquids as Thermal Energy Storage Media. *High Temp. Mater. Process.* **2003**, *22* (2), 87–94. https://doi.org/10.1515/HTMP.2003.22.2.87.

(18) Bridges, N. J.; Visser, A. E.; Fox, E. B. Potential of Nanoparticle-Enhanced Ionic Liquids (NEILs) as Advanced Heat-Transfer Fluids. *Energy & Fuels* **2011**, *25* (10), 4862–4864. https://doi.org/10.1021/ef2012084.

(19) Tay, N. H. S.; Belusko, M.; Bruno, F. Designing a PCM Storage System Using the Effectiveness-Number of Transfer Units Method in Low Energy Cooling of Buildings. *Energy Build.* **2012**, *50*, 234–242. https://doi.org/10.1016/j.enbuild.2012.03.041.

(20) Saman, W.; Bruno, F.; Halawa, E. Thermal Performance of PCM Thermal Storage Unit for a Roof Integrated Solar Heating System. *Sol. Energy* **2005**, *78* (2), 341–349. https://doi.org/10.1016/j.solener.2004.08.017.

(21) Feilchenfeld, H.; Sarig, S. Calcium Chloride Hexahydrate: A Phase-Changing Material for Energy Storage. *Ind. Eng. Chem. Prod. Res. Dev.* **1985**, *24* (1), 130–133. https://doi.org/10.1021/i300017a024.

(22) Eastman. Therminol VP-1, Technical Bulletin TF9141 https://www.eastman.com/Literature_Center/T/TF9141.pdf (accessed Dec 21, 2020).

(23) Sinha, A. A.; Shukla, A.; Prasad, R. B. A Review on CSP Technologies with Heat Transfer Fluids Used in Indian Power Plants. *Int. Conf. 21st Century Energy Needs - Mater. Syst. Appl. ICTFCEN 2016* **2017**, 1–6. https://doi.org/10.1109/ICTFCEN.2016.8052711.

(24) Kearney, D.; Herrmann, U.; Nava, P.; Kelly, B.; Mahoney, R.; Pacheco, J.; Cable, R.; Potrovitza, N.; Blake, D.; Price, H. Assessment of a Molten Salt Heat Transfer Fluid in a Parabolic Trough Solar Field. *J. Sol. Energy Eng. Trans. ASME* **2003**, *125* (2), 170–176. https://doi.org/10.1115/1.1565087.

(25) Valkenburg, M. E. Van; Vaughn, R. L.; Williams, M.; Wilkes, J. S. Thermochemistry of Ionic Liquid Heat-Transfer Fluids ☪. *Thermochim. Acta* **2005**, *425* (September 2004), 181–188. https://doi.org/10.1016/j.tca.2004.11.013.

(26) Rengstl, D.; Fischer, V.; Kunz, W. Low-Melting Mixtures Based on Choline Ionic Liquids. *Phys. Chem. Chem. Phys.* **2014**, *16* (41), 22815–22822. https://doi.org/10.1039/c4cp02860k.

(27) Singh, B. S.; Lobo, H. R.; Shankarling, G. S. Choline Chloride Based Eutectic Solvents: Magical Catalytic System for Carbon-Carbon Bond Formation in the Rapid Synthesis of β-Hydroxy Functionalized Derivatives. *Catal. Commun.* **2012**, *24*, 70–74. https://doi.org/10.1016/j.catcom.2012.03.021.

(28) Abbott, A. P.; Boothby, D.; Capper, G.; Davies, D. L.; Rasheed, R. K. Deep Eutectic Solvents Formed between Choline Chloride and Carboxylic Acids: Versatile Alternatives to Ionic Liquids. *J. Am. Chem. Soc.* **2004**, *126* (29), 9142–9147. https://doi.org/10.1021/ja048266j.

(29) Abbott, A. P.; Capper, G.; Davies, D. L.; Rasheed, R. K.; Tambyrajah, V. Novel Solvent Properties of Choline Chloride/Urea Mixtures. *Chem. Commun.* **2003**, *9* (1), 70–71. https://doi.org/10.1039/b210714g.

(30) Abbott, A. P.; Capper, G.; Davies, D. L.; McKenzie, K. J.; Obi, S. U. Solubility of

Metal Oxides in Deep Eutectic Solvents Based on Choline Chloride. *J. Chem. Eng. Data* **2006**, *51* (4), 1280–1282. https://doi.org/10.1021/je060038c.

(31) Abbott, A. P.; Capper, G.; Gray, S. Design of Improved Deep Eutectic Solvents Using Hole Theory. *ChemPhysChem* **2006**, *7* (4), 803–806. https://doi.org/10.1002/cphc.200500489.

(32) Nkuku, C. A.; LeSuer, R. J. Electrochemistry in Deep Eutectic Solvents. *J. Phys. Chem. B* **2007**, *111* (46), 13271–13277. https://doi.org/10.1021/jp075794j.

(33) Abbott, A. P.; Capper, G.; McKenzie, K. J.; Ryder, K. S. Electrodeposition of Zinc-Tin Alloys from Deep Eutectic Solvents Based on Choline Chloride. *J. Electroanal. Chem.* **2007**, *599* (2), 288–294. https://doi.org/10.1016/j.jelechem.2006.04.024.

(34) Liao, H.-G.; Jiang, Y.-X.; Zhou, Z.-Y.; Chen, S.-P.; Sun, S.-G. Shape-Controlled Synthesis of Gold Nanoparticles in Deep Eutectic Solvents for Studies of Structure-Functionality Relationships in Electrocatalysis. *Angew. Chemie* **2008**, *120* (47), 9240–9243. https://doi.org/10.1002/ange.200803202.

(35) Liao, H. G.; Jiang, Y. X.; Zhou, Z. Y.; Chen, S. P.; Sun, S. G. Shape-Controlled Synthesis of Gold Nanoparticles in Deep Eutectic Solvents for Studies of Structure-Functionality Relationships in Electrocatalysis. *Angew. Chemie - Int. Ed.* **2008**, *47* (47), 9100–9103. https://doi.org/10.1002/anie.200803202.

(36) Pollet, B. G.; Hihn, J. Y.; Mason, T. J. Sono-Electrodeposition (20 and 850 KHz) of Copper in Aqueous and Deep Eutectic Solvents. *Electrochim. Acta* **2008**, *53* (12), 4248–4256. https://doi.org/10.1016/j.electacta.2007.12.059.

(37) Liu, L.; Kong, Y.; Xu, H.; Li, J. P.; Dong, J. X.; Lin, Z. Ionothermal Synthesis of a Three-Dimensional Zinc Phosphate with DFT Topology Using Unstable Deep-Eutectic Solvent as Template-Delivery Agent. *Microporous Mesoporous Mater.* **2008**, *115* (3), 624–628. https://doi.org/10.1016/j.micromeso.2008.03.005.

(38) Gorke, J. T.; Srienc, F.; Kazlauskas, R. J. Hydrolase-Catalyzed Biotransformations in Deep Eutectic Solvents. *Chem. Commun.* **2008**, No. 10, 1235–1237. https://doi.org/10.1039/b716317g.

(39) Jhong, H. R.; Wong, D. S. H.; Wan, C. C.; Wang, Y. Y.; Wei, T. C. A Novel Deep Eutectic Solvent-Based Ionic Liquid Used as Electrolyte for Dye-Sensitized Solar Cells. *Electrochem. commun.* **2009**, *11* (1), 209–211. https://doi.org/10.1016/j.elecom.2008.11.001.

(40) Figueiredo, M.; Gomes, C.; Costa, R.; Martins, A.; Pereira, C. M.; Silva, F. Differential Capacity of a Deep Eutectic Solvent Based on Choline Chloride and Glycerol on Solid Electrodes. *Electrochim. Acta* **2009**, *54* (9), 2630–2634. https://doi.org/10.1016/j.electacta.2008.10.074.

(41) Zhang, J.; Wu, T.; Chen, S.; Feng, P.; Bu, X. Versatile Structure-Directing Roles of Deep-Eutectic Solvents and Their Implication in the Generation of Porosity and Open Metal Sites for Gas Storage. *Angew. Chemie* **2009**, *121* (19), 3538–3542. https://doi.org/10.1002/ange.200900134.

(42) Zhang, J.; Wu, T.; Chen, S.; Feng, P.; Bu, X. Versatile Structure-Directing Roles of Deep-Eutectic Solvents and Their Implication in the Generation of Porosity and Open Metal Sites for Gas Storage. *Angew. Chemie - Int. Ed.* **2009**, *48* (19), 3486–3490. https://doi.org/10.1002/anie.200900134.

(43) Morrison, H. G.; Sun, C. C.; Neervannan, S. Characterization of Thermal Behavior of Deep Eutectic Solvents and Their Potential as Drug Solubilization Vehicles. *Int. J. Pharm.* **2009**, *378* (1–2), 136–139. https://doi.org/10.1016/j.ijpharm.2009.05.039.

(44) Wang, N.; Zheng, A. Q.; Liu, X.; Chen, J. J.; Yang, T.; Chen, M. L.; Wang, J. H. Deep Eutectic Solvent-Assisted Preparation of Nitrogen/Chloride-Doped Carbon Dots for Intracellular Biological Sensing and Live Cell Imaging. *ACS Appl. Mater. Interfaces* **2018**, *10* (9), 7901–7909. https://doi.org/10.1021/acsami.8b00947.

(45) Wikene, K. O.; Rukke, H. V.; Bruzell, E.; Tønnesen, H. H. Investigation of the Antimicrobial Effect of Natural Deep Eutectic Solvents (NADES) as Solvents in Antimicrobial Photodynamic Therapy. *J. Photochem. Photobiol. B Biol.* **2017**, *171* (April), 27–33. https://doi.org/10.1016/j.jphotobiol.2017.04.030.

(46) Zdanowicz, M.; Jędrzejewski, R.; Pilawka, R. Deep Eutectic Solvents as Simultaneous Plasticizing and Crosslinking Agents for Starch. *Int. J. Biol. Macromol.* **2019**, *129*, 1040–1046. https://doi.org/10.1016/j.ijbiomac.2019.02.103.

(47) Khataei, M. M.; Yamini, Y.; Nazaripour, A.; Karimi, M. Novel Generation of Deep Eutectic Solvent as an Acceptor Phase in Three-Phase Hollow Fiber Liquid Phase Microextraction for Extraction and Preconcentration of Steroidal Hormones from Biological Fluids. *Talanta* **2018**, *178* (August 2017), 473–480. https://doi.org/10.1016/j.talanta.2017.09.068.

(48) Procentese, A.; Raganati, F.; Olivieri, G.; Russo, M. E.; Rehmann, L.; Marzocchella,

A. Low-Energy Biomass Pretreatment with Deep Eutectic Solvents for Bio-Butanol Production. *Bioresour. Technol.* **2017**, *243*, 464–473. https://doi.org/10.1016/j.biortech.2017.06.143.

(49) Boldrini, C. L.; Manfredi, N.; Perna, F. M.; Trifiletti, V.; Capriati, V.; Abbotto, A. Dye-Sensitized Solar Cells That Use an Aqueous Choline Chloride-Based Deep Eutectic Solvent as Effective Electrolyte Solution. *Energy Technol.* **2017**, *5* (2), 345–353. https://doi.org/10.1002/ente.201600420.

(50) Wang, Q.; Yao, X.; Geng, Y.; Zhou, Q.; Lu, X.; Zhang, S. Deep Eutectic Solvents as Highly Active Catalysts for the Fast and Mild Glycolysis of Poly(Ethylene Terephthalate)(PET). *Green Chem.* **2015**, *17* (4), 2473–2479. https://doi.org/10.1039/c4gc02401j.

(51) Alhassan, Y.; Kumar, N.; Bugaje, I. M. Catalytic Upgrading of Waste Tire Pyrolysis Oil via Supercritical Esterification with Deep Eutectic Solvents (Green Solvents and Catalysts). *J. Energy Inst.* **2016**, *89* (4), 683–693. https://doi.org/10.1016/j.joei.2015.05.003.

(52) Maka, H.; Spychaj, T.; Adamus, J. Lewis Acid Type Deep Eutectic Solvents as Catalysts for Epoxy Resin Crosslinking. *RSC Adv.* **2015**, *5* (101), 82813–82821. https://doi.org/10.1039/c5ra12664a.

(53) Shuwa, S. M.; Al-Hajri, R. S.; Jibril, B. Y.; Al-Waheibi, Y. M. Novel Deep Eutectic Solvent-Dissolved Molybdenum Oxide Catalyst for the Upgrading of Heavy Crude Oil. *Ind. Eng. Chem. Res.* **2015**, *54* (14), 3589–3601. https://doi.org/10.1021/ie5050082.

(54) Dindarloo Inaloo, I.; Majnooni, S. Carbon Dioxide Utilization in the Efficient Synthesis of Carbamates by Deep Eutectic Solvents (DES) as Green and Attractive Solvent/Catalyst Systems. *New J. Chem.* **2019**, *43* (28), 11275–11281. https://doi.org/10.1039/c9nj02810b.

(55) Chen, J.; Zhang, J.; Xu, H.; Ouyang, Y.; Zhan, F.; Li, Q. Fabrication of PbS Thin Films Composed of Highly (200)-Oriented Nano-/Micro-Rods in Deep Eutectic Solvent. *Phys. E Low-Dimensional Syst. Nanostructures* **2015**, *72*, 48–52. https://doi.org/10.1016/j.physe.2015.04.014.

(56) Wei, L.; Lu, B.; Sun, M.; Tian, N.; Zhou, Z.; Xu, B.; Zhao, X.; Sun, S. Overpotential-Dependent Shape Evolution of Gold Nanocrystals Grown in a Deep Eutectic

Solvent. *Nano Res.* **2016**, *9* (11), 3547–3557. https://doi.org/10.1007/s12274-016-1236-1.

(57) Zulkurnai, N. Z.; Mohammad Ali, U. F.; Ibrahim, N.; Abdul Manan, N. S. Carbon Dioxide (CO2) Adsorption by Activated Carbon Functionalized with Deep Eutectic Solvent (DES). *IOP Conf. Ser. Mater. Sci. Eng.* **2017**, *206* (1). https://doi.org/10.1088/1757-899X/206/1/012001.

(58) Fatma, T.; Banerjee, T. Wet Beneficiation Characteristics of Indian Bituminous Coal with Low Cost Choline Chloride Based Deep Eutectic Solvents. *Int. J. Coal Prep. Util.* **2019**, *00* (00), 1–15. https://doi.org/10.1080/19392699.2019.1672668.

(59) Naik, P. K.; Dehury, P.; Paul, S.; Banerjee, T. Evaluation of Deep Eutectic Solvent for the Selective Extraction of Toluene and Quinoline at T = 308.15 K and p = 1 Bar. *Fluid Phase Equilib.* **2016**, *423*, 146–155. https://doi.org/10.1016/j.fluid.2016.04.018.

(60) Saravanan, G.; Mohan, S. Structure, Composition and Corrosion Resistance Studies of Co-Cr Alloy Electrodeposited from Deep Eutectic Solvent (DES). *J. Alloys Compd.* **2012**, *522*, 162–166. https://doi.org/10.1016/j.jallcom.2012.01.140.

(61) Mahanta, U.; Choudhury, S.; Venkatesh, R. P.; Sarojiniamma, S.; Ilangovan, S. A.; Banerjee, T. Ionic-Liquid-Based Deep Eutectic Solvents as Novel Electrolytes for Supercapacitors: COSMO-SAC Predictions, Synthesis, and Characterization. *ACS Sustain. Chem. Eng.* **2020**, *8* (1), 372–381. https://doi.org/10.1021/acssuschemeng.9b05596.

(62) Kareem, M. A.; Mjalli, F. S.; Hashim, M. A.; Alnashef, I. M. Phosphonium-Based Ionic Liquids Analogues and Their Physical Properties. *J. Chem. Eng. Data* **2010**, *55* (11), 4632–4637. https://doi.org/10.1021/je100104v.

(63) Shahbaz, K.; Bagh, F. S. G.; Mjalli, F. S.; AlNashef, I. M.; Hashim, M. A. Prediction of Refractive Index and Density of Deep Eutectic Solvents Using Atomic Contributions. *Fluid Phase Equilib.* **2013**, *354*, 304–311. https://doi.org/10.1016/j.fluid.2013.06.050.

(64) Zhang, J. Y.; Huang, K. Densities and Viscosities of, and NH3 Solubilities in Deep Eutectic Solvents Composed of Ethylamine Hydrochloride and Acetamide. *J. Chem. Thermodyn.* **2019**, *139*, 105883. https://doi.org/10.1016/j.jct.2019.105883.

(65) Ijardar, S. P. Deep Eutectic Solvents Composed of Tetrabutylammonium Bromide

and PEG: Density, Speed of Sound and Viscosity as a Function of Temperature. *J. Chem. Thermodyn.* **2020**, *140*, 105897. https://doi.org/10.1016/j.jct.2019.105897.

(66) Bonĥte, P.; Dias, A. P.; Papageorgiou, N.; Kalyanasundaram, K.; Grätzel, M. Hydrophobic, Highly Conductive Ambient-Temperature Molten Salts. *Inorg. Chem.* **1996**, *35* (5), 1168–1178. https://doi.org/10.1021/ic951325x.

(67) Siongco, K. R.; Leron, R. B.; Li, M. H. Densities, Refractive Indices, and Viscosities of N,N-Diethylethanol Ammonium Chloride-Glycerol or -Ethylene Glycol Deep Eutectic Solvents and Their Aqueous Solutions. *J. Chem. Thermodyn.* **2013**, *65*, 65–72. https://doi.org/10.1016/j.jct.2013.05.041.

(68) Johnson, J. A.; Maznev, A. A.; Bulsara, M. T.; Fitzgerald, E. A.; Harman, T. C.; Calawa, S.; Vinels, C. J.; Turner, G.; Nelson, K. A. Phase-Controlled, Heterodyne Laser-Induced Transient Grating Measurements of Thermal Transport Properties in Opaque Material. *J. Appl. Phys.* **2012**, *111* (2). https://doi.org/10.1063/1.3675467.

(69) Jeong, J.; Chen, K.; Walker, E. S.; Roy, N.; He, F.; Liu, P.; Willson, C. G.; Cullinan, M.; Bank, S. R.; Wang, Y. In-Plane Thermal Conductivity Measurement with Nanosecond Grating Imaging Technique. *Nanoscale Microscale Thermophys. Eng.* **2018**, *22* (2), 83–96. https://doi.org/10.1080/15567265.2017.1416713.

(70) Mostert, R.; Van Den Berg, H. R.; Van Der Gulik, P. S. A Guarded Parallel-Plate Instrument for Measuring the Thermal Conductivity of Fluids in the Critical Region. *Rev. Sci. Instrum.* **1989**, *60* (11), 3466–3474. https://doi.org/10.1063/1.1140494.

(71) Merckx, B.; Dudoignon, P.; Garnier, J. P.; Marchand, D. Simplified Transient Hot-Wire Method for Effective Thermal Conductivity Measurement in Geo Materials: Microstructure and Saturation Effect. *Adv. Civ. Eng.* **2012**, *2012* (1). https://doi.org/10.1155/2012/625395.

(72) Gautam, R. K.; Seth, D. Thermal Conductivity of Deep Eutectic Solvents. *J. Therm. Anal. Calorim.* **2019**, No. November. https://doi.org/10.1007/s10973-019-09000-2.

(73) Yan, Y. C.; Rashmi, W.; Khalid, M.; Shahbaz, K.; Gupta, T. C. S. M.; Mase, N. Potential Application of Deep Eutectic Solvents in Heat Transfer Application. *J. Eng. Sci. Technol.* **2017**, *12* (Special Issue 2), 1–14.

(74) Naser, J.; Mjalli, F. S.; Gano, Z. S. Molar Heat Capacity of Selected Type III Deep Eutectic Solvents. *J. Chem. Eng. Data* **2016**, *61* (4), 1608–1615. https://doi.org/10.1021/acs.jced.5b00989.

(75) Leron, R. B.; Li, M. H. Molar Heat Capacities of Choline Chloride-Based Deep Eutectic Solvents and Their Binary Mixtures with Water. *Thermochim. Acta* **2012**, *530*, 52–57. https://doi.org/10.1016/j.tca.2011.11.036.

(76) Siongco, K. R.; Leron, R. B.; Caparanga, A. R.; Li, M. H. Molar Heat Capacities and Electrical Conductivities of Two Ammonium-Based Deep Eutectic Solvents and Their Aqueous Solutions. *Thermochim. Acta* **2013**, *566*, 50–56. https://doi.org/10.1016/j.tca.2013.05.023.

(77) Zhang, K.; Li, H.; Ren, S.; Wu, W.; Bao, Y. Specific Heat Capacities of Two Functional Ionic Liquids and Two Functional Deep Eutectic Solvents for the Absorption of SO2. *J. Chem. Eng. Data* **2017**, *62* (9), 2708–2712. https://doi.org/10.1021/acs.jced.7b00102.

(78) Fang, Y. K.; Osama, M.; Rashmi, W.; Shahbaz, K.; Khalid, M.; Mjalli, F. S.; Farid, M. M. Synthesis and Thermo-Physical Properties of Deep Eutectic Solvent-Based Graphene Nanofluids. *Nanotechnology* **2016**, *27* (7). https://doi.org/10.1088/0957-4484/27/7/075702.

(79) Choi, S. U. S. Enhancing Thermal Conductivity of Fluids with Nanoparticles. *Am. Soc. Mech. Eng. Fluids Eng. Div. FED* **1995**, *231*, 99–105.

(80) Lee, J. H.; Hwang, K. S.; Jang, S. P.; Lee, B. H.; Kim, J. H.; Choi, S. U. S.; Choi, C. J. Effective Viscosities and Thermal Conductivities of Aqueous Nanofluids Containing Low Volume Concentrations of Al2O3 Nanoparticles. *Int. J. Heat Mass Transf.* **2008**, *51* (11–12), 2651–2656. https://doi.org/10.1016/j.ijheatmasstransfer.2007.10.026.

(81) Wei, X.; Wang, L. Synthesis and Thermal Conductivity of Microfluidic Copper Nanofluids. *Particuology* **2010**, *8* (3), 262–271. https://doi.org/10.1016/j.partic.2010.03.001.

(82) Murshed, S. M. S.; Leong, K. C.; Yang, C. Enhanced Thermal Conductivity of TiO2 - Water Based Nanofluids. *Int. J. Therm. Sci.* **2005**, *44* (4), 367–373. https://doi.org/10.1016/j.ijthermalsci.2004.12.005.

(83) Mazumder, A.; Davis, J.; Rangari, V.; Curry, M. Synthesis, Characterization, and Applications of Dendrimer-Encapsulated Zero-Valent Ni Nanoparticles as Antimicrobial Agents. *ISRN Nanomater.* **2013**, *2013*, 1–9. https://doi.org/10.1155/2013/843709.

(84) Maxwell, J. C. A Treatise on Electricity and Magnetism. *Nature* **1873**, *7* (182), 1873.

(85) Hamilton, R. L. Thermal Conductivity of Heterogeneous Two-Component Systems. *Ind. Eng. Chem. Fundam.* **1962**, *1* (3), 187–191. https://doi.org/10.1021/i160003a005.

(86) Bruggeman, D. A. G. Berechnung Verschiedener Physikalischer Konstanten von Heterogenen Substanzen. III. Die Elastischen Konstanten Der Quasiisotropen Mischkörper Aus Isotropen Substanzen. *Ann. Phys.* **1937**, *421* (2), 160–178. https://doi.org/10.1002/andp.19374210205.

(87) Avenue, T. Geometric Amplitude Factors in Adiabatic Quantum Transitions. *Proc. R. Soc. London. Ser. A Math. Phys. Sci.* **1990**, *430* (1879), 405–411. https://doi.org/10.1098/rspa.1990.0096.

(88) Bonnecaze, R. T.; Brady, J. F. The Effective Conductivity of Random Suspensions of Spherical Particles. *Proc. R. Soc. London. Ser. A Math. Phys. Sci.* **1991**, *432* (1886), 445–465. https://doi.org/10.1098/rspa.1991.0025.

(89) Gaganpreet; Srivastava, S. Effect of Aggregation on Thermal Conductivity and Viscosity of Nanofluids. *Appl. Nanosci.* **2012**, *2* (3), 325–331. https://doi.org/10.1007/s13204-012-0082-z.

(90) Leong, K. C.; Yang, C.; Murshed, S. M. S. A Model for the Thermal Conductivity of Nanofluids - The Effect of Interfacial Layer. *J. Nanoparticle Res.* **2006**, *8* (2), 245–254. https://doi.org/10.1007/s11051-005-9018-9.

(91) Chen, H.; Ding, Y.; He, Y.; Tan, C. Rheological Behaviour of Ethylene Glycol Based Titania Nanofluids. *Chem. Phys. Lett.* **2007**, *444* (4–6), 333–337. https://doi.org/10.1016/j.cplett.2007.07.046.

(92) Putra, N.; Roetzel, W.; Das, S. K. Natural Convection of Nano-Fluids. *Heat Mass Transf. und Stoffuebertragung* **2003**, *39* (8–9), 775–784. https://doi.org/10.1007/s00231-002-0382-z.

(93) Wen, D.; Ding, Y. Formulation of Nanofluids for Natural Convective Heat Transfer Applications. *Int. J. Heat Fluid Flow* **2005**, *26* (6), 855–864. https://doi.org/10.1016/j.ijheatfluidflow.2005.10.005.

(94) Zeinali Heris, S.; Nasr Esfahany, M.; Etemad, S. G. Experimental Investigation of Convective Heat Transfer of Al2O3/Water Nanofluid in Circular Tube. *Int. J. Heat Fluid Flow* **2007**, *28* (2), 203–210.

https://doi.org/10.1016/j.ijheatfluidflow.2006.05.001.

(95) Bridges, N. J.; Visser, A. E.; Fox, E. B. Potential of Nanoparticle-Enhanced Ionic Liquids (NEILs) as Advanced Heat-Transfer Fluids. *Energy and Fuels* **2011**, *25* (10), 4862–4864. https://doi.org/10.1021/ef2012084.

(96) Bharti, A.; Kundu, D.; Rabari, D.; Banerjee, T. *Phase Equilibria in Ionic Liquid Facilitated Liquid–Liquid Extractions*; 2017. https://doi.org/10.1201/9781315367163.

(97) Frisch, M. J.; Trucks, G. W.; Schlegel, H. B.; Scuseria, G. E.; Robb, M. A.; Cheeseman, J. R.; Scalmani, G.; Barone, V.; Mennucci, B.; Petersson, G. A.; et al. *Gaussian 09, Revision C. 01*; 2010.

(98) Delso, I.; Lafuente, C.; Muñoz-Embid, J.; Artal, M. NMR Study of Choline Chloride-Based Deep Eutectic Solvents. *J. Mol. Liq.* **2019**, *290*. https://doi.org/10.1016/j.molliq.2019.111236.

(99) Hildal, K.; Perepezko, J. H. Chapter 19 - Metals and Alloys. In *Recent Advances, Techniques and Applications*; Vyazovkin, S., Koga, N., Schick, C. B. T.-H. of T. A. and C., Eds.; Elsevier Science B.V., 2018; Vol. 6, pp 781–828. https://doi.org/https://doi.org/10.1016/B978-0-444-64062-8.00017-6.

(100) van der Merwe, E. M.; Strydom, C. A. Quantitative Thermogravimetric Analysis of Binary Mixtures. *J. Therm. Anal. Calorim.* **2004**, *76* (1), 149–156. https://doi.org/10.1023/b:jtan.0000027814.93703.0c.

(101) Scholz, E. *Karl Fischer Titration Determination of Water Chemical Laboratory Practice*, 1st ed.; 1984. https://doi.org/10.1007/978-3-642-69989-4.

(102) Ronkart, S. N.; Paquot, M.; Fougnies, C.; Deroanne, C.; Van Herck, J. C.; Blecker, C. Determination of Total Water Content in Inulin Using the Volumetric Karl Fischer Titration. *Talanta* **2006**, *70* (5), 1006–1010. https://doi.org/10.1016/j.talanta.2006.02.024.

(103) Papai, R.; Romano, M. A.; Arroyo, A. R.; Rodrigues Da Silva, B.; Tresoldi, B.; Winter, G. C.; Costa, J. M.; Freitas Santos, M. A.; Prata, M. D.; Gaubeur, I. Creating and Experimenting with a Low-Cost, Rugged System to Visually Demonstrate the Vapor Pressure of Liquids as a Function of Temperature. *J. Chem. Educ.* **2019**, *96* (2), 335–341. https://doi.org/10.1021/acs.jchemed.8b00381.

(104) Koubek, E.; Paulson, D. R. A Simple Apparatus Designed to Maasure Vapor

Pressures and Demonstrate the Principles of Raoult's Law. *J. Chem. Educ.* **1983**, *60* (12), 1069. https://doi.org/10.1021/ed060p1069.1.

(105) States, U. *Standard Test Method for Vapor Pressure of Liquids by Ebulliometry 1*; 2010; Vol. 12. https://doi.org/10.1520/E1719-05.2.

(106) Shrivastava, A. 2 - Polymerization. In *Plastics Design Library*; Shrivastava, A. B. T.-I. to P. E., Ed.; William Andrew Publishing, 2018; pp 17–48. https://doi.org/https://doi.org/10.1016/B978-0-323-39500-7.00002-2.

(107) Mirza, N. R.; Nicholas, N. J.; Wu, Y.; Kentish, S.; Stevens, G. W. Estimation of Normal Boiling Temperatures, Critical Properties, and Acentric Factors of Deep Eutectic Solvents. *J. Chem. Eng. Data* **2015**, *60* (6), 1844–1854. https://doi.org/10.1021/acs.jced.5b00046.

(108) Joback, K. G.; Reid, R. C. Estimation of Pure-Component Properties from Group-Contributions. *Chem. Eng. Commun.* **1987**, *57* (1–6), 233–243. https://doi.org/10.1080/00986448708960487.

(109) Li, X.; Zhu, D.; Wang, X. Evaluation on Dispersion Behavior of the Aqueous Copper Nano-Suspensions. *J. Colloid Interface Sci.* **2007**, *310* (2), 456–463. https://doi.org/10.1016/j.jcis.2007.02.067.

(110) Ilyas, S. U.; Pendyala, R.; Marneni, N. Preparation, Sedimentation, and Agglomeration of Nanofluids. *Chem. Eng. Technol.* **2014**, *37* (12), 2011–2021. https://doi.org/10.1002/ceat.201400268.

(111) Singh, A. K.; Raykar, V. S. Microwave Synthesis of Silver Nanofluids with Polyvinylpyrrolidone (PVP) and Their Transport Properties. *Colloid Polym. Sci.* **2008**, *286* (14–15), 1667–1673. https://doi.org/10.1007/s00396-008-1932-9.

(112) Vadasz, P. Heat Conduction in Nanofluid Suspensions. *J. Heat Transfer* **2006**, *128* (5), 465–477. https://doi.org/10.1115/1.2175149.

(113) Lee, D.; Kim, J. W.; Kim, B. G. A New Parameter to Control Heat Transport in Nanofluids: Surface Charge State of the Particle in Suspension. *J. Phys. Chem. B* **2006**, *110* (9), 4323–4328. https://doi.org/10.1021/jp057225m.

(114) Vandsburger, L. Synthesis and Covalent Surface Modification of Carbon Nanotubes for Preparation of Stabilized Nanofluid Suspensions, McGill University, 2009.

(115) Anushree, C.; Philip, J. Assessment of Long Term Stability of Aqueous Nanofluids Using Different Experimental Techniques. *J. Mol. Liq.* **2016**, *222*, 350–358.

https://doi.org/10.1016/j.molliq.2016.07.051.

(116) Umar, S.; Sulaiman, F.; Abdullah, N.; Mohamad, S. N. Investigation of the Effect of PH Adjustment on the Stability of Nanofluid. *AIP Conf. Proc.* **2018**, *2031* (November). https://doi.org/10.1063/1.5066987.

(117) Liu, M. S.; Lin, M. C. C.; Tsai, C. Y.; Wang, C. C. Enhancement of Thermal Conductivity with Cu for Nanofluids Using Chemical Reduction Method. *Int. J. Heat Mass Transf.* **2006**, *49* (17–18), 3028–3033. https://doi.org/10.1016/j.ijheatmasstransfer.2006.02.012.

(118) Atkins Peter, P. J. de. *ATKINS' PHYSICAL CHEMISTRY*, 8th ed.; Oxford University Press, 2006.

(119) Mouromtseff, I. E. Water and Forced-Air Cooling of Vacuum Tubes Nonelectronic Problems in Electronic Tubes. *Proc. IRE* **1942**, *30* (4), 190–205. https://doi.org/10.1109/JRPROC.1942.234654.

(120) Dalal, A.; Eswaran, V.; Biswas, G. A Finite-Volume Method for Navier-Stokes Equations on Unstructured Meshes. *Numer. Heat Transf. Part B Fundam.* **2008**, *54* (3), 238–259. https://doi.org/10.1080/10407790802182653.

(121) Manik, J.; Parmanand, M.; Kotoky, S.; Borgohain, P.; Dalal, A.; Natarajan, G. Lessons from AnuPravaha: Towards a General Purpose Computational Framework on Hybrid Unstructured Meshes for Multi-Physics Applications. In *Proceedings of CHT-17 ICHMT International Symposium on Advances in Computational Heat Transfer*; 2017; pp 1189–1202.

(122) Rhie, C. M.; Chow, W. L. Numerical Study of the Turbulent Flow Past an Airfoil with Trailing Edge Separation. *AIAA J.* **1983**, *21* (11), 1525–1532. https://doi.org/10.2514/3.8284.

(123) Larriba, M.; de Riva, J.; Navarro, P.; Moreno, D.; Delgado-Mellado, N.; García, J.; Ferro, V. R.; Rodríguez, F.; Palomar, J. COSMO-Based/Aspen Plus Process Simulation of the Aromatic Extraction from Pyrolysis Gasoline Using the {[4empy][NTf2] + [Emim][DCA]} Ionic Liquid Mixture. *Sep. Purif. Technol.* **2018**, *190* (August 2017), 211–227. https://doi.org/10.1016/j.seppur.2017.08.062.

(124) de Riva, J.; Suarez-Reyes, J.; Moreno, D.; Díaz, I.; Ferro, V.; Palomar, J. Ionic Liquids for Post-Combustion CO2 Capture by Physical Absorption: Thermodynamic, Kinetic and Process Analysis. *Int. J. Greenh. Gas Control* **2017**,

61, 61–70. https://doi.org/10.1016/j.ijggc.2017.03.019.

(125) Wasserscheid, P.; Welton, T. *Ionic Liquids in Synthesis*; John Wiley & Sons, 2008.

(126) Jansma, A.; Zhang, Q.; Li, B.; Ding, Q.; Uno, T.; Bursulaya, B.; Liu, Y.; Furet, P.; Gray, N. S.; Geierstanger, B. H. Verification of a Designed Intramolecular Hydrogen Bond in a Drug Scaffold by Nuclear Magnetic Resonance Spectroscopy. *J. Med. Chem.* **2007**, *50* (24), 5875–5877. https://doi.org/10.1021/jm700983a.

(127) Chen, H.; He, Y.; Zhu, J.; Alias, H.; Ding, Y.; Nancarrow, P.; Hardacre, C.; Rooney, D.; Tan, C. Rheological and Heat Transfer Behaviour of the Ionic Liquid, [C4mim][NTf2]. *Int. J. Heat Fluid Flow* **2008**, *29* (1), 149–155. https://doi.org/10.1016/j.ijheatfluidflow.2007.05.002.

(128) Paul, T. C.; Morshed, A. K. M. M.; Fox, E. B.; Visser, A. E.; Bridges, N. J.; Khan, J. A. Thermal Performance of Ionic Liquids for Solar Thermal Applications. *Exp. Therm. Fluid Sci.* **2014**, *59*, 88–95. https://doi.org/10.1016/j.expthermflusci.2014.08.002.

(129) Liu, H.; Maginn, E.; Visser, A. E.; Bridges, N. J.; Fox, E. B. Thermal and Transport Properties of Six Ionic Liquids: An Experimental and Molecular Dynamics Study. *Ind. Eng. Chem. Res.* **2012**, *51* (21), 7242–7254. https://doi.org/10.1021/ie300222a.

(130) Li, W. G. Effects of Viscosity of Fluids on Centrifugal Pump Performance and Flow Pattern in the Impeller. *Int. J. Heat Fluid Flow* **2000**, *21* (2), 207–212. https://doi.org/10.1016/S0142-727X(99)00078-8.

(131) Chen, Z.; Ludwig, M.; Warr, G. G.; Atkin, R. Effect of Cation Alkyl Chain Length on Surface Forces and Physical Properties in Deep Eutectic Solvents. *J. Colloid Interface Sci.* **2017**, *494*, 373–379. https://doi.org/10.1016/j.jcis.2017.01.109.

(132) Dutta, B. K. *HEAT TRANSFER: PRINCIPLES AND APPLICATIONS*; PHI Learning Private Limited, Delhi, 2013.

(133) Fang, Y. K.; Osama, M.; Rashmi, W.; Shahbaz, K.; Khalid, M.; Mjalli, F. S.; Farid, M. M. Synthesis and Thermo-Physical Properties of Deep Eutectic Solvent-Based Graphene Nanofluids. *Nanotechnology* **2016**, *27* (7). https://doi.org/10.1088/0957-4484/27/7/075702.

(134) Ghosh, P. *Numerical Methods With Computer Programs In C++*; Easter Eco. PHI Learning Private Limited: Delhi, 2009.

(135) Shin, D.; Banerjee, D. Specific Heat of Nanofluids Synthesized by Dispersing

Alumina Nanoparticles in Alkali Salt Eutectic. *Int. J. Heat Mass Transf.* **2014**, *74*, 210–214. https://doi.org/10.1016/j.ijheatmasstransfer.2014.02.066.

(136) Navas, J.; Sánchez-Coronilla, A.; Martín, E. I.; Teruel, M.; Gallardo, J. J.; Aguilar, T.; Gómez-Villarejo, R.; Alcántara, R.; Fernández-Lorenzo, C.; Piñero, J. C.; et al. On the Enhancement of Heat Transfer Fluid for Concentrating Solar Power Using Cu and Ni Nanofluids: An Experimental and Molecular Dynamics Study. *Nano Energy* **2016**, *27*, 213–224. https://doi.org/10.1016/j.nanoen.2016.07.004.

(137) Haar, L.; Gallagher, J. S.; Kell, G. S. *NBS/NRC Steam Tables : Thermodynamic and Transport Properties and Computer Programs for Vapor and Liquid States of Water in SI Units*; Washington (D.C.) : Hemisphere, 1984.

Research Output

Patent

1. A Deep Eutectic solution as heat transfer fluid comprising Diphenyl Ether and Benzophenone, **Pyarimohan Dehury**, and Tamal Banerjee, (*TEMP/E-1/63172/2020-KOL, Patent Appl. No. 202031057115*), Date of Filing, 30th December, 2020.

Journal Publications

1. **Pyarimohan Dehury**, Janardan Singh and Tamal Banerjee. Thermophysical and Forced Convection Studies on (Alumina + Menthol)-Based Deep Eutectic Solvents for Their Use as a Heat Transfer Fluid. *ACS Omega*, 3 (2018) 18016-18027 (**IF: 2.87**). *https://pubs.acs.org/doi/10.1021/acsomega.8b02661*
2. **Pyarimohan Dehury**, Ashvini Kumar Upadhyay and Tamal Banerjee. Evaluation and Conceptual Design of Triphenylphosphonium Bromide based Deep Eutectic Solvent as Novel Thermal Nanofluid for Concentrated Solar Power. *Bulletin of Materials Science*, 42 (2019), 1-8 (**IF: 1.392**). *https://link.springer.com/article/10.1007/s12034-019-1946-6*
3. **Pyarimohan Dehury**, Rahul K. Chaudhary, Tamal Banerjee and Amaresh Dalal. Evaluation of Thermophysical Properties of Menthol-Based Deep Eutectic Solvent as a Thermal Fluid: Forced Convection and Numerical Studies. *Industrial & Engineering Chemistry Research*, 58 (2019) 20125-20133 (**IF: 3.573**), *https://doi.org/10.1021/acs.iecr.9b01836*
4. **Pyarimohan Dehury**, Upasana Mahanta, and Tamal Banerjee. A Comprehensive Assessment on the use of Boron Nitride based Nanofluids Comprising Eutectic mixtures of Diphenyl Ether and Menthol for Enhanced Thermal Media. *ACS Sustainable Chemistry & Engineering* 8 (2020) 14595−14604 (**IF: 7.632**), *https://pubs.acs.org/doi/10.1021/acssuschemeng.0c05648*

Conferences

1. **Pyarimohan Dehury** and Tamal Banerjee. Nanoparticles dispersed deep eutectic solvents (NDDES) as heat transfer fluid (HTF) for solar heat collector. *Global Energy Technology Summit 2015*, November 07-09, 2015, New Delhi, India.
2. **Pyarimohan Dehury** and Tamal Banerjee. Nanoparticles Dispersed Deep Eutectic solvents (NDDES) as Heat Transfer Fluid (HTF) for solar heat collector International *Conference on Nano for Energy and Water (NEW) 2017 and Indo French Workshop on Water Networking*, February 22-24, 2017, UPES, Dehradun, India
3. **Pyarimohan Dehury** and Tamal Banerjee1. Physiochemical Properties of Triphenylphosphonium Bromide based Deep Eutectic Solvent as Novel Thermal Nanofluid. *Materials & Technologies for Energy Conversion and Storage (M-TECS 2018)*, September 26-29, 2018, DAE Convention Centre, Mumbai, India.

ACS OMEGA

Article

Cite This: ACS Omega 2018, 3, 18016−18027

http://pubs.acs.org/journal/acsodf

Thermophysical and Forced Convection Studies on (Alumina + Menthol)-Based Deep Eutectic Solvents for Their Use as a Heat Transfer Fluid

Pyarimohan Dehury, Janardan Singh,[#] and Tamal Banerjee*

Department of Chemical Engineering, Indian Institute of Technology, Guwahati 781039, Assam, India

Supporting Information

ABSTRACT: The current work reports the thermophysical and flow measurements of novel thermal solvents based on deep eutectic solvents (DESs) and alumina-based nanoparticle-dispersed deep eutectic solvents (NDDESs) for its use as a potential solar energy storage medium. The DESs were synthesized using a hydrogen bond donor (i.e., oleic acid) and a hydrogen bond acceptor (i.e., DL-menthol) by using the COSMO-SAC-predicted equimolar ratio at a temperature of 350.15 K. Thereafter, NDDESs or nanofluids were formed by dispersing different volume fractions (0.001, 0.005, 0.0075, and 0.01) of Al_2O_3 nanoparticles in the DESs. The optimum volume fraction (0.005) of Al_2O_3 nanoparticles was selected through their thermophysical properties (density, viscosity, thermal conductivity, and specific heat capacity) and its agglomeration or stability behavior. As expected, NDDESs with a 0.005 volume fraction gave a higher enhancement in thermal conductivity, viscosity, heat capacity, and density as compared to DESs. To evaluate the heat transfer coefficient, forced convection experiments were conducted in a circular test section for both DESs and NDDESs under laminar conditions (Re = 124, 186, and 250). The enhancement of the local heat transfer coefficient was found to be higher when compared to their thermophysical properties. This was due to the nanoparticle migration resulting in a non-uniform distribution of both thermal conductivity and viscosity fields, which was inherently found to reduce the thermal boundary layer thickness. In the final section, the heat transfer coefficient and the Nusselt number were also validated with COMSOL Multiphysics simulations.

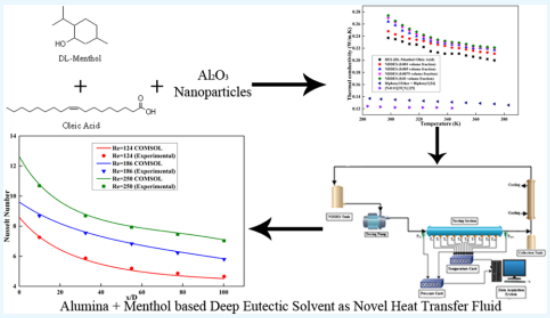

1. INTRODUCTION

Concentrating solar power (CSP) is currently recognized as a valuable source of renewable energy.[1] The stored thermal energy can be utilized in various thermodynamic cycles such as Brayton cycle to generate turbine power from gas turbine engines. The advantage of CSP is that the energy stored in daylight can be used at nighttime where the thermal fluid can potentially reuse the solar energy. The main drawback includes its elevated cost as compared to conventional energy sources. For this reason, the scientific community aims to improve the overall efficiency of these solar plants. One of them is to improve the efficiency of the heat transfer processes that occur in this application. CSP plants usually adopt a technology involving parabolic cylindrical collectors, which in turn uses a heat transfer fluid for the storage and transport of heat. Keeping the CSP process in mind, increasing the heat transfer effect is a key deliverable usually obtained by enhancing the thermophysical properties of these fluids. The current study is thus meant for generating turbine power using the CSP energy storage.

In CSP, the solar energy is usually concentrated using mirrors and lenses and stored in a thermal fluid. The working fluid used in the CSP plant plays an important role in determining the overall efficiency of the system. The conventional thermal fluids have low-to-moderate thermal stability and heat storage capacity, which results in high operating costs.[1] Researchers have tried ionic liquids (ILs) as one of the alternatives for heat transfer fluid for future generations.[2] However, ILs are highly viscous, costly, and difficult to synthesize. Application of ILs in solar collector applications[3,4] have been recently reported. Wu et al.[3] have focused the applicability of 1-butyl-3-methylimidazolium hexafluorophosphate, 1-octyl-3-methylimidazolium hexafluorophosphate, 1-butyl-3-methylimidazolium *bis*-trifluromethane sulfonamide, 1-butyl-3-methylimidazolium tetrafluoroborate, 1-octyl-3-methylimidazolium tetrafluoroborate, and 1-butyl-3-methylimidazolium *bis*-trifluromethane sulfonamide as a thermal energy storage medium for solar collectors. The storage density of 1-octyl-3-methylimidazolium hexafluorophosphate was found to be 378 MJ/m^3. Moens and Blake[4] have performed an overall assessment of ILs for its use as a heat transfer fluid in solar parabolic trough systems.

Received: October 5, 2018
Accepted: December 10, 2018
Published: December 21, 2018

DOI: 10.1021/acsomega.8b02661
ACS Omega 2018, 3, 18016−18027

Bull. Mater. Sci. (2019) 42:262
https://doi.org/10.1007/s12034-019-1946-6

Evaluation and conceptual design of triphenylphosphonium bromide-based deep eutectic solvent as novel thermal nanofluid for concentrated solar power

PYARIMOHAN DEHURY, ASHVINI KUMAR UPADHYAY and TAMAL BANERJEE*
Indian Institute of Technology, Guwahati 781039, India
*Author for correspondence (tamalb@iitg.ac.in)

MS received 24 October 2018; accepted 22 February 2019

Abstract. In a concentrated solar power (CSP) plant, an increase of heat transfer effect of the working fluid is a key deliverable which is usually obtained by enhancing its thermo-physical properties. The current work reports the synthesis of heat transfer fluids (HTF) based on deep eutectic solvents (DESs) consisting of a hydrogen bond donor (HBD), namely, triphenylphosphonium bromide, and a hydrogen bond acceptor (HBA), namely, ethylene glycol. Initially, the thermophysical properties, namely, density, viscosity, thermal conductivity (TC) and specific heat capacity were measured and compared with the conventional solvents. The properties were further enhanced by the dispersion of spherical Al_2O_3 nanoparticles in DESs. The alumina nanoparticles were found to have a negligible effect on the physical properties (density and viscosity) of the base fluid, thereby limiting the pressure drop and also the coefficient of friction. For their potential application as thermal fluids for CSP plants, the thermal properties of DESs and nanoparticle dispersed deep eutectic solvents (NDDESs) were measured within a temperature range of 25–60°C. The TC of 1 wt% Al_2O_3 with the base fluid was around eight times higher than the base DES. It was found that the TCs of DES and NDDES were higher when compared to the commercial HTF, namely, Therminol VP-1. Eventually, the Aspen plus flowsheet was conceptualized to ascertain the steam generation rate and the overall heat transfer coefficient of these novel solvents. A combination of U-shaped for latent heat and shell and tube heat for sensible heat was employed in the flowsheet. The CSP scheme gave a steam generation rate of 1.7 kg h^{-1} at 180°C with a corresponding DES flow rate of 1 m^3 h^{-1}.

Keywords. Deep eutectic solvents; heat transfer fluid; Aspen plus; steam properties.

1. Introduction

Concentrated solar power (CSP) is a valuable source of renewable energy. The solar energy stored in the form of thermal fluid can be exploited in thermodynamic cycles such as Brayton cycle to generate turbine power from gas turbine engines. The advantage of such a system is that the energy stored during the sun hours can be used at night-time primarily due to the reusability of solar energy. One of the main limitations for such a process is its elevated cost owing to parabolic mirrors or collectors and a need for a large land area. This makes the process economically faring poorly when compared to conventional energy sources. It is for this reason that methodology should be developed for utilizing the stored energy in an effective manner. It implies that the scientific community needs to improve the overall efficiency of these solar plants. One of them is to improve the overall heat transfer coefficient of the fluid which usually carries the sensible heat.

In this scenario heat transfer fluids (HTF) play an important role, particularly in CSP, where the solar collectors absorb the solar radiation and convert it into heat energy. This energy is then transferred as heat through a HTF [1]. This makes the evaluation of the thermodynamic properties such as viscosity, density, thermal conductivity (TC) and specific heat capacity (C_p) highly desirable [2,3]. But the limitations of the presently used HTF in CSP are manifested in its lower storage capacity and thermal stability. This ultimately results in a lower cycle efficiency and higher operating cost. Therefore, it is essential to enhance the working efficiency of HTF for achieving a cost-effective CSP system. To meet these requirements, nanoparticle dispersed deep eutectic solvents (NDDESs) have great potential as an alternative to conventional HTF. NDDESs, a class of nanofluids, can be synthesized by dispersing a small amount of nanoparticles in bare deep eutectic solvents (DESs). This synthesis is of one pot in nature and usually occurs within a few hours of the metathesis reaction.

DESs refer to mixtures of two or more compounds in which hydrogen bond donors (HBDs) and hydrogen bond acceptors (HBAs) combine together to form liquids upon mixing. These have melting points below than that of the individual components [4–6]. DESs are now considered as low-cost green solvents having equivalent characteristics compared to ionic liquids (ILs) which are also green in nature but expensive.

Published online: 11 September 2019

I&EC research
Industrial & Engineering Chemistry Research

Article

Cite This: Ind. Eng. Chem. Res. 2019, 58, 20125−20133

pubs.acs.org/IECR

Evaluation of Thermophysical Properties of Menthol-Based Deep Eutectic Solvent as a Thermal Fluid: Forced Convection and Numerical Studies

Pyarimohan Dehury,[†] Rahul K. Chaudhary,[‡] Tamal Banerjee,*[,†] and Amaresh Dalal[‡]

[†]Department of Chemical Engineering and [‡]Department of Mechanical Engineering, Indian Institute of Technology Guwahati, Guwahati 781039, India

ABSTRACT: Concentrated solar power (CSP) is one of the emerging renewable energy technology, where sunlight is concentrated from a large area and is stored in a collector filled with heat-transfer fluid (HTF). The current work reports the synthesis of novel HTF based on menthol-based deep eutectic solvents (DESs). DES consisting of a hydrogen bond acceptor, namely, DL-menthol and a hydrogen bond donor (oleyl alcohol), has been prepared and explored to evaluate its effectiveness as a thermal fluid. The thermal properties, namely, viscosity, density, thermal conductivity (TC), and heat capacity, are measured and compared with both conventional and commercial solvents within the temperature range T = 298.15−353.15 K. The density of DES was found to decrease with increase in temperature, while the rheological measurements suggest a Newtonian fluid with its shear viscosity decreasing exponentially with increasing temperature. The TC of the DES was found to be ∼0.161 W/m K, which decreases linearly with temperature, while a contrary was observed for heat capacity. Further, the performance of these solvents has been evaluated in a forced convective heat-transfer configuration under laminar flow conditions with N_{Re} = 105, 155, and 260. The convective heat-transfer experiments demonstrated the fact that the thermal entrance length of the DES is very large because of its high viscosity and low TC. The convective heat-transfer data, namely, heat-transfer coefficient and Nusselt number, were compared with the in-house AnuPravaha CFD simulator under laminar conditions. From the obtained thermophysical properties, it is confirmed that the synthesized DES can be used as a next-generation heat storage media in the CSP plant.

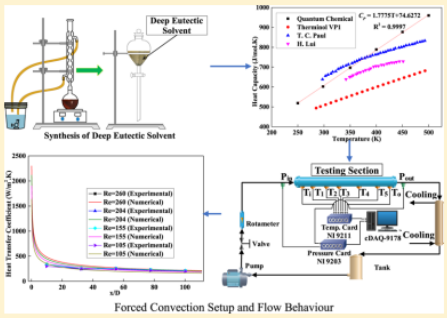

1. INTRODUCTION

The remarkable decrease in the fossil fuels and the simultaneous increase in energy demand has become a challenge for the scientific community. To overcome the ever-expanding energy demand, solar energy can be an alternative source of energy. This is the most copious and readily available sustainable source of energy with zero environmental pollution. The solar energy can be collected and used as potential power sources. In this scenario, heat-transfer fluid (HTF) plays an important role wherein the concentrated solar power (CSP) system[1] is created in terms of parabolic mirrors or solar collectors so as to reflect a higher fraction of sunlight to store energy. Being an important component of any solar thermal system, the solar radiation is absorbed by solar collectors in the form of heat energy and then transfer the heat to a HTF for useful applications. Previously, black liquids have been used as HTF for collecting solar energy.[2] The thermophysical properties for determining the efficiencies for such fluids are thermal conductivity (TC) and specific heat. Additionally, viscosity and density of HTFs also determine the flow behavior of such fluids. Overall, these properties play a vital role in determining the overall efficiency of solar energy utilization.[3,4] However, the restrictions of currently used HTF in CSP are its lower storage capacity and lower thermal stability, resulting in lower cycle efficiency and higher operating cost. Therefore, it is necessary to increase the working efficiency of HTF to achieve a cost-effective efficient CSP system. In general, the CSP is designed based on the thermal fluid. Therefore, CSP is capable of being operated from 473.15 to 1375.15 K.[5−8] Furthermore, for low-to-high-temperature applications, the HTFs deserve superior thermodynamic properties and good thermal stability. In such a scenario, researchers have explored alternative fluids, one of them the conventional eutectic mixtures, comprising of biphenyl derivatives,[9] that is, a combination of diphenyl ether and biphenyl (Therminol VP1). However, these conventional fluids suffer from disadvantages such as high freezing point and lower thermal stability. It is in this scenario, the current work explores alternative solvents, which are also known as deep eutectic solvents (DESs).

Received: April 3, 2019
Revised: September 27, 2019
Accepted: October 4, 2019
Published: October 4, 2019

ACS Sustainable Chemistry & Engineering

pubs.acs.org/journal/ascecg

Research Article

Comprehensive Assessment on the Use of Boron Nitride-Based Nanofluids Comprising Eutectic Mixtures of Diphenyl Ether and Menthol for Enhanced Thermal Media

Pyarimohan Dehury, Upasana Mahanta, and Tamal Banerjee*

Cite This: *ACS Sustainable Chem. Eng.* 2020, 8, 14595−14604

Read Online

ACCESS | Metrics & More | Article Recommendations | Supporting Information

ABSTRACT: The current work explores deep eutectic solvents (DESs) as heat transfer fluids (HTFs) primarily for generating concentrated solar power. The eutectic composition of the DES comprising diphenyl ether and DL-menthol as the hydrogen bond acceptor and hydrogen bond donor was initially computed through the quantum chemical-based COSMO-SAC model. To improve upon the thermal performance and reduce the interfacial resistance, DESs were modified by dispersing hexagonal boron nitride nanoparticles with weight percent ranging from 0.02 to 0.10. Thermophysical properties, namely, density, viscosity, thermal conductivity, and heat capacity, of the HTFs were then measured as a function of temperature. Further, based on these four parameters, the Mouromtseff number (*Mo*) was calculated to rank the nanoparticle-dispersed DESs. The nanofluid consisting of DES-1 with 0.02 wt % of nanoparticles gave the highest *Mo* value, and hence, it was further considered for the experimental forced convection study and process simulation using an Aspen Plus simulator. From the forced convection experiment temperature profiles, the heat transfer coefficient and Nusselt number (*Nu*) were evaluated and compared for nanofluids with the corresponding base fluid. The flow behavior of the thermal fluid along the characteristic length of the test section was investigated for both the laminar and turbulent regimes. The effectiveness of the HTF in terms of steam generation capacity was predicted, and it was observed that the nanofluid with 0.02 wt % was able to successfully convert 100% of the input water (15 kg/h) into superheated steam at the temperature of 494.15 K.

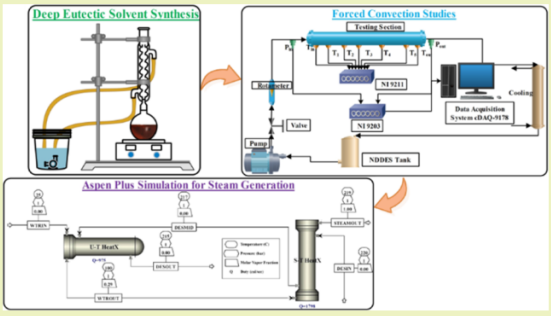

KEYWORDS: *Deep eutectic solvents, Heat transfer fluids, Concentrated solar power, Hexagonal boron nitride*

INTRODUCTION

Solar energy has embarked on its journey in the field of applied energy research as a promising renewable and nonconventional energy resource. It is a clean and abundant source of energy when compared to fossil fuels. The storage of solar radiation in the form of either thermal or electrical energy is an important and key factor for solar energy applications. Solar photovoltaic and concentrated solar power (CSP) are the major industrial level techniques for harvesting solar energy.[1] Several applications of solar energy can be segregated according to temperature levels.[2] Space heating and domestic hot water production are two of the low-temperature applications of solar radiation by direct heating. In most of the commercial CSP plants, solar radiation is collected by a parabolic trough, stored using a heat transfer fluid (HTF), and finally transferred to a steam generator.[1,3] Solar energy can also be stored directly by HTF without the presence of concentrating mirrors.[3] The HTF plays an important role in determining the effectiveness and cost of the process with respect to both CSP and direct storage systems. Examples of commonly used HTFs are molten salts and mineral oils.[4] The melting point of molten salts is above 200 °C, which restricts their application at lower weather conditions.[3,4] Mineral oils need additives in order to enhance the thermal stability. Some of the commercially available HTFs have trade names such as Dowtherm, Syltherm, and Therminol (comprising diphenyl ether and biphenyl).[5] Conventionally, molten salts are primarily used as HTFs in medium- to high-temperature applications. The thermal performance of molten salt-based steam generator technology has been already reported .[6−8] Water was also used in industrial applications such as HTFs.[3,9] However, a narrow liquid range (0−100 °C) and a high vapor pressure of water limit its usability.

Ionic liquids (ILs) have already evolved as a potential solvent for a wide range of industrial applications. The physicochemical

Received: August 2, 2020
Published: August 28, 2020

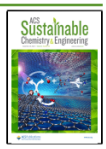

Other Journal Publications

1. Papu Kumar Naik, **Pyarimohan Dehury**, Sandip Paul, Tamal Banerjee. Evaluation of Deep Eutectic Solvent for the selective extraction of toluene and quinoline at T = 308.15 K and p = 1 bar. *Fluid Phase Equilibria*, 423 (2016),146-155 (**IF: 2.838**). *https://doi.org/10.1016/j.fluid.2016.04.018*
2. **Pyarimohan Dehury**, Upasana Mahanta, Tamal Banerjee, Partitioning of butanol between a hydrophobic ionic liquid and aqueous phase: Insights from Liquid Liquid Equilibria measurements and Molecular Dynamics simulations. *Fluid Phase Equilibria*, 425 (2016), 421-431 (**IF: 2.838**). *https://doi.org/10.1016/j.fluid.2016.06.007*
3. Rupesh Verma, **Pyarimohan Dehury**, Anand Bharti and Tamal Banerjee. Liquid-liquid extraction, COSMO-SAC predictions and process flow sheeting of 1-butanol enhancement using mesitylene and oleyl alcohol. *Journal of Molecular Liquids*, 265 (2018), 824-839 (**IF: 5.065**). *https://doi.org/10.1016/j.molliq.2018.06.088*

Other Conferences

1. **Pyarimohan Dehury** and Tamal Banerjee. Process flowsheet and butanol enhancement from aqueous stream. *Outstanding young chemical engineers (OYCE)* March 13-14, 2015, Mumbai, India.
2. **Pyarimohan Dehury** and Tamal Banerjee. Butanol and Ethanol Recovery Using Liquid-Liquid Extraction by Ionic Liquid Solvent [OMIM][Tf2N] at T=298.15 K and p=1 atm. *7th DAE-BRNS Biennial Symposium on Emerging Trends in Separation Science and Technology-SESTEC 2016*, May 17-20, 2016, Indian Institute of Technology, Guwahati, India
3. Rupesh Verma, Anand Bharti, **Pyarimohan Dehury** and Tamal Banerjee. Liquid-Liquid Extraction and Process Flow sheeting of bio-butanol Enhancement using Mesitylene and Oleyl Alcohol. *BIOPROCESSING INDIA 2017*, December 9-11, 2017, Department of Biosciences and Bioengineering, IIT Guwahati, India